



biomimetics

Special Issue Reprint

Advances in Biomimetics

Edited by
Stanislav N. Gorb, Giuseppe Carbone, Thomas Speck and Andreas Taubert

www.mdpi.com/journal/biomimetics



Advances in Biomimetics

Advances in Biomimetics

Editors

Stanislav N. Gorb

Giuseppe Carbone

Thomas Speck

Andreas Taubert

MDPI • Basel • Beijing • Wuhan • Barcelona • Belgrade • Manchester • Tokyo • Cluj • Tianjin



Editors

Stanislav N. Gorb
Department Functional
Morphology and
Biomechanics
University of Kiel
Kiel
Germany

Giuseppe Carbone
Department of Mechanics
Mathematics and
Management
Polytechnic University of Bari
Bari
Italy

Thomas Speck
Botanic Garden
University of Freiburg
Freiburg
Germany

Andreas Taubert
Institute of Chemistry
University of Potsdam
Potsdam
Germany

Editorial Office

MDPI
St. Alban-Anlage 66
4052 Basel, Switzerland

This is a reprint of articles from the Special Issue published online in the open access journal *Biomimetics* (ISSN 2313-7673) (available at: www.mdpi.com/journal/biomimetics/special_issues/Advances_Biomimetics).

For citation purposes, cite each article independently as indicated on the article page online and as indicated below:

LastName, A.A.; LastName, B.B.; LastName, C.C. Article Title. <i>Journal Name</i> Year , <i>Volume Number</i> , Page Range.
--

ISBN 978-3-0365-8469-0 (Hbk)

ISBN 978-3-0365-8468-3 (PDF)

© 2023 by the authors. Articles in this book are Open Access and distributed under the Creative Commons Attribution (CC BY) license, which allows users to download, copy and build upon published articles, as long as the author and publisher are properly credited, which ensures maximum dissemination and a wider impact of our publications.

The book as a whole is distributed by MDPI under the terms and conditions of the Creative Commons license CC BY-NC-ND.

Contents

Preface to "Advances in Biomimetics"	vii
Stanislav N. Gorb, Giuseppe Carbone, Thomas Speck and Andreas Taubert Advances in Biomimetics: Combination of Various Effects at Different Scales Reprinted from: <i>Biomimetics</i> 2023, 8, 329, doi:10.3390/biomimetics8030329	1
Hao Liu, Yue Zhao and Jing Sun Heterogeneous Nucleation in Protein Crystallization Reprinted from: <i>Biomimetics</i> 2023, 8, 68, doi:10.3390/biomimetics8010068	5
Xiao Yang, Wei Zhang, Xuezhi Qin, Miaomiao Cui, Yunting Guo and Ting Wang et al. Recent Progress on Bioinspired Antibacterial Surfaces for Biomedical Application Reprinted from: <i>Biomimetics</i> 2022, 7, 88, doi:10.3390/biomimetics7030088	23
Can Gao, Lei Jiang and Zhichao Dong Effect of Wettability and Adhesion Property of Solid Margins on Water Drainage Reprinted from: <i>Biomimetics</i> 2023, 8, 60, doi:10.3390/biomimetics8010060	49
Carolina Casagualda, Juan Mancebo-Aracil, Miguel Moreno-Villaécija, Alba López-Moral, Ramon Alibés and Félix Busqué et al. Mussel-Inspired Lego Approach for Controlling the Wettability of Surfaces with Colorless Coatings Reprinted from: <i>Biomimetics</i> 2022, 8, 3, doi:10.3390/biomimetics8010003	61
Karuppiiah Nagaraj, Subramanian Sakthinathan, Te-Wei Chiu, Subramaniam Kamalesu, Snehal Lokhandwala and Nikhil M. Parekh et al. States of Aggregation and Phase Transformation Behavior of Metallosurfactant Complexes by Hexacyanoferrate(II): Thermodynamic and Kinetic Investigation of ETR in Ionic Liquids and Liposome Vesicles Reprinted from: <i>Biomimetics</i> 2022, 7, 221, doi:10.3390/biomimetics7040221	73
Elisabetta Rosellini, Nicoletta Barbani, Luigi Lazzeri and Maria Grazia Cascone Biomimetic and Bioactive Small Diameter Tubular Scaffolds for Vascular Tissue Engineering Reprinted from: <i>Biomimetics</i> 2022, 7, 199, doi:10.3390/biomimetics7040199	89
Dolev Frenkel, Eran Ginsbury and Mirit Sharabi The Mechanics of Bioinspired Stiff-to-Compliant Multi-Material 3D-Printed Interfaces Reprinted from: <i>Biomimetics</i> 2022, 7, 170, doi:10.3390/biomimetics7040170	109
Abu A. Ansary, Asad Syed, Abdallah M. Elgorban, Ali H. Bahkali, Rajender S. Varma and Mohd Sajid Khan Neodymium Selenide Nanoparticles: Greener Synthesis and Structural Characterization Reprinted from: <i>Biomimetics</i> 2022, 7, 150, doi:10.3390/biomimetics7040150	123
Falk J. Tauber, Philipp Auth, Joscha Teichmann, Frank D. Scherag and Thomas Speck Novel Motion Sequences in Plant-Inspired Robotics: Combining Inspirations from Snap-Trapping in Two Plant Species into an Artificial Venus Flytrap Demonstrator Reprinted from: <i>Biomimetics</i> 2022, 7, 99, doi:10.3390/biomimetics7030099	133
Ameer Tamoor Khan, Xinwei Cao, Bolin Liao, Adam Francis Bio-inspired Machine Learning for Distributed Confidential Multi-Portfolio Selection Problem Reprinted from: <i>Biomimetics</i> 2022, 7, 124, doi:10.3390/biomimetics7030124	157

Preface to "Advances in Biomimetics"

Biomimetics (also known as bionics or bioinspired technology) refers to research on living systems and attempts to transfer their properties to engineering applications. Biological materials, structures, and processes are predominantly based on the combination of various effects at different scales: from the nano- and microscales through the mesoscale and, finally, to the macroscale. This Special Issue is devoted to the latest advances in biomimetics, covering all of its subfields: (1) materials and structures; (2) design and construction of devices; (3) surfaces and interfaces; (4) architecture and climatization; (5) locomotion and bioinspired robotics; (6) sensorics, information processing, and control; (7) chemical biomimetics; and (8) energy biomimetics. The Guest Editors invited the submission of manuscripts that explore the relationships between the abovementioned topics, especially manuscripts devoted to the development of biomimetic methodology. This Special Issue showcases contributions from biological fields focusing on the identification of underlying principles in living systems, and manuscripts that apply findings obtained from existing systems to modern technologies.

Stanislav N. Gorb, Giuseppe Carbone, Thomas Speck, and Andreas Taubert
Editors



Editorial

Advances in Biomimetics: Combination of Various Effects at Different Scales

Stanislav N. Gorb ^{1,*}, Giuseppe Carbone ², Thomas Speck ³ and Andreas Taubert ⁴

¹ Department of Functional Morphology and Biomechanics, Zoological Institute, Kiel University, D-24118 Kiel, Germany

² Dipartimento di Meccanica-Matematica-Management DMMM, Campus, Via Orabona 4, 70125 Bari, Italy; giuseppe.carbone@poliba.it

³ Plant Biomechanics Group, Botanic Garden, Faculty of Biology, University of Freiburg, Schänzlestraße 1, D-79104 Freiburg, Germany; thomas.speck@biologie.uni-freiburg.de

⁴ Institute of Chemistry, University of Potsdam, Karl-Liebknecht-Str. 24-25, D-14476 Golm, Germany; ataubert@uni-potsdam.de

* Correspondence: sgorb@zoologie.uni-kiel.de

1. Introduction

Biomimetics (bionics, bioinspired technology) refers to research on living systems and attempts to transfer their properties to engineering applications. Biological materials, structures, and processes are predominantly based on the combination of various effects at different scales: from the nano- and microscales, through the mesoscale, and, finally, to the macroscale. This Special Issue is devoted to the latest advances in biomimetics in all its subfields: (1) materials and structures; (2) design, construction, and devices; (3) surfaces and interfaces; (4) architecture and climatization; (5) locomotion and bioinspired robotics; (6) sensorics, information processing, and control; (7) chemical biomimetics; and (8) energy biomimetics. The guest editors encouraged the submission of manuscripts that explore the relationships between these mentioned topics, and especially those devoted to the development of biomimetic methodology. This paper collection contains contributions from biological fields focusing on the proper identification of the underlying principles in nature, and manuscripts that apply the findings on existing systems to modern technologies.

This inaugural Special Issue of *Biomimetics*, celebrating its first impact factor (3.743, June 2022), contains theoretical, experimental, and review contributions from researchers from the fields of biology, physics, material science, and engineering, who are engaged in this fast-growing field of science.

2. Discussion of the Papers

It is important to highlight the review paper on heterogeneous nucleation in protein crystallization by Hao Liu and coworkers (2023) [Contribution 1], and the review paper on the recent progress in bioinspired antibacterial surfaces for biomedical applications by Xiao Yang et al. (2022) [Contribution 2]. Protein crystallization technology is widely used in many fields, and the key to successful crystallization is nucleation in the protein solution. The first review is focused on the key factors influencing protein nucleation, such as the precipitating agent, temperature, solution concentration, and pH. It summarizes crystallization methods and their applications in the crystallography and biopharmaceutical fields (Liu et al., 2023). The second review deals with bacterial fouling, which has become an urgent global challenge in the medical field. In nature, many organisms have evolved numerous surfaces with specific properties to prevent bacterial settlement, and this review highlights biological antibacterial surfaces (Yang et al., 2022). The recent progress in the bioinspired antibacterial strategies and biomedical applications of these antibacterial surfaces is discussed.

Citation: Gorb, S.N.; Carbone, G.; Speck, T.; Taubert, A. Advances in Biomimetics: Combination of Various Effects at Different Scales. *Biomimetics* **2023**, *8*, 329. <https://doi.org/10.3390/biomimetics8030329>

Received: 16 July 2023

Accepted: 18 July 2023

Published: 24 July 2023



Copyright: © 2023 by the authors. Licensee MDPI, Basel, Switzerland. This article is an open access article distributed under the terms and conditions of the Creative Commons Attribution (CC BY) license (<https://creativecommons.org/licenses/by/4.0/>).

The adhesion and wettability of surfaces remain hot topics in biomimetics research. Three contributions in this Special Issue deal with these problems. The paper by Can Gao et al. (2023) [Contribution 3] studies the effects of wettability and adhesion on water drainage. The authors report solid surfaces with high-adhesion hydrophilic margins and hydrophobic margins that stably pin the air–water–solid triple-contact lines at the solid bottom and solid margin, respectively, and then drain water faster through stable water channels. This article provides insights into drainage system design for various applications. The paper by Carolina Casagualda et al. (2023) [Contribution 4] deals with L-DOPA, a catecholic amino acid, present in high amounts in mussel foot proteins and capable of changing the physicochemical properties of surfaces. The authors present a mussel-inspired approach to controlling the wettability of surfaces, which enables the development of coatings with various applications, such as textiles for oil-spill water treatment and multifunctional colorless coatings (Casagualda et al., 2023). Karupiah Nagaraj et al. (2022) [Contribution 5] studied the effects of surfactant complex ions on liposome vesicles. The results differed depending on the presence of hydrophobicity and were interpreted based on the self-aggregation, hydrophobicity, and charge densities of the co-ligand and reactants with opposite charges (Nagaraj et al., 2022).

Biological tissues may show promising biomimetic strategies for the synthesis of scaffolds in tissue engineering. The work by Elisabetta Rosellini et al. (2022) [Contribution 6] aimed at the production and characterization of small biomimetic and bioactive tubular scaffolds for potential application in vascular tissue engineering. The scaffolds were synthesized using a molding technique, starting from a gelatin/gellan/elastin blend mimicking the composition of the extracellular matrix of native blood vessels. Then, the scaffolds were functionalized using different bioactive peptides and later characterized using physicochemical, mechanical, functional, and biological approaches. The developed scaffolds showed good hydrophilicity, an elastic behavior similar to that of natural vessels, no cytotoxic activity, and high suitability for sterilization (Rosellini et al., 2022).

Since biological materials and structures are always composites at several hierarchical levels, they are good examples for creating novel bioinspired stiff-to-compliant multi-materials with enhanced mechanical behavior. Dolev Frenkel et al. (2022) [Contribution 7] used a multi-material 3D printing approach to design complex interfaces that involve a combination of stiff and compliant materials. The authors found that the bioinspired interfaces significantly increased the strain, toughness, and tensile modulus compared with the simple interface. These bioinspired interfaces can be potentially used in the biomedical and robotics fields (Frenkel et al., 2022).

The bioinspired synthesis of nanoparticles remains a rapidly growing field of nanotechnology. The green synthesis and structural characterization of neodymium selenide nanoparticles are the topics of the paper by Abu A. Ansary et al. (2022) [Contribution 8]. For this purpose, they used a reducing agent extracted from the fungus *Fusarium oxysporum*. The hydrodynamic radii of biogenic polydispersed neodymium selenide nanoparticles were 57 nm, with no visible sign of agglomeration, which makes them excellent candidates for applications in labeling and bioimaging technology (Ansary et al., 2022).

Plant-inspired robotics, combining principles underlying the movements, attachment, and adaptability strategies of plants, is a rather novel field of biomimetics research. Falk J. Tauber et al. (2022) [Contribution 9] took combined inspirations from snap trapping in two plant species (*Aldrovanda vesiculosa* and *Dionaea muscipula*) and designed an artificial Venus flytrap demonstrator. The novel motion pattern of the designed technical system is characterized by autonomous motion generation via changes in environmental conditions. The system is not only faster than biological models in its closing movement but also requires less energy for the execution of this movement (Tauber et al., 2022).

Since privacy is of major concern these days, in the paper by Ameer Tamoor Khan et al. (2022) [Contribution 10], the authors proposed a variant of Beetle Antennae Search (BAS) known as Distributed Beetle Antennae Search (DBAS), to optimize multi-portfolio selection problems without violating the privacy of individual portfolios. They applied bioinspired

machine learning to this problem to ensure that client privacy and database secrecy remain intact. The simulation results demonstrated that DBAS not only ensures portfolio privacy but is also efficient and robust in selecting the optimal portfolios (Khan et al., 2022).

3. Conclusions

Due to the success of this first Special Issue of *Advances in Biomimetics*, the guest editor team intends to call for a second Special Issue. This new Special Issue will accept manuscripts on the following: (1) biomimetics of materials and structures; (2) biomimetic design, construction, and devices; (3) biomimetic surfaces and interfaces; (4) bioinspired architecture and climatization; (5) locomotion and bioinspired robotics; (6) bioinspired sensorics, information processing, and control; (7) biomimetic processing, optimization, and management; (8) biomimetic processing and molecular biomimetics; (9) energy biomimetics; and (10) development of biomimetic methodology.

List of Contributions

1. Liu, H.; Zhao, Y.; Sun, J. Heterogeneous Nucleation in Protein Crystallization. *Biomimetics* **2023**, *8*, 68. <https://doi.org/10.3390/biomimetics8010068>.
2. Yang, X.; Zhang, W.; Qin, X.; Cui, M.; Guo, Y.; Wang, T.; Wang, K.; Shi, Z.; Zhang, C.; Li, W.; et al. Recent Progress on Bioinspired Antibacterial Surfaces for Biomedical Application. *Biomimetics* **2022**, *7*, 88. <https://doi.org/10.3390/biomimetics7030088>.
3. Gao, C.; Jiang, L.; Dong, Z. Effect of Wettability and Adhesion Property of Solid Margins on Water Drainage. *Biomimetics* **2023**, *8*, 60. <https://doi.org/10.3390/biomimetics8010060>.
4. Casagualda, C.; Mancebo-Aracil, J.; Moreno-Villaécija, M.; López-Moral, A.; Alibés, R.; Busqué, F.; Ruiz-Molina, D. Mussel-Inspired Lego Approach for Controlling the Wettability of Surfaces with Colorless Coatings. *Biomimetics* **2023**, *8*, 3. <https://doi.org/10.3390/biomimetics8010003>.
5. Nagaraj, K.; Sakthinathan, S.; Chiu, T.-W.; Kamalesu, S.; Lokhandwala, S.; Parekh, N.M.; Karuppiyah, C. States of Aggregation and Phase Transformation Behavior of Metallosurfactant Complexes by Hexacyanoferrate(II): Thermodynamic and Kinetic Investigation of ETR in Ionic Liquids and Liposome Vesicles. *Biomimetics* **2022**, *7*, 221. <https://doi.org/10.3390/biomimetics7040221>.
6. Rosellini, E.; Barbani, N.; Lazzeri, L.; Cascone, M.G. Biomimetic and Bioactive Small Diameter Tubular Scaffolds for Vascular Tissue Engineering. *Biomimetics* **2022**, *7*, 199. <https://doi.org/10.3390/biomimetics7040199>.
7. Frenkel, D.; Ginsbury, E.; Sharabi, M. The Mechanics of Bioinspired Stiff-to-Compliant Multi-Material 3D-Printed Interfaces. *Biomimetics* **2022**, *7*, 170. <https://doi.org/10.3390/biomimetics7040170>.
8. Ansary, A.A.; Syed, A.; Elgorban, A.M.; Bahkali, A.H.; Varma, R.S.; Khan, M.S. Neodymium Selenide Nanoparticles: Greener Synthesis and Structural Characterization. *Biomimetics* **2022**, *7*, 150. <https://doi.org/10.3390/biomimetics7040150>.
9. Tauber, F.J.; Auth, P.; Teichmann, J.; Scherag, F.D.; Speck, T. Novel Motion Sequences in Plant-Inspired Robotics: Combining Inspirations from Snap-Trapping in Two Plant Species into an Artificial Venus Flytrap Demonstrator. *Biomimetics* **2022**, *7*, 99. <https://doi.org/10.3390/biomimetics7030099>.
10. Khan, A.T.; Cao, X.; Liao, B.; Francis, A. Bio-inspired Machine Learning for Distributed Confidential Multi-Portfolio Selection Problem. *Biomimetics* **2022**, *7*, 124. <https://doi.org/10.3390/biomimetics7030124>.

Conflicts of Interest: The authors declare no conflict of interest.

Disclaimer/Publisher’s Note: The statements, opinions and data contained in all publications are solely those of the individual author(s) and contributor(s) and not of MDPI and/or the editor(s). MDPI and/or the editor(s) disclaim responsibility for any injury to people or property resulting from any ideas, methods, instructions or products referred to in the content.

Review

Heterogeneous Nucleation in Protein Crystallization

Hao Liu ¹, Yue Zhao ¹ and Jing Sun ^{2,*} 

¹ Key Laboratory of Biobased Polymer Materials, College of Polymer Science and Engineering, Qingdao University of Science and Technology, Qingdao 266042, China

² State Key Laboratory of Supramolecular Structure and Materials, College of Chemistry, Jilin University, Changchun 130012, China

* Correspondence: jingsun@jlu.edu.cn

Abstract: Protein crystallization was first discovered in the nineteenth century and has been studied for nearly 200 years. Protein crystallization technology has recently been widely used in many fields, such as drug purification and protein structure analysis. The key to successful crystallization of proteins is the nucleation in the protein solution, which can be influenced by many factors, such as the precipitating agent, temperature, solution concentration, pH, etc., among which the role of the precipitating agent is extremely important. In this regard, we summarize the nucleation theory of protein crystallization, including classical nucleation theory, two-step nucleation theory, and heterogeneous nucleation theory. We focus on a variety of efficient heterogeneous nucleating agents and crystallization methods as well. The application of protein crystals in crystallography and biopharmaceutical fields is further discussed. Finally, the bottleneck of protein crystallization and the prospect of future technology development are reviewed.

Keywords: protein crystallization; crystallography; heterogeneous nucleation; crystallization strategy

1. Introduction

Proteins are biological macromolecules composed of one or more long chains of amino acid residues [1]. In the normal functions of an organism, such as metabolic catalysis, stimulation responses require the participation of proteins to function properly. The special biological function of proteins mainly comes from their special three-dimensional arrangement of amino acid residues in the active region. Since protein crystals were first observed in blood in 1840 [2], protein crystallization technology has undergone considerable developments and has been widely used in many fields. With the development of X-ray diffraction, it has become the core technology for analyzing protein crystal structure, which is the most effective means to determine the three-dimensional structure of proteins so far [3–5]. Compared with small molecular crystals, macromolecular protein crystals are smaller in size, less stable, easier to disintegrate, and not easy to subject to X-ray diffraction. The size and quality of the protein crystal will greatly affect the collection of X-ray diffraction data [6]. Obtaining high-quality crystals is the goal that has been pursued in the development of protein crystallography.

In the protein crystallization process, the first step is to reach supersaturation, which has a decisive impact on the nucleation and growth of protein crystals, further affecting the morphology, quality, and size distribution of crystals [7,8]. The nucleation and growth of protein crystals are complex processes that can be influenced by many factors, including the buffer solution, pH [9], temperature [10,11], precipitant, and protein concentration [12]. In particular, precipitants, which can be mainly divided into inorganic salts and organic polymers, are of great importance [13]. Different precipitants have different mechanisms to promote protein crystallization. Inorganic salt precipitants can destroy the hydration layer of proteins, thereby reducing the binding capacity of proteins to water and increasing the binding capacity between proteins. In contrast, organic precipitants enhance the

Citation: Liu, H.; Zhao, Y.; Sun, J. Heterogeneous Nucleation in Protein Crystallization. *Biomimetics* **2023**, *8*, 68. <https://doi.org/10.3390/biomimetics8010068>

Academic Editors: Stanislav N. Gorb and Andreas Taubert

Received: 5 January 2023

Revised: 26 January 2023

Accepted: 1 February 2023

Published: 6 February 2023



Copyright: © 2023 by the authors. Licensee MDPI, Basel, Switzerland. This article is an open access article distributed under the terms and conditions of the Creative Commons Attribution (CC BY) license (<https://creativecommons.org/licenses/by/4.0/>).

electrostatic repulsion and polarity between protein molecules by reducing the dielectric constant [14]. The concentration of precipitant can directly affect the supersaturation of the solution. When the concentration of precipitant is high, the solution is in the nucleation zone or even the precipitation zone. In contrast, a low precipitant concentration results in long crystallization induction time, less crystal nucleation, and slow growth rate [15]. In order to obtain perfect crystals, scientists have also explored various crystallization methods, such as the use of microgravity [16] or an electromagnetic field [17,18]. Lately, new crystallization methods such as *in vivo* protein crystallization [19], counter diffusion technology [20], supercritical fluid crystallization [21], microgravity-controlled precipitation [22], and agarose gel solution crystallization have been developed to prepare protein crystals [23,24]. Additionally, researchers have also developed a series of fluid manipulation technologies and equipment, providing effective and reliable solutions for high-quality protein crystallization screening [25]. All these developments have greatly promoted the recognition of the three-dimensional structure of proteins, which plays a very important role in the research of small-molecule drugs targeting proteins and promoting the development of protein crystallography [26].

In this review, we introduce the development of protein crystallization from the aspects of nucleation mechanisms, heterogeneous nucleating agents, the development of crystallization strategies, and applications in X-ray diffraction and pharmaceuticals. Finally, the bottleneck of protein crystallization and the prospect of future technology development are reviewed.

2. Protein Crystallization Nucleation

2.1. Homogeneous Nucleation

Nucleation is known as a key step to determine protein crystallization [27,28]. The classical nucleation theory is the most widely used theory to describe the nucleation process. A fluctuation in solution concentration enables the formation of reversible and droplet-like molecular clusters, which develop into thermodynamically stable crystal nuclei and then grow into crystals [29]. The classical theory is typically used to describe single component nucleation, whereas it shows limitations in binary or multicomponent nucleation [30].

Wolde and Frenkel reported a two-step mechanism, which exhibited a metastable intermediate phase before the formation of the final crystal structure [31]. A solute molecular cluster of sufficient size was first formed, followed by reorganizing into metastable mesophase, where the nucleation takes place [29]. Protein molecules form a crystal nucleus, which will serve as a structural template to guide the orderly arrangement of other molecules (Figure 1) [32]. This is supported by both experimental results and theoretical simulations. Although the two-step nucleation theory was initially proposed to illustrate the process of protein nucleation and crystallization, recent experimental and theoretical studies show that the theory is also applicable to elucidate the nucleation and crystallization of macromolecules and organic small molecules. For example, Sun et al. demonstrated a two-step strategy to construct supramolecular structures, which mimics the multiple pathways of protein crystallization [33,34].

2.2. Heterogeneous Nucleation

In addition to the above two crystallization theories, heterogeneous nucleation theory also plays an important role in protein crystallization. In 1988, heterogeneous nucleation was first reported as a nucleating manner for protein crystallization [35]. Heterogeneous nucleation can be considered surface- or particle-assisted nucleation [36]. In this process, supersaturation is typically not enough to achieve homogeneous nucleation [29]. This theory proposes that heterogeneous nucleating agents interact with protein molecules and then produce a higher local active protein concentration, which is conducive to the formation of pre-nucleation clusters [37]. Heterogeneous nucleating agents can stabilize these clusters and promote further growth [27,38].

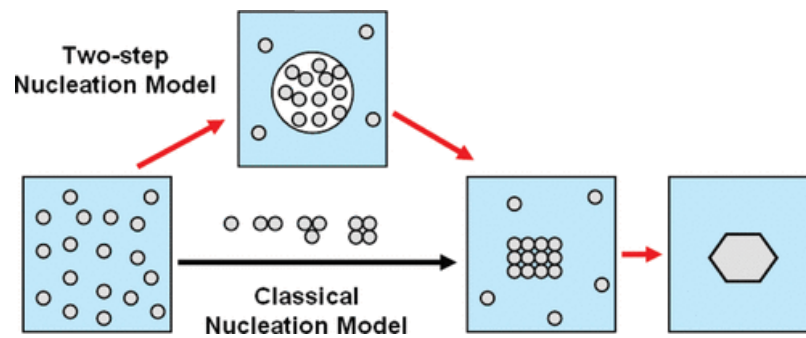


Figure 1. Classical and two-step nucleation models. Reprinted from [32] with permission.

3. Heterogeneous Nucleating Agents

3.1. Nucleating Agents from Natural Sources

Many reports have shown that proteins can nucleate on contaminants such as dust and fibers in crystal droplets. Hair, especially horse hair, has also been used to promote protein crystallization, which is an ideal choice for capturing protein molecules due to its sharp microstructure and overlapping cuticle (Figure 2) [7]. Experimental results show that horse hair can effectively promote the crystallization of three proteins, including Fab-D protein. In addition, human hair can also promote efficient crystallization of the potato serine protein inhibitor that is typically very difficult to crystallize. Thakur et al. tested 9 natural nucleating agents for 10 model proteins and demonstrated that dried seaweed powder can effectively promote protein crystallization [39]. In addition, cellulose and hydroxyapatite powder also have a nucleation effect, but not as obvious as the seaweed. Another interesting phenomenon is that these natural nucleating agents can also inhibit the crystallization of other proteins while promoting the crystallization of specific proteins. Natural minerals can also promote protein crystallization [7]. In 1988, Mcpherson and Paul used 15 different minerals as nucleating agents to conduct crystallization experiments of four model proteins, including canavalin, concanavalin B, beef liver catalase, and lysozyme. They showed that minerals can effectively promote protein nucleation and crystal growth [40].



Figure 2. Crystals of potato serine-protease inhibitor growing on a hair fiber. Reprinted from [7] with permission. The scale bar corresponds to 100 μ m.

3.2. Short Peptide Supramolecular Hydrogels

At present, supramolecular hydrogels can be used as nonconvection media to grow high-quality protein crystals [41,42]. Such supramolecular hydrogels have been widely used in the biomedical field due to their biocompatibility [43]. In particular, short peptide hydrogels are known to form a well-defined 3D ordered structure in stereochemistry [44]. Cienfuegos et al. used the intrinsic chirality of short peptides that can interact with protein diastereomers [45]. This makes short peptide supramolecular hydrogel a good medium for obtaining high-quality protein crystals (Figure 3) [43]. Therefore, short peptide hydrogels have received extensive attention in protein crystallization [46]. They have the potential to manipulate protein solubility without affecting the protein structure or biochemical properties. Although several factors can affect protein crystallization, solubility is a key and relatively atypical factor. In particular, short peptide supramolecular hydrogels can stabilize insulin crystals to a higher degree and slow their release [47,48].

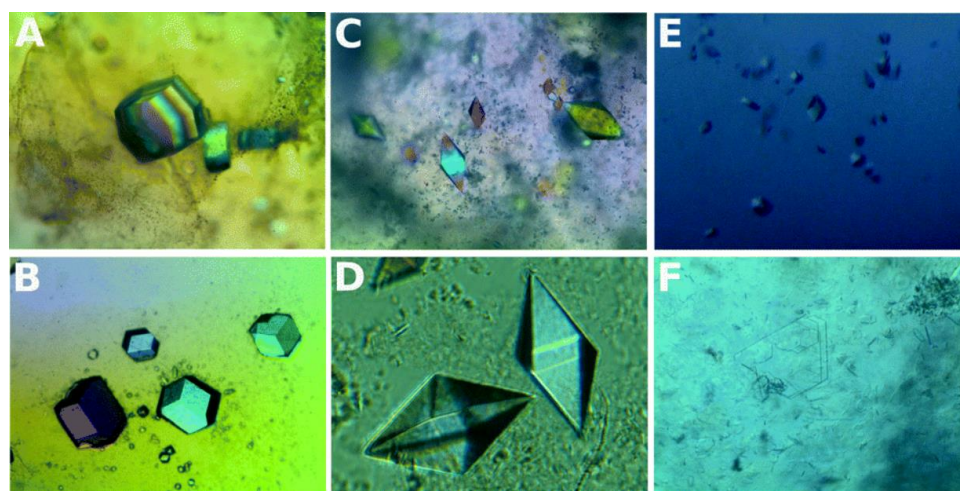


Figure 3. Crystals of lysozyme (A), glucose isomerase (B), thaumatin (C,D), insulin (E), and FASE (F) grown in hydrogels. Reprinted from [43] with permission.

3.3. DNA

A large number of experiments have proved that DNA can be used to promote protein crystallization and may be applied to proteins with difficulty in crystallization. Seeman et al. proposed a few decades ago that protein crystallization can be realized by a series of molecules arranged in the highly ordered structure of DNA building blocks [49,50]. Heng et al. proposed for the first time that DNA origami can be used as a seed to promote protein crystallization [51]. The size and shape of DNA origami are precisely controlled through programmable characteristics and accurate recognition, and the performance of this material is completely consistent. The existence of DNA origami improves the possibility of low-concentration protein crystallization. DNA was found to shorten the induction time of protein crystallization and increase the number of crystals per drop (Figure 4) [52]. In Figure 4, the samples (B, C) with calf DNA have the largest number of crystals per drop, whereas the samples with salmon and herring DNA form larger crystals (D–I). In addition, it was shown that DNA as a heterogeneous nucleating agent could also effectively improve the crystallization rate and control the crystal size. In general, DNA, as a new polymer additive, promotes protein crystallization and greatly improves the success rate of low-concentration protein crystallization. Considering the programmable and designable characteristics of DNA, specific DNA with a clear sequence and length can be synthesized. Therefore, DNA is expected to have excellent potential for improving systems where biomolecules are difficult to crystallize, thus making maximum use of scarce resources [53].

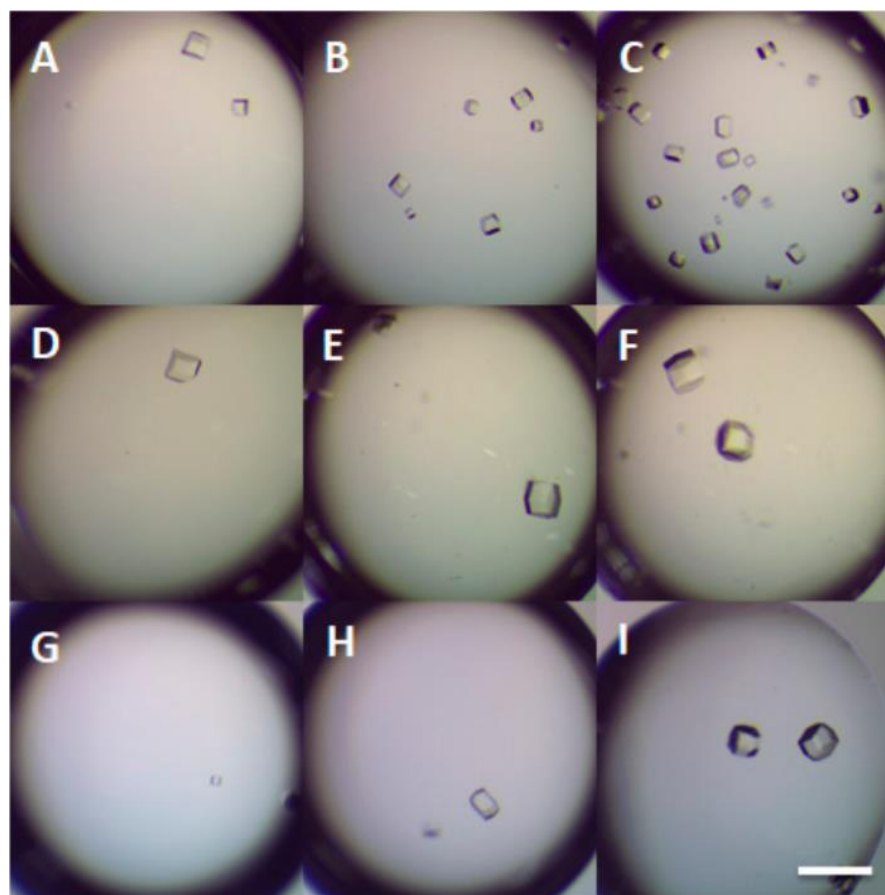


Figure 4. Crystal pictures of 10 mg/mL lysozyme crystallization for 24 h using (A) 0 mg/mL calf DNA, (B) 1.0 mg/mL calf DNA, (C) 5.0 mg/mL calf DNA, (D) 0 mg/mL salmon DNA, (E) 10 mg/mL salmon DNA, (F) 20 mg/mL salmon DNA, (G) 0 mg/mL herring DNA, (H) 10 mg/mL herring DNA, and (I) 20 mg/mL herring DNA. Scale bar: 600 μ m. Reprinted from [52] with permission.

3.4. Nanoparticles

Nanoparticles have a large adsorption surface area, which improves the possibility of binding with protein molecules. In addition, nanoparticles can effectively reduce the nuclear barrier, increase the amount of protein nucleation, and thus promote protein crystallization [54–57]. It has been reported that nanomaterials in the form of aggregates or films could improve the crystallization efficiency of all proteins [58,59]. Nanodiamond (ND) is a kind of carbon-based nanomaterial that has extensive biological application potential [60]. One such application is to promote the nucleation of protein crystals in aqueous solutions (Figure 5) [59]. Through lysozyme, ribonuclease A, proteinase K, and catalase tests, it was found that ND with smaller particle size can adsorb protein more efficiently. Gold nanoparticles (AuNPs) in particular have unique properties, as gold occupies a unique position in the periodic table of elements [47]. Its chemical properties are stable, and it has unique optical properties. Nanoscale gold has better properties than other metals and shows a unique structure and electronic, magnetic, optical, and catalytic properties. This makes it a very attractive material for developing biological nanosystems. Carvalho and Franco et al. concluded from systematic tests and subsequent observation that the introduction of AuNPs should be explicitly considered in the crystal optimization test to improve the previously determined crystallization conditions (Figure 6) [61]. For many proteins that are difficult to crystallize, such as phenylalanine hydroxylase (PHA), myoglobin, native aldehyde oxidase (AOH), its mutant AOH-Y885 M, and albumin, AuNP showed good ability to induce crystallization and the obtained protein crystals possessed good diffraction. Based on the coupling of AuNPs with biomacromolecules and their wide

application and interesting interactions in biomaterials, AuNPs may become potential reagents in protein crystallization experiments [61].

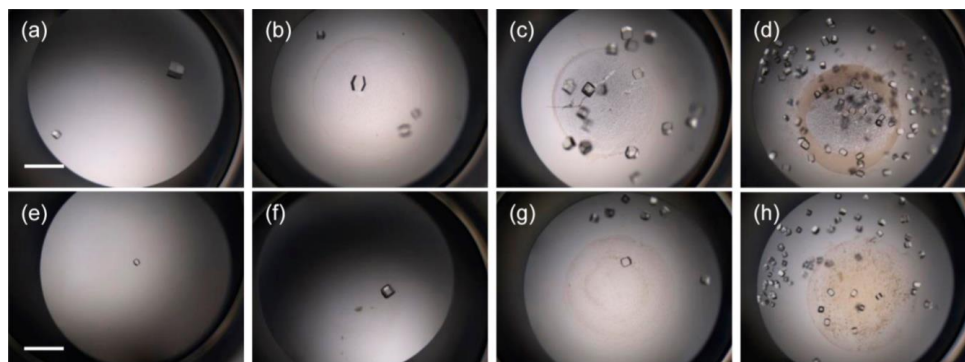


Figure 5. Lysozyme (20 mg/mL) crystallization in the presence of 100 nm ND films (a–d) and 30 nm ND films (e–h) at concentrations of 0, 50, 250, and 500 µg/mL. Scale bar: 500 µm. Reprinted from [59] with permission.

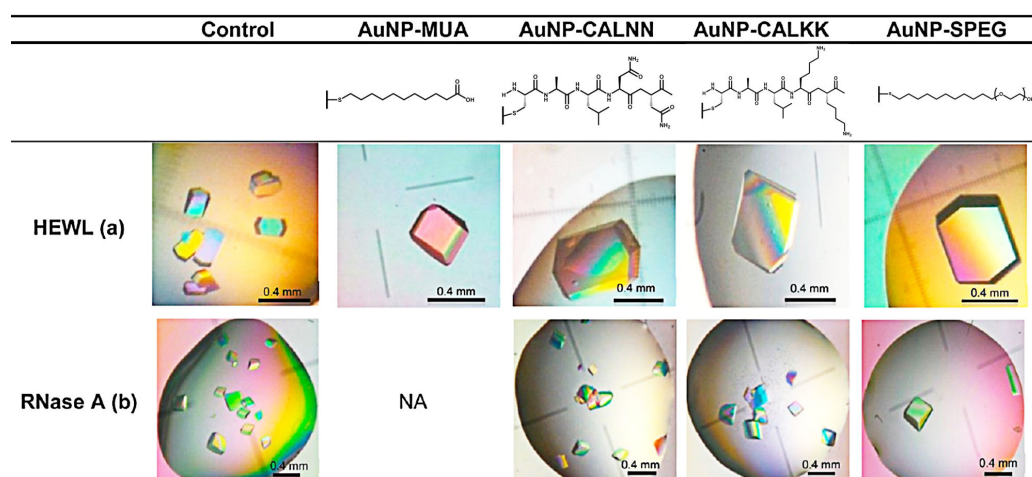


Figure 6. Proteins incubated in the presence of 3 nM AuNPs solutions with (a) 25 mg/mL in 50 mM CH_3COONa and pH 4.5 + 5% NaCl, (b) 50 mg/mL in 50 mM CH_3COONa and pH 5.5 + 3 M NaCl + 1.2 M $(\text{NH}_4)_2\text{SO}_4$. Reprinted from [61] with permission.

3.5. Ionic Liquids

Ionic liquids (ILs) are liquids composed of positive (cationic) and negative (anionic) charges combined by electrostatic interaction [62]. The electromigration of ionic liquids is usually lower than that of the corresponding free ions in aqueous solutions, but it is still too high to observe molecular packing in crystalline solid salts [63]. Therefore, ILs can be regarded as a charged space, which does not form a regular structure, but still maintains a close relationship. Ionic liquids are ideal solvents for biomaterials because of their various properties. Ionic liquids cause changes in crystal morphology and in some cases promote significant increases in crystal size. Crystals grown by Judge et al., using ionic liquids as precipitants or additives, provided a similar or better X-ray diffraction resolution than crystals obtained without ionic liquids (Figure 7) [64]. ILs have been widely used as additives for protein crystallization. Free ionic monomers in ionic liquid solvents provide the possibility to regulate specific interactions, especially anionic hydrogen bonds and cationic surfactant effects. Protein solubility is affected by the action of ionic liquids, inducing protein precipitation and crystallization [65]. Since ionic liquids can slow down the vapor transport rate and control the crystal growth rate, the influence of ionic liquids on the crystallization process is even more obvious than that of precipitation [66].

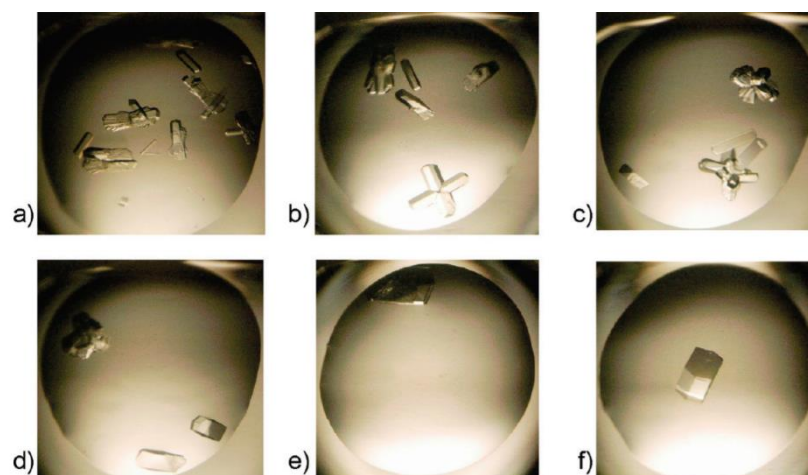


Figure 7. Lysozyme crystallization promoted in the presence of (a) 6%, (b) 9%, (c) 12%, (d) 15%, (e) 18%, and (f) 21% (*w/v*) of 1-ethyl-3-methylimidazolium chloride. Reprinted from [64] with permission.

3.6. Porous Materials

Porous materials can adsorb protein molecules, which are liable to arrange in crystal order. Large single crystals have been reported by using porous materials without sufficient spontaneous nucleation [67]. The holes in porous materials will capture the protein molecules, and the combined diffusion adsorption action can increase the concentration of protein in the holes [68]. It can also enable the crystals to nucleate, which promotes the formation of crystals, thus improving the crystallization rate and quality. Porous silicon is the first reported porous material to promote protein crystallization [69]. Zhang et al. developed a type of CaO-P₂O₅-SiO₂, an amorphous mesoporous bioactive gel glass with pore size distribution in the range of 2–10 nm in diameter. They demonstrated that the obtained bioactive gel glass can effectively promote protein crystallization [70]. Bioglass has been reported to succeed in producing high-quality crystals of model proteins and target proteins. Nanev et al. reported that bioglass promoted the crystallization of 14 proteins, the highest number of mononuclear reagents known. Moreover, most of these proteins are difficult to crystallize under normal conditions (Figure 8) [71].

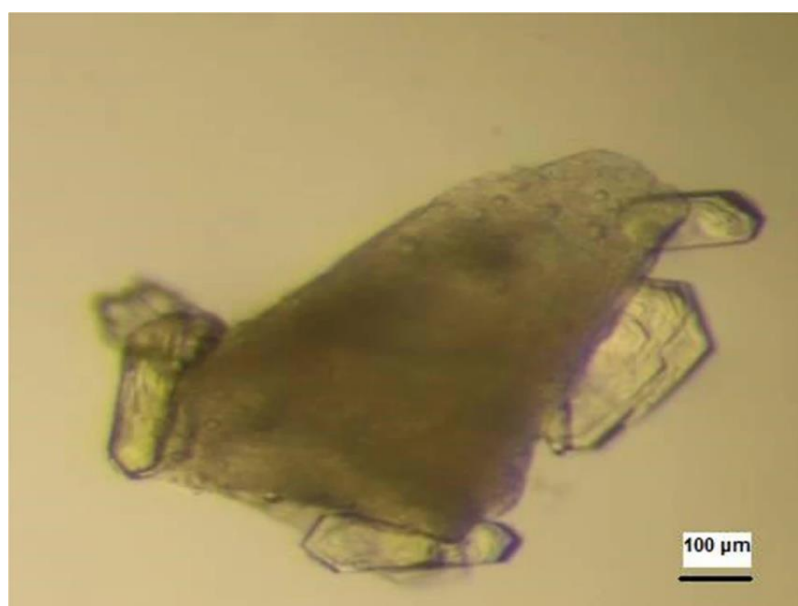


Figure 8. Crystals of a beta lactamase growing on bioglass. Reprinted from [71] with permission.

In particular, molecularly imprinted polymer (MIPs), also known as “smart materials”, employ molecular self-assembly to create cavities that can rebind the corresponding proteins [72]. Such unique properties enable MIPs to serve as ideal templates for crystal formation. Ren et al. successfully fixed the zwitterion on molecularly imprinted polymers and obtained zwitterion-immobilized molecularly imprinted polymers (ziMIPs). ZiMIPs could effectively improve the crystal quality of lysozyme, trypsin, catalase, proteinase K, concanavalin A-IV, and somatine, and greatly shorten the crystallization time (Figure 9) [73]. Chayen et al. used six different molecularly imprinted polymers to promote the crystallization of nine different proteins [74]. No crystals were generated without the addition of molecularly imprinted polymers.

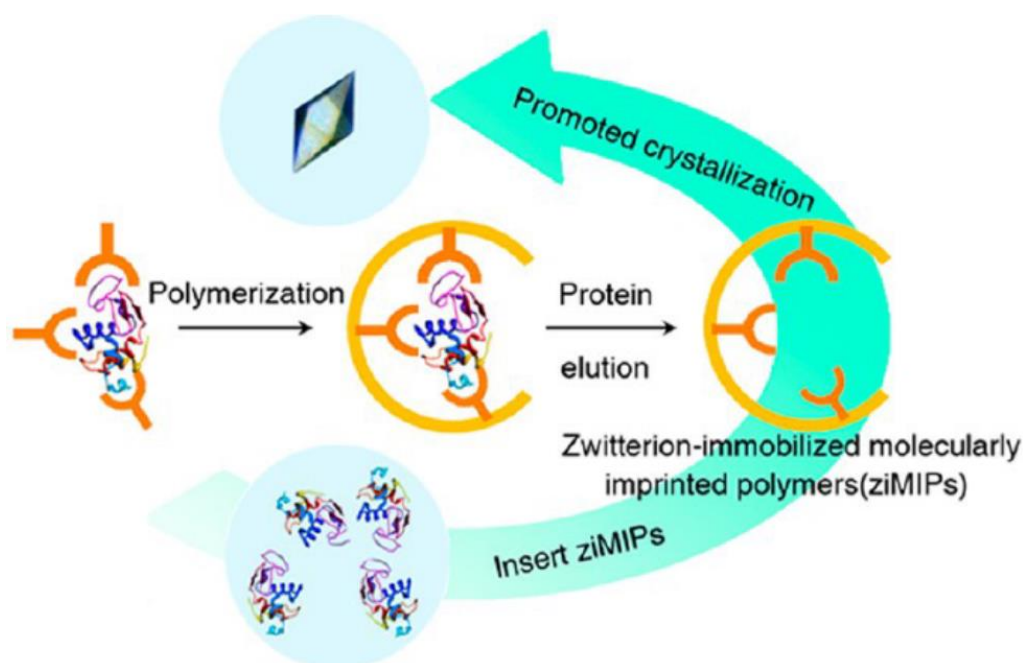


Figure 9. Schematic diagram of zwitterion-immobilized molecularly imprinted polymer synthesis. Reprinted from [73] with permission.

4. Crystallization Strategies

4.1. Functional Interfaces

The crystallization of most proteins begins via heterogeneous nucleation. In fact, the crystallization process usually occurs at the solid interface present in the solution [53]. The solid surface provides nucleation sites such that the nucleation potential barrier on the surface is lower than that in the bulk solution. Different types of solid surfaces exhibit different surface energies, and the nucleation barrier depends on the characteristics of the solid surface [75]. Therefore, treatment of the solid surface may change the surface properties to increase the chances of obtaining protein crystals. Solid surfaces with relatively large sizes (smaller particles) were also tested as effective heterogeneous nuclei (Figure 10) [76]. A mineral matrix [40], silylated mica surface [77], lipid bilayer deposited on a glass cover sheet (for membrane protein crystallization) [78,79], a polymer film containing a poly-L-lysine or poly-L-aspartate ionizable group [80], and modified surfaces with different roughness have all been proven to contribute to protein crystallization [81,82]. These processes depend on the electrostatic interaction between the charged surface and surface proteins with the opposite sign net charge [83]. If the surface can be directly used as a crystal plate or glass cover sheet, the additional step of adding nuclei can be avoided, and heterogeneous nucleation can be more easily applied to high-throughput protein crystallization [84,85].

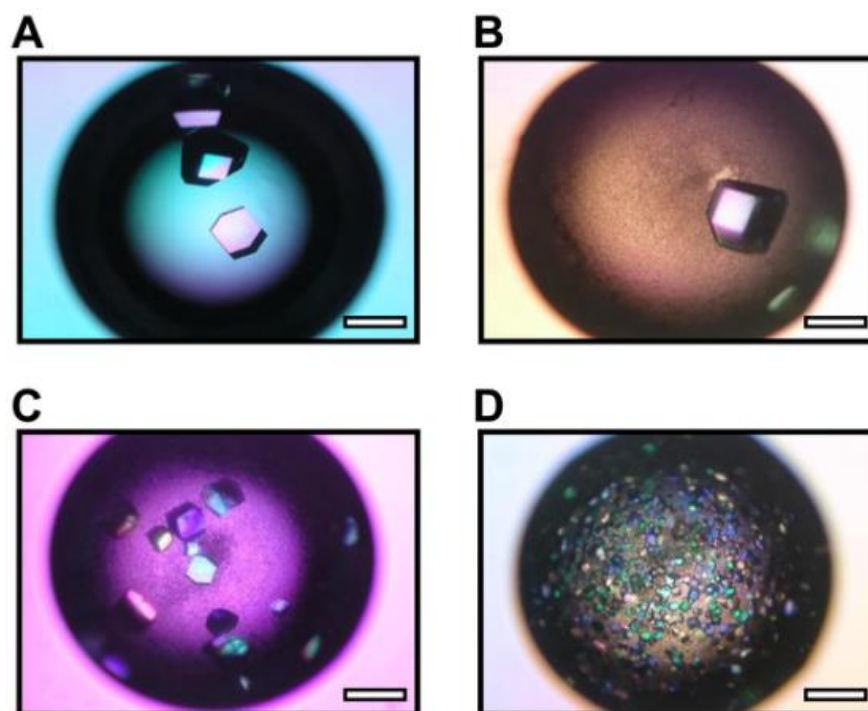


Figure 10. Micrographs of lysozyme crystals in the absence of layered silicate (Control) (A) and in the presence of sericite (B), K-tetrasilic fluoromica (C), and Na-tetrasilic fluoromica (D). Scale bar: 0.5 mm. Reprinted from [76] with permission.

4.2. Electricity and Magnetic Fields

Rothgeb and Oldfield first observed the orientation of myoglobin and cobalt myoglobin microcrystal suspensions in the direction of an applied magnetic field in 1981 [86]. Gavira et al. found that the uniform and constant magnetic field shortened the nucleation induction time, resulting in higher nucleation density, larger crystal size, and improved crystal quality (Figure 11) [87,88]. Experimental studies on protein crystallization using high magnetic fields showed that the number of crystal nuclei decreases, the magnetic orientation of microcrystals decreases, the crystal growth rate is relatively slow, and the crystal dissolution rate decreases when compared with those under normal gravity conditions outside the magnetic field [89,90]. Song et al. developed a small and portable device using a 200 mT magnetic field, which improved the nucleation rate, ensured the growth of large single crystals in a short time, and promoted the crystallization of various proteins [91].

In addition, an electric field can also promote the formation of protein crystals [92]. A large number of experiments showed that lysozyme crystals only appear around the cathode (negatively charged electrode), while amorphous precipitates are observed near the anode (positively charged electrode) (Figure 12) [93]. By applying a direct current, the number of crystals deposited is significantly reduced, and thus, the size of the crystals is increased. A direct current also shortens the nucleation induction time. For example, using the droplet technique developed in Aubry and colleagues' laboratory, it has been proved that the external electric field inhibits the nucleation of HEWL crystals, thereby improving the growth rate of lysozyme crystals in the external electric field [94]. The effect of an external electric field and an ultrasonic field on lysozyme crystallization was evaluated by the batch method. It was also observed that the directional growth of the crystals followed a preferential direction toward the cathode [95]. The application of an electric field will produce a small number of large crystals [96]. Crystals grow on the surface of droplets near the cathode. The nucleation rate is greatly reduced, and this experimental method can be used to control the number of crystals in the droplet [97].

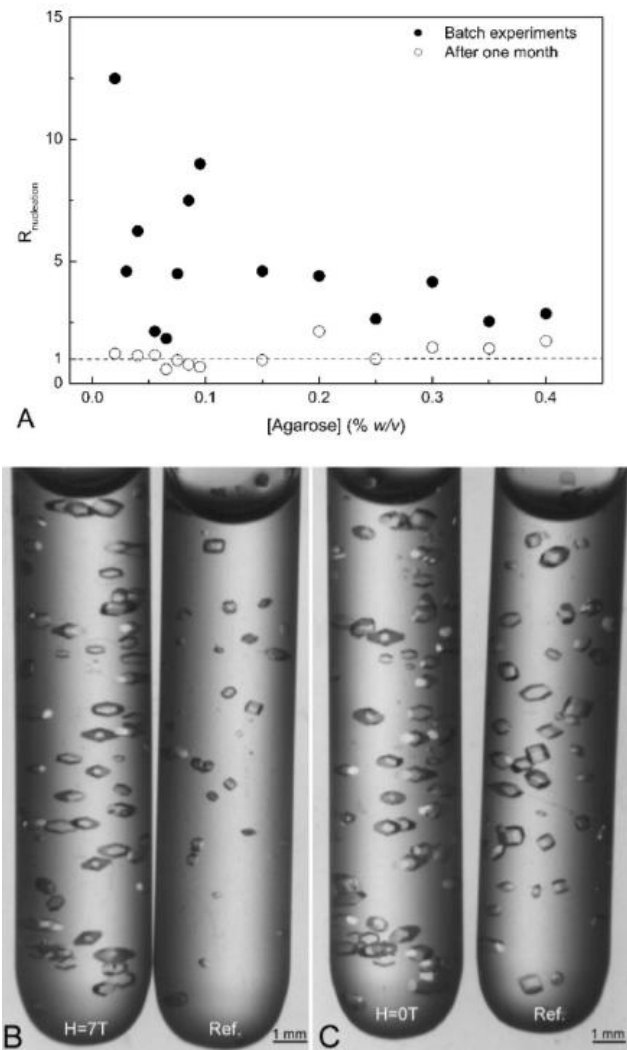


Figure 11. Effects of magnetic field intensity on lysozyme crystallization. (A) The number of crystals in magnetic field divided by the number of crystals in the references. (B,C) Crystals in 0.055% w/v agarose just after being removed from the magnet. Reprinted from [87] with permission.

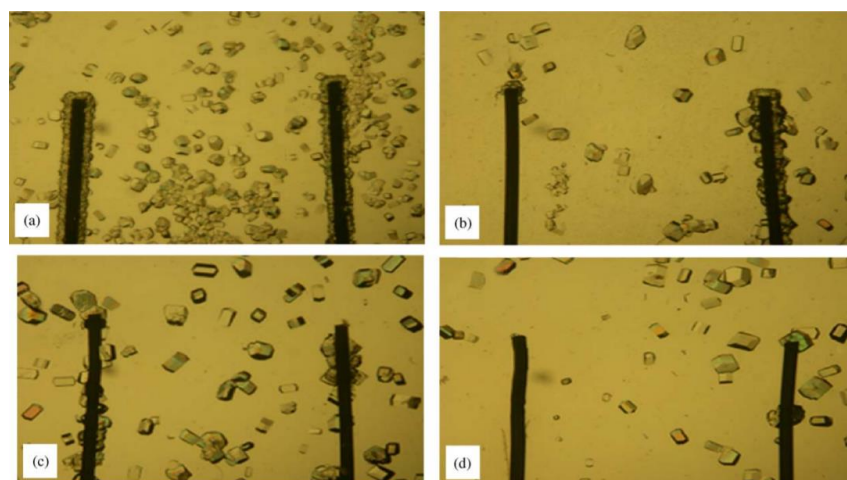


Figure 12. Electric field promotes protein crystallization. Experiments in solution (a) without current, (b) with current, (c) growth in gels without current, and (d) growth in gels in the presence of a constant current. Reprinted from [93] with permission.

4.3. Ultrasonic Field

Ultrasonic crystallization has been widely used in many fields, such as pharmaceutical, chemical, and food applications [98]. In the application of food science in particular, high-intensity ultrasound has been explored as a means to improve the crystallization behavior of fat [99]. The effect of ultrasound on primary nucleation and secondary nucleation may be due to a process called cavitation. Ultrasonic cavitation can be defined as the formation of a vapor cavity or bubble in response to an ultrasonic pressure field. The bubbles generated in the process of cavitation can oscillate around their equilibrium position (stable cavitation) or collapse to form a new bubble group (inertial cavitation). The bubbles generated by cavitation can be used as nucleation sites to induce primary nucleation. On the other hand, if crystals are present before the ultrasonic wave is applied, the high shear force generated during the ultrasonic treatment may induce secondary nucleation through cavitation. Ultrasound can promote the formation of a variety of stable crystal forms in lipid materials and control the polymorphs of crystals. Hao et al. studied the effect of ultrasound on lysozyme crystallization. They demonstrated that under the effect of an ultrasound field, the induction time was significantly shortened, and the aggregation of protein molecules was reduced, which promoted nucleation and increased the crystal size (Figure 13) [100]. Martins et al. also showed that an ultrasonic field could facilitate protein nucleation and improve the quality of protein crystals, which resulted in improved diffraction performance [101]. However, in other research by Hao et al., it was shown that the energy of the ultrasonic field could denature the protein and inhibit protein crystallization once the ultrasonic field was performed for a long time [102].

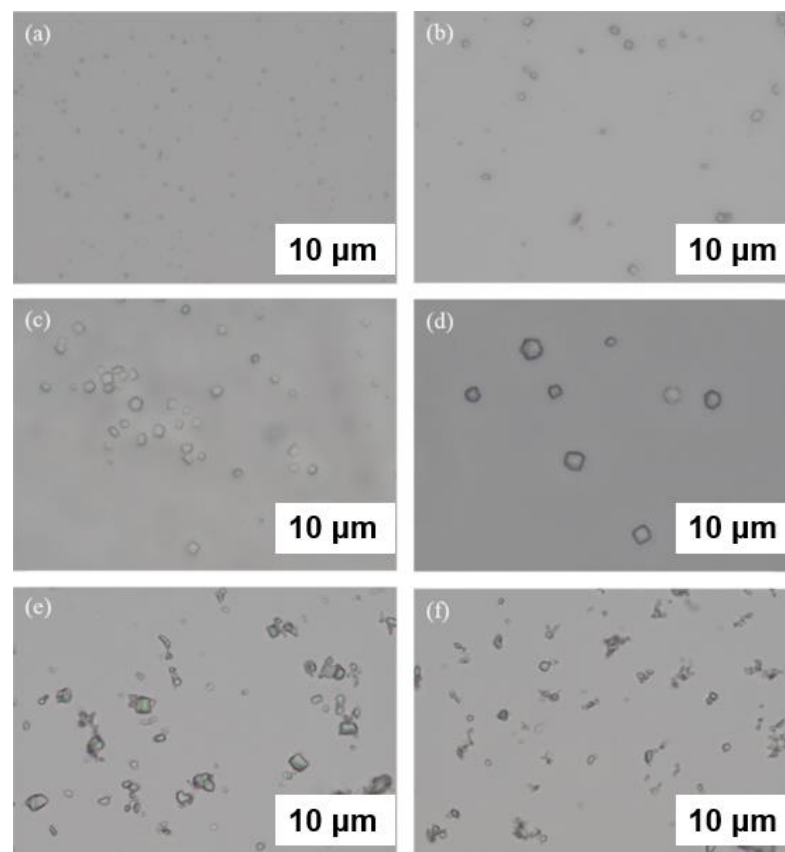


Figure 13. Microscopy images for lysozyme crystals in the nucleation and growth regions (a) in the nucleation region of the ultrasound group at $c_i = 70$ g/g buffer solution, (b) in the nucleation region of the ultrasound group at $c_i = 80$ g/g buffer solution, (c) in the growth region of the ultrasound group at $c_i = 70$ g/g buffer solution, (d) in the growth region of the ultrasound group at $c_i = 80$ g/g buffer solution, (e) in the growth region of the control group at $c_i = 70$ g/g buffer solution, and (f) in the growth region of the control group at $c_i = 80$ g/g buffer solution. Reprinted from [100] with permission.

5. Applications of Protein Crystallization

5.1. X-ray Crystallography

Protein crystals can be used not only for protein purification but also for the determination of protein structure by X-ray diffraction [103]. X-ray crystallography is the primary means and the most important technology to obtain the atomic resolution of a protein structure. The XRD data of protein crystals are analyzed, calculated, and simulated to achieve the protein model (Figure 14) [104]. Obtaining high-quality protein crystals has always been the bottleneck of X-ray single-crystal diffraction technology [105]. The addition of heterogeneous nucleating agents can promote the formation of well-defined crystals, which facilitate improved X-ray diffraction results. As a standard technology in biochemistry and molecular biology, X-ray crystallography has made great progress in the past two decades [106]. At present, X-ray crystallography is becoming a source of information that can not only explain the structure of proteins but also predict the biological characteristics of proteins [107,108].

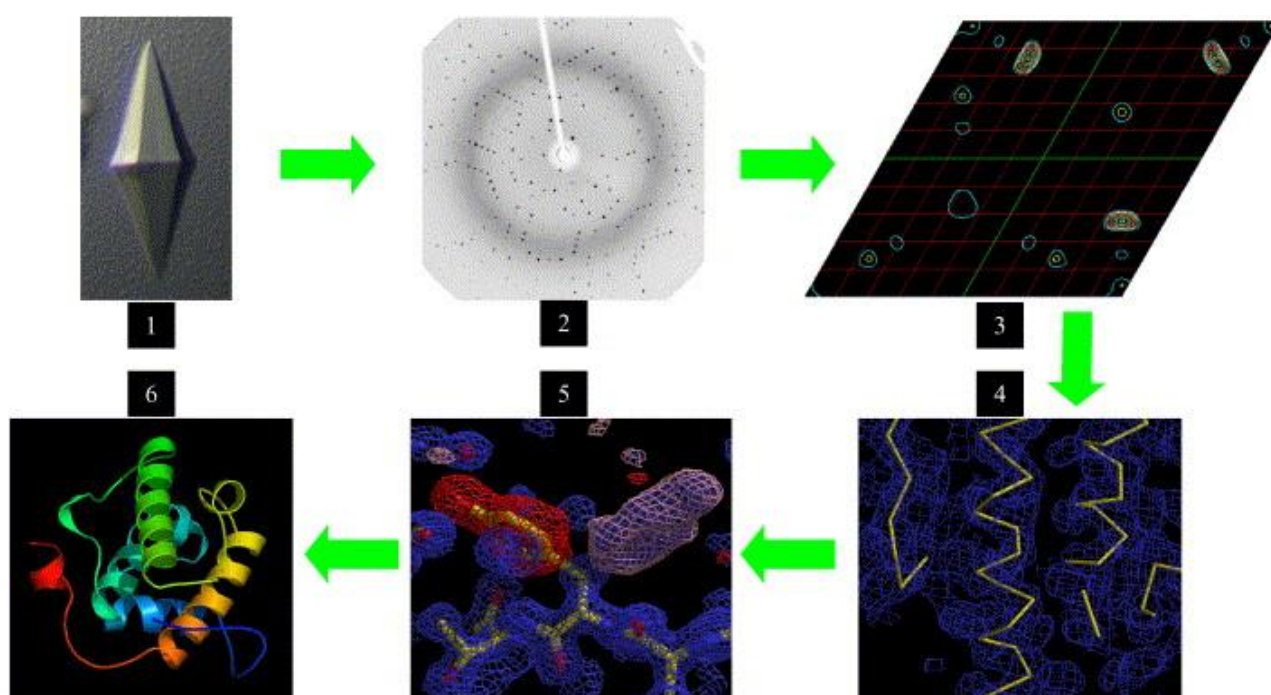


Figure 14. A refinement–analysis–adjustment–refinement cycle to generate the protein model (6). (1) single crystals, (2) oscillation images, (3) a Patterson map, (4) an initial trace of the model, (5) multiple cycles of validation, model re-fitting, and refinement. Reprinted from [104] with permission.

5.2. Pharmaceuticals

Protein crystallization technology is widely used in the biological pharmacy and food industries [109]. Crystallization is typically the last step in many industrial processes used to produce drugs [110]. The function of a protein is closely related to its three-dimensional structure, which plays a very important role in the research of small-molecule drugs targeting certain proteins [111,112]. With more and more protein structures being determined, structure-guided drug design has become an important method for many companies to develop excellent candidate drugs (Figure 15). Agouron Pharmaceuticals has developed Nelfinavir through structural analysis of protein, which is a key component of antiretroviral therapy for AIDS [113].

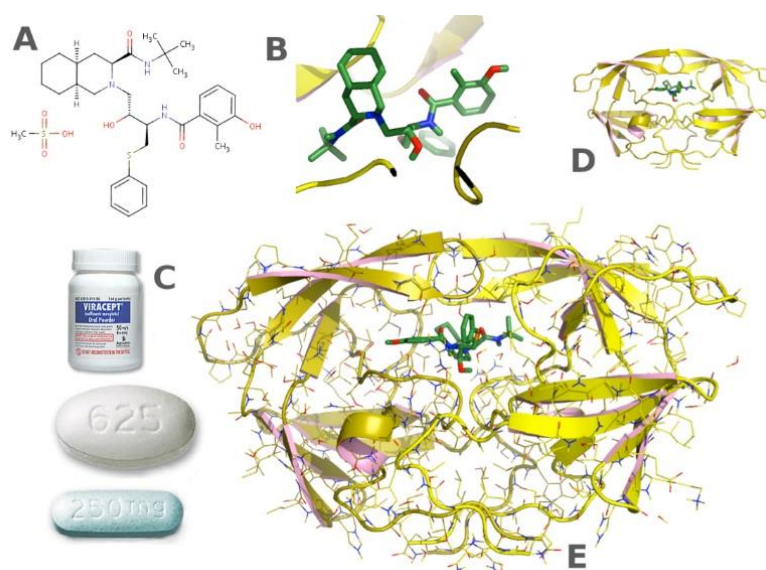


Figure 15. Application of the protein crystallization in pharmaceuticals. (A,B,D,E) Structure-based drug design of HIV protease inhibitors. (C) The formulation for the patient. Reprinted from [113] with permission.

6. Discussion and Perspectives

With the increasing demand for biological drugs in the market, macromolecular drugs such as proteins have attracted more and more attention due to their unique functions. A therapeutic protein in crystalline form has many advantages over its solution form, including higher stability, higher dose concentration, and better release control, such as insulin, infliximab, and trastuzumab. Developing a method that can enhance the protein crystallization process is key to the successful development and large-scale production of protein crystallization drugs. Due to the characteristics of protein such as large molecular weight and high molecular flexibility, it is difficult to obtain high-quality protein crystals. Heterogeneous nucleating agents can reduce the potential barrier to nucleation and make protein crystallization easier. The protein crystallization process is not only sensitive but also has poor repeatability. The strict control of various conditions will also have an impact due to subtle changes in some external factors, such as temperature, pressure, pH, and other factors. Although many methods have been used to conduct the process of protein crystallization, the crystallization effect is very limited and cannot meet expectations. In protein crystallinity research, most of the studies are only conducted for several commonly used proteins, so when these techniques are used to screen other protein crystallization conditions, they lack universal applicability. To resolve this problem, it is necessary to fully understand the crystallization laws of proteins, combine advanced science and technology, and adopt more crystallization strategies and methods to make the target protein easier to crystallize.

Author Contributions: Conceptualization, J.S.; writing—original draft preparation, J.S., H.L., Y.Z.; writing—review and editing, J.S.; supervision, J.S.; project administration, J.S.; funding acquisition, J.S. All authors have read and agreed to the published version of the manuscript.

Funding: This research was funded by the National Natural Science Foundation of China (52273294 and 52073153).

Institutional Review Board Statement: Not applicable.

Informed Consent Statement: Not applicable.

Data Availability Statement: Not applicable.

Conflicts of Interest: The authors declare no conflict of interest.

References

1. Sanvictores, T.; Farci, F. Biochemistry, Primary Protein Structure. In *StatPearls*; StatPearls Publishing: Treasure Island, FL, USA, 2021.
2. McPherson, A. A brief history of protein crystal growth. *J. Cryst. Growth* **1991**, *110*, 1–10. [CrossRef]
3. McPherson, A. Two approaches to the rapid screening of crystallization conditions. *J. Cryst. Growth* **1992**, *122*, 161–167. [CrossRef]
4. Dale, G.E.; Oefner, C.; D'Arcy, A. The protein as a variable in protein crystallization. *J. Struct. Biol.* **2003**, *142*, 88–97. [CrossRef] [PubMed]
5. Chayen, N.E.; Saridakis, E. Protein crystallization: From purified protein to diffraction-quality crystal. *Nat. Methods* **2008**, *5*, 147–153. [CrossRef]
6. Wlodawer, A.; Dauter, Z.; Jaskolski, M. Collection of X-Ray Diffraction Data from Macromolecular Crystals. In *Protein Crystallography. Methods in Molecular Biology*; Wlodawer, A., Dauter, Z., Jaskolski, M., Eds.; Humana Press: New York, NY, USA, 2017; Volume 1607, pp. 165–184.
7. Saridakis, E.; Chayen, N.E. Towards a “universal” nucleant for protein crystallization. *Trends Biotechnol.* **2009**, *27*, 99–106. [CrossRef]
8. Löffelmann, M.; Mersmann, A. How to measure supersaturation? *Chem. Eng. Sci.* **2002**, *57*, 4301–4310. [CrossRef]
9. Zhang, C.Y.; Wu, Z.Q.; Yin, D.C.; Zhou, B.R.; Guo, Y.Z.; Lu, H.M.; Zhou, R.B.; Shang, P. A strategy for selecting the pH of protein solutions to enhance crystallization. *Acta Crystallogr. Sect. F Struct. Biol. Cryst. Commun.* **2013**, *69*, 821–826. [CrossRef]
10. Zhang, C.-Y.; Yin, D.-C.; Lu, Q.-Q.; Guo, Y.; Guo, W.; Wang, X.; Li, H.; Lu, H.; Ye, Y. Cycling Temperature Strategy: A Method to Improve the Efficiency of Crystallization Condition Screening of Proteins. *Cryst. Growth. Des.* **2008**, *8*, 4227–4232. [CrossRef]
11. Liu, J.; Yin, D.C.; Guo, Y.Z.; Wang, X.K.; Xie, S.X.; Lu, Q.Q.; Liu, Y.M. Selecting temperature for protein crystallization screens using the temperature dependence of the second virial coefficient. *PLoS ONE* **2011**, *6*, e17950. [CrossRef]
12. Saridakis, E.; Dierks, K.; Moreno, A.; Dieckmann, M.W.M.; Chayen, N.E. Separating nucleation and growth in protein crystallization using dynamic light scattering. *Acta Crystallogr. D Biol. Crystallogr.* **2002**, *58*, 1597–1600. [CrossRef]
13. Majeed, S.; Ofek, G.; Belachew, A.; Huang, C.-C.; Zhou, T.; Kwong, P.D. Enhancing Protein Crystallization through Precipitant Synergy. *Structure* **2003**, *11*, 1061–1070. [CrossRef] [PubMed]
14. McPherson, A. Crystallization of Macromolecules: General Principles. In *Crystallization and Treatment of Crystals*; Academic Press: Cambridge, MA, USA, 1985.
15. Muschol, M.; Rosenberger, F. Liquid–liquid phase separation in supersaturated lysozyme solutions and associated precipitate formation/crystallization. *J. Chem. Phys.* **1997**, *107*, 1953–1962. [CrossRef]
16. Kundrot, C.E.; Judge, R.A.; Pusey, M.L.; Snell, E.H. Microgravity and Macromolecular Crystallography. *Cryst. Growth. Des.* **2001**, *1*, 87–99. [CrossRef]
17. Cao, H.L.; Sun, L.H.; Li, J.; Tang, L.; Lu, H.M.; Guo, Y.Z.; He, J.; Liu, Y.M.; Xie, X.Z.; Shen, H.F.; et al. A quality comparison of protein crystals grown under containerless conditions generated by diamagnetic levitation, silicone oil and agarose gel. *Acta Crystallogr. D Biol. Crystallogr.* **2013**, *69*, 1901–1910. [CrossRef] [PubMed]
18. Koizumi, H.; Uda, S.; Fujiwara, K.; Nozawa, J. Control of effect on the nucleation rate for hen egg white lysozyme crystals under application of an external ac electric field. *Langmuir* **2011**, *27*, 8333–8338. [CrossRef]
19. Koopmann, R.; Cupelli, K.; Redecke, L.; Nass, K.; Deponte, D.P.; White, T.A.; Stellato, F.; Rehders, D.; Liang, M.; Andreasson, J.; et al. In vivo protein crystallization opens new routes in structural biology. *Nat. Methods* **2012**, *9*, 259–262. [CrossRef]
20. Otalora, F.; Gavira, J.A.; Ng, J.D.; Garcia-Ruiz, J.M. Counterdiffusion methods applied to protein crystallization. *Prog. Biophys. Mol. Biol.* **2009**, *101*, 26–37. [CrossRef]
21. Jarmer, D.J.; Lengsfeld, C.S.; Anseth, K.S.; Randolph, T.W. Supercritical fluid crystallization of griseofulvin: Crystal habit modification with a selective growth inhibitor. *J. Pharm. Sci.* **2005**, *94*, 2688–2702. [CrossRef]
22. Carruthers, C.W., Jr.; Gerdtts, C.; Johnson, M.D.; Webb, P. A microfluidic, high throughput protein crystal growth method for microgravity. *PLoS ONE* **2013**, *8*, e82298. [CrossRef]
23. Moreno, A. Advanced Methods of Protein Crystallization. *Methods Mol. Biol.* **2017**, *1607*, 51–76. [CrossRef]
24. Biertümpfel, C.; Basquin, J.; Suck, D.; Sauter, C. Crystallization of biological macromolecules using agarose gel. *Acta Crystallogr. D Biol. Crystallogr.* **2002**, *58*, 1657–1659. [CrossRef] [PubMed]
25. Stewart, P.S.; Mueller-Dieckmann, J. Automation in biological crystallization. *Acta Crystallogr. F Struct. Biol. Commun.* **2014**, *70*, 686–696. [CrossRef]
26. Stewart, L.; Clark, R.; Behnke, C. High-throughput crystallization and structure determination in drug discovery. *Drug Discov. Today* **2002**, *7*, 187–196. [CrossRef]
27. Zhou, R.-B.; Cao, H.-L.; Zhang, C.-Y.; Yin, D.-C. A review on recent advances for nucleants and nucleation in protein crystallization. *CrystEngComm* **2017**, *19*, 1143–1155. [CrossRef]
28. Vekilov, P.G. Nucleation. *Cryst. Growth Des.* **2010**, *10*, 5007–5019. [CrossRef] [PubMed]
29. Tosi, G.; Fermani, S.; Falini, G.; Gavira, J.A.; Garcia Ruiz, J.M. Hetero- vs Homogeneous Nucleation of Protein Crystals Discriminated by Supersaturation. *Cryst. Growth Des.* **2011**, *11*, 1542–1548. [CrossRef]
30. Nanev, C. Recent Insights into Protein Crystal Nucleation. *Crystals* **2018**, *8*, 219. [CrossRef]

31. Wolde, P.R.T.; Frenkel, D. Enhancement of protein crystal nucleation by critical density fluctuations. *Science* **1997**, *277*, 1975–1978. [CrossRef]
32. Erdemir, D.; Lef, A.Y.; Myerson, A.S. Nucleation of Crystals from Solution: Classical and Two-Step Models. *Acc. Chem. Res.* **2009**, *42*, 621–629. [CrossRef]
33. Shi, Z.; Wei, Y.; Zhu, C.; Sun, J.; Li, Z. Crystallization-Driven Two-Dimensional Nanosheet from Hierarchical Self-Assembly of Polypeptoid-Based Diblock Copolymers. *Macromolecules* **2018**, *51*, 6344–6351. [CrossRef]
34. Sun, J.; Wang, Z.; Zhu, C.; Wang, M.; Shi, Z.; Wei, Y.; Fu, X.; Chen, X.; Zuckermann, R.N. Hierarchical supramolecular assembly of a single peptoid polymer into a planar nanobrush with two distinct molecular packing motifs. *Proc. Natl. Acad. Sci. USA* **2020**, *117*, 31639–31647. [CrossRef] [PubMed]
35. Manuel García-Ruiz, J. Nucleation of protein crystals. *J. Struct. Biol.* **2003**, *142*, 22–31. [CrossRef]
36. Sear, R.P. Nucleation: Theory and applications to protein solutions and colloidal suspensions. *J. Phys. Condens. Matter* **2007**, *19*, 033101. [CrossRef]
37. Tuovinen, S.; Kontkanen, J.; Jiang, J.; Kulmala, M. Investigating the effectiveness of condensation sink based on heterogeneous nucleation theory. *J. Aerosol Sci.* **2020**, *149*, 105613. [CrossRef]
38. Khurshid, S.; Saridakis, E.; Govada, L.; Chayen, N.E. Porous nucleating agents for protein crystallization. *Nat. Protoc.* **2014**, *9*, 1621–1633. [CrossRef]
39. Thakur, A.S.; Robin, G.; Guncar, G.; Saunders, N.F.; Newman, J.; Martin, J.L.; Kobe, B. Improved success of sparse matrix protein crystallization screening with heterogeneous nucleating agents. *PLoS ONE* **2007**, *2*, e1091. [CrossRef]
40. McPherson, A.; Shlichta, P. Heterogeneous and Epitaxial Nucleation of Protein Crystals on Mineral Surfaces. *Science* **1988**, *239*, 385–387. [CrossRef]
41. Artusio, F.; Castellví, A.; Sacristán, A.; Pisano, R.; Gavira, J.A. Agarose Gel as a Medium for Growing and Tailoring Protein Crystals. *Cryst. Growth. Des.* **2020**, *20*, 5564–5571. [CrossRef]
42. Artusio, F.; Castellví, A.; Pisano, R.; Gavira, J.A. Tuning Transport Phenomena in Agarose Gels for the Control of Protein Nucleation Density and Crystal Form. *Crystals* **2021**, *11*, 466. [CrossRef]
43. Conejero-Muriel, M.; Contreras-Montoya, R.; Díaz-Mochón, J.J.; Álvarez de Cienfuegos, L.; Gavira, J.A. Protein crystallization in short-peptide supramolecular hydrogels: A versatile strategy towards biotechnological composite materials. *CrystEngComm* **2015**, *17*, 8072–8078. [CrossRef]
44. Qing, G.; Shan, X.; Chen, W.; Lv, Z.; Xiong, P.; Sun, T. Solvent-Driven Chiral-Interaction Reversion for Organogel Formation. *Angew. Chem. Int. Ed.* **2014**, *53*, 2124–2129. [CrossRef]
45. Conejero-Muriel, M.; Gavira, J.A.; Pineda-Molina, E.; Belsom, A.; Bradley, M.; Moral, M.; Garcia-Lopez Duran Jde, D.; Luque Gonzalez, A.; Diaz-Mochon, J.J.; Contreras-Montoya, R.; et al. Influence of the chirality of short peptide supramolecular hydrogels in protein crystallogenesis. *Chem. Commun.* **2015**, *51*, 3862–3865. [CrossRef] [PubMed]
46. Contreras-Montoya, R.; Arredondo-Amador, M.; Escolano-Casado, G.; Manas-Torres, M.C.; Gonzalez, M.; Conejero-Muriel, M.; Bhatia, V.; Diaz-Mochon, J.J.; Martinez-Augustin, O.; de Medina, F.S.; et al. Insulin Crystals Grown in Short-Peptide Supramolecular Hydrogels Show Enhanced Thermal Stability and Slower Release Profile. *ACS Appl. Mater. Interfaces* **2021**, *13*, 11672–11682. [CrossRef]
47. Tao, K.; Levin, A.; Adler-Abramovich, L.; Gazit, E. Fmoc-modified amino acids and short peptides: Simple bio-inspired building blocks for the fabrication of functional materials. *Chem. Soc. Rev.* **2016**, *45*, 3935–3953. [CrossRef]
48. Fleming, S.; Ulijn, R.V. Design of nanostructures based on aromatic peptide amphiphiles. *Chem. Soc. Rev.* **2014**, *43*, 8150–8177. [CrossRef]
49. Seeman, N.C.; Sleiman, H.F. DNA nanotechnology. *Nat. Rev. Mater.* **2017**, *3*, 17068. [CrossRef]
50. Seeman, N.C. Nucleic Acid Junctions and Lattices. *J. Theor. Biol.* **1982**, *99*, 237–247. [CrossRef]
51. Zhang, B.; Mei, A.R.; Isbell, M.A.; Wang, D.; Wang, Y.; Tan, S.F.; Teo, X.L.; Xu, L.; Yang, Z.; Heng, J.Y.Y. DNA Origami as Seeds for Promoting Protein Crystallization. *ACS Appl. Mater. Interfaces* **2018**, *10*, 44240–44246. [CrossRef] [PubMed]
52. Zhang, B.; Wang, Y.; Thi, S.; Toong, V.; Luo, P.; Fan, S.; Xu, L.; Yang, Z.Q.; Heng, J. Enhancement of Lysozyme Crystallization Using DNA as a Polymeric Additive. *Crystals* **2019**, *9*, 186. [CrossRef]
53. Tosi, G.; Fermani, S.; Falini, G.; Gavira Gallardo, J.A.; Garcia Ruiz, J.M. Crystallization of proteins on functionalized surfaces. *Acta Crystallogr. D Biol. Crystallogr.* **2008**, *64*, 1054–1061. [CrossRef]
54. Mohanraj, V.; Chen, Y. Nanoparticles—A Review. *Trop. J. Pharm. Res.* **2006**, *5*, 561–573. [CrossRef]
55. Hodzhaoglu, F.; Kurniawan, F.; Mirsky, V.; Nanev, C. Gold nanoparticles induce protein crystallization. *Cryst. Res. Technol.* **2008**, *43*, 588–593. [CrossRef]
56. Holcomb, J.; Spellmon, N.; Zhang, Y.; Doughan, M.; Li, C.; Yang, Z. Protein crystallization: Eluding the bottleneck of X-ray crystallography. *AIMS Biophys.* **2017**, *4*, 557–575. [CrossRef] [PubMed]
57. Takeda, Y.; Mafuné, F. Induction of protein crystallization by platinum nanoparticles. *Chem. Phys. Lett.* **2016**, *647*, 181–184. [CrossRef]
58. Chen, W.; Cheng, T.N.H.; Khaw, L.F.; Li, X.; Yang, H.; Ouyang, J.; Heng, J.Y.Y. Protein purification with nanoparticle-enhanced crystallisation. *Sep. Purif. Technol.* **2021**, *255*, 117384. [CrossRef]
59. Chen, Y.W.; Lee, C.H.; Wang, Y.L.; Li, T.L.; Chang, H.C. Nanodiamonds as Nucleating Agents for Protein Crystallization. *Langmuir* **2017**, *33*, 6521–6527. [CrossRef] [PubMed]

60. Kang, M.; Lee, G.; Jang, K.; Jeong, D.W.; Lee, J.-O.; Kim, H.; Kim, Y.J. Graphene Quantum Dots as Nucleants for Protein Crystallization. *Cryst. Growth Des.* **2021**, *22*, 269–276. [CrossRef]
61. Ribeiro, D.; Kulakova, A.; Quaresma, P.; Pereira, E.; Bonifácio, C.; Romão, M.J.; Franco, R.; Carvalho, A.L. Use of Gold Nanoparticles as Additives in Protein Crystallization. *Cryst. Growth Des.* **2013**, *14*, 222–227. [CrossRef]
62. Belviso, B.D.; Caliandro, R.; Salehi, S.M.; Di Profio, G.; Caliandro, R. Protein Crystallization in Ionic-Liquid Hydrogel Composite Membranes. *Crystals* **2019**, *9*, 253. [CrossRef]
63. Garlitz, J.A.; Summers, C.A.; Flowers, R.A., II; Borgstahl, G.E.O. Ethylammonium nitrate: A protein crystallization reagent. *Acta Crystallogr. D Biol. Crystallogr.* **1999**, *D55*, 2037–2038. [CrossRef]
64. Judge, R.A.; Takahashi, S.; Longenecker, K.L.; Fry, E.H.; Abad-Zapatero, C.; Chiu, M.L. The Effect of Ionic Liquids on Protein Crystallization and X-ray Diffraction Resolution. *Cryst. Growth Des.* **2009**, *2009*, 3463–3469. [CrossRef]
65. Schroder, C. Proteins in Ionic Liquids: Current Status of Experiments and Simulations. *Top. Curr. Chem.* **2017**, *375*, 25. [CrossRef]
66. Kowacz, M.; Marchel, M.; Juknaitė, L.; Esperança, J.M.S.S.; Romão, M.J.; Carvalho, A.L.; Rebelo, L.P.N. Ionic-Liquid-Functionalized Mineral Particles for Protein Crystallization. *Cryst. Growth Des.* **2015**, *15*, 2994–3003. [CrossRef]
67. Chayen, N.E.; Saridakis, E.; Sear, R.P. Experiment and theory for heterogeneous nucleation of protein crystals in a porous medium. *Proc. Natl. Acad. Sci. USA* **2006**, *103*, 597–601. [CrossRef] [PubMed]
68. Guo, Y.Z.; Sun, L.H.; Oberthuer, D.; Zhang, C.Y.; Shi, J.Y.; Di, J.L.; Zhang, B.L.; Cao, H.L.; Liu, Y.M.; Li, J.; et al. Utilisation of adsorption and desorption for simultaneously improving protein crystallization success rate and crystal quality. *Sci. Rep.* **2014**, *4*, 7308. [CrossRef] [PubMed]
69. Chayen, N.E.; Saridakis, E.; El-Bahar, R.; Nemirovsky, Y. Porous silicon: An effective nucleation-inducing material for protein crystallization. *J. Mol. Biol.* **2001**, *312*, 591–595. [CrossRef] [PubMed]
70. Zhang, X.; Guo, X.; Zhang, J.; Fan, X.; Chen, M.; Yang, H. Nucleation, crystallization and biological activity of Na₂O-CaO-P₂O₅-SiO₂ bioactive glass. *J. Non-Cryst. Solids* **2021**, *568*, 120929. [CrossRef]
71. Nanev, C.N.; Saridakis, E.; Chayen, N.E. Protein crystal nucleation in pores. *Sci. Rep.* **2017**, *7*, 35821. [CrossRef]
72. Saridakis, E.; Khurshid, S.; Govada, L.; Phan, Q.; Hawkins, D.; Crichlow, G.V.; Lolis, E.; Reddy, S.M.; Chayen, N.E. Protein crystallization facilitated by molecularly imprinted polymers. *Proc. Natl. Acad. Sci. USA* **2011**, *108*, 11081–11086. [CrossRef]
73. Xing, Y.; Hu, Y.; Jiang, L.; Gao, Z.; Chen, Z.; Ren, X. Zwitterion-Immobilized Imprinted Polymers for Promoting the Crystallization of Proteins. *Cryst. Growth Des.* **2015**, *15*, 4932–4937. [CrossRef]
74. Saridakis, E.; Chayen, N.E. Imprinted polymers assisting protein crystallization. *Trends Biotechnol.* **2013**, *31*, 515–520. [CrossRef] [PubMed]
75. Zhang, C.-Y.; Shen, H.-F.; Wang, Q.-J.; Guo, Y.-Z.; He, J.; Cao, H.-L.; Liu, Y.-M.; Shang, P.; Yin, D.-C. An Investigation of the Effects of Self-Assembled Monolayers on Protein Crystallisation. *Int. J. Mol. Sci.* **2013**, *14*, 12329–12345. [CrossRef]
76. Ino, K.; Udagawa, I.; Iwabata, K.; Takakusagi, Y.; Kubota, M.; Kurosaka, K.; Arai, K.; Seki, Y.; Nogawa, M.; Tsunoda, T.; et al. Heterogeneous nucleation of protein crystals on fluorinated layered silicate. *PLoS ONE* **2011**, *6*, e22582. [CrossRef]
77. Tang, L.; Huang, Y.B.; Liu, D.Q.; Li, J.L.; Mao, K.; Liu, L.; Cheng, Z.J.; Gong, W.M.; Hu, J.; He, J.H. Effects of the silanized mica surface on protein crystallization. *Acta Crystallogr. D Biol. Crystallogr.* **2005**, *61*, 53–59. [CrossRef]
78. Hemming, S.A.; Bochkarev, A.; Kornberg, R.D.; Ala, P.; Edwards, A.M. The Mechanism of Protein Crystal Growth from Lipid Layers. *J. Mol. Biol.* **1995**, *246*, 308–316. [CrossRef]
79. Wallace, E.; Dranow, D.; Laible, P.D.; Christensen, J.; Nollert, P. Monoolein lipid phases as incorporation and enrichment materials for membrane protein crystallization. *PLoS ONE* **2011**, *6*, e24488. [CrossRef] [PubMed]
80. Fermani, S.; Falini, G.; Minnucci, M.; Ripamonti, A. Protein crystallization on polymeric film surfaces. *J. Cryst. Growth* **2001**, *224*, 327–334. [CrossRef]
81. Liu, Y.-X.; Wang, X.-J.; Lu, J.; Ching, C.-B. Influence of the Roughness, Topography, and Physicochemical Properties of Chemically Modified Surfaces on the Heterogeneous Nucleation of Protein Crystals. *J. Phys. Chem. B* **2007**, *111*, 13971–13978. [CrossRef]
82. Guo, Y.-Z.; Yin, D.-C.; Lu, Q.-Q.; Wang, X.-K.; Liu, J. Enhancement of nucleation during hanging drop protein crystallization using HF Treatment of cover glasses. *Cryst. Res. Technol.* **2010**, *45*, 158–166. [CrossRef]
83. Pham, T.; Lai, D.; Ji, D.; Tuntiwechapikul, W.; Friedman, J.M.; Lee, T.R. Well-ordered self-assembled monolayer surfaces can be used to enhance the growth of protein crystals. *Colloids Surf. B Biointerfaces* **2004**, *34*, 191–196. [CrossRef] [PubMed]
84. Ji, D.; Arnold, C.M.; Graupe, M.; Beadle, E.; Dunn, R.V.; Phan, M.N.; Villazana, R.J.; Benson, R.; Colorado, R., Jr; Lee, T.R.; et al. Improved protein crystallization by vapor diffusion from drops in contact with transparent, self-assembled monolayers on gold-coated glass coverslips. *J. Cryst. Growth* **2000**, *218*, 390–398. [CrossRef]
85. Pechkova, E.; Nicolini, C. Accelerated protein crystal growth by protein thin film template. *J. Cryst. Growth* **2001**, *231*, 599–602. [CrossRef]
86. Rothgeb, T.M.; Oldfield, E. Nuclear magnetic resonance of heme protein crystals. General aspects. *J. Biol. Chem.* **1981**, *256*, 1432–1446. [CrossRef] [PubMed]
87. Gavira, J.A.; Garcí'a-Ruiz, J.M. Effects of a Magnetic Field on Lysozyme Crystal Nucleation and Growth in a Diffusive Environment. *Cryst. Growth Des.* **2009**, *9*, 2610–2615. [CrossRef]
88. Satoa, T.; Yamadaa, Y.; Saijoa, S.; Horia, T.; Hirosea, R.; Tanakaa, N.; Sazakib, G.; Nakajimab, K.; Igarashid, N.; Tanakad, M.; et al. Improvement in diffraction maxima in orthorhombic HEWL crystal grown under high magnetic field. *J. Cryst. Growth* **2001**, *232*, 229–236. [CrossRef]

89. Nakamura, A.; Ohtsuka, J.; Miyazono, K.-i.; Yamamura, A.; Kubota, K.; Hirose, R.; Hirota, N.; Ataka, M.; Sawano, Y.; Tanokura, M. Improvement in Quality of Protein Crystals Grown in a High Magnetic Field Gradient. *Cryst. Growth Des.* **2012**, *12*, 1141–1150. [CrossRef]
90. Sazaki, G.; Yoshida, E.; Komatsu, H.T.; Nakada, S.M.; Watanabe, K. Effects of a magnetic field on the nucleation and growth of protein crystals. *J. Cryst. Growth* **1997**, *173*, 231–234. [CrossRef]
91. Ryu, S.; Oh, I.; Cho, S.; Kim, S.; Song, H. Enhancing Protein Crystallization under a Magnetic Field. *Crystals* **2020**, *10*, 821. [CrossRef]
92. Chin, C.C.; Dence, J.B.; Warren, J.C. Crystallization of human placental estradiol 17beta-dehydrogenase. A new method for crystallizing labile enzymes. *J. Biol. Chem.* **1976**, *251*, 3700–3705. [CrossRef]
93. Moreno, A.; Sazaki, G. The use of a new ad hoc growth cell with parallel electrodes for the nucleation control of lysozyme. *J. Cryst. Growth* **2004**, *264*, 438–444. [CrossRef]
94. Nanev, C.N.; Penkova, A. Nucleation and growth of lysozyme crystals under external electric field. *Colloids Surf. A* **2002**, *209*, 139–145. [CrossRef]
95. Mirkin, N.; Frontana-Uribe, B.A.; Rodríguez-Romero, A.; Hernández-Santoyo, A.; Moreno, A. The influence of an internal electric field upon protein crystallization using the gel-acupuncture method. *Acta Crystallogr. D Biol. Crystallogr.* **2003**, *59 Pt 9*, 1533–1538. [CrossRef]
96. Penkova, A.; Gliko, O.; Dimitrov, I.L.; Hodjaoglu, F.V.; Nanev, C.; Vekilov, P.G. Enhancement and suppression of protein crystal nucleation due to electrically driven convection. *J. Cryst. Growth* **2005**, *275*, e1527–e1532. [CrossRef]
97. Taleb, M.; Didierjean, C.; Jelsch, C.; Mangeot, J.P.; Capelle, B.; Aubry, A. Crystallization of proteins under an external electric field. *J. Cryst. Growth* **1999**, *200*, 575–582. [CrossRef]
98. Sabnis, S.S.; Gogate, P.R. Ultrasound assisted size reduction of DADPS based on recrystallization. *Ultrason. Sonochem.* **2019**, *54*, 198–209. [CrossRef] [PubMed]
99. Suzuki, A.H.; Lee, J.; Padilla, S.G.; Martini, S. Altering functional properties of fats using power ultrasound. *J. Food Sci.* **2010**, *75*, E208–E214. [CrossRef]
100. Yu, F.; Mao, Y.; Zhao, H.; Zhang, X.; Wang, T.; Yuan, M.; Ding, S.; Wang, N.; Huang, X.; Hao, H. Enhancement of Continuous Crystallization of Lysozyme through Ultrasound. *Org. Process Res. Dev.* **2021**, *25*, 2508–2515. [CrossRef]
101. Crespo, R.; Martins, P.M.; Gales, L.; Rocha, F.; Damas, A.M. Potential use of ultrasound to promote protein crystallization. *J. Appl. Crystallogr.* **2010**, *43*, 1419–1425. [CrossRef]
102. Mao, Y.; Li, F.; Wang, T.; Cheng, X.; Li, G.; Li, D.; Zhang, X.; Hao, H. Enhancement of lysozyme crystallization under ultrasound field. *Ultrason. Sonochem.* **2020**, *63*, 104975. [CrossRef] [PubMed]
103. Bailey, J. X-ray Crystallography of Biomolecules. In *Inventive Geniuses Who Changed the World*; Springer: Cham, Switzerland, 2022; pp. 301–312.
104. Pusey, M.L.; Liu, Z.J.; Tempel, W.; Praissman, J.; Lin, D.; Wang, B.C.; Gavira, J.A.; Ng, J.D. Life in the fast lane for protein crystallization and X-ray crystallography. *Prog. Biophys. Mol. Biol.* **2005**, *88*, 359–386. [CrossRef]
105. Stojanoff, V.; Northrup, P.; Pietri, R.; Zhong, Z. Synchrotron Radiation in Life Sciences. *Protein Pept. Lett.* **2012**, *19*, 761–769. [CrossRef]
106. Kojić-Prodić, B. A century of X-ray crystallography and 2014 international year of X-ray crystallography. *Maced. J. Chem. Chem. Eng.* **2015**, *34*, 19–32. [CrossRef]
107. Sherwood, D.; Cooper, J. *Crystals, X-rays and Proteins: Comprehensive Protein Crystallography*; Sherwood, D., Ed.; Oxford University Press: Oxford, UK, 2010.
108. Yonekura, K.; Kato, K.; Ogasawara, M.; Tomita, M.; Toyoshima, C. Electron crystallography of ultrathin 3D protein crystals: Atomic model with charges. *Proc. Natl. Acad. Sci. USA* **2015**, *112*, 3368–3373. [CrossRef] [PubMed]
109. McLaughlin, K.J. Developing a macromolecular crystallography driven CURE. *Struct. Dyn.* **2021**, *8*, 020406. [CrossRef] [PubMed]
110. Alexandrov, D.V.; Nizovtseva, I.G. On the theory of crystal growth in metastable systems with biomedical applications: Protein and insulin crystallization. *Philos. Trans. A Math. Phys. Eng. Sci.* **2019**, *377*, 20180214. [CrossRef]
111. Klabunde, T.; Hessler, G. Drug Design Strategies for Targeting G-Protein-Coupled Receptors. *Chembiochem* **2002**, *3*, 928–944. [CrossRef]
112. Reed, J.C. Apoptosis-regulating proteins as targets for drug discovery. *Trends Mol. Med.* **2001**, *7*, 314–319. [CrossRef]
113. Stura, E.A. Protein crystallization for drug design in the last 50 years. *Arbor* **2015**, *191*, 8. [CrossRef]

Disclaimer/Publisher’s Note: The statements, opinions and data contained in all publications are solely those of the individual author(s) and contributor(s) and not of MDPI and/or the editor(s). MDPI and/or the editor(s) disclaim responsibility for any injury to people or property resulting from any ideas, methods, instructions or products referred to in the content.



Review

Recent Progress on Bioinspired Antibacterial Surfaces for Biomedical Application

Xiao Yang^{1,2,†}, Wei Zhang^{1,3,†}, Xuezhi Qin^{1,4,†} , Miaomiao Cui¹, Yunting Guo¹, Ting Wang¹, Kaiqiang Wang^{1,5}, Zhenqiang Shi⁶, Chao Zhang¹, Wanbo Li^{1,*}  and Zuankai Wang^{1,2,3,*} 

¹ Department of Mechanical Engineering, City University of Hong Kong, Kowloon, Hong Kong 999077, China; xyang@hkcoche.org (X.Y.); wzhang469-c@my.cityu.edu.hk (W.Z.); xuezhi.qin@cityu.edu.hk (X.Q.); miaomicui2-c@my.cityu.edu.hk (M.C.); yuntiguo@cityu.edu.hk (Y.G.); twang259@cityu.edu.hk (T.W.); wkq19@mails.tsinghua.edu.cn (K.W.); czhan25@cityu.edu.hk (C.Z.)

² Hong Kong Centre for Cerebro-Caradiovascular Health Engineering (COCHE), Shatin, Hong Kong 999077, China

³ Centre for Nature-Inspired Engineering, City University of Hong Kong, Kowloon, Hong Kong 999077, China

⁴ School of Mechanical and Aerospace Engineering, Jilin University, Changchun 130022, China

⁵ State Key Laboratory of Tribology, Tsinghua University, Beijing 100084, China

⁶ CAS Key Laboratory of Separation Science for Analytical Chemistry, Dalian Institute of Chemical Physics, Chinese Academy of Sciences, Dalian 116023, China; shizhenqiang@dicp.ac.cn

* Correspondence: wanboli@cityu.edu.hk (W.L.); zuanwang@cityu.edu.hk (Z.W.)

† These authors contributed equally to this work.

Citation: Yang, X.; Zhang, W.; Qin, X.; Cui, M.; Guo, Y.; Wang, T.; Wang, K.; Shi, Z.; Zhang, C.; Li, W.; et al. Recent Progress on Bioinspired Antibacterial Surfaces for Biomedical Application. *Biomimetics* **2022**, *7*, 88. <https://doi.org/10.3390/biomimetics7030088>

Academic Editors: Stanislav N. Gorb, Giuseppe Carbone, Thomas Speck and Andreas Taubert

Received: 11 June 2022

Accepted: 29 June 2022

Published: 4 July 2022

Publisher's Note: MDPI stays neutral with regard to jurisdictional claims in published maps and institutional affiliations.



Copyright: © 2022 by the authors. Licensee MDPI, Basel, Switzerland. This article is an open access article distributed under the terms and conditions of the Creative Commons Attribution (CC BY) license (<https://creativecommons.org/licenses/by/4.0/>).

Abstract: Surface bacterial fouling has become an urgent global challenge that calls for resilient solutions. Despite the effectiveness in combating bacterial invasion, antibiotics are susceptible to causing microbial antibiotic resistance that threatens human health and compromises the medication efficacy. In nature, many organisms have evolved a myriad of surfaces with specific physicochemical properties to combat bacteria in diverse environments, providing important inspirations for implementing bioinspired approaches. This review highlights representative natural antibacterial surfaces and discusses their corresponding mechanisms, including repelling adherent bacteria through tailoring surface wettability and mechanically killing bacteria via engineering surface textures. Following this, we present the recent progress in bioinspired active and passive antibacterial strategies. Finally, the biomedical applications and the prospects of these antibacterial surfaces are discussed.

Keywords: biomimetic; antibiofouling; surface modification; physical removal; wound dressing

1. Introduction

Manifesting a typical size at least ten orders of magnitude smaller than human beings, bacteria present in various environments and are important to the human being, and ecosystem. Most bacteria are harmless to us, help our bodies digest food and absorb nutrients, and even produce multivitamins in the gut [1]. However, some diseases caused by pathogenic bacteria, such as tuberculosis, pneumonia, endocarditis, sepsis, and osteomyelitis, invade the host and cause various infectious diseases [2–4]. Additionally, bacteria such as methicillin-resistant *Staphylococcus aureus* and *Pseudomonas aeruginosa* are well known to trigger surgical site infections through the incision, which threatens millions of patients every year and induces the spread of antibiotic resistance all around the world [5,6]. According to the Centers for Disease Control and Prevention of the United States, antibiotic-resistant bacteria may result in at least 70,000 deaths worldwide per year. By 2050, this number will exceed 10 million [7].

Mitigating or even preventing bacterial infection has been a historic challenge. In ancient times, many natural agents such as herbs, honey, animal feces, and moldy bread have been widely used for treating patients with bacterial infections. Among these, the most effective and widespread agent was moldy bread, although its mechanisms were not

clear at that time [8]. Meanwhile, many metals, e.g., copper and silver and their alloys, were also utilized to disinfect wounds and drinking water [9]. The discovery of penicillin was a milestone in the fight against bacterial infections, and saved thousands of wounded soldiers and civilians in wars and started the era of antibiotics and the subsequent development of new generation antibiotics. The use of systemic antibiotic therapy has been a traditional and common method for eradicating the cause of infection, yet was often unsatisfactory. For example, only a 22–37% effective rate has been reported when combating bacterial infection of medical implants such as catheters and subcutaneous sensors, because most systemic antibiotics did not reach an effective local concentration [2]. However, increasing the administrative doses of antibiotics causes cytotoxicity and side effects in the patient's body. Another serious problem associated with the use of antibiotics is the emergence of multidrug resistance to bacterial strains, which renders current antibiotics ineffective and requires additional interventions such as more radical surgery. Therefore, ways to prevent bacterial infection and mitigate multidrug resistance simultaneously have receiving growing attention.

Nature, however, has evolved ingenious solutions based on topological surfaces to fight bacterial infection in green and efficient manners. Typical examples of natural surfaces that exhibit antibacterial properties include the lotus leaf, wings of cicadae, wings of dragonflies, wings of planthoppers, springtail skin, shark skin, and gecko feet. Unlike antibiotic treatment, natural surfaces can physiochemically minimize bacterial infection by interfering with the surface–bacteria interaction, which fundamentally avoids the evolution of multidrug resistance [1,10–18]. Inspired by these elegant biological surfaces, manmade antibacterial surfaces have emerged as an efficient alternative to antibiotics for addressing bacterial challenges. In this review, we first briefly introduce the mechanism of bacterial adhesion and biofilm formation. The progress of a series of natural antibacterial surfaces is then comprehensively summarized and their antibacterial pathways discussed. Furthermore, we classify surface engineering approaches into active and passive bioinspired antibacterial surfaces, with some of their representatives being discussed in detail. Finally, recent applications of bioinspired antibacterial surfaces are illustrated, and the prospects of bioinspired antibacterial materials are proposed.

2. Bacterial Adhesion and Biofilm Formation

An infection starts from the contact of an individual bacterium, during which the bacterium can actively propel itself to the surface using its flagella. When bacteria reach the surface, flagella also play an important role in adhesion by providing physical contact with surfaces, exploring local surface topography, and entering a microenvironment inaccessible to relatively large cell bodies. The interaction between flagella and surfaces could enhance adhesion, because of the inherent hydrophobicity of flagella, which allows them to adhere to hydrophobic surfaces. By contrast, the presence of flagella may also weaken adhesion as found in *Caulobacter crescentus*. Therefore, the influence of flagella on adhesion is much more complex and fully understanding it requires in-depth investigations. In addition to the flagella, some other filamentous protein extensions on the cell surface, including fimbriae, curli and pili, are also involved in nonspecific initial adhesion to abiotic surfaces [19]. For example, pili can use their specific receptors to bind to substrates through an unidentified mechanism, and most pili show no preference for substrates. Such an attachment process is sensitive to bacterial characteristics (e.g., cell development, exopolysaccharide production, metabolic activity, cell viability, cell-wall stiffness and adhesin-mediated receptor-ligand binding) and surface physicochemical properties (e.g., surface charge, surface free energy, wettability, roughness, morphology). After adhering to the surface, the cells grow, divide, and secrete exopolysaccharides to encapsulate themselves as a three-dimensional bacterial community, a so-called biofilm, in an extracellular matrix when the cell density reaches a certain level. Typical biofilms are supported by self-produced three-dimensional polymer matrix networks containing proteins, carbohydrates, nucleic acids, and other biomolecules, which can create an optimized and dynamic environment for bacterial cell growth and

proliferation, protect these sessile bacterial communities from antimicrobial agents, and mediate cell-to-cell and cell-to-surface adhesion [20]. In the final stage, small pieces of cells or individual cells may be released from the biofilm and thus another infection cycle begins (Figure 1) [21–23].

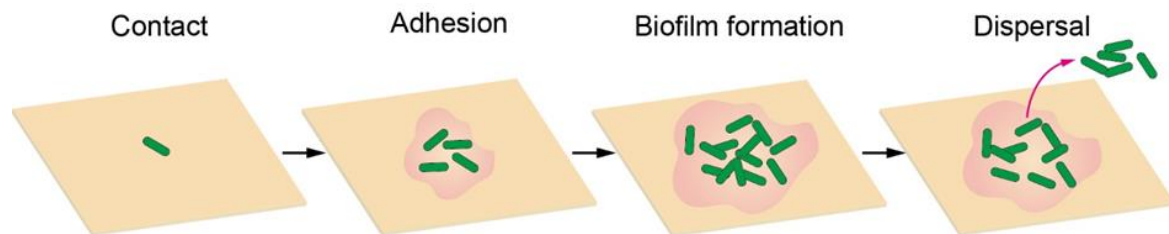


Figure 1. Schematic diagram of bacterial adhesion and biofilm formation process.

3. Natural Antibacterial Surfaces

Over millions of years of evolution, nature has evolved ingenious strategies to prevent bacterial infection by breaking the transmission chain, i.e., preventing bacterial adhesion or biofilm attachment [24–26]. On the basis of the fundamental mechanisms, antibacterial surfaces can be classified into bacteria-repellent surfaces (e.g., marine organisms' mucus, reptiles' skin and plant leaves [27]) and contact-killing surfaces (e.g., insect wings) [28–30].

3.1. Natural Bacteria-Repellent Surface

A bacteria-repellent surface is usually achieved by introducing superhydrophobicity to remarkably lower bacterial adhesion. Superhydrophobic or the so-called self-cleaning surfaces can be widely found on plant leaves, insect cuticles, fish skin, etc., which enable these species to passively control bacterial colonization (Figure 2A). For example, a lotus leaf was the first reported to have superhydrophobicity and bacterial repellence [31]. The underpinning mechanism was the combination of low surface energy and the multiscale roughness of surface lipid structures, which allowed the surface to have a high water contact angle ($\theta^* > 150^\circ$) and a low sliding angle ($\theta_s < 10^\circ$), and trapped large amounts of air cushion, which significantly minimizes the surface/bacteria contact (Figure 2B). Bacterial cells colonizing such surfaces would be removed before they had a chance to form biofilms [32]. Similar phenomena have also been observed on some insect surfaces, such as planthoppers and springtails [33]. Planthoppers' hindwings feature topographical and functional similarities to lotus leaves, thus exhibiting non-wetting behavior and low adhesion to pollutants [34,35]. Springtail skin is another kind of superhydrophobic surface consisting of a microcolumnar with a double nanoreentrant (Figure 2C) [36–38]. The superhydrophobic skin endowed it with an anti-adhesion property to protect springtails from bacterial attaching and infection [39]. Shark's hydrophobic skin, leveraging flat scales or dermal denticle arrays, offers another ingenious strategy to prevent the attachment and growth of microorganisms, with additional benefits in drag reduction (Figure 2D) [40–43].

3.2. Natural Contact-Killing Surface

Unlike the bacteria-repellent strategy, many other biological surfaces violently kill the bacteria in contact with them. The contact killing effect lies in that their extremely fine structures can pierce the cell membrane due to the concentrated mechanical stress and gradually rupture the cell (Figure 2E). While varying in shape and other properties, the common feature of these natural contact-killing surfaces is their pattern in nanoscale size (50–250 nm) and two-dimensional arrangement [44]. For example, A cicada wing's surface has uniform nanocone arrays with a height of 200 nm, a top diameter of 60 nm, a bottom diameter of 100 nm, and an interpillar space of 170 nm (Figure 2F). Unlike the lotus leaf, a cicada wing is a surface manifesting a large water contact angle of 158.8° but a high degree of bacterial adhesion. Bacteria on such a surface can be pierced through by the nanotopography [45]. Specifically, bacterial cell membranes that contact the sur-

face patterns bear a large stretching force, accompanied by a sharp increase in the total membrane area, which collectively results in irreversible membrane rupture and bacteria death [46–48]. Gram-positive cells have thicker layers of peptidoglycan and are therefore generally more rigid, which may explain their increased resistance in comparison to Gram-negative cells. This is why cicadas' wings are only effective against Gram-negative bacteria. Such functional shortcomings can be well tackled by the surface of dragonfly wings, on which both Gram-negative bacteria (*P. aeruginosa*) and Gram-positive bacteria (*S. aureus* and *Bacillus* sp.) and even endospores can be mechanically ruptured. A dragonfly wing is also covered with high aspect-ratio nanostructures that can pierce almost all bacterial membranes in contact with it (Figure 2G) [49,50]. A gecko with a unique hair structure has drawn much attention due to its superhydrophobicity and associated topographical antimicrobial effects [51]. The gecko's skin is composed of small hairs (often called spines or microspines) a few microns in height, with an interspace of 0.2–0.7 μm (Figure 2H). Because gecko hair possesses a tip shape and size similar to the nanocones on cicadas, it can be an alternative for studying antimicrobial properties. Gecko skin has been proved to be antibacterial, with a remarkable killing effect on *Porphyromonas gingivalis*, a clinically significant bacterium [52,53].

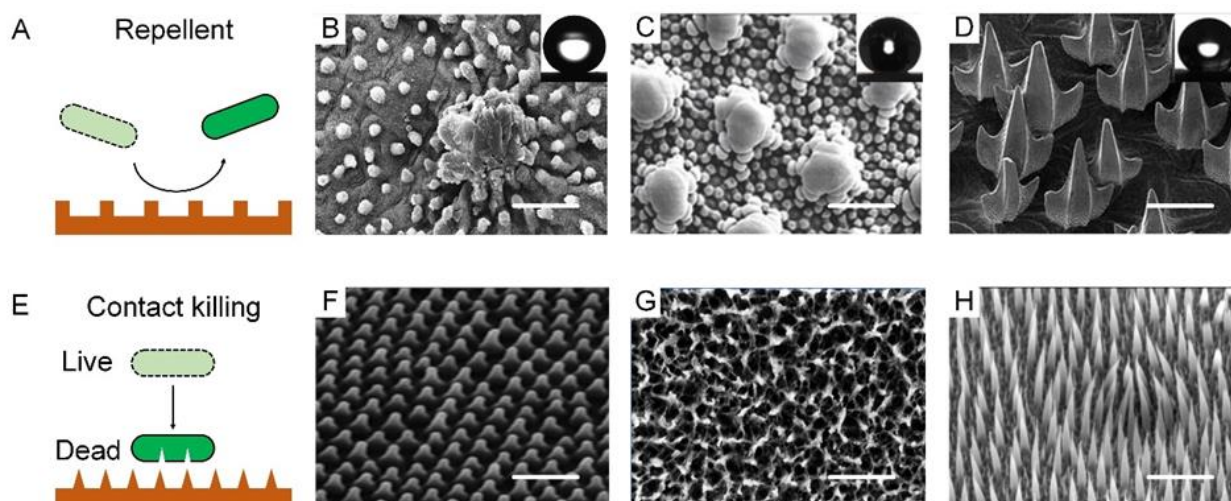


Figure 2. Nature bacteria-repellent surface and contact-killing surfaces. (A) Schematic diagram of natural bacteria-repellent surface. (B) Lotus leaves. SEM images showing “micropapilla” structures in lotus leaves. Scale bar: 50 μm . Reproduced with permission [54]. 2008, American Institute of Physics (United States). (C) Springtail skin. SEM images showing “doubly-reentrant” structures in springtail skin. Scale bar: 2 μm . Reproduced with permission [34]. 2017, Wiley-VCH. (D) Sharkskin. SEM images showing “microdenticle” structures in sharkskin. Scale bar: 100 μm . Reproduced with permission [55]. 2019, Nature Portfolio. (E) Schematic diagram of natural contact-killing surface. (F) Cicada wings. SEM images showing “nanocone” structures in cicada wings. Scale bar: 2 μm . Reproduced with permission [56]. 2012, Public Library of Science. (G) Dragonfly wings. SEM images showing “disordered nanopillar” structures in dragonfly wings. Scale bar: 200 nm. Reproduced with permission [49]. 2013, Nature Portfolio. (H) Lizard skin. SEM images showing “microspine” structures in lizard skin. Scale bar: 2.5 μm . Reproduced with permission [51]. 2017, Nature Portfolio.

4. Bioinspired Antibacterial Surfaces

In-depth studies of natural antibacterial surfaces offer viable strategies for developing high-performance bioinspired counterparts to effectively prevent bacterial infection [23,24]. A summary of current antibacterial surfaces is shown in Table 1 [57–59]. Briefly, depending on whether extra interventions are needed, bioinspired antibacterial surfaces can be categorized into passive and active ones (Figure 3).

Table 1. Current surface-modification approaches in the design of passive bioinspired antibacterial surfaces.

Approach	Preparation Methods	Antibacterial Effects		Comments
		Bacteria-Repellent Surface	Contact-Killing Surface	
Chemical modification	1. Surface-initiated polymerization	1. Antibiofouling polymer	1. Antibiotics	1. Uneven
	2. Vapor-deposition polymerization	2. Fluoride	2. Antibacterial metal	2. Mechanically weak
	3. Electrospinning	3. Zwitterion	3. Antibacterial polymer	3. Lack long-term stability
	4. Sedimentation	4. SLIPs	4. Antibacterial peptide	4. Concentration dependent and needs further chemical reactions
	5. Spin-coating			
	6. Layer-by-layer deposition			
	7. Oil-impregnation			
Passive bioinspired antibacterial surface	1. Plasma etching	1. Black silicon		1. Fast processing
	2. Hydrothermal etching	2. Ti nanowires		2. High precision
	3. Anodic oxidation	3. Titanium dioxide nanotubes		3. Needs the assistance of related processing equipment to complete
	4. Magnetron sputtering	4. Nanocolumnar thin film on Si substrate		
	5. Epitaxial growth	5. 2D honeycomb structure		
	6. Exfoliation	6. Single-layer graphene sheet		
	7. Chemical vapor deposition	7. Carbon nanotube “forest”		
	8. Nano-imprint lithography	8. Thin needle-like structure		
	9. Templating	9. Homogenous monolayered films/graphene flakes		
	10. Electrospinning	10. Sharp high-aspect-ratio structures		
Bioinspired responsive surface		11. Slightly rounded		
		12. High aspect ratio structures		
		13. Superhydrophobic fibrous mat		
		1. pH-responsive		
		2. Enzyme-responsive		
		3. Temperature-responsive		
		4. Ion-responsive		
		5. Light-responsive		

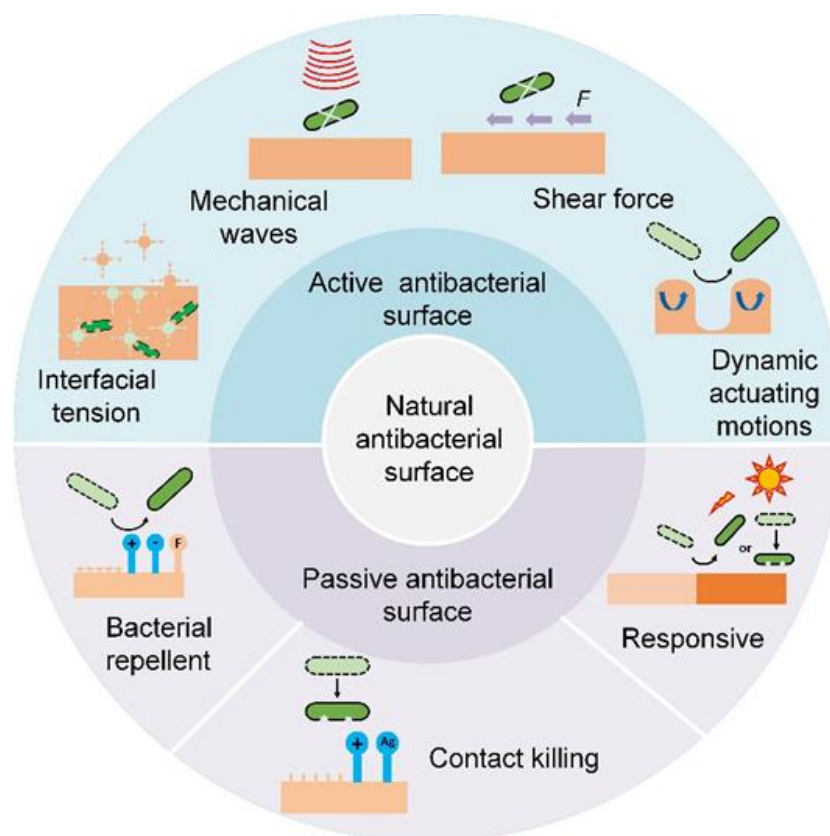


Figure 3. Scheme of nature and bioinspired antibacterial surfaces.

4.1. Passive Antibacterial Surface

4.1.1. Bacteria-Repellent Surface

Boosting the surface repulsion of bacteria, which is mainly inspired by superhydrophobic biological skins, can remarkably minimize the bacterial infection rate. Generally, the factors that can control bacterial repellence include wettability, topography, material stiffness, surface charge, and their combinations.

The most common approach to interfere with the surface–bacteria interaction is to regulate the surface wettability, i.e., hydrophobicity or hydrophilicity (Figure 4(Ai)). For example, the surface can be rendered hydrophobic by grafting low-surface-energy molecules or infusing liquid lubricant, the result of the latter being named slippery liquid-infused porous surfaces (SLIPs) [60–62]. A novel SLIPs consisting of microporous poly (butyl methacrylate-co-ethylene dimethacrylate) films infused with the perfluoropolyether fluid–slippery poly (butyl methacrylate-co-ethylene dimethacrylate) was demonstrated to prevent different strains of the opportunistic pathogen *P. aeruginosa* from biofilm formation for 7 days [63]. Further combining low-surface-energy components with a large microroughness can amplify the apparent wettability, which tremendously weakened bacterial adhesion [64,65]. One typical example was a lotus-leaf-inspired surface patterned with regularly spaced micro-pillar arrays and packed nanoneedles, allowing a more than 98% antibacterial rate against *Escherichia coli* at high-concentration (10^8 colony-forming unit/mL) and long-term-culture conditions [66–71]. A mimic of shark skin with superhydrophobicity also showed a similar inhibition to the adhesion of the zoospores *Ulva* (~5 μm diameter) and *S. aureus* (1 μm diameter) [72–74].

On the other hand, causing surface hydrophilicity can also decrease the total contact and inhibit bacterial adhesion, because the hydrophilicity helps to reduce the number of bacteria proteins attached to the surface. A simple way to make surfaces hydrophilic is directly coating hydrophilic components such as polymers and zwitterions [75–79]. For example, a branched-chain-polymer-based surface with antibiofouling properties was de-

veloped by conjugating dioxy-containing polyethylene glycol with gentamicin terminals. The introduction of polyethylene glycol increased the surface hydrophilicity, which inhibited protein adhesion and repelled bacterial fouling. In addition, the transplanted *S. aureus* infection model showed that the branched-chain polymers have good antibacterial and antifouling ability in vivo. (Figure 4(Aii)) [80]. For zwitterions, the introduction of zwitterions onto cotton-texture surfaces significantly increased surface hydrophilicity. The modified cotton texture surfaces can effectively resist initial bacterial adhesion, kill attached bacteria, and release dead bacteria [81–83].

Solely topographical modifications also provide a persistent and predictable form for control of bacterial behavior, especially using ordered patterns (Figure 4(Bi)). M. Yang et al. showed that submicron-scale pillar patterns strikingly inhibit bacterial adhesion, growth, and colonization by physically hindering bacterial cell-to-cell interactions. Furthermore, they investigated the effect of morphology (e.g., honeycomb) and sizes on the adhesion and growth of bacterium with different shapes (e.g., rod *E. coli* and spherical *S. aureus*). The fluorescent image results showed that a 1- μm patterned surface significantly reduced bacterial adhesion and growth while inhibiting bacterial colonization compared with a flat surface (Figure 4(Bii)). From a dynamic perspective, the selective adhesion of bacterial cells to patterns was synergistically mediated by maximizing cell–substrate contact area and minimizing cell deformation. They established that two main factors, namely energetically favorable adhesion sites and physical confinement, contribute to the antibacterial properties of the honeycomb-like pattern [84].

Adopting soft materials, e.g., hydrogel, with low stiffness, can tune the surface bacterial adhesion (Figure 4(Ci)). Harder polymer surfaces typically have higher network densities than softer polymer surfaces, resulting in a higher density of functional groups that liquid media and bacterial cells can interact with. Generally, a soft hydrogel surface with low stiffness exhibits better antibacterial performance. A positive correlation between the surface stiffness and adhesion was demonstrated by larger bacteria colonization on the stiffer surface (Figure 4(Cii)). Polyelectrolyte multilayer membranes from polyacrylamine hydrochloride and polyacrylic acid were prepared with Young's moduli ranging from 1 to 100 MPa. A positive correlation between the surface stiffness and adhesion with *E. coli* and *S. aureus* was found on such surfaces [85]. A cross-linked membrane composed of poly(L-lysine) and hyaluronic acid was prepared, and the number of bacteria on the non-cross-linked membrane at 30 kPa was lower than that on the cross-linked membrane at 150 kPa [86]. Polydimethylsiloxane substrates with a stiffness of 100 to 2600 kPa were found that affected the physiology of *E. coli* and *P. aeruginosa* [87]. A positive relationship between the fouling intensity of *E. coli* and *S. aureus* and hydrogel stiffness was reported by conducting tests of bacterial attachment on three poly (ethylene glycol) dimethacrylate surfaces with low (44.05–308.5 kPa), moderate (1495–2877 kPa), and high (5152–6489 kPa) stiffness, respectively [88].

The additional benefit of the polymeric modification is its static charge, which can interact with bacterial membranes (Figure 4(Di)). In general, most bacterial cells are surrounded by a layer of peptidoglycan (composed of sugars and amino acids) that are negatively charged, which can be trapped or even killed on positively charged polymeric surfaces, or repelled by negatively charged surfaces. However, this repellency is largely dependent on the species of bacteria. For example, Gram-positive bacteria with a polycationic glycocalyx were more likely to adhere to negatively charged surfaces than Gram-negative bacteria with a polyanionic glycocalyx. Due to the larger discharge capacity, the direct current positive charging method had a better antibacterial effect than the alternating current charging method. In addition, the capacitance-based platform can effectively prevent the formation of biofilms by means of cyclic charging. Extracellular electron transfer between bacteria and charged titania nanotubes doped with carbon-disrupted bacterial morphology and induced intrabacterial ROS burst, leading to bacterial death upon charging (Figure 4(Dii)) [89].

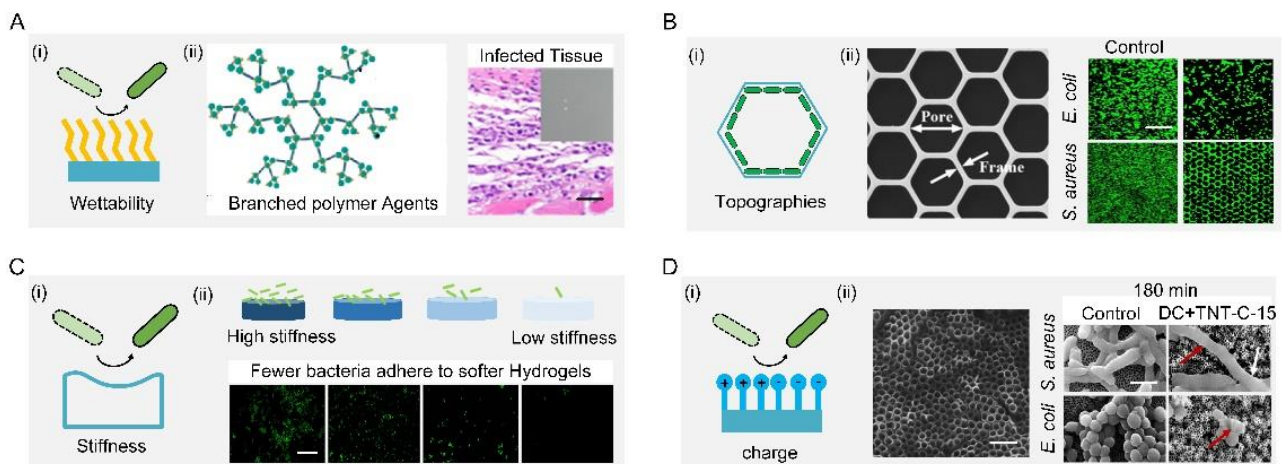


Figure 4. Bacteria-repellent surfaces. (A) Surface hydrophilization by modifying antibiofouling polymer (i) antibiofouling polymeric agents and their application for the surface functionalization of Ti substrate; the resultant surface can effectively repel bacterial adhesion in vivo (ii). Scale bar: 100 μm . Reproduced with permission [80]. 2018, American Chemical Society (United States). (B) Schematic diagram of topographies' surfaces (i) SEM and fluorescent images of selective adhesion of bacterial cells on the honeycomb platform (ii). Scale bar: 50 μm . Reproduced with permission [84]. 2015, Elsevier. (C) Schematic diagram of stiffness surface (i) schematic diagram of the antifouling property of stiffness surface (ii). Scale bar: 10 μm . Reproduced with permission [88]. 2015, American Chemical Society (United States). (D) Schematic diagram of charge surface (i) Scale bar: 500 nm. Schematic diagram of the antifouling property of charge surface (ii) Scale bar: 2 μm . Reproduced with permission [89]. 2018, Nature Portfolio.

4.1.2. Contact-Killing Surfaces

It has to be admitted that bacteria-repellent surfaces cannot always successfully prevent bacteria from attaching to them. In this case, we need another effective strategy to resist bacterial infection, namely contact-killing surfaces, where bacteria are killed once they come into contact with the surface. Contact-killing surfaces can be designed and engineered via coating with bactericidal layers or tuning mechanical properties.

Bactericidal substances such as antibacterial metal, antibacterial polymers, and antibacterial peptides can be covalently immobilized on the surfaces [90]. Antibacterial metals should be toxic to a broad spectrum of bacteria, such as Zn^{2+} , Na^+ , Mg^{2+} , Ca^{2+} , K^+ , Ag^+ , Hg^{2+} , and As^{3+} , most of which have been used as antibacterial agents since ancient times [91]. While how antibacterial metals kill bacteria has not yet been fully understood, two possible mechanisms have been proposed to try to explain this phenomenon. First, antibacterial metal could generate oxidative stress to form reactive oxygen species that can kill bacteria. For example, Au was added to the Pd catalyst to promote the release of oxygen-based radical species. It was found that this method was more bactericidal and virucidal and inhibited biofilm formation compared to other methods based on chlorination or pre-formed H_2O_2 alone [92,93]. Second, the release of free metal ions from metal surfaces was responsible for bacteria inactivation (Figure 5(Ai)) [94–104]. For example, compared with a pure strontium calcium phosphate coating, the addition of Zn^{2+} increased the killing rates for *S. aureus* and *E. coli* from 61.25% and 55.38% to 83.01% and 71.28%, respectively. Bacteria on such surfaces with Zn^{2+} underwent partial shrinking, twisting, and even dissolving before death (red arrows) (Figure 5(Aii)) [105].

Negative charges enrich surfaces and generate an attraction force that destroys the integrity of cell membranes and inactivates bacterial enzymes. Most negatively charged materials are polymers, which can be covalently bonded with surfaces with long-term effectiveness. Commonly used antibacterial polymers include quaternary ammonium compounds (QACs), quaternary phosphoniums, and N-chloramines. Taking QACs as an

example, they have strong contact-killing activity against both Gram-positive bacteria and Gram-negative bacteria by destroying their membrane (Figure 5(Bi)). A QAC (s-poly (2,3-dimethylmaleic anhydride) (melittin)-b-poly (2-hydroxyethyl methacrylate) was modified on a surface as a multistage polymer brush to combat bacterial infection [106]. However, these QAC-based surfaces tended to induce irritation and inflammation, which hindered their practical application in the biomedical field [107–114]. In contrast to antibacterial polymers, antibacterial peptides hold great potential to solve the issues of irritation and inflammation and reduce the possibility of induced resistance. When interacting with negatively charged bacterial membranes, antibacterial peptides that usually carry a positive charge in the physiological environment would self-assemble into secondary structures such as α -helical structures, β -sheet structures, ring structures, extended structures, and mixed structures. These shape changes of antibacterial surfaces induced by self-assembly exposed their initially hidden amino acid, which can destroy the integrity of a cell membrane and further kill bacteria [115–117]. For example, WRWRWR-G₄-(dihydroxyphenylalanine)₄ was allowed to first self-assemble, and then screws with this coating were implanted into femurs near the joints of Sprague–Dawley rats to evaluate their antibacterial performance in vivo. This animal experiment indicated that the number of bacteria on both the screws and the surrounding tissues were reduced compared with those on bare screws (Figure 5(Bii)), indicating good antibacterial properties [118].

The contact-killing function can also be achieved by the mechanical rupturing of cells using fine surface structures, such as nanopatterns [119–121], nanowires [122], nanotubes [123], and nanopillars [124–136]. The rupturing of the bacterial membrane occurs when the cell membrane is not elastic enough to bear the exerted tensile force (Figure 5(Ci)). For example, a dragonfly-wing-inspired surface patterned with nanopillars possessed a mechanical bactericidal effect. As a result, this surface was highly bactericidal against all Gram-negative and Gram-positive bacteria. It showed an estimated average kill rate of up to 450,000 cells/min cm². The cell integrity of the bacteria was mechanically disrupted by the patterned nanopillars on the surface. Moreover, the viability analysis of bacteria using confocal laser scanning microscopy (CLSM) confirmed that all bacteria were dead after attachment (red color) (Figure 5(Cii)). This biomimetic work demonstrated promising prospects for the development of a new generation of antibacterial surfaces [50].

4.1.3. Responsive Surfaces

The aforementioned passive antibacterial surface shares a bottleneck: the killing efficiency of antibacterial surfaces may become weakened while the toxicity to normal cells and tissues may be exacerbated during long-term use. A potential alternative candidate is responsive surfaces that can be switched on/off in an on-demand manner [137]. Surface responsiveness is attributed to the use of agents that can be stimuli-triggered by the change in certain bacterial chemical cues (i.e., pH and enzymes) or external triggers (i.e., temperature, ions, light, and magnetism).

Bacterial infections are always accompanied by acidification of the environment (the pH of the infection site drops to 5.5). Such a change in pH can act as a powerful trigger to turn on the antibacterial function by exposing a surface-bound bactericide or releasing preloaded antibacterial agent [138]. The acidic effect mainly stems from low-oxygen fermentation triggering the production of organic acids, such as lactic acid secreted by *S. aureus* or acetic acid secreted by *E. coli*. (Figure 6(Ai)). Such characteristics can be harnessed to selectively release the antibacterial substances, killing bacteria in real time. For example, a hierarchical antibacterial surface was constructed with a top layer of pH-responsive polymer brush and a bottom layer of bactericidal agents. Decreases in pH could collapse the top layer and induce the exposure of the bactericidal agents, and ultimately activate the bactericidal function. More importantly, the recovery of pH could reconfigure the top layer and switch off the bactericidal function, demonstrating reversibility [139]. When the pH drops from 7.4 to 5.0, the killing efficiency of the proposed surface changes from 9.3% to 77.5% (Figure 6(Aii)).

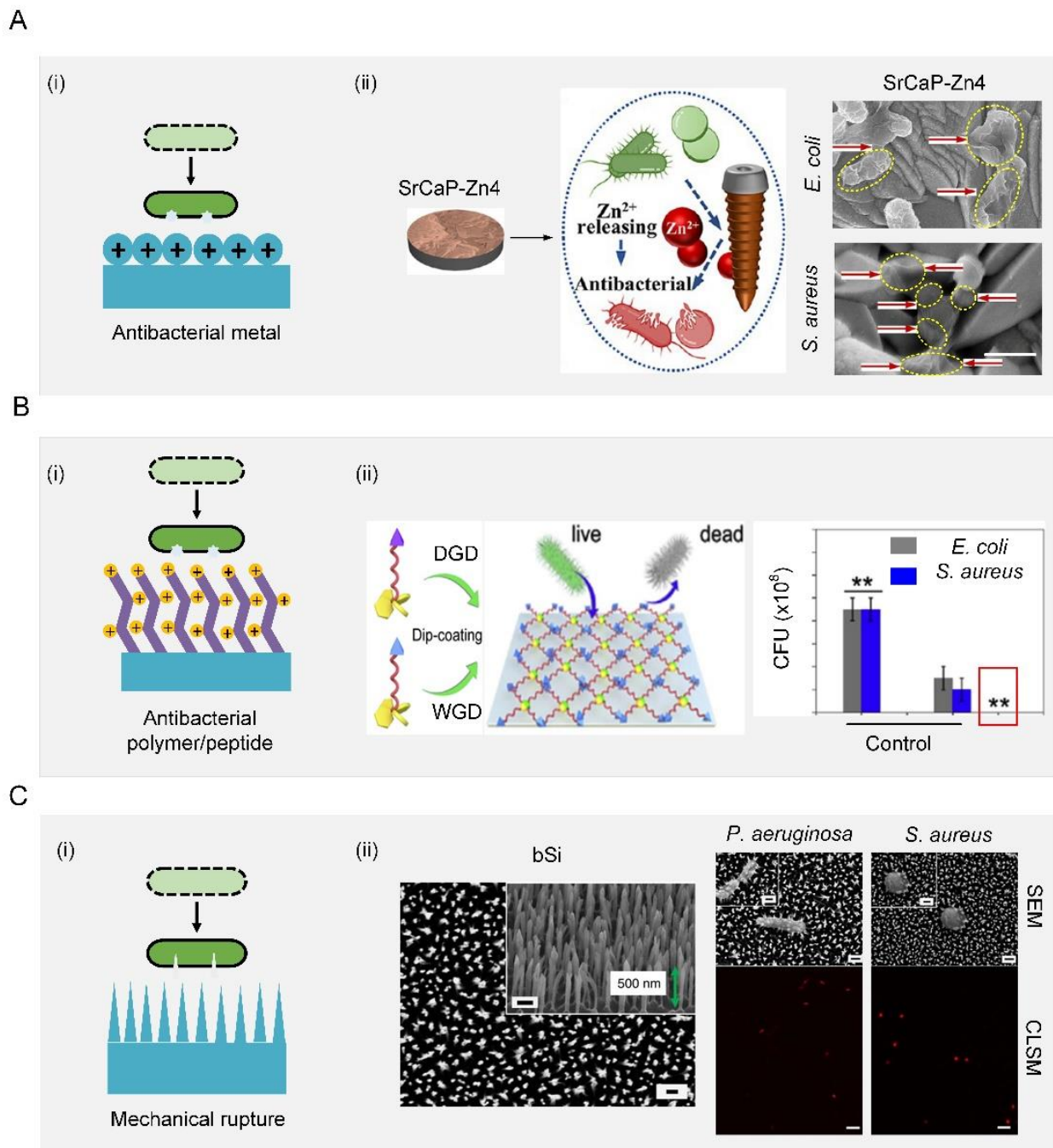


Figure 5. Contact-killing surfaces. (A) Schematic diagram of an antibacterial metal surface (i) Schematic illustration of antibacterial metal for synergistic photothermal/pharmacological antibacterial therapy (ii). Scale bar: 500 nm. Reproduced with permission [105]. 2021, Elsevier. (B) Schematic diagram of antibacterial polymer/peptide surface (i) schematic illustration of antibacterial polypeptide WRWRWR-G₄-(dihydroxyphenylalanine)₄ and their application for the surface functionalization of medical implants (ii). Reproduced with permission [118]. 2019, Elsevier. (C) Schematic diagram of mechanical rupture surface (i) SEM image of the upper surface of black silicon. Scale bars: 200 nm. SEM images of *P. aeruginosa* and *S. aureus* were significantly disrupted through interaction with black silicon. Scale bars, 200 nm. CLSM images confirmed that disruption by black silicon was lethal to the cells; non-viable bacterial cells and spores were stained with propidium iodide (red) whereas the living cells were stained with SYTO 9 (green). Scale bars: 5 μm (ii). Reproduced with permission [50]. 2013, Nature Portfolio.

In addition to pH, substances secreted by bacteria during metabolism, such as enzymes, can also act as a powerful trigger for killing activity (Figure 6(Bi)). For example, an enzyme-responsive peptide biointerface was designed based on the saliva-acquired pellicle bioinspired polypeptide DDDEEKRRWRWGPLGVRGD (SAP-MP196-G-1) that consists of the enzyme-responsive sequence GPLDV and the antimicrobial peptide RWRWRW. When the biointerface was invaded by *S. aureus*, the enzyme response sequence GPLDV was cleaved by the secreted enzyme from *S. aureus*. As a result, the antimicrobial peptide RWRWRW was exposed to kill bacteria. By measuring the number of bacteria in the different groups through quantification of OD₆₀₀, it was found that bacterial growth was markedly lower on the proposed surface than in a control. (Figure 6(Bii)) [140].

An ion-responsive surface can be achieved by grafting specific ion-pair polymers on the surface, which can endow surfaces with conformational change, high surface wettability, and electrostatic repulsion under the action of external ions. The additional ion-responsive polymer consists of anionic and cationic ionizable units in each repeating unit. The strong hydration of anionic and cationic ionizable units makes the surface excellent in antibiofouling properties. With such beneficial characteristics, the ion-responsive surface appeared a good candidate for achieving antibiofouling function through ion variation (Figure 6(Ci)) [141,142]. As a three-function surface, the reusable antibacterial surface was prepared with comprehensive antibiofouling, antibacterial, and self-cleaning properties. This antibacterial surface comprised (1) poly-n-hydroxyethyl acrylamide hydrophilic polymer as an ultralow-pollution background that can prevent long-term bacterial colonization; (2) triclosan, which can effectively kill attached bacteria; (3) a salt-sensitive polymer, namely, poly(3-(dimethyl(4-vinylbenzyl) amino) propyl sulfonate), which was used to release attached bacteria in the salt solution. The antibacterial surface exhibited three functional antimicrobial activities: poly-n-hydroxyethyl acrylamide resisted bacterial attachment, triclosan killed about 90% of the bacteria on the surface, and poly(3-(dimethyl(4-vinylbenzyl) amino) propyl sulfonate) released about 90% of the dead bacteria on the surface (Figure 6(Cii)) [143].

The temperature has been widely used to control antimicrobials on solid surfaces made of thermally responsive polymers. One typical example of thermally responsive polymers is poly(n-isopropylacrylamide) (PNIPAAm), which can be utilized to achieve a temperature-responsive surface with wettability for bacterial adhesion and separation (Figure 6(Di)) [144,145]. When the temperature rises higher than the lower critical solution temperature of PNIPAAm, the hydrogen bond between PNIPAAm and water is severely broken, resulting in the hydrophobicity of PNIPAAm. A new thermally responsive surface consisting of thermally responsive hydrogel regions and mechanically supported elastomer regions were prepared. The alternative microscale arrangement of these two regions enabled the surface morphology to have a significant effect on disrupting bacterial colonization and dispersing heat-sensitive individual bacteria. This can effectively prevent bacterial infection without inducing the cohesive loss of human epidermal tissue, thereby serving as an extracellular biointerface for precise local antimicrobial therapy (Figure 6(Dii)) [146].

Many surfaces are sensitive to light, including ultraviolet, visible, or near infra-red light. In practical applications, visible or near infra-red light is more attractive for clinical applications due to its low toxicity and deep tissue penetration. For example, light-responsive surfaces with antibacterial strategies such as antimicrobial photothermal therapy (APTT) and antimicrobial photodynamic therapy (APDT) rely on the generation of local antimicrobial properties to kill cells driven by different frequencies of light (Figure 6(Ei)). APTT is a physical antibacterial strategy, in which the photothermal agent can continuously heat up under specific light, and the high temperature induces cell-membrane rupture, protein/enzyme denaturation, cell cavitation, and cell-fluid evaporation [147]. For example, two-dimensional Nb₂C Mxene nanosheets as a photothermal agent with implanted medical titanium plates were prepared. The temperature of modified titanium plates was raised steadily to 70 °C within 2 min under the irradiation of a high-power density near-infrared laser. The bacterial survival rates for *S. aureus* and *E. coli* dropped

sharply from $100.4\% \pm 3.12\%$ and $100.02\% \pm 2.76\%$ in the control group to $1.19\% \pm 0.93\%$ and $1.06\% \pm 0.58\%$ in the modified titanium plates + near-infrared laser group, respectively [148]. APDT is a minimally invasive strategy that uses light-responsive photosensitizers to generate reactive oxygen species through photochemical reactions, resulting in irreversible damage and cell death [149,150]. For example, smart nanoplateforms with photosensitizer molecule chlorin e6 were prepared. When light irradiated the above platform, the ratio of anaerobic *P. gingivalis* and *Fusobacterium nucleatum* was reduced from 66.21% in the control group to 51.91% [151]. Combining APTT and APDT, a red phosphorus/zinc oxide heterojunction was prepared that has excellent solar photothermal conversion and photocatalytic efficiency, further leading to the death of bacteria through hyperthermia and reactive oxygen species. The bacteriostatic effectiveness on *S. aureus* at 5 min was $99.96 \pm 0.03\%$, and that on *E. coli* at 4 min was $99.97 \pm 0.02\%$ (Figure 6(Eii)) [152].

A magnetic responsive surface is also a good antibacterial surface. The application of the magnetic field induced the magnetic metal to spin, deform, and exert physical forces on the bacteria, which resulted in the disruption of the dense biofilm matrix and simultaneous lysis of the cells. Once exposed to a low-intensity rotating magnetic field, the liquid metal droplets are physically driven to change shape, creating sharp edges. When in contact with bacterial biofilms, the particle motion created by the magnetic field, coupled with the presence of nanoedges, physically ruptures the bacterial cells and disrupts the dense biofilm matrix. For example, magnetic galinstan-based liquid metal platforms can also kill bacteria under an external magnetic field (Figure 6(Fi)). After introducing two major pathogens biofilms, specifically *P. aeruginosa* and *S. aureus*, the system was exposed to a dynamic magnetic field of 775 mGs. Following 90 min of exposure to the magnetic field with the gallium-based liquid metal ferrofluid platforms, it was observed that the average colony-forming unit /mm² was reduced for both biofilms of *S. aureus* (99.85%, $p < 0.001$) and *P. aeruginosa* (96.51%, $p < 0.01$) when compared to controls (Figure 6(Fii)) [153].

4.2. Active Antibacterial Surface

Unlike the biological antibacterial surfaces that are adaptive and flexible to diverse harsh environments, an artificial surface usually displays relatively short-term bacterial resistance. To prevent bacterial adhesion and biofilm formation, new physical removal strategies relying on external sources such as mechanical force or energy waves have emerged as alternatives to an antibacterial agent. Generally, these external sources include shear force, interfacial tension, mechanical waves, dynamic actuating motions, and plasma treatment. Unlike passive antibacterial surfaces, the antibacterial process of the active antibacterial surface is controllable and acts directly on bacteria.

The shear-force-based method is very effective to remove bacteria directly by generating shear force sufficient to balance the bacterial adhesion force (Figure 7(Ai)). Shear forces can be produced by the external application of force parallel to the surface. The inner wall of the microfluidic device is composed of the copolymers, 2-methacryloyloxyethyl phosphorylcholine, 3-methacryloxypropyl trimethoxysilane and 3-(methacryloyloxy) propyl-tris(trimethylsilyloxy) silane, with two typical thicknesses (20 and 40 nm), forming a cross-linked film. Shear forces were generated by friction between the fluid and the inner wall of the microfluidic device. Under the same shear stress, thicker surfaces could weaken the adhesion of *S. aureus*, which leads to more bacteria detachment (Figure 7(Aii)) [154].

Surface antibacterial performance can also be improved by adjusting the interfacial tension with surfactants. Among those, one effective way to control interfacial tension is the use of biosurfactant, a kind of surface-active biomolecule produced by many microorganisms. It has been reported that the aggregation of biosurfactants at the interface can reduce the interfacial tension of the solution and form a microcellular structure, which can disrupt the bacterial cell membrane to produce antibacterial properties (Figure 7(Bi)). Moreover, the properties of the biosurfactant itself, such as its concentration, also influence the antimicrobial performance. Taking sophorolipids (a type of biosurfactant) as an example, at a concentration above 5% v/v, they can inhibit the growth of Gram-negative

Cupriavidus necator and Gram-positive *Bacillus* sp. with a bactericidal effect. Below this concentration, the antibacterial properties are greatly reduced [155]. In addition, Zein/gum Arabic nanoparticles were prepared to stabilize the oil–water interface of Pickering emulsions, which strikingly inhibited the growth of *E. coli*. The stabilized emulsion exhibited a controlled release and the antibacterial activity of thymol due to the protective effect from its stable interfacial layer (Figure 7(Bii)) [156].

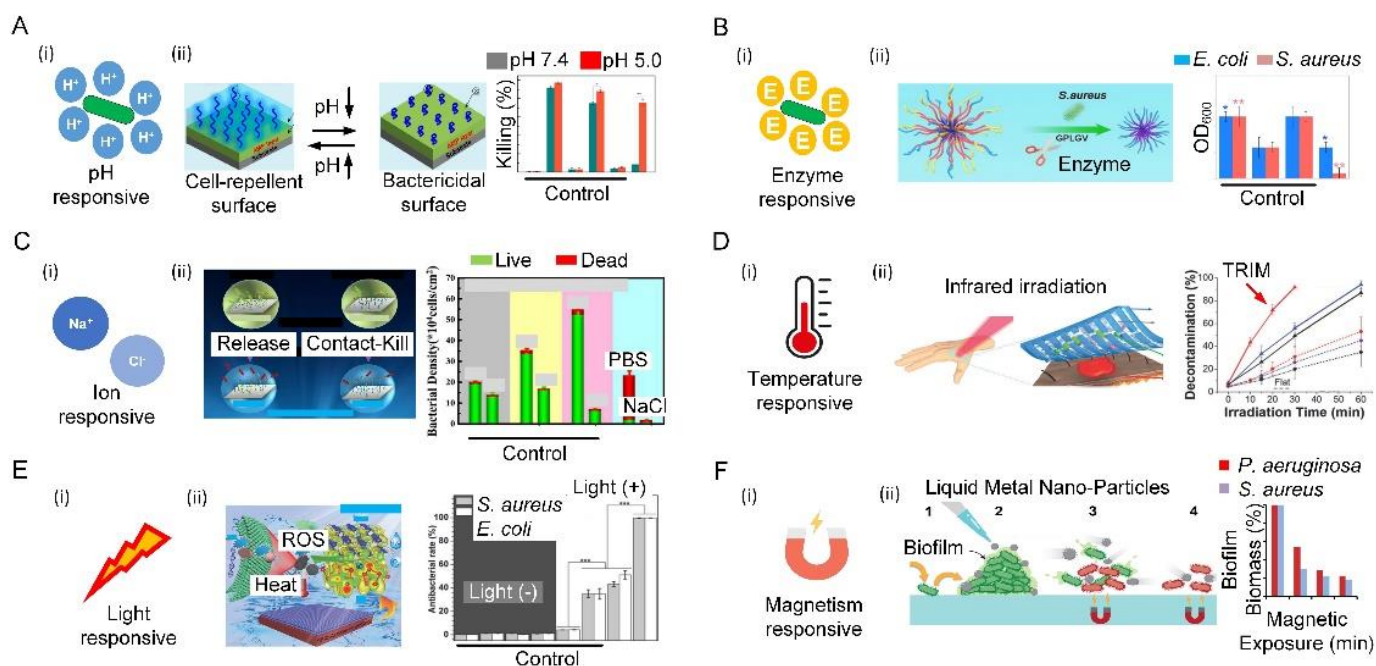


Figure 6. Bioinspired responsive surfaces. (A) Schematic illustration of pH-responsive antibacterial surfaces (i) a hierarchical surface, when bacteria colonize surfaces, bacteria-induced acidification collapses the outermost poly (methacrylic acid) chains, thereby exposing the underlying antimicrobial peptides to kill bacteria on demand. Additionally, dead bacteria can be released after the PMAA chains recover hydrophilicity due to an increase in ambient pH (ii). Reproduced with permission [141]. 2016, American Chemical Society (United States). (B) Schematic diagram of the enzyme-responsive antibacterial surface (i) illustration of the bio-interface with enzyme-responsive, antibacterial, and cell-adhesion functions for tissue engineering (ii). Reproduced with permission [142]. 2021, Elsevier. (C) Schematic diagram of ion-responsive antibacterial surface (i) salt-responsive poly(3-(dimethyl(4-vinylbenzyl) ammonio) propyl sulfonate), antifouling poly (N-hydroxyethyl acrylamide), and bactericidal triclosan to form two types of brushes, which demonstrated their tri-functional antibacterial activity to resist bacterial attachment by poly (N-hydroxyethyl acrylamide), to release ~90% of dead bacteria from the surface by poly(3-(dimethyl(4-vinylbenzyl) ammonio) propyl sulfonate), and to kill ~90% of bacteria on the surface by triclosan (ii). Reproduced with permission [145]. 2019, Royal Society of Chemistry. (D) Schematic illustration of temperature-responsive antibacterial surfaces (i) the thermal-disrupting interface induced mitigation film attached to the skin, absorbing infrared light and generating localized heat that kills bacteria in the recessed areas of the film while sparing surrounding epithelial host cells (ii). Reproduced with permission [146]. 2020, Wiley-VCH. (E) Schematic illustration of light-responsive antibacterial surfaces (i) Schematic illustration of photocatalytic and photothermal efficiency of red phosphorus/zinc oxide heterojunction thin film for rapid point-of-use disinfection (ii). Reproduced with permission [152]. 2019, Wiley-VCH. (F) Schematic illustration of magnetism-responsive antibacterial surfaces (i) Magnetically responsive gallium-based liquid metal droplets act as antimicrobial materials to physically damage, decompose, and kill pathogens within mature biofilms (ii). Reproduced with permission [153]. 2020, American Chemical Society (United States).

Mechanical waves such as ultrasound waves could induce surfaces made of piezoelectric materials to generate reactive oxygen species to make them antibacterial (Figure 7(Ci)). For example, a piezoelectric surface was prepared by using barium titanate nanocubes whose Schottky junctions were modified with gold nanoparticles. This surface could sense exogenous ultrasound waves and produce highly reactive oxygen species as a response to obtain antibacterial ability (Figure 7(Cii)). It was demonstrated that this surface exhibited high antibacterial efficiency against both typical Gram-negative and Gram-positive bacteria, offering a promising method for efficient ultrasonic therapy [157].

Dynamic actuating motions of surfaces can prevent bacterial attachment to suppress surface fouling (Figure 7(Di)). This phenomenon has been widely found in nature, such as red blood cells, arteries, blood vessels, starfish, seaweed, mussels, and the skin of batoidea and pilot whales. Particularly, batoidea manipulate their body in an undulatory style to generate vortices to repel bacteria. Inspired by this, a flexible multilayer responsive surface was designed to integrate dynamic undulatory motion with bactericidal nanospine arrays (Figure 7(Dii)). Under an applied magnetic field, this surface behaved with a batoidea-like undulatory motion, which generated strong vortices to repel bacteria. Moreover, the integration of a dynamic undulatory motion and static nanospine array enabled this surface to repel and kill bacteria simultaneously, effectively inhibiting biofilm formation for an extended period of 7 days [158].

Plasma treatment is commonly used to make surfaces antibacterial owing to its ability to change the surface wettability. For example, after being treated by non-thermal atmospheric pressure plasma jets (NTAPPJs), the titanium surface became antibacterial against two bacteria with different cell-wall structures, including Gram-positive and Gram-negative bacteria. The adhesion and biofilm formation rates of bacteria on NTAPPJ-treated titanium surfaces were significantly reduced compared to untreated samples. Surfaces treated with NTAPPJ can induce oxidation in bacteria, which were more susceptible to Gram-negative bacteria due to differences in the cell-wall structure. In samples treated with NTAPPJs for a longer time, the adhesion rate and biofilm formation rate of Gram-negative bacteria were significantly lower than those of Gram-positive bacteria [159].

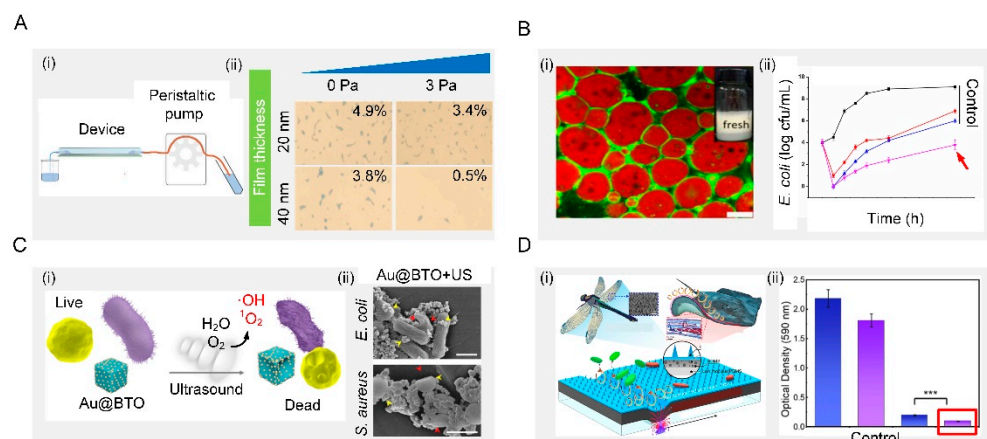


Figure 7. Active removal. (A) Shear removal. Schematic illustration of the process of bacterial adhesion strength assay in the microfluidic device. After pre-seed of *S. aureus* in a microfluidic device, many bacterial cells detached from the C-40 surface under the same shear stress. Reproduced with permission [154]. 2016, Royal Society of Chemistry. (B) Interfacial tension. Schematic illustration of fresh Pickering emulsions. Effects of Zein/GA-thymol Pickering emulsions on the growth of *E. coli*. Reproduced with permission [156]. 2021, Elsevier. (C) Mechanical waves. Schematic diagram of sonodynamic bacterial elimination based on piezoelectric nanocomposite. Reproduced with permission [157]. 2021, Elsevier. (D) Dynamic actuating motions. Conceptual schematic of dynamic nanoneedle composites and long-term antibiofilm testing. Reproduced with permission [158]. 2021, Elsevier.

5. Applications of Bioinspired Antibacterial Surfaces

5.1. Biomedical Devices/Implants

The past 30 years have seen the explosive development of biomedical devices and implants, such as hips, knee-implant screws, stents, heart valves, and blood-vessel grafts, for saving lives and tremendously restoring the quality of human life. However, these devices/implants face the risk of function failure induced by bacterial infection, which may lead to secondary damage to patients or even death. Therefore, the quest for durable biomedical equipment to control bacterial attachment and multiplication has become ever more urgent [160–164]. In pursuit of this, S. Sang et al. used polydopamine as intermediate and loaded strontium carbonate nanoparticles on porous sulfonated PEEK materials through inlays to obtain strontium-doped SPEEK, which could promote bone formation and osseointegration ability. Subsequently, they loaded a layer of silk protein-gentamicin coating on the SPEEK material to endow it with antibacterial ability. This provided innovative inspiration for developing novel functional orthopedic implants, such as antibacterial and antiloose implants [165].

5.2. Wound Dressing

Open wounds and burns are susceptible to bacterial infection due to the lack of protection of the superficial skin. A traditional dressing was made from silver or an antibacterial agent, or was manufactured with slow-release silver or an antibacterial agent while considering safety issues such as the induction potential and the consumption of biological substances from this slow-spreading material [166]. For example, the preparation of durable antibacterial wound dressings by using the strong interfacial interaction between polyhydroxy antibiotics and gelatin and its in situ cross-linking with polydopamine [167]. However, an antibiotic-based dressing can easily induce multidrug resistance in bacteria and even the emergence of super bacteria, greatly limiting its practical application. As an alternative, researchers have explored bioinspired dressings by mimicking the way the host immune system detects and eliminates bacteria. A bioinspired dressing with a catechol-chitosan film-like melanin structure and redox activity was prepared. The film had reversible redox activity and could catalyze the repeated transfer of electrons from ascorbic acid to oxygen to continuously generate reactive oxygen species. Furthermore, this bioinspired dressing can also generate reactive oxygen species, impart antibacterial activity and promote wound healing [168]. Considering the uncertainty and possibility of pathogen invasion during a relatively long wound-healing process, an ideal dressing should be able to monitor wound conditions and effectively suppress pathogens in a timely way. Toward this end, a multifunctional wound dressing based on a novel self-healing elastomer was developed, which can enable real-time monitoring of temperature, pH, and glucose in the healing area and sutureless closure (Figure 8A) [169].

5.3. Electronic Skin

Electronic skin with functions like natural skin has attracted intense interest in a variety of applications including wearables, person-centric health monitoring, smart prosthetics and robotics, and human-machine interfaces. Since electronic skin is usually attached to the human body, it is prone to microbial growth due to the contamination from sweat containing organic matter. Such a microbial growth could lead to inflammation and bacterial infections in the users, which are detrimental to their health. To fundamentally overcome this issue, electronic skin should be endowed with additional antibacterial ability on top of its original function. On one hand, the antibacterial properties can remove the interference of bacteria on the electronic skin and obtain more stable bioelectronic signals, including electrocardiography and electromyography information (Figure 8B). At the same time, the electronic skin had a strong inherent antibacterial effect on *E. coli* and *S. aureus*, effectively limiting the development of microorganisms and preventing bacterial infection, and thus providing users with a comfortable and safe environment [170]. On the other hand, a self-driven antibacterial electronic skin with antibacterial was built based on an all-

nanofiber triboelectric nanogenerator. This electronic skin enabled real-time, self-powered monitoring of whole-body physiological signals and joint movements. More importantly, the electronic skin had excellent antibacterial activity against *E. coli* and *S. aureus*, which can greatly inhibit bacterial growth and prevent bacterial infection [171].

5.4. Air Disinfection System

The disinfection of air, water, equipment surfaces and even the human body is indispensable for disease prevention and public safety, playing a crucial role in the health of human beings and the sustainable development of society. As population and human activities increase rapidly, the uncontrolled discharge of polluted air and wastewater has been irreversibly damaging human health, natural resources, and biological chains. For example, such pollution would produce a large number of airborne pathogens, the carrier of many bacteria that could cause the transmission of pneumonia, asthma, and influenza. In response to these great threats to public health, urgent action was therefore needed to address such pollution at the source. One typical example was a self-powered disinfection system that can quickly disinfect airborne bacteria and viruses (Figure 8C). This system relied on an efficient nanowire-assisted electroporation mechanism, which was actuated by a vibration-driven triboelectric nanogenerator. More than 99.99% of bacteria and viruses are inactivated in the air at a fast airflow rate (2 m/s), which is equivalent to a processing time of 0.025 s while maintaining a low pressure drop of only 24 Pa. This work provides a proof-of-concept demonstration for the practical application of green ventilation systems in buildings [172].

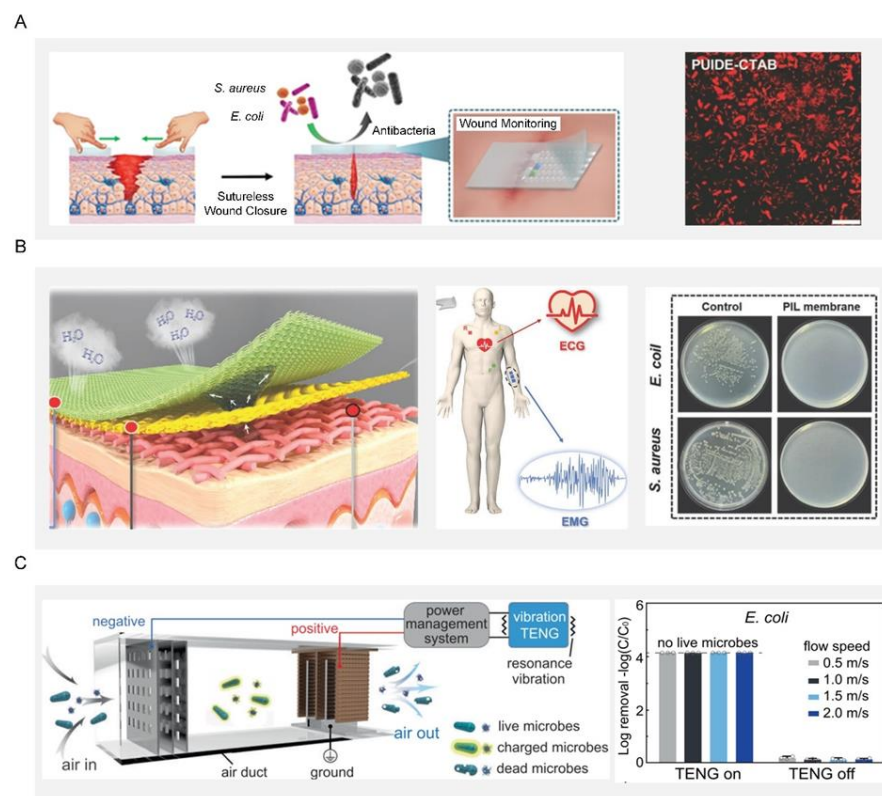


Figure 8. Applications of bioinspired antibacterial surfaces. (A) Schematic diagram of self-healing elastomer multifunctional wound dressing. Bacteria after being cocultured with PUIDE-CTAB for 6 h. Reproduced with permission [169]. 2021, Wiley-VCH. (B) Schematic diagram of fabrication and application of PIL-membrane electronic skin with hygrosopic, breathable, and antibacterial properties for bioelectric signal monitoring. Reproduced with permission [171]. 2022, Wiley-VCH. (C) Schematic diagram of the resonance-vibration-driven disinfection system in the air duct. Disinfection efficiency for *E. coli*. Reproduced with permission [172]. 2021, Nature Portfolio.

6. Conclusions and Perspectives

Bacteria have and will coexist with humans forever; as such, how do humans survive an environment with ubiquitous bacteria that remarkably impact our health and ecological safety? Considering that conventional solutions such as antibacterial agents are very likely to lose their effectiveness when used frequently, developing alternative methods that are smart, eco-friendly, and effective long-term has become more and more urgent. Fortunately, the emergence of bioinspired antibacterial surfaces that mimic optimal natural strategies has shown enormous potential in preventing bacterial infection. In this review, we first described the fundamental process of bacterial infection and the factors that may potentially affect the process. We next summarized several typical natural antibacterial surfaces and their antibacterial mechanisms. We also presented the key bioinspired surfaces that can break down the bacterial transmission chain. The excellent performance of these bioinspired surfaces demonstrates the feasibility of them serving as potential alternatives to antibacterial agents. Despite their remarkable capability to suppress bacterial invasion, bioinspired antibacterial surfaces are facing some limitations and concerns that hinder their practical applications [173].

To promote the transition from lab research to practical applications, the overall performance of the bioinspired antibacterial surfaces should be improved enough to cope with complex, transient scenarios in the real world [76,174–184]. First, a bioinspired antibacterial surface should be highly adaptive to a wide spectrum of bacteria. Currently, a certain bioinspired antibacterial surface is designed to be solely effective against a certain type of bacteria. Such a one-to-one relationship is ineffective in a practical environment teeming with a variety of bacteria and needs to be upgraded to a one-to-many relationship, in which a given surface can defend against infections from multiple types of bacteria. Toward this end, the surface may be fundamentally redesigned from the perspectives of topology and materials to integrate various abilities effective against different bacteria. Briefly, a multiscale hierarchical structure is realized by combining bacteria-repellent surfaces, such as lotus-leaf, springtail-skin, and shark-skin structures, with contact-killing surfaces such as cicada-wing, dragonfly-wing, and lizard-skin structures. This multiscale hierarchical structure can achieve the repelling or contact-killing of a broad spectrum of bacteria, even fungi and viruses. Implementing the two functions simultaneously can require resorting to decomposing them into multiscale hierarchical structures. Second, a bioinspired antibacterial surface should be highly durable for long-term use. At present, those surfaces suffer from function deterioration owing to the long-time exposure to the working environment, greatly impairing the antibacterial performance. By contrast, such a problem is not found in their natural counterparts living in moist environments. Therefore, an innovative bottom-up strategy is required to fundamentally reveal natural mechanisms and design bioinspired surfaces that can rival their natural counterparts in terms of functionality and durability. Third, bioinspired antibacterial surfaces need to achieve biocompatibility. For now, bioinspired antibacterial surfaces remain controversial due to the biological complexity of medical conditions. A low-biocompatibility surface can lead to blood clotting and all manner of other inflammation and tissue-sensitization problems. The above problems can be improved by optimizing biocompatible materials and bionics design. Bioinspired antibacterial surfaces with biocompatibility can reduce inflammation and increase the success rate of implants.

As for the transformation of bioinspired antibacterial science to actual productivity, the fabrication technique for bioinspired antibacterial surfaces needs to be revolutionized to realize some essential advantages including their large-scale, cost-effective, and eco-friendly use. First, large-scale fabrication capability, while not sacrificing the quality and performance of the surfaces, is fundamental to driving mass adoption, which is, however, inaccessible in current strategies that commonly rely on microfabricated equipment. Specifically, the manufacture of high-precision lithography machines for surface processing is a difficult problem. Second, manufacturers are constantly trying to find ways to make their processes more cost-effective, including continuously developing advanced and so-

phisticated production machinery, improving cutting tools, and optimizing overall cutting systems. Specific strategies include high-speed machining, high-feed machining, high-performance machining, and digital machining [173]. Third, eco-friendliness is also very important in the processing process. In the production of materials, or as raw materials, or due to technological requirements, many processes inevitably introduce some harmful substances, which not only cause pollution in production and worsen labor conditions but also cause long-term damage to human health and the environment after they are transformed into products.

Focusing on the biomedical applications of the bioinspired antibacterial surfaces, safety becomes the first and foremost priority. Currently, it is still controversial whether the organic or inorganic compounds contained in bioinspired antibacterial surfaces will cause adverse effects on mammalian cells during long-term use. In this vein, the toxicity of bioinspired antibacterial surfaces resulting from extra-immune responses should be minimized or even eliminated before they enter the market. Indeed, achieving full commercialization of bioinspired antibacterial surfaces involves highly interdisciplinary problems, ranging from chemistry and engineering to biomedicine and clinical medicine, and still has a long way to go. To bridge this gap, one feasible solution may be to decompose the highly interdisciplinary problems into smaller and more manageable pieces. This calls for continuous and collective efforts from chemists, engineers, biomedical researchers, and clinicians to design, develop, demonstrate, and deliver next-generation bioinspired antibacterial surfaces and products. We envision that, with the support of constant effort, remarkable breakthroughs will be made in the development of bioinspired antibacterial surfaces, which will further enrich the library of antibacterial strategies for human health.

Author Contributions: Writing—original draft (lead), X.Y. and W.Z.; Writing—review and editing (lead), X.Q., W.L. and Z.W.; Writing—review and editing (Supporting), M.C., Y.G., T.W., K.W., Z.S. and C.Z. All authors have read and agreed to the published version of the manuscript.

Funding: This work was supported by the Funding from Health @ InnoHK (Hong Kong Centre for Cerebro-Cardiovascular Health Engineering (COCHE)), Innovation and Technology Commission, The Government of the Hong Kong Special Administrative Region of the People’s Republic of China.

Conflicts of Interest: The authors declare no conflict of interest.

References

- Rossi, M.; Amaretti, A.; Raimondi, S. Folate production by probiotic bacteria. *Nutrients* **2011**, *3*, 118–134. [CrossRef]
- Li, W.; Thian, E.S.; Wang, M.; Wang, Z.; Ren, L. Surface Design for Antibacterial Materials: From Fundamentals to Advanced Strategies. *Adv. Sci.* **2021**, *8*, 2100368. [CrossRef]
- Sharma, S.K.; Mohan, A.; Kohli, M. Extrapulmonary tuberculosis. *Expert Rev. Respir. Med.* **2021**, *15*, 931–948. [CrossRef]
- Chakaya, J.; Khan, M.; Ntoumi, F.; Aklillu, E.; Fatima, R.; Mwaba, P.; Kapata, N.; Mfinanga, S.; Hasnain, S.; Katoto, P.D.M.C.; et al. Global Tuberculosis Report 2020—Reflections on the Global TB burden, treatment and prevention efforts. *Int. J. Infect. Dis.* **2021**, *113*, S7–S12. [CrossRef]
- Pastena, M.D.; Paiella, S.; Marchegiani, G.; Malleo, G.; Ciprani, D.; Gasparini, C.; Secchettin, E.; Salvia, R.; Bassi, C. Postoperative infections represent a major determinant of outcome after pancreaticoduodenectomy: Results from a high-volume center. *Surgery* **2017**, *162*, 792–801. [CrossRef]
- Magill, S.S.; Edwards, J.R.; Beldavs, Z.G.; Dumyati, G.; Janelle, S.J.; Kainer, M.A.; Lynfield, R.; Nadle, J.; Neuhauser, M.M.; Ray, S.M.; et al. Prevalence of Antimicrobial Use in US Acute Care Hospitals, May–September 2011. *JAMA* **2014**, *312*, 1438–1446. [CrossRef]
- Thappeta, K.R.V.; Vikhe, Y.S.; Yong, A.M.H.; Chan-Park, M.B.; Kline, K.A. Combined Efficacy of an Antimicrobial Cationic Peptide Polymer with Conventional Antibiotics to Combat Multidrug-Resistant Pathogens. *ACS Infect. Dis.* **2020**, *6*, 1228–1237. [CrossRef]
- Buhner, S.H. *Herbal Antibiotics: Natural Alternatives for Treating Drug-Resistant Bacteria*; Storey Publishing: North Adams, MA, USA, 2012.
- Mangindaan, D.; Lin, G.Y.; Kuo, C.J.; Chien, H.W. Biosynthesis of silver nanoparticles as catalyst by spent coffee ground/recycled poly (ethylene terephthalate) composites. *Food Bioprod. Process.* **2020**, *121*, 193–201. [CrossRef]
- Hasan, J.; Crawford, R.J.; Ivanova, E.P. Antibacterial surfaces: The quest for a new generation of biomaterials. *Trends Biotechnol.* **2013**, *31*, 295–304. [CrossRef]
- Xu, L.Q.; Neoh, K.G.; Kang, E.T. Natural polyphenols as versatile platforms for material engineering and surface functionalization. *Prog. Polym. Sci.* **2018**, *87*, 165–196. [CrossRef]

12. Tavakolian, M.; Jafari, S.M.; van de Ven, T.G.M. A Review on Surface-Functionalized Cellulosic Nanostructures as Biocompatible Antibacterial Materials. *Nano-Micro Lett.* **2020**, *12*, 73. [CrossRef]
13. Yimyai, T.; Thiramanas, R.; Phakkeeree, T.; Iamsaard, S.; Crespy, D. Adaptive Coatings with Anticorrosion and Antibiofouling Properties. *Adv. Funct. Mater.* **2021**, *31*, 2102568. [CrossRef]
14. Shen, S.; Hao, Y.; Zhang, Y.; Zhang, G.; Zhou, X.; Bai, R.B. Enhancing the Antifouling Properties of Poly(vinylidene fluoride) (PVDF) Membrane through a Novel Blending and Surface-Grafting Modification Approach. *ACS Omega* **2018**, *3*, 17403–17415. [CrossRef]
15. Chen, R.; Zhang, Y.; Xie, Q.; Chen, Z.; Ma, C.; Zhang, G. Transparent Polymer-Ceramic Hybrid Antifouling Coating with Superior Mechanical Properties. *Adv. Funct. Mater.* **2021**, *31*, 2011145. [CrossRef]
16. Liang, Z.H.; Wu, S.L.; Liu, C.; Yang, H.C.; Darling, S.B.; Xu, Z.K. When SLIPS meets TIPS: An endogenous lubricant-infused surface by taking the diluent as the lubricant. *Chem. Eng. J.* **2021**, *425*, 130600. [CrossRef]
17. Li, J.; Ueda, E.; Paulssen, D.; Levkin, P.A. Slippery Lubricant-Infused Surfaces: Properties and Emerging Applications. *Adv. Funct. Mater.* **2019**, *29*, 1802317. [CrossRef]
18. Bixler, G.D.; Bhushan, B. Biofouling: Lessons from nature. *Philos. Trans. R. Soc. A* **2012**, *370*, 2381–2417. [CrossRef]
19. Berne, C.; Ellison, C.K.; Ducret, A.; Brun, Y.V. Bacterial adhesion at the single-cell level. *Nat. Rev. Microbiol.* **2018**, *16*, 616–627. [CrossRef]
20. Kreve, S.; Dos Reis, A.C. Bacterial adhesion to biomaterials: What regulates this attachment? A review. *Jpn. Dent. Sci. Rev.* **2021**, *57*, 85–96. [CrossRef]
21. Glinel, K.; Thebault, P.; Humblot, V.; Pradier, C.M.; Jouenne, T. Antibacterial surfaces developed from bio-inspired approaches. *Acta Biomater.* **2012**, *8*, 1670–1684. [CrossRef]
22. Nguyen, S.H.; Webb, H.K.; Crawford, R.J.; Ivanova, E.P. Natural Antibacterial Surfaces. In *Antibacterial Surfaces*; Springer: Cham, Switzerland, 2015; pp. 9–26.
23. Rumbaugh, K.P.; Sauer, K. Biofilm dispersion. *Nat. Rev. Microbiol.* **2020**, *18*, 571–586. [CrossRef]
24. Zhao, C.; Zhou, L.; Chiao, M.; Yang, W. Antibacterial hydrogel coating: Strategies in surface chemistry. *Adv. Colloid Interface Sci.* **2020**, *285*, 102280. [CrossRef]
25. Kaur, R.; Liu, S. Antibacterial surface design—Contact kill. *Prog. Surf. Sci.* **2016**, *91*, 136–153. [CrossRef]
26. Bridges, A.A.; Fei, C.; Bassler, B.L. Identification of signaling pathways, matrix-digestion enzymes, and motility components controlling *Vibrio cholerae* biofilm dispersal. *Proc. Natl. Acad. Sci. USA* **2020**, *117*, 32639–32647. [CrossRef]
27. Jayaprakashvel, M.; Sami, M.; Subramani, R. Antibiofilm, Antifouling, and Anticorrosive Biomaterials and Nanomaterials for Marine Applications. In *Nanostructures for Antimicrobial and Antibiofilm Applications*; Springer: Cham, Switzerland, 2020; Volume 233.
28. Wong, T.S.; Kang, S.H.; Tang, S.K.Y.; Smythe, E.J.; Hatton, B.D.; Grinthal, A.; Aizenberg, J. Bioinspired self-repairing slippery surfaces with pressure-stable omniphobicity. *Nature* **2011**, *477*, 443–447. [CrossRef]
29. Rigo, S.; Cai, C.; Gunkel-Grabole, G.; Maurizi, L.; Zhang, X.; Xu, J.; Palivan, C.G. Nanoscience-Based Strategies to Engineer Antimicrobial Surfaces. *Adv. Sci.* **2018**, *5*, 1700892. [CrossRef]
30. Wang, Y.; Yang, Y.; Shi, Y.; Song, H.; Yu, C. Antibiotic-Free Antibacterial Strategies Enabled by Nanomaterials: Progress and Perspectives. *Adv. Mater.* **2020**, *32*, 1904106. [CrossRef]
31. Miao, W.; Wang, J.; Liu, J.; Zhang, Y. Self-Cleaning and Antibacterial Zeolitic Imidazolate Framework Coatings. *Adv. Mater. Interfaces* **2018**, *5*, 1800167. [CrossRef]
32. Barthlott, W.; Neinhuis, C. Purity of the sacred lotus, or escape from contamination in biological surfaces. *Planta* **1997**, *202*, 1–8. [CrossRef]
33. Larrañaga-Altuna, M.; Zabala, A.; Llavori, I.; Pearce, O.; Nguyen, D.T.; Caro, J.; Mescheder, H.; Endrino, J.L.; Goel, G.; Ayre, W.N.; et al. Bactericidal surfaces: An emerging 21st-century ultra-precision manufacturing and materials puzzle. *Appl. Phys. Rev.* **2021**, *8*, 021303. [CrossRef]
34. Schroeder, T.B.H.; Houghtaling, J.; Wilts, B.D.; Mayer, M. It's Not a Bug, It's a Feature: Functional Materials in Insects. *Adv. Mater.* **2018**, *30*, 1705322. [CrossRef]
35. Watson, G.S.; Green, D.W.; Cribb, B.W.; Brown, C.L.; Meritt, C.R.; Tobin, M.J.; Vongsivut, J.; Sun, M.; Liang, A.P.; Watson, J.A. Insect Analogue to the Lotus Leaf: A Planthopper Wing Membrane Incorporating a Low-Adhesion, Nonwetting, Superhydrophobic, Bactericidal, and Biocompatible Surface. *ACS Appl. Mater. Interfaces* **2017**, *9*, 24381–24392. [CrossRef]
36. Hensel, R.; Neinhuis, C.; Werner, C. The springtail cuticle as a blueprint for omniphobic surfaces. *Chem. Soc. Rev.* **2016**, *45*, 323. [CrossRef]
37. Liu, M.; Li, J.; Zhou, X.; Li, J.; Feng, S.; Cheng, Y.; Wang, S.; Wang, Z. Inhibiting Random Droplet Motion on Hot Surfaces by Engineering Symmetry-Breaking Janus-Mushroom Structure. *Adv. Mater.* **2020**, *32*, 1907999. [CrossRef]
38. Li, W.; Yu, M.; Sun, J.; Mochizuki, K.; Chen, S.; Zheng, H.; Li, J.; Yao, S.; Wu, H.; Ong, B.S.; et al. Crack engineering for the construction of arbitrary hierarchical architectures. *Proc. Natl. Acad. Sci. USA* **2019**, *116*, 23909–23914. [CrossRef]
39. Hannig, C.; Helbig, R.; Hilsenbeck, J.; Werner, C.; Hannig, M. Impact of the springtail's cuticle nanotopography on bioadhesion and biofilm formation in vitro and in the oral cavity. *R. Soc. Open Sci.* **2018**, *5*, 171742. [CrossRef]
40. Huang, J.; Wang, Q.; Wu, Z.; Ma, Z.; Yan, C.; Shi, Y.; Su, B. 3D-Printed Underwater Super-Oleophobic Shark Skin toward the Electricity Generation through Low-Adhesion Sliding of Magnetic Nanofluid Droplets. *Adv. Funct. Mater.* **2021**, *31*, 2103776. [CrossRef]

41. Gosline, J.M. *Mechanical Design of Structural Materials in Animals*; Princeton University Press: Princeton, NJ, USA, 2018.
42. Chien, H.W.; Chen, X.Y.; Tsai, W.P.; Lee, M. Inhibition of biofilm formation by rough shark skin-patterned surfaces. *Colloids Surf. B* **2020**, *186*, 110738. [CrossRef]
43. Chien, H.W.; Chen, X.Y.; Tsai, W.P. Poly (methyl methacrylate)/titanium dioxide (PMMA/TiO₂) nanocomposite with shark-skin structure for preventing biofilm formation. *Mater. Lett.* **2021**, *285*, 129098. [CrossRef]
44. Bazaka, K.; Crawford, R.J.; Ivanova, E.P. Do bacteria differentiate between degrees of nanoscale surface roughness? *Biotechnol. J.* **2011**, *6*, 1103–1114. [CrossRef]
45. Tripathy, A.; Sen, P.; Su, B.; Briscoe, W.H. Natural and bioinspired nanostructured bactericidal surfaces. *Adv. Colloid Interface Sci.* **2017**, *248*, 85–104. [CrossRef]
46. Pogodin, S.; Hasan, J.; Baulin, V.A.; Webb, H.K.; Truong, V.K.; Nguyen, T.H.P.; Boshkovikj, V.; Fluke, C.J.; Watson, G.S.; Watson, J.A.; et al. Biophysical Model of Bacterial Cell Interactions with Nanopatterned Cicada Wing Surfaces. *Biophys. J.* **2013**, *104*, 835–840. [CrossRef]
47. Yang, S.; Wu, C.; Zhao, G.; Sun, J.; Yao, X.; Ma, X.; Wang, Z. Condensation frosting and passive anti-frosting. *Cell Rep. Phys. Sci.* **2021**, *2*, 100474. [CrossRef]
48. Watson, G.S.; Green, D.W.; Sun, M.; Liang, A.; Xin, L.; Cribb, B.W.; Watson, J.A. The Insect (cicada) Wing Membrane Micro/Nano Structure–Nature’s Templates for Control of Optics, Wetting, Adhesion, Contamination, Bacteria and Eukaryotic Cells. *J. Nanosci. Adv. Technol.* **2015**, *1*, 6–16. [CrossRef]
49. Bandara, C.D.; Singh, S.; Afara, I.O.; Wolff, A.; Tesfamichael, T.; Ostrikov, K.; Oloyede, A. Bactericidal Effects of Natural Nanotopography of Dragonfly Wing on *Escherichia coli*. *ACS Appl. Mater. Interfaces* **2017**, *9*, 6746–6760. [CrossRef]
50. Ivanova, E.P.; Hasan, J.; Webb, H.K.; Gervinskas, G.; Juodkakis, S.; Truong, V.K.; Wu, A.H.F.; Lamb, R.N.; Baulin, V.A.; Watson, G.S.; et al. Bactericidal activity of black silicon. *Nat. Commun.* **2013**, *4*, 2838. [CrossRef]
51. Green, D.W.; Lee, K.K.H.; Watson, J.A.; Kim, H.Y.; Yoon, K.S.; Kim, E.J.; Lee, J.M.; Watson, G.S.; Jung, H.S. High Quality Bioreplication of Intricate Nanostructures from a Fragile Gecko Skin Surface with Bactericidal Properties. *Sci. Rep.* **2017**, *7*, 41023. [CrossRef]
52. Watson, G.S.; Green, D.W.; Schwarzkopf, L.; Li, X.; Cribb, B.W.; Myhra, S.; Watson, J.A. A gecko skin micro/nano structure—A low adhesion, superhydrophobic, anti-wetting, self-cleaning, biocompatible, antibacterial surface. *Acta Biomater.* **2015**, *21*, 109–122. [CrossRef]
53. Li, X.; Cheung, G.S.; Watson, G.S.; Watson, J.A.; Lin, S.; Schwarzkopf, L.; Green, D.W. The nanotipped hairs of gecko skin and biotemplated replicas impair and/or kill pathogenic bacteria with high efficiency. *Nanoscale* **2016**, *8*, 18860–18869. [CrossRef]
54. Guo, Z.; Liu, W.; Su, B.L. Why so strong for the lotus leaf? *Appl. Phys. Lett.* **2008**, *93*, 201909. [CrossRef]
55. Dziergwa, J.; Singh, S.; Bridges, C.R.; Kerwath, S.E.; Enax, J.; Auerswald, L. Acid-base adjustments and first evidence of denticle corrosion caused by ocean acidification conditions in a demersal shark species. *Sci. Rep.* **2019**, *9*, 18668. [CrossRef]
56. Sun, M.; Liang, A.; Watson, G.S.; Watson, J.A.; Zheng, Y.; Lu, J.; Jiang, L. Influence of Cuticle Nanostructuring on the Wetting Behaviour/States on Cicada Wings. *PLoS ONE* **2012**, *7*, e35056. [CrossRef]
57. Linklater, D.P.; Juodkakis, S.; Ivanova, E.P. Nanofabrication of mechano-bactericidal surfaces. *Nanoscale* **2017**, *9*, 16564–16585. [CrossRef]
58. Totani, M.; Liu, L.; Matsuno, H.; Tanaka, K. Design of a star-like hyperbranched polymer having hydrophilic arms for anti-biofouling coating. *J. Mater. Chem. B* **2019**, *7*, 1045. [CrossRef]
59. Su, X.; Hao, D.; Li, Z.; Guo, X.; Jiang, L. Design of hierarchical comb hydrophilic polymer brush (HCHPB) surfaces inspired by fish mucus for anti-biofouling. *J. Mater. Chem. B* **2019**, *7*, 1322. [CrossRef]
60. Song, F.; Zhang, L.; Chen, R.; Liu, Q.; Liu, J.; Yu, J.; Liu, P.; Duan, J.; Wang, J. Bioinspired Durable Antibacterial and Antifouling Coatings Based on Borneol Fluorinated Polymers: Demonstrating Direct Evidence of Antiadhesion. *ACS Appl. Mater. Interfaces* **2021**, *13*, 33417–33426. [CrossRef]
61. Luo, L.; Zhou, Y.; Xu, X.; Shi, W.; Hu, J.; Li, G.; Qu, X.; Guo, Y.; Tian, X.; Zaman, A.; et al. Progress in construction of bio-inspired physico-antimicrobial surfaces. *Nanotechnol. Rev.* **2020**, *9*, 1562–1575. [CrossRef]
62. Keller, N.; Bruchmann, J.; Sollich, T.; Richter, C.; Thelen, R.; Kotz, F.; Schwartz, T.; Helmer, D.; Rapp, B.E. Study of Biofilm Growth on Slippery Liquid-Infused Porous Surfaces Made from Fluoropor. *ACS Appl. Mater. Interfaces* **2019**, *11*, 4480–4487. [CrossRef]
63. Li, J.; Kleintschek, T.; Rieder, A.; Cheng, Y.; Baumbach, T.; Obst, U.; Schwartz, T.; Levkin, P.A. Hydrophobic liquid-infused porous polymer surfaces for antibacterial applications. *ACS Appl. Mater. Interfaces* **2013**, *5*, 6704–6711. [CrossRef]
64. Hizal, F.; Rungraeng, N.; Lee, J.; Jun, S.; Busscher, H.J.; van der Mei, H.C.; Choi, C.H. Nanoengineered Superhydrophobic Surfaces of Aluminum with Extremely Low Bacterial Adhesivity. *ACS Appl. Mater. Interfaces* **2017**, *9*, 12118–12129. [CrossRef]
65. Li, M.; Schlaich, C.; Kulka, M.W.; Donskyi, I.S.; Schwerdtle, T.; Unger, W.E.S.; Haag, R. Mussel-inspired coatings with tunable wettability, for enhanced antibacterial efficiency and reduced bacterial adhesion. *J. Mater. Chem. B* **2019**, *7*, 3438. [CrossRef]
66. Jiang, R.; Hao, L.; Song, L.; Tian, L.; Fan, Y.; Zhao, J.; Liu, C.; Ming, W.; Ren, L. Lotus-leaf-inspired hierarchical structured surface with non-fouling and mechanical bactericidal performances. *Chem. Eng. J.* **2020**, *398*, 125609. [CrossRef]
67. Su, M.; Zhang, R.; Li, H.; Jin, X.; Li, J.; Yue, X.; Qin, D. In situ deposition of MOF199 onto hierarchical structures of bamboo and wood and their antibacterial properties. *RSC Adv.* **2019**, *9*, 40277. [CrossRef]
68. Song, M.; Hu, D.; Zheng, X.; Wang, L.; Yu, Z.; An, W.; Na, R.; Li, C.; Li, N.; Lu, Z.; et al. Enhancing Droplet Deposition on Wired and Curved Superhydrophobic Leaves. *ACS Nano* **2019**, *13*, 7966–7974. [CrossRef]

69. Wang, X.; Ding, B.; Yu, J.; Wang, M. Engineering biomimetic superhydrophobic surfaces of electrospun nanomaterials. *Nano Today* **2011**, *6*, 510–530. [CrossRef]
70. Chi, J.; Zhang, X.; Wang, Y.; Shao, C.; Shang, L.; Zhao, Y. Bio-inspired wettability patterns for biomedical applications. *Mater. Horiz.* **2021**, *8*, 124–144. [CrossRef]
71. Zhou, Z.L.; Cao, C.; Cao, L.D.; Zheng, L.; Xu, J.; Li, F.M.; Huang, Q.L. Evaporation kinetics of surfactant solution droplets on rice (*Oryza sativa*) leaves. *PLoS ONE* **2017**, *12*, e0176870. [CrossRef]
72. Schumacher, J.F.; Carman, M.L.; Estes, T.G.; Feinberg, A.W.; Wilson, L.H.; Callow, M.E.; Callow, J.A.; Finlay, J.A.; Brennan, A.B. Engineered antifouling microtopographies—effect of feature size, geometry, and roughness on settlement of zoospores of the green alga *Ulva*. *Biofouling* **2007**, *23*, 55–62. [CrossRef]
73. Reddy, S.T.; Chung, K.K.; McDaniel, C.J.; Darouiche, R.O.; Landman, J.; Brennan, A.B. Micropatterned Surfaces for Reducing the Risk of Catheter-Associated Urinary Tract Infection: An In Vitro Study on the Effect of Sharklet Micropatterned Surfaces to Inhibit Bacterial Colonization and Migration of Uropathogenic *Escherichia coli*. *J. Endourol.* **2011**, *25*, 1547–1552. [CrossRef]
74. Arisoy, F.D.; Kolewe, K.W.; Homyak, B.; Kurtz, I.S.; Schiffman, J.D.; Watkins, J.J. Bioinspired Photocatalytic Shark-Skin Surfaces with Antibacterial and Antifouling Activity via Nanoimprint Lithography. *ACS Appl. Mater. Interfaces* **2018**, *10*, 20055–20063. [CrossRef]
75. Erathodiyil, N.; Chan, H.M.; Wu, H.; Ying, J.Y. Zwitterionic polymers and hydrogels for antibiofouling applications in implantable devices. *Mater. Today* **2020**, *38*, 84–98. [CrossRef]
76. Prieto-López, L.O.; Herbeck-Engel, P.; Yang, L.; Wu, Q.; Li, J.; Cui, J. When Ultimate Adhesive Mechanism Meets Ultimate Anti-Fouling Surfaces—Polydopamine Versus SLIPS: Which One Prevails? *Adv. Mater. Interfaces* **2020**, *7*, 2000876. [CrossRef]
77. Lowe, S.; O'Brien-Simpson, N.M.; Connal, L.A. Antibiofouling polymer interfaces: Poly (ethylene glycol) and other promising candidates. *Polym. Chem.* **2015**, *6*, 198–212. [CrossRef]
78. Wang, C.; Chen, J.; Xu, J.; Fu, J. Transparent, Mechanically Strong, Amphiphilic Antibiofouling Coatings Integrating Antismudge and Intrinsic Self-Healing Capabilities. *ACS Appl. Polym. Mater.* **2021**, *3*, 3416–3427. [CrossRef]
79. Yang, L.; Wang, C.; Li, L.; Zhu, F.; Ren, X.; Huang, Q.; Cheng, Y.; Li, Y. Bioinspired Integration of Naturally Occurring Molecules towards Universal and Smart Antibacterial Coatings. *Adv. Funct. Mater.* **2022**, *32*, 2108749. [CrossRef]
80. Zeng, Q.; Zhu, Y.; Yu, B.; Sun, Y.; Ding, X.; Xu, C.; Wu, Y.W.; Tang, Z.; Xu, F.J. Antimicrobial and Antifouling Polymeric Agents for Surface Functionalization of Medical Implants. *Biomacromolecules* **2018**, *19*, 2805–2811. [CrossRef]
81. Luan, Y.; Liu, S.; Pihl, M.; van der Mei, H.C.; Liu, J.; Hizal, F.; Choi, C.H.; Chen, H.; Ren, Y.; Busscher, H.J. Bacterial interactions with nanostructured surfaces. *Curr. Opin. Colloid Interface Sci.* **2018**, *38*, 170–189. [CrossRef]
82. Hu, P.; Zeng, H.; Zhou, H.; Zhang, C.; Xie, Q.; Ma, C.; Zhang, G. Silicone Elastomer with Self-Generating Zwitterions for Antifouling Coatings. *Langmuir* **2021**, *37*, 8253–8260. [CrossRef]
83. Chen, S.; Yuan, L.; Li, Q.; Li, J.; Zhu, X.; Jiang, Y.; Sha, O.; Yang, X.; Xin, J.; Wang, J.; et al. Durable Antibacterial and Nonfouling Cotton Textiles with Enhanced Comfort via Zwitterionic Sulfopropylbetaine Coating. *Small* **2016**, *12*, 3516–3521. [CrossRef]
84. Yang, M.; Ding, Y.; Ge, X.; Leng, Y. Control of bacterial adhesion and growth on honeycomb-like patterned surfaces. *Colloid Surf. B* **2015**, *135*, 549–555. [CrossRef]
85. Lichter, J.A.; Thompson, M.T.; Delgadillo, M.; Nishikawa, T.; Rubner, M.F.; Van Vliet, K.J. Substrata Mechanical Stiffness Can Regulate Adhesion of Viable Bacteria. *Biomacromolecules* **2008**, *9*, 1571–1578. [CrossRef]
86. Saha, N.; Monge, C.; Dulong, V.; Picart, C.; Glinel, K. Influence of Polyelectrolyte Film Stiffness on Bacterial Growth. *Biomacromolecules* **2013**, *14*, 520–528. [CrossRef]
87. Song, F.; Ren, D. Stiffness of Cross-Linked Poly (Dimethylsiloxane) Affects Bacterial Adhesion and Antibiotic Susceptibility of Attached Cells. *Langmuir* **2014**, *30*, 10354–10362. [CrossRef]
88. Kolewe, K.W.; Peyton, S.R.; Schiffman, J.D. Fewer Bacteria Adhere to Softer Hydrogels. *ACS Appl. Mater. Interfaces* **2015**, *7*, 19562–19569. [CrossRef] [PubMed]
89. Wang, G.; Feng, H.; Hu, L.; Jin, W.; Hao, Q.; Gao, A.; Peng, X.; Li, W.; Wong, K.Y.; Wang, H.; et al. An antibacterial platform based on capacitive carbon-doped TiO₂ nanotubes after direct or alternating current charging. *Nat. Commun.* **2018**, *9*, 2055. [CrossRef]
90. Radovic-Moreno, A.F.; Lu, T.K.; Puscasu, V.A.; Yoon, C.J.; Langer, R.; Farokhzad, O.C. Surface Charge-Switching Polymeric Nanoparticles for Bacterial Cell Wall-Targeted Delivery of Antibiotics. *ACS Nano* **2012**, *6*, 4279–4287. [CrossRef]
91. Kohanski, M.A.; Dwyer, D.J.; Collins, J.J. How antibiotics kill bacteria: From targets to networks. *Nat. Rev. Microbiol.* **2010**, *8*, 423–435. [CrossRef] [PubMed]
92. Richards, T.; Harrhy, J.H.; Lewis, R.J.; Howe, A.G.R.; Suldecki, G.M.; Folli, A.; Morgan, D.J.; Davies, T.E.; Loveridge, E.J.; Crole, D.A.; et al. A residue-free approach to water disinfection using catalytic in situ generation of reactive oxygen species. *Nat. Catal.* **2021**, *4*, 575–585. [CrossRef]
93. Xiao, Y.; Xu, M.; Lv, N.; Cheng, C.; Huang, P.; Li, J.; Hu, Y.; Sun, M. Dual stimuli-responsive metal-organic framework-based nanosystem for synergistic photothermal/pharmacological antibacterial therapy. *Acta Biomater.* **2021**, *122*, 291–305. [CrossRef] [PubMed]
94. Li, X.; Bai, H.; Yang, Y.; Yoon, J.; Wang, S.; Zhang, X. Supramolecular Antibacterial Materials for Combatting Antibiotic Resistance. *Adv. Mater.* **2019**, *31*, 1805092. [CrossRef]
95. Mi, G.; Shi, D.; Wang, M.; Webster, T.J. Reducing Bacterial Infections and Biofilm Formation Using Nanoparticles and Nanostructured Antibacterial Surfaces. *Adv. Healthc. Mater.* **2018**, *7*, 1800103. [CrossRef] [PubMed]

96. Rubin, H.N.; Neufeld, B.H.; Reynolds, M.M. Surface-Anchored Metal–Organic Framework–Cotton Material for Tunable Antibacterial Copper Delivery. *ACS Appl. Mater. Interfaces* **2018**, *10*, 15189–15199. [CrossRef] [PubMed]
97. Panda, S.; Rout, T.K.; Prusty, A.D.; Ajayan, P.M.; Nayak, S. Electron Transfer Directed Antibacterial Properties of Graphene Oxide on Metals. *Adv. Mater.* **2018**, *30*, 1702149. [CrossRef] [PubMed]
98. Mitra, D.; Li, M.; Kang, E.T.; Neoh, K.G. Transparent Copper-Based Antibacterial Coatings with Enhanced Efficacy against *Pseudomonas aeruginosa*. *ACS Appl. Mater. Interfaces* **2019**, *11*, 73–83. [CrossRef]
99. Lee, J.; Yoo, J.; Kim, J.; Jang, Y.; Shin, K.; Ha, E.; Ryu, S.; Kim, B.G.; Wooh, S.; Char, K. Development of Multimodal Antibacterial Surfaces Using Porous Amine-Reactive Films Incorporating Lubricant and Silver Nanoparticles. *ACS Appl. Mater. Interfaces* **2019**, *11*, 6550–6560. [CrossRef]
100. Zhao, Y.Q.; Sun, Y.; Zhang, Y.; Ding, X.; Zhao, N.; Yu, B.; Zhao, H.; Duan, S.; Xu, F.J. Well-Defined Gold Nanorod/Polymer Hybrid Coating with Inherent Antifouling and Photothermal Bactericidal Properties for Treating an Infected Hernia. *ACS Nano* **2020**, *14*, 2265–2275. [CrossRef] [PubMed]
101. He, X.; Gopinath, K.; Sathishkumar, G.; Guo, L.; Zhang, K.; Lu, Z.; Li, C.; Kang, E.T.; Xu, L. UV-Assisted Deposition of Antibacterial Ag–Tannic Acid Nanocomposite Coating. *ACS Appl. Mater. Interfaces* **2021**, *13*, 20708–20717. [CrossRef] [PubMed]
102. Dong, Y.; Wang, L.; Yuan, K.; Ji, F.; Gao, J.; Zhang, Z.; Du, X.; Tian, Y.; Wang, Q.; Zhang, L. Magnetic Microswarm Composed of Porous Nanocatalysts for Targeted Elimination of Biofilm Occlusion. *ACS Nano* **2021**, *15*, 5056–5067. [CrossRef]
103. Su, C.; Ye, Y.; Qiu, H.; Zhu, Y. Solvent-free fabrication of self-regenerating antibacterial surfaces resisting biofilm formation. *ACS Appl. Mater. Interfaces* **2021**, *13*, 10553–10563. [CrossRef]
104. Li, L.; Cao, L.; Xiang, X.; Wu, X.; Ma, L.; Chen, F.; Cao, S.; Cheng, C.; Deng, D.; Qiu, L. ROS-Catalytic Transition-Metal-Based Enzymatic Nanoagents for Tumor and Bacterial Eradication. *Adv. Funct. Mater.* **2022**, *32*, 2107530. [CrossRef]
105. Zuo, K.; Wang, L.; Wang, Z.; Yin, Y.; Du, C.; Liu, B.; Sun, L.; Li, X.; Xiao, G.; Lu, Y. Zinc-Doping Induces Evolution of Biocompatible Strontium–Calcium-Phosphate Conversion Coating on Titanium to Improve Antibacterial Property. *ACS Appl. Mater. Interfaces* **2022**, *14*, 7690–7705. [CrossRef] [PubMed]
106. Liu, T.; Yan, S.; Zhou, R.; Zhang, X.; Yang, H.; Yan, Q.; Yang, R.; Luan, S. Self-Adaptive Antibacterial Coating for Universal Polymeric Substrates Based on a Micrometer-Scale Hierarchical Polymer Brush System. *ACS Appl. Mater. Interfaces* **2020**, *12*, 42576–42585. [CrossRef] [PubMed]
107. Ding, X.; Duan, S.; Ding, X.; Liu, R.; Xu, F.J. Versatile Antibacterial Materials: An Emerging Arsenal for Combatting Bacterial Pathogens. *Adv. Funct. Mater.* **2018**, *28*, 1802140. [CrossRef]
108. Schlaich, C.; Li, M.; Cheng, C.; Donskyi, S.I.; Yu, L.; Song, G.; Osorio, E.; Wei, Q.; Haag, R. Mussel-Inspired Polymer-Based Universal Spray Coating for Surface Modification: Fast Fabrication of Antibacterial and Superhydrophobic Surface Coatings. *Adv. Mater. Interfaces* **2018**, *5*, 1701254. [CrossRef]
109. Li, M.; Mitra, D.; Kang, E.T.; Lau, T.; Chiong, E.; Neoh, K.G. Thiol-ol Chemistry for Grafting of Natural Polymers to Form Highly Stable and Efficacious Antibacterial Coatings. *ACS Appl. Mater. Interfaces* **2017**, *9*, 1847–1857. [CrossRef]
110. Misra, A.; Castillo, I.F.; Muller, D.P.; Gonzalez, C.; Eyssautier-Chuine, S.; Ziegler, A.; de la Fuente, J.M.; Mitchell, S.G.; Streb, C. Polyoxometalate-Ionic Liquids (POM-ILs) as Anticorrosion and Antibacterial Coatings for Natural Stones. *Angew. Chem. Int. Ed.* **2018**, *57*, 14926–14931. [CrossRef]
111. Cuthbert, T.J.; Hisey, B.; Harrison, T.D.; Trant, J.F.; Gillies, E.R.; Ragogna, P.J. Surprising Antibacterial Activity and Selectivity of Hydrophilic Polyphosphoniums Featuring Sugar and Hydroxy Substituents. *Angew. Chem. Int. Ed.* **2018**, *57*, 12707–12710. [CrossRef]
112. Huang, L.; Zhang, L.; Xiao, S.; Yang, Y.; Chen, F.; Fan, P.; Zhao, Z.; Zhong, M.; Yang, J. Bacteria killing and release of salt-responsive, regenerative, double-layered polyzwitterionic brushes. *Chem. Eng. J.* **2018**, *333*, 1–10. [CrossRef]
113. Shi, Z.; Jin, L.; He, C.; Li, Y.; Jiang, C.; Wang, H.; Zhang, J.; Wang, J.; Zhao, W.; Zhao, C. Hemocompatible magnetic particles with broad-spectrum bacteria capture capability for blood purification. *J. Colloid Interface Sci.* **2020**, *576*, 1–9. [CrossRef]
114. Shi, Z.; Zhang, Y.; Dai, R.; Chen, S.; Zhang, M.; Jin, L.; Wang, J.; Zhao, W.; Zhao, C. Rationally designed magnetic poly(catechol-hexanediamine) particles for bacteria removal and on-demand biofilm eradication. *Colloids Surf. B* **2020**, *186*, 110728. [CrossRef]
115. Gou, Y.; Yang, X.; He, L.; Xu, X.; Liu, Y.; Liu, Y.; Gao, Y.; Huang, Q.; Liang, K.; Ding, C.; et al. Bio-inspired peptide decorated dendrimers for a robust antibacterial coating on hydroxyapatite. *Polym. Chem.* **2017**, *8*, 4264–4279. [CrossRef]
116. Yang, X.; Huang, P.; Wang, H.; Cai, S.; Liao, Y.; Mo, Z.; Xu, X.; Ding, C.; Zhao, C.; Li, J. Antibacterial and anti-biofouling coating on hydroxyapatite surface based on peptide-modified tannic acid. *Colloids Surf. B* **2017**, *160*, 136–143. [CrossRef] [PubMed]
117. Lu, Z.; Wu, Y.; Cong, Z.; Qian, Y.; Wu, X.; Shao, N.; Qiao, Z.; Zhang, H.; She, Y.; Chen, K.; et al. Effective and biocompatible antibacterial surfaces via facile synthesis and surface modification of peptide polymers. *Bioact. Mater.* **2021**, *6*, 4531–4541. [CrossRef] [PubMed]
118. Yang, X.; Zhang, D.; Liu, G.; Wang, J.; Luo, Z.; Peng, X.; Zeng, X.; Wang, X.; Tan, H.; Li, J. Bioinspired from mussel and salivary acquired pellicle: A universal dual-functional polypeptide coating for implant materials. *Mater. Today Chem.* **2019**, *14*, 100205. [CrossRef]
119. Bing, W.; Tian, L.; Wang, Y.; Jin, H.; Ren, L.; Dong, S. Bio-Inspired Non-Bactericidal Coating Used for Antibiofouling. *Adv. Mater. Technol.* **2018**, *4*, 1800480. [CrossRef]
120. Wong, H.M.; Zhang, Y.Y.; Li, Q.L. An enamel-inspired bioactive material with multiscale structure and antibacterial adhesion property. *Bioact. Mater.* **2022**, *7*, 491–503.

121. Jenkins, J.; Mantell, J.; Neal, C.; Gholinia, A.; Verkade, P.; Nobbs, A.H.; Su, B. Antibacterial effects of nanopillar surfaces are mediated by cell impedance, penetration and induction of oxidative stress. *Nat. Commun.* **2020**, *11*, 1626. [CrossRef]
122. Yasui, T.; Yanagida, T.; Shimada, T.; Otsuka, K.; Takeuchi, M.; Nagashima, K.; Rahong, S.; Naito, T.; Takeshita, D.; Yonese, A.; et al. Engineering Nanowire-Mediated Cell Lysis for Microbial Cell Identification. *ACS Nano* **2019**, *13*, 2262–2273. [CrossRef]
123. Linklater, D.P.; Volder, M.D.; Baulin, V.A.; Werner, M.; Jessl, S.; Golozar, M.; Maggini, L.; Rubanov, S.; Hanssen, E.; Juodkakis, S.; et al. High Aspect Ratio Nanostructures Kill Bacteria via Storage and Release of Mechanical Energy. *ACS Nano* **2018**, *12*, 6657–6667. [CrossRef]
124. Yi, G.; Yuan, Y.; Li, X.; Zhang, Y. ZnO Nanopillar Coated Surfaces with Substrate-Dependent Superbactericidal Property. *Small* **2018**, *14*, 1703159. [CrossRef]
125. Valiei, A.; Lin, N.; Bryce, J.F.; McKay, G.; Canva, M.; Charette, P.G.; Nguyen, D.; Moraes, C.; Tufenkji, N. Hydrophilic Mechano-Bactericidal Nanopillars Require External Forces to Rapidly Kill Bacteria. *Nano Lett.* **2020**, *20*, 5720–5727. [CrossRef]
126. Hu, H.; Siu, V.S.; Gifford, M.S.; Kim, S.; Lu, M.; Meyer, P.; Stolovitzky, G.A. Bio-inspired silicon nanopikes fabricated by metal-assisted chemical etching for antibacterial surfaces. *Appl. Phys. Lett.* **2017**, *111*, 253701. [CrossRef]
127. Bhadra, C.M.; Werner, M.; Baulin, V.A.; Truong, V.K.; Al Kobaisi, M.; Nguyen, S.H.; Balcytis, A.; Juodkakis, S.; Wang, J.Y.; Mainwaring, D.E.; et al. Subtle Variations in Surface Properties of Black Silicon Surfaces Influence the Degree of Bactericidal Efficiency. *Nano-Micro Lett.* **2018**, *10*, 36. [CrossRef]
128. Singh, J.; Jadhav, S.; Avasthi, S.; Sen, P. Designing Photocatalytic Nanostructured Antibacterial Surfaces: Why Is Black Silica Better than Black Silicon? *ACS Appl. Mater. Interfaces* **2020**, *12*, 20202–20213. [CrossRef] [PubMed]
129. Encinas, N.; Yang, C.Y.; Geyer, F.; Kaltbeitzel, A.; Baumli, P.; Reinholz, J.; Mailänder, V.; Butt, H.J.; Vollmer, D. Submicrometer-Sized Roughness Suppresses Bacteria Adhesion. *ACS Appl. Mater. Interfaces* **2020**, *12*, 21192–21200. [CrossRef] [PubMed]
130. Ivanova, E.P.; Linklater, D.P.; Werner, M.; Baulin, V.A.; Xu, X.; Vrancken, N.; Rubanov, S.; Hanssen, E.; Wandiyanto, J.; Truong, V.K.; et al. The multi-faceted mechano-bactericidal mechanism of nanostructured surfaces. *Proc. Natl. Acad. Sci. USA* **2020**, *117*, 12598–12605. [CrossRef]
131. Jiang, J.; Zhang, H.; He, W.; Li, T.; Li, H.; Liu, P.; Liu, M.; Wang, Z.; Wang, Z.; Yao, X. Adhesion of Microdroplets on Water-Repellent Surfaces toward the Prevention of Surface Fouling and Pathogen Spreading by Respiratory Droplets. *ACS Appl. Mater. Interfaces* **2017**, *9*, 6599–6608. [CrossRef] [PubMed]
132. Zhang, M.; Peltier, R.; Zhang, M.; Lu, H.; Bian, H.; Li, Y.; Xu, Z.; Shen, Y.; Sun, H.; Wang, Z. In situ reduction of silver nanoparticles on hybrid polydopamine–copper phosphate nanoflowers with enhanced antimicrobial activity. *J. Mater. Chem. B* **2017**, *5*, 5311–5317. [CrossRef]
133. Zhang, M.; Zhao, Y.; Yan, L.; Peltier, R.; Hui, W.; Yao, X.; Cui, Y.; Chen, X.; Sun, H.; Wang, Z. Interfacial Engineering of Bimetallic Ag/Pt Nanoparticles on Reduced Graphene Oxide Matrix for Enhanced Antimicrobial Activity. *ACS Appl. Mater. Interfaces* **2016**, *8*, 8834. [CrossRef]
134. Zhao, Y.; Zhang, M.; Wang, Z. Underwater Superoleophobic Membrane with Enhanced Oil–Water Separation, Antimicrobial, and Antifouling Activities. *Adv. Mater. Interfaces* **2016**, *3*, 1500664. [CrossRef]
135. Zhang, M.; Wang, P.; Sun, H.; Wang, Z. Superhydrophobic Surface with Hierarchical Architecture and Bimetallic Composition for Enhanced Antibacterial Activity. *ACS Appl. Mater. Interfaces* **2014**, *6*, 22108–22115. [CrossRef]
136. Cui, M.; Wang, Z.; Wang, B. Survival strategies of mangrove (*Ceriops tagal* (Perr.) C. B. Rob) and the inspired corrosion inhibitor. *Front. Mater.* **2022**, *9*, 879525. [CrossRef]
137. Gu, H.; Lee, S.; Carnicelli, J.; Zhang, T.; Ren, D. Magnetically driven active topography for long-term biofilm control. *Nat. Commun.* **2020**, *11*, 2211. [CrossRef] [PubMed]
138. Wei, T.; Yu, Q.; Chen, H. Responsive and Synergistic Antibacterial Coatings: Fighting against Bacteria in a Smart and Effective Way. *Adv. Healthc. Mater.* **2019**, *8*, 1801381. [CrossRef] [PubMed]
139. Yan, S.; Shi, H.; Song, L.; Wang, X.; Liu, L.; Luan, S.; Yang, Y.; Yin, J. Nonleaching Bacteria-Responsive Antibacterial Surface Based on a Unique Hierarchical Architecture. *ACS Appl. Mater. Interfaces* **2016**, *8*, 24471–24481. [CrossRef]
140. Yang, X.; Ding, C.; Wu, M.; Xu, X.; Ke, X.; Xu, H.; Li, J.; Lou, F.; Zhou, K.; Jiang, H.; et al. Biomineral interface with superior cell adhesive and antibacterial properties based on enzyme-triggered digestion of saliva acquired pellicle-inspired polypeptide coatings. *Chem. Eng. J.* **2021**, *415*, 128955. [CrossRef]
141. Wang, Y.; Wei, T.; Qu, Y.; Zhou, Y.; Zheng, Y.; Huang, C.; Zhang, Y.; Yu, Q.; Chen, H. Smart, Photothermally Activated, Antibacterial Surfaces with Thermally Triggered Bacteria-Releasing Properties. *ACS Appl. Mater. Interfaces* **2020**, *12*, 21283–21291. [CrossRef]
142. He, M.; Wang, Q.; Zhang, J.; Zhao, W.; Zhao, C. Substrate-Independent Ag-Nanoparticle-Loaded Hydrogel Coating with Regenerable Bactericidal and Thermoresponsive Antibacterial Properties. *ACS Appl. Mater. Interfaces* **2017**, *9*, 44782–44791. [CrossRef]
143. Wang, Y.; Wu, J.; Zhang, D.; Chen, F.; Fan, P.; Zhong, M.; Xiao, S.; Chang, Y.; Gong, X.; Yang, J.; et al. Design of salt-responsive and regenerative antibacterial polymer brushes with integrated bacterial resistance, killing, and release properties. *J. Mater. Chem. B* **2019**, *7*, 5762–5774. [CrossRef]
144. Wang, T.; Huang, L.; Liu, Y.; Li, X.; Liu, C.; Handschuh-Wang, S.; Xu, Y.; Zhao, Y.; Tang, Y. Robust Biomimetic Hierarchical Diamond Architecture with a Self-Cleaning, Antibacterial, and Antibiofouling Surface. *ACS Appl. Mater. Interfaces* **2020**, *12*, 24432–24441. [CrossRef]

145. Mo, S.; Mehrjou, B.; Tang, K.; Wang, H.; Huo, K.; Qasim, A.M.; Wang, G.; Chu, P.K. Dimensional-dependent antibacterial behavior on bioactive micro/nano polyetheretherketone (PEEK) arrays. *Chem. Eng. J.* **2020**, *392*, 123736. [CrossRef]
146. Hu, B.; Berkey, C.; Feliciano, T.; Chen, X.; Li, Z.; Chen, C.; Amini, S.; Nai, M.; Lei, Q.L.; Ni, R.; et al. Thermal-Disrupting Interface Mitigates Intercellular Cohesion Loss for Accurate Topical Antibacterial Therapy. *Adv. Mater.* **2020**, *32*, 1907030. [CrossRef] [PubMed]
147. Li, S.; Liu, Y.; Zheng, Z.; Liu, X.; Huang, H.; Han, Z.; Ren, L. Biomimetic robust superhydrophobic stainless-steel surfaces with antimicrobial activity and molecular dynamics simulation. *Chem. Eng. J.* **2019**, *372*, 852–861. [CrossRef]
148. Yang, C.; Luo, Y.; Lin, H.; Ge, M.; Shi, J.; Zhang, X. Niobium Carbide MXene Augmented Medical Implant Elicits Bacterial Infection Elimination and Tissue Regeneration. *ACS Nano* **2021**, *15*, 1086–1099. [CrossRef] [PubMed]
149. Zou, Y.; Zhang, Y.; Yu, Q.; Chen, H. Photothermal bactericidal surfaces: Killing bacteria using light instead of biocides. *Biomater. Sci.* **2021**, *9*, 10–22. [CrossRef]
150. Li, Y.; Zhao, Z.; Zhang, J.; Kwok, R.T.K.; Xie, S.; Tang, R.; Jia, Y.; Yang, J.; Wang, L.; Lam, J.W.Y.; et al. A Bifunctional Aggregation-Induced Emission Luminogen for Monitoring and Killing of Multidrug-Resistant Bacteria. *Adv. Funct. Mater.* **2018**, *28*, 1804632. [CrossRef]
151. Sun, X.; Sun, J.; Sun, Y.; Li, C.; Fang, J.; Zhang, T.; Wan, Y.; Xu, L.; Zhou, Y.; Wang, L.; et al. Oxygen Self-Sufficient Nanoplatfor for Enhanced and Selective Antibacterial Photodynamic Therapy against Anaerobe-Induced Periodontal Disease. *Adv. Funct. Mater.* **2021**, *31*, 2101040. [CrossRef]
152. Li, J.; Liu, X.; Tan, L.; Liang, Y.; Cui, Z.; Yang, X.; Zhu, S.; Li, Z.; Zheng, Y.; Yeung, K.W.K.; et al. Light-Activated Rapid Disinfection by Accelerated Charge Transfer in Red Phosphorus/ZnO Heterointerface. *Small Methods* **2019**, *3*, 1900048. [CrossRef]
153. Elbourne, A.; Cheeseman, S.; Atkin, P.; Truong, N.P.; Syed, N.; Zavabeti, A.; Mohiuddin, M.; Esrafilzadeh, D.; Cozzolino, D.; McConville, C.F.; et al. Antibacterial Liquid Metals: Biofilm Treatment via Magnetic Activation. *ACS Nano* **2020**, *14*, 802–817. [CrossRef]
154. Kozuka, Y.; Lu, Z.; Masuda, T.; Hara, S.; Kasama, T.; Miyake, R.; Isu, N.; Takai, M. Evaluation of bacterial adhesion strength on phospholipid copolymer films with antibacterial ability using microfluidic shear devices. *J. Mater. Chem. B* **2021**, *9*, 4480–4487. [CrossRef]
155. Diaz De Rienzo, M.A.; Banat, I.M.; Dolman, B.; Winterburn, J.; Martin, P.J. Sophorolipid biosurfactants: Possible uses as antibacterial and antibiofilm agent. *New Biotechnol.* **2015**, *32*, 720–726. [CrossRef]
156. Li, J.; Xu, X.; Chen, Z.; Wang, T.; Lu, Z.; Hu, W.; Wang, L. Zein/gum Arabic nanoparticle-stabilized Pickering emulsion with thymol as an antibacterial delivery system. *Carbohydr. Polym.* **2018**, *200*, 416–426. [CrossRef] [PubMed]
157. Wu, M.; Zhang, Z.; Liu, Z.; Zhang, J.; Zhang, Y.; Ding, Y.; Huang, T.; Xiang, D.; Wang, Z.; Dai, Y.; et al. Piezoelectric nanocomposites for sonodynamic bacterial elimination and wound healing. *Nano Today* **2021**, *37*, 101104. [CrossRef]
158. Jang, H.; Choi, G.; Kang, M.; Kim, S.; Seong, M.; Lee, S.H.; Park, H.W.; Jeong, H.E. Dynamically Actuating Nanospine Composites as a Bioinspired Antibiofilm Material. *Compos. Sci. Technol.* **2022**, *220*, 109267. [CrossRef]
159. Lee, M.J.; Kwon, J.S.; Jiang, H.B.; Choi, E.H.; Park, G.; Kim, K.M. The antibacterial effect of non-thermal atmospheric pressure plasma treatment of titanium surfaces according to the bacterial wall structure. *Sci. Rep.* **2019**, *9*, 1938. [CrossRef] [PubMed]
160. Ge, X.; Ren, C.; Ding, Y.; Chen, G.; Lu, X.; Wang, K.; Ren, F.; Yang, M.; Wang, Z.; Li, J.; et al. Micro/nano-structured TiO₂ surface with dual-functional antibacterial effects for biomedical applications. *Bioact. Mater.* **2019**, *4*, 346–357. [CrossRef] [PubMed]
161. Mehrjou, B.; Mo, S.; Dehghan-Baniani, D.; Wang, G.; Qasim, A.M.; Chu, P.K. Antibacterial and Cytocompatible Nanoengineered Silk-Based Materials for Orthopedic Implants and Tissue Engineering. *ACS Appl. Mater. Interfaces* **2019**, *11*, 31605–31614. [CrossRef]
162. Miguel, I.D.; Prieto, I.; Albornoz, A.; Sanz, V.; Weis, C.; Turon, P.; Quidant, R. Plasmon-Based Biofilm Inhibition on Surgical Implants. *Nano Lett.* **2019**, *19*, 2524–2529. [CrossRef]
163. Zhang, W.; Jin, Y.; Yang, S.; Zhang, H.; Wang, Z. Bio-Inspired Topological Surfaces for Mitigating Water, Thermal and Energy Crises. *Acc. Mater. Res.* **2022**, *3*, 199–212. [CrossRef]
164. Yang, M.; Qiu, S.; Coy, E.; Li, S.; Załęski, K.; Zhang, Y.; Pan, H.; Wang, G. NIR-Responsive TiO₂ Biometasurfaces: Toward In Situ Photodynamic Antibacterial Therapy for Biomedical Implants. *Adv. Mater.* **2021**, *34*, 2106314. [CrossRef]
165. Sang, S.; Yang, C.; Chai, H.; Yuan, X.; Liu, W.; Zhang, X. The sulfonated polyetheretherketone with 3D structure modified by two bio-inspired methods shows osteogenic and antibacterial functions. *Chem. Eng. J.* **2021**, *420*, 130059. [CrossRef]
166. Darvishi, S.; Tavakoli, S.; Kharaziha, M.; Girault, H.H.; Kaminski, C.F.; Mela, I. Advances in the Sensing and Treatment of Wound Biofilms. *Angew. Chem. Int. Ed.* **2021**, *61*, e202112218.
167. Dhand, C.; Venkatesh, M.; Barathi, V.A.; Harini, S.; Bairagi, S.; Leng, E.G.T.; Muruganandham, N.; Low, K.Z.W.; Fazil, M.H.U.T.; Loh, X.J.; et al. Bio-inspired crosslinking and matrix-drug interactions for advanced wound dressings with long-term antimicrobial activity. *Biomaterials* **2017**, *138*, 153–168. [CrossRef] [PubMed]
168. Liu, H.; Qu, X.; Kim, E.; Lei, M.; Dai, K.; Tan, X.; Liu, C. Bio-inspired redox-cycling antimicrobial film for sustained generation of reactive oxygen species. *Biomaterials* **2018**, *162*, 109–122. [CrossRef]
169. Tang, N.; Zhang, R.; Zheng, Y.; Wang, J.; Khatib, M.; Jiang, X.; Zhou, C.; Omar, R.; Saliba, W.; Wu, W.; et al. Highly Efficient Self-Healing Multifunctional Dressing with Antibacterial Activity for Sutureless Wound Closure and Infected Wound Monitoring. *Adv. Mater.* **2021**, *34*, 2106842. [CrossRef]

170. Zheng, S.; Li, W.; Ren, Y.; Liu, Z.; Zou, X.; Hu, Y.; Guo, J.; Sun, Z.; Yan, F. Moisture-Wicking, Breathable, and Intrinsically Antibacterial Electronic Skin Based on Dual-Gradient Poly(ionic liquid) Nanofiber Membranes. *Adv. Mater.* **2022**, *34*, 2106570. [CrossRef]
171. Peng, X.; Dong, K.; Ye, C.; Jiang, Y.; Zhai, S.; Cheng, R.; Liu, D.; Gao, X.; Wang, J.; Wang, Z. A breathable, biodegradable, antibacterial, and self-powered electronic skin based on all-nanofiber triboelectric nanogenerators. *Sci. Adv.* **2020**, *6*, eaba9624. [CrossRef]
172. Huo, Z.; Kim, Y.J.; Suh, I.Y.; Lee, D.M.; Lee, J.H.; Du, Y.; Wang, S.; Yoon, H.J.; Kim, S.W. Triboelectrification induced self-powered microbial disinfection using nanowire-enhanced localized electric field. *Nat. Commun.* **2021**, *12*, 3693. [CrossRef] [PubMed]
173. Luo, H.; Yin, X.Q.; Tan, P.; Gu, Z.; Liu, Z.; Tan, L. Polymeric antibacterial materials: Design, platforms and applications. *J. Mater. Chem. B* **2021**, *9*, 2802–2815. [CrossRef]
174. Li, S.; Dong, S.; Xu, W.; Tu, S.; Yan, L.; Zhao, C.; Ding, J.; Chen, X. Antibacterial Hydrogels. *Adv. Sci.* **2018**, *5*, 1700527. [CrossRef]
175. Linklater, D.P.; Baulin, V.A.; Juodkasis, S.; Crawford, R.J.; Stoodley, P.; Ivanova, E.P. Mechano-bactericidal actions of nanostructured surfaces. *Nat. Rev. Microbiol.* **2021**, *19*, 8–22. [CrossRef]
176. Valverde, A.; Pérez-Álvarez, L.; Ruiz-Rubio, L.; Olivenza, M.A.P.; Blanco, M.B.G.; Díaz-Fuentes, M.; Vilas-Vilela, J.L. Antibacterial hyaluronic acid/chitosan multilayers onto smooth and micropatterned titanium surfaces. *Carbohydr. Polym.* **2019**, *207*, 824–833. [CrossRef] [PubMed]
177. Zare, M.; Zare, M.; Butler, J.A.; Ramakrishna, S. Nanoscience-Led Antimicrobial Surface Engineering to Prevent Infections. *ACS Appl. Nano Mater.* **2021**, *4*, 4269–4283. [CrossRef]
178. Zhu, M.; Wang, Y.; Lou, M.; Yu, J.; Li, Z.; Ding, B. Bioinspired transparent and antibacterial electronic skin for sensitive tactile sensing. *Nano Energy* **2021**, *81*, 105669. [CrossRef]
179. Liang, Y.; Li, Z.; Huang, Y.; Yu, R.; Guo, B. Dual-Dynamic-Bond Cross-Linked Antibacterial Adhesive Hydrogel Sealants with On-Demand Removability for Post-Wound-Closure and Infected Wound Healing. *ACS Nano* **2021**, *15*, 7078–7093. [CrossRef]
180. Mallakpour, S.; Azadi, E.; Hussain, C.M. Recent breakthroughs of antibacterial and antiviral protective polymeric materials during COVID-19 pandemic and after pandemic: Coating, packaging, and textile applications. *Curr. Opin. Colloid Interface Sci.* **2021**, *55*, 101480. [CrossRef]
181. Kim, M.; Phama, T.K.; Kim, D.; Park, M.; Kim, B.; Cho, Y.H.; Kim, Y.W.; Lee, C. Identification of brevinin-1EMa-derived stapled peptides as broad-spectrum virus entry blockers. *Virology* **2021**, *561*, 6–16. [CrossRef] [PubMed]
182. Jana, I.D.; Kumbhakar, P.; Banerjee, S.; Gowda, C.C.; Kedia, N.; Kuila, S.K.; Banerjee, S.; Das, N.C.; Das, A.K.; Manna, I.; et al. Copper Nanoparticle–Graphene Composite-Based Transparent Surface Coating with Antiviral Activity against Influenza Virus. *ACS Appl. Nano Mater.* **2021**, *4*, 352–362. [CrossRef]
183. Koo, H.; Allan, R.N.; Howlin, R.P.; Stoodley, P.; Hall-Stoodley, L. Targeting microbial biofilms: Current and prospective therapeutic strategies. *Nat. Rev. Microbiol.* **2017**, *15*, 740–755. [CrossRef]
184. Zhan, Y.; Yu, S.; Amirfazli, A.; Siddiqui, A.R.; Li, W. Recent Advances in Antibacterial Superhydrophobic Coatings. *Adv. Eng. Mater.* **2022**, *24*, 2101053. [CrossRef]



Article

Effect of Wettability and Adhesion Property of Solid Margins on Water Drainage

Can Gao^{1,2}, Lei Jiang^{1,2} and Zhichao Dong^{1,2,*}

¹ CAS Key Laboratory of Bio-Inspired Materials and Interfacial Science, Technical Institute of Physics and Chemistry, Chinese Academy of Sciences, Beijing 100190, China

² School of Future Technology, University of Chinese Academy of Sciences, Beijing 100049, China

* Correspondence: dongzhichao@mail.ipc.ac.cn

Abstract: Liquid flows at the solid surface and drains at the margin under gravity are ubiquitous in our daily lives. Previous research mainly focuses on the effect of substantial margin's wettability on liquid pinning and has proved that hydrophobicity inhibits liquids from overflowing margins while hydrophilicity plays the opposite role. However, the effect of solid margins' adhesion properties and their synergy with wettability on the overflowing behavior of water and resultant drainage behaviors are rarely studied, especially for large-volume water accumulation on the solid surface. Here, we report the solid surfaces with high-adhesion hydrophilic margin and hydrophobic margin stably pin the air-water-solid triple contact lines at the solid bottom and solid margin, respectively, and then drain water faster through stable water channels termed water channel-based drainage over a wide range of water flow rates. The hydrophilic margin promotes the overflowing of water from top to bottom. It constructs a stable "top + margin + bottom" water channel, and a high-adhesion hydrophobic margin inhibits the overflowing from margin to bottom and constructs a stable "top + margin" water channel. The constructed water channels essentially decrease marginal capillary resistances, guide top water onto the bottom or margin, and assist in draining water faster, under which gravity readily overcomes the surface tension resistance. Consequently, the water channel-based drainage mode achieves 5–8 times faster drainage behavior than the no-water channel drainage mode. The theoretical force analysis also predicts the experimental drainage volumes for different drainage modes. Overall, this article reveals marginal adhesion and wettability-dependent drainage modes and provides motivations for drainage plane design and relevant dynamic liquid-solid interaction for various applications.

Keywords: solid margin; high adhesion; water channel; fast water drainage

Citation: Gao, C.; Jiang, L.; Dong, Z. Effect of Wettability and Adhesion Property of Solid Margins on Water Drainage. *Biomimetics* **2023**, *8*, 60. <https://doi.org/10.3390/biomimetics8010060>

Academic Editors: Stanislav N. Gorb, Giuseppe Carbone, Thomas Speck and Andreas Taubert

Received: 11 January 2023

Revised: 28 January 2023

Accepted: 30 January 2023

Published: 1 February 2023



Copyright: © 2023 by the authors. Licensee MDPI, Basel, Switzerland. This article is an open access article distributed under the terms and conditions of the Creative Commons Attribution (CC BY) license (<https://creativecommons.org/licenses/by/4.0/>).

1. Introduction

Fast water drainage, ranging from tiny droplets [1–4] to large-volume liquid [5–8], from solid surfaces is ubiquitous and critical to self-cleaning [9], water harvesting [1–4,10], and creature survival [11–13]. Natural surfaces, such as mosquito compound eyes [14], water strider legs [15], and drain fly tentacles [16], utilize complicated microstructures to quickly drain tiny water droplets based on surface energy or Laplace pressure gradient. Artificial surfaces can achieve preferable spontaneous and rapid water droplet removal under asymmetrical surface tension force [17–20] or external forces [21–28]. Plants' leaves have evolved special structures, such as the drip tip apex structure [12], to rapidly remove large-volume rainwater under the gravity effect. In practice, large-volume water drainage behavior based on the overflowing of water around the solid margin can also be manipulated depending on the water flow rate and solid margin wettability [5–8,29] in a controllable manner. However, previous research mainly focuses on tiny droplet drainage at sharp spine-shaped margins or liquid columns/sheets at circle-shaped margins. Studies on the effect of the wettability and adhesion property of the macroscopic square-shaped

margins on water drainage are rare, mainly when large-volume water accumulates at margins with a low slope.

Here, we establish a water channel-based faster drainage mode based on the high-adhesion hydrophilic and hydrophobic solid margins over a wide range of water flow rates. We demonstrate that the low-adhesion margins, the superhydrophobic one, the original one, and the hydrophobic one result in more significant marginal resistances and subsequent higher drainage time and drainage volumes. In contrast, the high-adhesion margins, the hydrophilic and the hydrophobic ones, construct stable water channels, quickly transport top water onto the bottom or margin, and drain water faster with less drainage time and drainage volumes. In this condition, water droplet gravity readily overcomes surface tension resistance based on the as-formed water channels. Notably, the high-adhesion hydrophobic margin sample with the highest contact angle hysteresis exhibits the fastest drainage behavior. We emphasize that stable water channels always exist for the high-adhesion margins regardless of different water flow rates, initial incline angles, and sample thicknesses. We also show the determination of the critical water flow rates versus sample thicknesses for water channel constructions associated with the original margin sample. That is, only more considerable inertia can sustain stable water channels. Further, this investigation will offer us an innovative insight into how to design structured margin planes with high-efficiency drainage behavior, especially in large-volume water accumulation situations.

2. Materials and Methods

2.1. Experimental Setup

To present the process of the water channel-based fast drainage mode, we built a drainage system including a cuboid sample connecting to a force sensor and a water injection device controlled by an injection pump (Figure 1a). First, a nozzle injects water that accumulates on the sample top. Then, the accumulated water spread on the top, and the air-water-solid triple contact line was pinned at the margin-top of the sample. At some critical conditions, the gravity component overcame the marginal surface tension resistance, and a certain volume of water was separated from the top. That is, one drainage happened. Next, constant water injection resulted in cyclical drainage behavior. Figure 1b,c shows the critical drainage images from the side view and the front view for the original margin sample, respectively. The injection needle tip was fixed at a preliminary vertical and horizontal length of $L_v = 0.6$ mm and $L_h = 20.0$ mm away from the sample surface and sample front margin, respectively, to promote the experimental stability during the water injection and drainage process. The samples were fixed at an initial incline angle of $\alpha = 5^\circ$ and connected to the force sensor. The in-situ force sensor recorded the vertical force variations during the water injection process. An injection pump was applied to control the water flow rate $Q \in \{0.5\text{--}40\}$ mL/min.

A digital camera recorded the experimental drainage process at 60 fps (Nikon D750, Japan) from the side view and a high-speed camera at 500 fps (SK 1910, Shenzhen Obeero Technology Co., Ltd., Shenzhen, China) from the front view. The in-situ vertical force F_z was measured by the universal material tester (Tribometer UMT-Tribolab, CETR, Bruker, Germany) connecting to an FL force sensor to ensure the test precision at a 50 μ N force accuracy. The water flow rate $Q \in \{0.5\text{--}40\}$ mL/min was regulated by an injection pump (Leadfluid TYD 02-02 Pump, China). All the water used was deionized (18.2 M Ω -cm) from Milli-Q equipment.

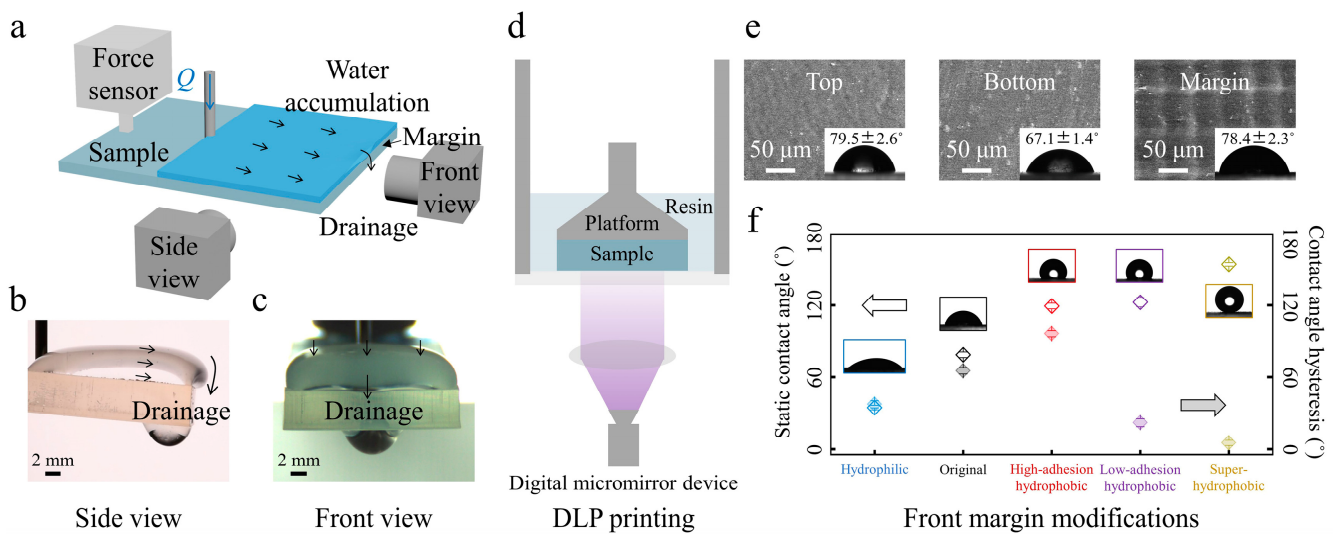


Figure 1. Experimental setup and material characterizations. (a) Schematic illustration of the experimental design. Injection water accumulates on the sample top and drains at the front margin at critical conditions. Selected essential snapshots of drainage from the side view (b) and the front view (c) for the original margin sample. (d) Schematic diagram of the DLP printing for sample fabrication. (e) Scanning electron microscope (SEM) images and corresponding water contact angles (inset) of the top surface, the bottom surface, and the front margin of the sample, respectively. (f) Static water contact angles and contact angle hysteresis versus different front margin modifications.

2.2. Fabrications and Characterizations of Experimental Samples

The experimental samples were fabricated based on the polymerization reaction using the monomer methyl methacrylate via a commercial digital light processing printer (DLP) (Figure 1d) at a Z-axis resolution of 50 μm . After 3D printing, the prepared samples were first immersed in ethanol for 5 min to remove the uncured resin, dried with N_2 gas, and then post-cured using the dry-curing equipment. Scanning electron microscope (SEM) images of the sample's top, bottom, and front margins exhibit relatively smooth surface morphologies (Figure 1e, Figure S1). The corresponding water contact angles $\theta_{\text{top}} = 79.5 \pm 2.6^\circ$, $\theta_{\text{bottom}} = 67.1 \pm 1.4^\circ$ and $\theta_{\text{margin}} = 78.4 \pm 2.3^\circ$, respectively, showing hydrophilic features (Figure 1e, inset) of the top, bottom, and front margin of the sample. We did different margin modifications to differentiate the front margin's wettability and adhesion properties (Figure 1f, Figure S2) and studied their effects on the water overflowing and drainage behavior. Adhesive tapes covered the top and bottom surfaces before processing different margin modifications. To make the margin more hydrophilic, the front margin was processed with O_2 plasma (DT-03, Suzhou OPS Plasma Technology Co., Ltd., Suzhou, China) at 50 W for 5 min. To make the low-adhesion hydrophobic margin, the front margin was first processed by O_2 plasma at 200 W for 10 min, and then the sample was put into a vacuum dryer oven at 80 $^\circ\text{C}$ for 1 h with 10 μL 1H,1H,2H,2H-Perfluorodecyltrimethoxysilane. To make the high-adhesion hydrophobic margin, the low-adhesion hydrophobic front margin was then rubbed with a sandpaper of 200 mesh for a higher contact angle hysteresis. To make the margin superhydrophobic, the front margin was carefully brushed with the superhydrophobic solution by a hairbrush and dried under ambient conditions for 5 min. We prepared the superhydrophobic solution with a mix of 0.5 g Captone ST-200 (Dupont, Shenzhen, China), 1.0 g hydrophobic fumed silica nanoparticles (Evonik Degussa Co., Frankfurt, Germany), and 30 mL ethanol. We then stirred them in a bottle for 1 h [30]. Static water contact angles and contact angle hysteresis versus different front margin modifications are summarized in Figure 1f. Except when specifically stated, the sample has a length L of 4.0 cm, a width W of 2.2 cm, and a thickness t_s of 5.0 mm.

A field-emission SEM obtained SEM images of samples at 10 kV (SU8010, Hitachi, Japan). Before SEM imaging, the samples were cleaned with water, dried with N_2 , and then sputtered with a thin layer of platinum (EM ACE, Leica, Germany). We obtained the water contact angles and water contact angle hysteresis of different margins at room temperature (LSA 100 Surface Analyzer, LAUDA Scientific, Germany). The contact angle hysteresis was measured by the sessile droplet method. A sessile drop was slowly inflated or deflated on the samples. We used a dynamic contact angle machine (DCAT 21, Data Physics, Germany) to measure the adhesion forces of different margins with $3.0 \mu\text{L}$ water droplets. Each reported data was an average of at least five independent measurements.

3. Results and Discussion

3.1. Drainage Results and Drainage Mode Comparisons

In-situ vertical force F_z results illustrate the cyclical drainage process at $Q = 5.0 \text{ mL/min}$ (Figure 2a). For samples with different front margin modifications, the drainage time and weight distinguish each other (Figure 2a, Video S1). The drainage situations can be divided into no-water channel drainage (NWCD) mode and water channel-based drainage (WCD) mode. For the no-water channel drainage mode, no stable water channels exist. The drainage condition can be further divided into three circumstances according to the drainage separation zones: “T-drainage” for superhydrophobic margin-sample that inhibits water overflowing from the top to front margin and drains at the marginal top (Figure 2b, bottom left), “T+F-drainage” for low-adhesion hydrophobic margin-sample that allows water to overflow from top to front margin and then drains at the front margin (Figure 2b, bottom right), and “T+F+B-drainage” for original margin-sample that enables two successive overflowing from the top to front margin then bottom and drains at the bottom (Figure 2b, top), respectively. T, F, and B denote the sample’s top, front margin, and bottom, respectively. Selected snapshots and corresponding dashed outlines vividly demonstrate the critical drainage conditions (Figure 2b).

Water at the sample top needs to accumulate to a critical volume to overcome the barrier that emerged from the square low-adhesion superhydrophobic and hydrophobic margins. As a result, larger drainage weights collected by longer drainage time are achieved for each drainage (Figure 2a, yellow line, and purple line). For the original margin sample, a temporary, marginal water channel exists during one drainage, but it quickly dewets after the drainage. The lower-adhesion original margin fails to sustain a stable water channel during the drainage process (Figure S3, Video S1). And particular, the water droplet residue at the bottom after one drainage pulls more water to drain, and in turn, leads to longer drainage time and a more extensive drainage weight (Figure 2a, black line) than that of the superhydrophobic margin sample (Figure 2a, yellow line) and low-adhesion hydrophobic margin sample (Figure 2a, purple line). During drainage, the temporary water channel at the front margin slows down the drainage process. Overall, samples with these margins drain water without stable water channels with more significant marginal surface tension resistances and larger water drainage weights.

We then focus on the water channel-based drainage mode. In this situation, stable water channels exist, and the drainage condition can be further divided into two circumstances depending on the drainage zones: “T+F+B-drainage” for the hydrophilic margin sample (Figure 2c, left) and “T+F-drainage” for the high-adhesion hydrophobic margin sample (Figure 2c, right). The hydrophilic margin permits water to overflow from top to margin and then to bottom, and the high-adhesion property facilitates stable marginal water channel construction. Then the sample drains water faster with lower drainage time and drainage weight (Figure 2a, blue line). Notably, the hydrophobic margin sample with the highest contact angle hysteresis stably captures water at the margin. It resists advancing movements to the bottom and receding movements to the top [31]. Then the marginal stable water channel assists in achieving the fastest drainage behavior (Figure 2a, red line) without contacting the bottom surface. Consequently, the water channel-based drainage mode shows a lower drainage time and drainage volume, approximately

5–8 times less than that of the no-water channel drainage mode (Figure 2d,e) for water flow rates $Q \in \{0.5\text{--}40\}$ mL/min, suggesting that the faster water channel-based drainage mode applies to a broader range of water flow rates. Here, we obtain values of the drainage volume V as $V = Qt$ with Q the water flow rate and t the drainage time.

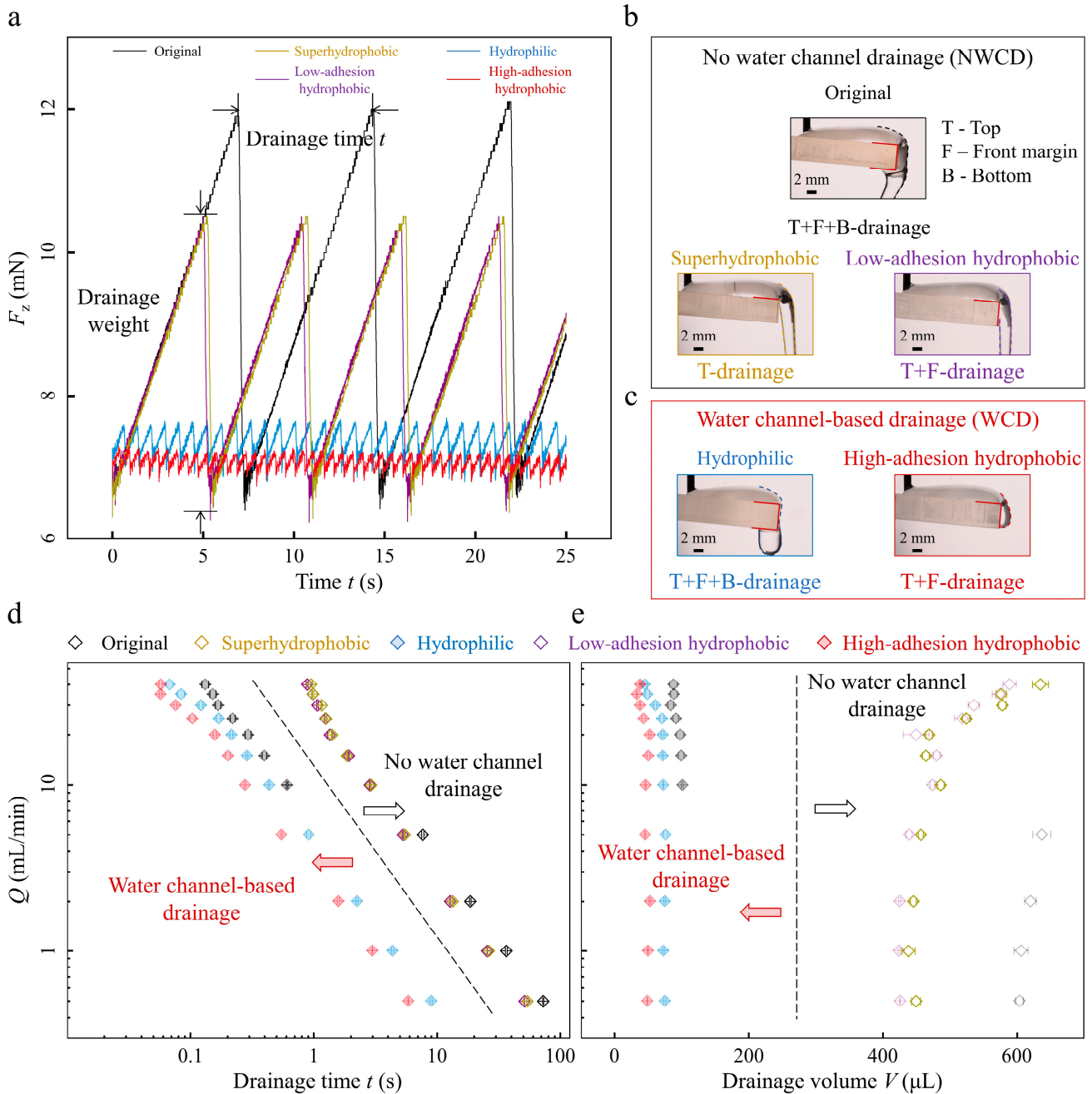


Figure 2. Drainage results and drainage mode comparisons. (a) In-situ vertical force F_z measurements versus time t for samples of different front margin modifications at water flow rate $Q = 5.0$ mL/min. (b,c) Critical drainage snapshots from the side view differentiate the no-water channel drainage mode (b) as “T+F+B drainage” (b, top), “T drainage” (b, bottom left), and “T+F drainage” (b, bottom right) and water channel-based drainage mode (c) as “T+F+B drainage” (c, left) and “T+F drainage” (c, right). Dashed outlines show the different critical drainage conditions. (d,e) Drainage time t and drainage volume V versus various water flow rates Q of the two drainage modes for samples with different front margin modifications. The error bar represents the standard deviations for at least five independent measurements.

3.2. Drainage Mechanisms and Experimental Parameters Regulating Different Drainage Modes

We next elucidate the different drainage mechanisms for the no-water and water channel-based drainage modes through detailed force analysis (Figure 3a–c). For the no-water channel drainage mode, we choose the “T-drainage” condition of the superhydrophobic margin sample as an example (Figure 3a). Water gradually accumulates on the sample top until the critical volume is achieved for water to drain. During the drainage process, the gravity component plays as the driving force F_d , which scales as $\rho V_{\text{SHB}} g \sin \alpha$. A marginal capillary force acts as the resisting force F_r , which scales as γw . At the critical drainage state, F_d equals F_r , and we obtain the drainage volume $V_{\text{SHB}} = \frac{w l_c^2}{\sin \alpha}$. Through further detailed calculation, we obtain $V_{\text{SHB}} \approx 480 \mu\text{L}$ at $\alpha = 5.0^\circ$, consistent with the experimental results (Figure 2e, open yellow diamond symbol). Here, ρ and γ are the water density and surface tension, g is the gravitational acceleration, l_c is the capillary length, α is the initial incline angle, and $w \approx 5.7 \text{ mm}$ is the drainage width obtained from the front-view picture (Figure 3a, inset).

In addition, we analyze the water channel-based drainage mode (Figure 3b,c). First, we consider the “T+F+B-drainage” of the hydrophilic margin sample (Figure 3b). At this condition, the water channel tightly adheres to the high-adhesion hydrophilic margin, and the injection water is quickly transferred from top to bottom via the marginal water channel. When water at the bottom surface accumulates to a critical volume, the droplet gravity $\rho V_{\text{HL}} g$ exceeds the surface tension force $\pi \gamma R_j$, and one droplet drainage happens. The drainage volume is $V_{\text{HL}} = \pi l_c^2 R_j$ and we find the $V_{\text{HL}} \approx 100 \mu\text{L}$. The $R_j \approx 4.5 \text{ mm}$ is the water jet width at the bottom surface (Figure 3b, inset). The theoretical result is slightly larger than the experimental result (Figure 2e, filled blue diamond symbol). This overestimation is rational because a slight droplet residue exists at the hydrophilic bottom surface after one drainage. Further, we consider the “T+F-drainage” of the high-adhesion hydrophobic margin one (Figure 3c). At this condition, the water channel stably pins at the high-adhesion margin without contacting the bottom surface and assists in draining via the marginal water channel. When water at the margin accumulates to some critical volume, the droplet gravity $\rho V_{\text{HA-H}} g$ exceeds the surface tension force $\gamma w_{\text{HA-H}}$, and one droplet drainage happens. The drainage volume $V_{\text{HA-H}} = w_{\text{HA-H}} l_c^2$ and we find the $V_{\text{HA-H}} \approx 30 \mu\text{L}$, consistent with the experimental result (Figure 2e, filled red diamond symbol). Here, $w_{\text{HA-H}} \approx 3.6 \text{ mm}$ is the drainage width obtained from the front-view picture (Figure 3c, inset). Overall, stable water channels for the water channel-based drainage mode provide more convenient drainage pathways with lower marginal capillary resistances.

We investigate how the initial incline angles α affect the drainage results of both no-water and water channel-based drainage modes. We change the incline angles as $\alpha = 5^\circ, 7^\circ$ and 9° in a small range to guarantee a similar, more considerable water accumulation and drainage process. We confirm the power-law dependence $t \propto \frac{1}{Q \sin \alpha}$ under various water flow rates Q for samples with different margin modifications (Figure 3d). For the no-water channel drainage mode, experimental data collapse onto the master curve (Figure 3d, open diamond symbols), showing the drainage time t closely relates with the incline angle α . On the contrary, for the water channel-based drainage mode, time t is similar at fixed water flow rate Q for varying incline angle α under hydrophilic “T+F+B drainage” condition (Figure 3d, filled blue diamond symbols) and high-adhesion hydrophobic “T+F drainage” condition (Figure 3d, filled red diamond symbols). These results show that the incline angle α barely affects the drainage time t for the water channel-based drainage mode, further verifying that the stable water channel construction is the central aspect for faster drainage.

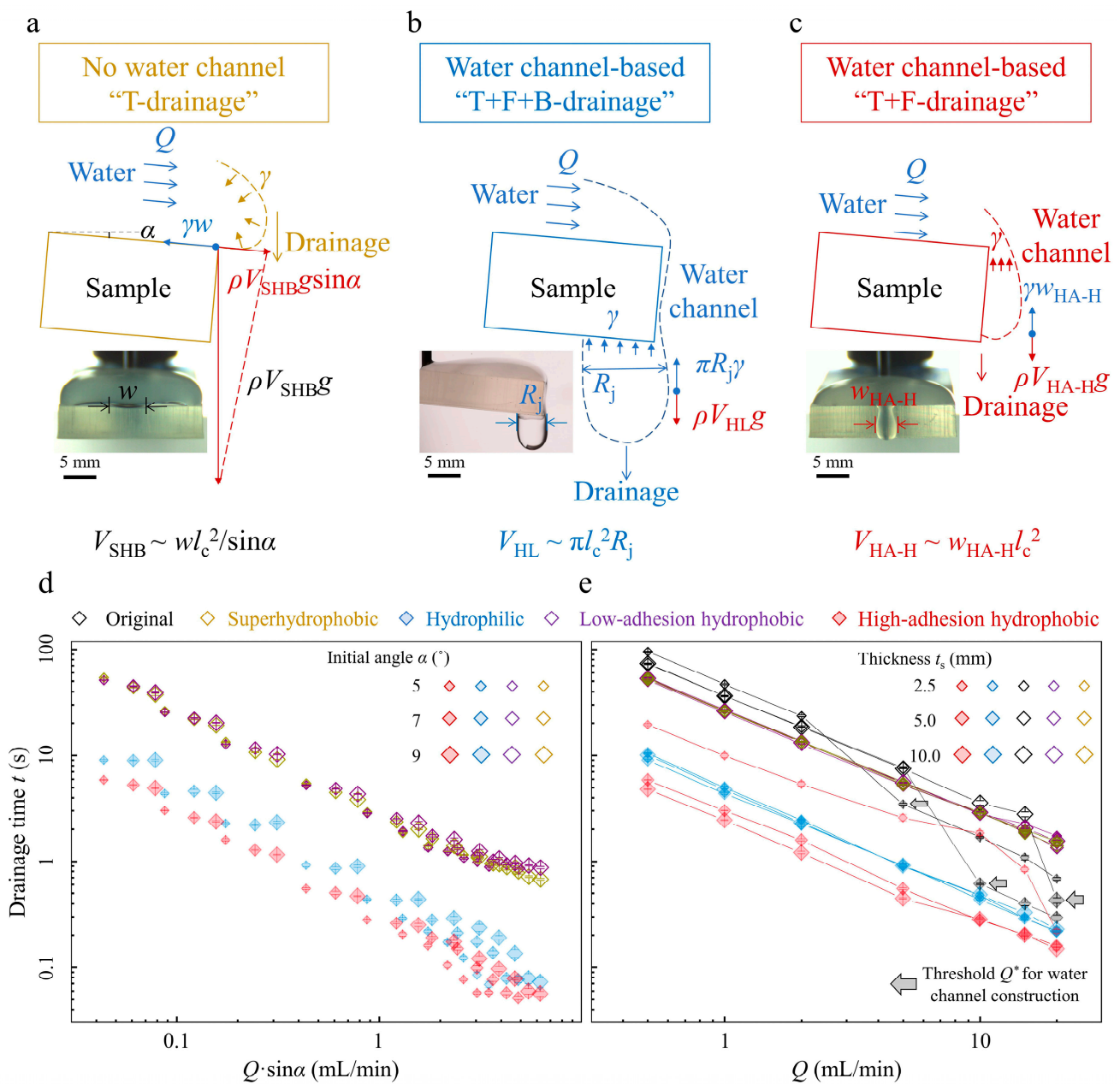


Figure 3. Drainage mechanisms and experimental parameters regulating different drainage modes. (a–c) Schematic diagrams and corresponding critical snapshots (inset) for different drainage modes. The driving force of gravity overcomes the resisting capillary resistance, and one droplet drainage happens. (d) Drainage time t versus water flow rate Q modified by the initial angle α for different margin modifications. (e) Drainage time t versus water flow rate Q under different margin thicknesses for various margin modifications. The arrows indicate the threshold water flow rates for the original margin samples. The error bar represents the standard deviations for at least five independent measurements.

Sample thickness t_s is another crucial variable that affects drainage results under different drainage modes (Figure 3e). We define a characteristic drainage droplet size as $t_c = \sqrt[3]{\frac{3V_{SHB}}{4\pi}} \sim 5.0$ mm. We design the sample thickness t_s as 2.5, 5.0, and 10.0 mm with $t_s = 2.5$ mm smaller than t_c , $t_s = 5.0$ mm comparable to t_c , and $t_s = 10.0$ mm bigger than t_c . Samples with various margin modifications and drainage modes exhibit different dependences on the sample thicknesses. First, for the “T drainage” and “T+F drainage” of the no-water channel drainage mode and “T+F+B drainage” of the water channel-

based drainage mode, the drainage time t nearly overlaps each other for various water flow rates Q at different sample thicknesses t_s . The reasons are as follows: for the no-water channel “T drainage” and “T+F drainage” conditions, sample margins are not involved in the drainage process; for the water channel-based “T+F+B drainage” condition, stable marginal water channels construct for different sample thicknesses t_s and bottom water jet width determines the drainage results (Figure 3b). Next, for the original margin “T+F+B drainage” of the no-water channel drainage mode, threshold water flow rate Q^* exists for water channel construction and increases with t_s : $Q^* = 5, 10, \text{ and } 20 \text{ mL/min}$ for $t_s = 2.5, 5.0, \text{ and } 10.0 \text{ mm}$, respectively (Figure 3e, as the arrows indicate). Moreover, for the high-adhesion hydrophobic “T+F drainage” of the water channel-based drainage mode, the drainage time t of samples with $t_s = 5.0 \text{ mm}$ and 10.0 mm are similar, while that of the sample with $t_s = 2.5 \text{ mm}$ is larger. This is because the fully constructed water channels along thicker margins ($t_s = 5.0 \text{ mm}$ and 10.0 mm) provide more unhindered pathways to drain water, while the water channel at the thinner margin ($t_s = 2.5 \text{ mm}$) is not fully constructed and cannot drain the injection water in time (Video S2). These results indicate that the sample thickness largely affects the drainage results for different drainage modes.

3.3. Critical Drainage Snapshots and Phase Maps of the Two Drainage Modes

Finally, we analyze the drainage conditions from critical front snapshots (Figures 4a–e and S3, Video S3) and summarize the phase map as no-water channel drainage mode and water channel-based drainage mode versus various water flow rates Q for different margin modifications (Figure 4f). Critical drainage conditions vary with margin modifications. First, for the superhydrophobic margin sample with varying thicknesses, water is quickly cut off at the marginal top (Figure 4a), and no-water channel constructs because inertia (even for $Q = 40 \text{ mL/min}$) cannot overcome the marginal capillary resistance (Figure 4f, open yellow diamond symbols). Then, water is also easily cut off at the margin top for the low-adhesion hydrophobic margin sample with varying thicknesses. The remaining water at the margin quickly dewets after one drainage (Figure 4b), and no marginal water exists before the next drainage for $Q \in \{0.5\text{--}40\} \text{ mL/min}$ (Figure 4f, open purple diamond symbols). Next, threshold water flow rates Q^* for water channel constructions exist for the original margin sample with varying thicknesses. At $Q < Q^*$, the capillary forces dominate, and the water channels gradually dewet because there is no sufficient water supply to sustain the marginal water channel (Figure 4c). At $Q > Q^*$, inertia forces dominate, and the injection water provides enough water to construct marginal water channels. Thicker margin samples need more water for water channel constructions, leading to higher Q^* (Figure 4f, open and filled black diamond symbols). Finally, water channels always tightly adhere to the higher-adhesion margins for the high-adhesion hydrophilic and hydrophobic margin samples with varying thicknesses (Figure 4d,e). Note that the drainage width for the high-adhesion hydrophilic margin is wider than the hydrophobic one (Figure 4d,e). This is because the water channel at the hydrophilic margin spreads out while the water channel at the hydrophobic one is more confined. And the samples drain water with the water channel-based drainage mode for various water flow rates $Q \in \{0.5\text{--}40\} \text{ mL/min}$ (Figure 4f, filled blue and red diamond symbols). In a broad aspect, lower-surface tension liquid in a realistic environment related to drainage technology can readily overflow from top to margin and then bottom [5,7] and further be drained faster based on the water channel construction. Considering the widespread distribution of exterior planes composed of intrinsically high-adhesion materials, such as glass, ceramics, metal, etc., the unveiled water channel-based faster drainage discovery in this work will undoubtedly manifest its available meanings in drainage plane design in our daily life.

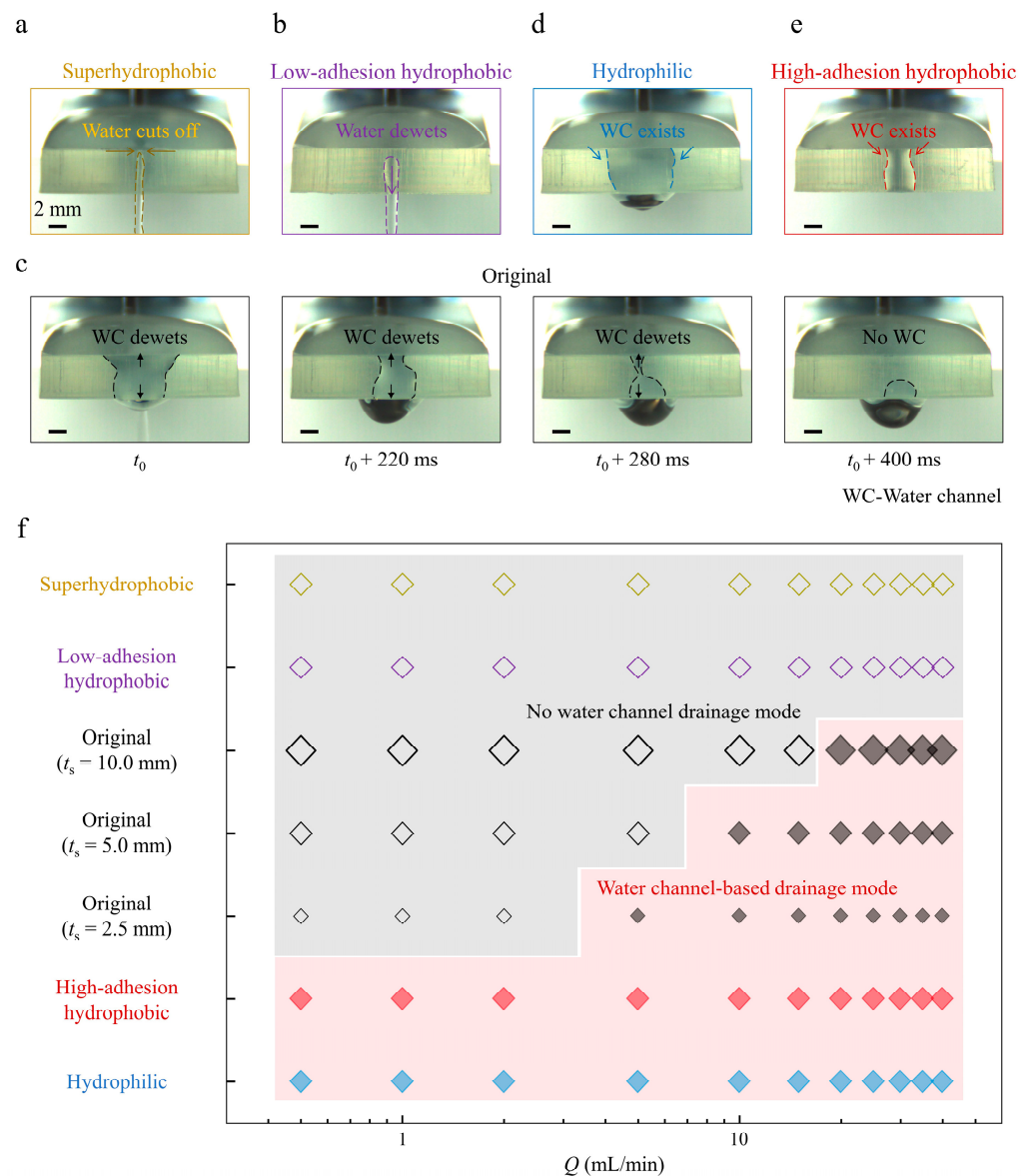


Figure 4. Critical drainage snapshots and phase map of the two drainage modes. (a–e) A series of critical front drainage snapshots demonstrating various marginal water channel conditions for different margin modifications. (f) Phase map for samples of varying margin modifications and thicknesses versus water flow rates Q .

4. Conclusions

In summary, we have presented a simple water channel-based drainage method for faster drainage based on the marginal water channel construction. The quicker water channel-based drainage mode utilizes the water channel to markedly reduce the more considerable marginal capillary resistance for the no-water channel drainage mode and exploits the gravity to overcome surface tension force readily. We confirm the effects of initial incline angles and sample thicknesses on the drainage results for samples with different margin modifications under various water flow rates for the two drainage modes. We also highlight that the sample with the highest contact angle hysteresis hydrophobic margin, previously mainly interpreted as the barrier for water transportation, exhibits the fastest drainage behavior. We believe these results provide inspiration for the widespread drainage plane design with fast water drainage behavior and may also offer insights for open high-speed water transport applications.

Supplementary Materials: The following supporting information can be downloaded at: <https://www.mdpi.com/article/10.3390/biomimetics8010060/s1>, Figure S1: SEM images of top, front margin and bottom of the 3D-printed samples; Figure S2: Adhesion forces of margin surfaces with different wettability modifications; Figure S3: Selected drainage snapshots for samples of margins with different wettability modifications at $Q = 5.0$ mL/min from the front view; Video S1: The drainage modes comparisons; Video S2: Drainage conditions for high-adhesion hydrophobic-margin samples; Video S3: Water channel construction comparisons.

Author Contributions: Conceptualization and methodology, C.G., Z.D. and L.J.; Software, C.G.; writing—original draft preparation, C.G.; writing—review and editing, C.G. and Z.D.; Visualization, C.G.; Supervision, Z.D. and L.J. All authors have read and agreed to the published version of the manuscript.

Funding: This study was funded by the National Natural Science Foundation (52173293) and the Key Research Program of the Chinese Academy of Sciences (KJZD-EW-M01).

Institutional Review Board Statement: Not applicable.

Informed Consent Statement: Not applicable.

Data Availability Statement: Not applicable.

Conflicts of Interest: The authors declare no conflict of interest.

References

1. Park, K.C.; Kim, P.; Grinthal, A.; He, N.; Fox, D.; Weaver, J.C.; Aizenberg, J. Condensation on Slippery Asymmetric Bumps. *Nature* **2016**, *531*, 78–82. [CrossRef] [PubMed]
2. Feng, S.L.; Delannoy, J.; Malod, A.; Zheng, H.X.; Quéré, D.; Wang, Z.K. Tip-Induced Flipping of Droplets on Janus Pillars: From Local Reconfiguration to Global Transport. *Sci. Adv.* **2020**, *6*, eabb4540. [CrossRef] [PubMed]
3. Li, J.; Ran, R.; Wang, H.; Wang, Y.; Chen, Y.; Niu, S.; Arratia, P.E.; Yang, S. Aerodynamics-Assisted, Efficient and Scalable Kirigami Fog Collectors. *Nat. Commun.* **2021**, *12*, 5484. [CrossRef] [PubMed]
4. Bintein, P.B.; Lhuissier, H.; Mongruel, A.; Royon, L.; Beysens, D. Grooves Accelerate Dew Shedding. *Phys. Rev. Lett.* **2019**, *122*, 098005. [CrossRef]
5. Duez, C.; Ybert, C.; Clanet, C.; Bocquet, L. Wetting Controls Separation of Inertial Flows from Solid Surfaces. *Phys. Rev. Lett.* **2010**, *104*, 084503. [CrossRef]
6. Dong, Z.C.; Wu, L.; Li, N.; Ma, J.; Jiang, L. Manipulating Overflow Separation Directions by Wettability Boundary Positions. *ACS Nano* **2015**, *9*, 6595–6602. [CrossRef]
7. Dong, Z.; Wu, L.; Wang, J.; Ma, J.; Jiang, L. Superwettability Controlled Overflow. *Adv. Mater.* **2015**, *27*, 1745–1750. [CrossRef]
8. Jambon-Puillet, E.; Bouwhuis, W.; Snoeijer, J.H.; Bonn, D. The Liquid Helix. *Phys. Rev. Lett.* **2019**, *122*, 184501. [CrossRef]
9. Feng, L.; Li, S.; Li, Y.; Li, H.; Zhang, L.; Zhai, J.; Song, Y.; Liu, B.; Jiang, L.; Zhu, D. Super-Hydrophobic Surfaces: From Natural to Artificial. *Adv. Mater.* **2002**, *14*, 1857–1860. [CrossRef]
10. Dai, X.M.; Sun, N.; Nielsen, S.O.; Stogin, B.B.; Wang, J.; Yang, S.K.; Wong, T.S. Hydrophilic Directional Slippery Rough Surfaces for Water Harvesting. *Sci. Adv.* **2018**, *4*, eaaq0919. [CrossRef]
11. Dickerson, A.K.; Shankles, P.G.; Madhavan, N.M.; Hu, D.L. Mosquitoes Survive Raindrop Collisions by Virtue of Their Low Mass. *Proc. Natl. Acad. Sci. USA* **2012**, *109*, 9822–9827. [CrossRef] [PubMed]
12. Wang, T.; Si, Y.; Dai, H.; Li, C.; Gao, C.; Dong, Z.; Jiang, L. Apex Structures Enhance Water Drainage on Leaves. *Proc. Natl. Acad. Sci. USA* **2020**, *117*, 1890–1894. [CrossRef]
13. Dickerson, A.K.; Mills, Z.G.; Hu, D.L. Wet Mammals Shake at Tuned Frequencies to Dry. *J. R. Soc. Interface* **2012**, *9*, 3208–3218. [CrossRef] [PubMed]
14. Gao, X.; Yan, X.; Yao, X.; Xu, L.; Zhang, K.; Zhang, J.; Yang, B.; Jiang, L. The Dry-Style Antifogging Properties of Mosquito Compound Eyes and Artificial Analogues Prepared by Soft Lithography. *Adv. Mater.* **2007**, *19*, 2213–2217. [CrossRef]
15. Wang, Q.; Yao, X.; Liu, H.; Quere, D.; Jiang, L. Self-Removal of Condensed Water on the Legs of Water Striders. *Proc. Natl. Acad. Sci. USA* **2015**, *112*, 9247–9252. [CrossRef] [PubMed]
16. Wang, L.; Li, J.; Zhang, B.; Feng, S.; Zhang, M.; Wu, D.; Lu, Y.; Kai, J.J.; Liu, J.; Wang, Z.; et al. Counterintuitive Ballistic and Directional Liquid Transport on a Flexible Droplet Rectifier. *Research* **2020**, *2020*, 6472313. [CrossRef] [PubMed]
17. Li, C.X.; Li, N.; Zhang, X.S.; Dong, Z.C.; Chen, H.W.; Jiang, L. Uni-Directional Transportation on Peristome-Mimetic Surfaces for Completely Wetting Liquids. *Angew. Chem. Int. Ed.* **2016**, *55*, 14988–14992. [CrossRef]
18. Si, Y.; Wang, T.; Li, C.; Yu, C.; Li, N.; Gao, C.; Dong, Z.; Jiang, L. Liquids Unidirectional Transport on Dual-Scale Arrays. *ACS Nano* **2018**, *12*, 9214–9222. [CrossRef]
19. Chen, H.; Ran, T.; Gan, Y.; Zhou, J.; Zhang, Y.; Zhang, L.; Zhang, D.; Jiang, L. Ultrafast Water Harvesting and Transport in Hierarchical Microchannels. *Nat. Mater.* **2018**, *17*, 935–942. [CrossRef]

20. Feng, S.L.; Zhu, P.A.; Zheng, H.X.; Zhan, H.Y.; Chen, C.; Li, J.Q.; Wang, L.Q.; Yao, X.; Liu, Y.H.; Wang, Z.K. Three-Dimensional Capillary Ratchet-Induced Liquid Directional Steering. *Science* **2021**, *373*, 1344–1348. [CrossRef]
21. Lv, J.-A.; Liu, Y.; Wei, J.; Chen, E.; Qin, L.; Yu, Y. Photocontrol of Fluid Slugs in Liquid Crystal Polymer Microactuators. *Nature* **2016**, *537*, 179–184. [CrossRef] [PubMed]
22. Lei, W.W.; Hou, G.L.; Liu, M.J.; Rong, Q.F.; Xu, Y.C.; Tian, Y.; Jiang, L. High-Speed Transport of Liquid Droplets in Magnetic Tubular Microactuators. *Sci. Adv.* **2018**, *4*, eaau8767. [CrossRef] [PubMed]
23. Li, N.; Wu, L.; Yu, C.; Dai, H.; Wang, T.; Dong, Z.; Jiang, L. Ballistic Jumping Drops on Superhydrophobic Surfaces Via Electrostatic Manipulation. *Adv. Mater.* **2018**, *30*, 1703838. [CrossRef] [PubMed]
24. Dai, H.; Gao, C.; Sun, J.; Li, C.; Li, N.; Wu, L.; Dong, Z.; Jiang, L. Controllable High-Speed Electrostatic Manipulation of Water Droplets on a Superhydrophobic Surface. *Adv. Mater.* **2019**, *31*, e1905449. [CrossRef] [PubMed]
25. Bouillant, A.; Mouterde, T.; Bourrienne, P.; Lagarde, A.; Clanet, C.; Quéré, D. Leidenfrost Wheels. *Nat. Phys.* **2018**, *14*, 1188–1192. [CrossRef]
26. Bintein, P.-B.; Bense, H.; Clanet, C.; Quéré, D. Self-Propelling Droplets on Fibres Subject to a Crosswind. *Nat. Phys.* **2019**, *15*, 1027–1032. [CrossRef]
27. Li, W.; Tang, X.; Wang, L.Q. Photopyroelectric Microfluidics. *Sci. Adv.* **2020**, *6*, eabc1693. [CrossRef]
28. Dai, H.Y.; Dong, Z.C.; Jiang, L. Directional Liquid Dynamics of Interfaces with Superwettability. *Sci. Adv.* **2020**, *6*, eabb5528. [CrossRef]
29. Ferrand, J.; Favreau, L.; Joubaud, S.; Freyssingéas, E. Wetting Effect on Torricelli's Law. *Phys. Rev. Lett.* **2016**, *117*, 248002. [CrossRef]
30. Dong, Z.; Ma, J.; Jiang, L. Manipulating and Dispensing Micro/Nanoliter Droplets by Superhydrophobic Needle Nozzles. *ACS Nano* **2013**, *7*, 10371–10379. [CrossRef]
31. De Gennes, P.G.; Brochard-Wyart, F.; Quéré, D. *Capillarity and Wetting Phenomena: Drops, Bubbles, Pearls and Waves*; Springer: Berlin/Heidelberg, Germany, 2004; pp. 69–71.

Disclaimer/Publisher's Note: The statements, opinions and data contained in all publications are solely those of the individual author(s) and contributor(s) and not of MDPI and/or the editor(s). MDPI and/or the editor(s) disclaim responsibility for any injury to people or property resulting from any ideas, methods, instructions or products referred to in the content.



Article

Mussel-Inspired Lego Approach for Controlling the Wettability of Surfaces with Colorless Coatings

Carolina Casagualda^{1,2}, Juan Mancebo-Aracil^{1,3}, Miguel Moreno-Villaécija¹, Alba López-Moral^{1,2} , Ramon Alibés² , Félix Busqué^{2,*} and Daniel Ruiz-Molina^{1,*}

¹ Catalan Institute of Nanoscience and Nanotechnology (ICN2), CSIC and The Barcelona Institute of Science and Technology (BIST), Campus UAB, Bellaterra, 08193 Barcelona, Spain

² Departament de Química, Universitat Autònoma de Barcelona, Bellaterra, 08193 Barcelona, Spain

³ Instituto de Química del Sur-INQUISUR (UNS-CONICET), Universidad Nacional del Sur, Bahía Blanca 8000, Argentina

* Correspondence: felix.busque@uab.cat (F.B.); dani.ruiz@icn2.cat (D.R.-M.)

Abstract: The control of surface wettability with polyphenol coatings has been at the forefront of materials research since the late 1990s, when robust underwater adhesion was linked to the presence of L-DOPA—a catecholic amino acid—in unusually high amounts, in the sequences of several mussel foot proteins. Since then, several successful approaches have been reported, although a common undesired feature of most of them is the presence of a remnant color and/or the intrinsic difficulty in fine-tuning and controlling the hydrophobic character. We report here a new family of functional catechol-based coatings, grounded in the oxidative condensation of readily available pyrocatechol and thiol-capped functional moieties. The presence of at least two additional thiol groups in their structure allows for polymerization through the formation of disulfide bonds. The synthetic flexibility, together with its modular character, allowed us to: (I) develop coatings with applications exemplified by textiles for oil-spill water treatment; (II) develop multifunctional coatings, and (III) fine-tune the WCA for flat and textile surfaces. All of this was achieved with the application of colorless coatings.

Keywords: bioinspired; catechol; coatings; multifunctional; oil spill

Citation: Casagualda, C.;

Mancebo-Aracil, J.; Moreno-Villaécija, M.; López-Moral, A.; Alibés, R.;

Busqué, F.; Ruiz-Molina, D.

Mussel-Inspired Lego Approach for Controlling the Wettability of Surfaces with Colorless Coatings.

Biomimetics **2023**, *8*, 3. <https://doi.org/10.3390/biomimetics8010003>

Academic Editors: Andreas Taubert, Stanislav N. Gorb, Giuseppe Carbone and Thomas Speck

Received: 11 November 2022

Revised: 14 December 2022

Accepted: 14 December 2022

Published: 21 December 2022



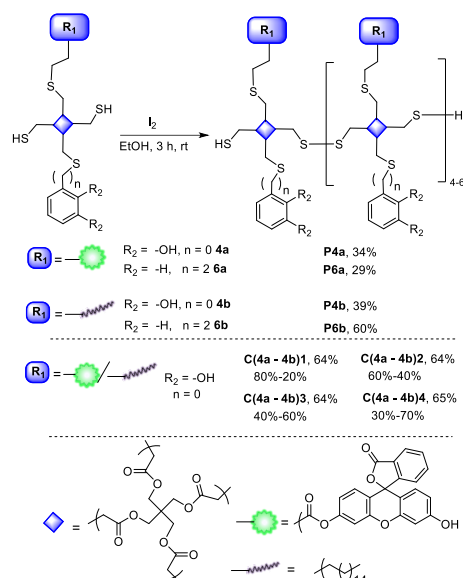
Copyright: © 2022 by the authors. Licensee MDPI, Basel, Switzerland. This article is an open access article distributed under the terms and conditions of the Creative Commons Attribution (CC BY) license (<https://creativecommons.org/licenses/by/4.0/>).

1. Introduction

Chemically engineered interfaces regulate the interaction with the nearby environment by endorsing functional properties such as chemical inertness, adhesion, biocompatibility and/or hydrophilicity/hydrophobicity, among others [1–5]. Most of the coatings so far reported, either as a polymer or self-assembled monolayer, Refs. [6–9] rely on specific chemical interactions between a given substrate and the material used as a coating. More recently, the development of substrate-independent functional thin films such as organic polydopamine (PDA) [10–15] coatings and hybrid metal–phenolic networks (MPNs), [16–21] have attracted widespread interest, owing to their universal adhesion and high stability. Such characteristics are all imparted by the incorporation of polyphenol-containing building blocks inspired by the strong adhesion of several marine organisms, such as mussels and sandcastle worms. Those species adhere to virtually any substrate in aqueous environments, and this is directly associated with the secretion of proteinaceous substances that contain a high concentration of the catecholic amino acid L-DOPA [22]. This compound can anchor by different mechanisms involving covalent bonds, coordination chemistry, π - π stacking, π -cation, electrostatic or hydrogen bonds [23]. Among the different functions that these coatings have been used for, the number of catechol-based examples targeted to systematically control and modify the wettability of surfaces are numbered [24–29]. This represents nowadays one of the biggest challenges in materials science, owing to its significance in many relevant application areas such as anti-corrosion and -frozen coatings, hydrophobic and stain-resistant textiles, or oil spill-treatment, inter alia. One of the most

straightforward approaches used is the self-polymerization under alkaline conditions of catechol-based compounds, such as dopamine or norepinephrine, and subsequently the functionalization with alkyl chains [30–33]. Alternatively, catechol-based molecules can be first functionalized with alkyl chains and then polymerized under alkaline media [34–38]. In a second approach, catechol units can be grafted onto an already formed polymer with additional functional groups that determines the wettability of the surface [39,40]. And finally, a third approach which has not been very much exploited consists of polymerization through a functionality present on the catechol (e.g., acrylate group) that allows for a higher degree of functionalization and synthetic control on the final structure [41,42]. However, despite the different examples so far reported, there are no cases where this property could be systematically fine-tuned at will over a broad range of water contact angles (WCA). Another important fact to mention is that most of the successful examples so far reported in the literature involve the coloration of the substrate, which is not desired in most cases. Therefore, the development of novel synthetic approaches that simultaneously overcome both relevant limitations are strongly required.

Herein, we report the design and synthesis of a new family of colorless coatings with fine-tuned hydrophobic character that relies on a catechol-grafted polymeric architecture linked through disulfide bridges (Scheme 1). The basic scaffold for the modular design of all monomers reported in this work is pentaerythritol tetrakis (3-mercaptopropionate) **1**, a cross-linking agent widely used in commercial coatings, adhesives and sealants. The catechol conjugation is achieved through the addition of one of the thiol groups to the corresponding oxidized *o*-quinone, inspired by the alleged role of free thiol groups of cysteine residues in mussel foot proteins [43–46]. A second thiol group allows for the simultaneous incorporation of an alkyl chain bearing a terminal vinyl or acrylate group using a thiol-ene click reaction [47–49]. And finally, the last two available thiols polymerize through the formation of disulfide bridges, in very mild and selective conditions, without protecting the catechol moieties, using iodine [50]. Following this approach, colorless and hydrophobic coatings have been obtained in flat substrates of a different nature, as well as on different textile pieces that were successfully used as filters to capture oil spills in water. Moreover, the alkyl can be replaced by a fluorescent tag. In addition to demonstrating the multifunctionality of our approach, the controlled combination of different fluorescent tag/alkyl-chain ratios along the polymerization process allows for the obtaining of coatings with control over the WCA. We will also demonstrate that the presence of catechol units is fundamental for good adhesion, which we will do by synthesizing and testing blank coating where the catechol moiety has been replaced by a phenylethenyl fragment.



Scheme 1. Synthesis of the functional polymers through the formation of disulfide bridges.

2. Materials and Methods

2.1. General Procedures

The high quality solvents, chemicals, and reagents were acquired without any need for further purification from various commercial chemical companies such as Merck (Darmstadt, Germany), Scharlab (Sentmenat, Spain), Apollo Scientific (Cheshire, UK), Alfa Aesar (Kandel, Germany), and TCI (Zwijndrecht, Belgium). All reactions were monitored using analytical thin-layer chromatography (TLC) using silica-gel-60-precoated aluminum plates (0.20 mm thickness). Flash column chromatography was performed, using silica gel Geduran[®] SI 60 (40–63 μm). The ^1H NMR and ^{13}C NMR spectra were recorded at 298 K at 250, 360, 400 MHz and 90, 100 MHz, respectively. Proton chemical shifts are reported in ppm (δ) (CDCl_3 , δ 7.26 or CD_3COCD_3 , δ 2.06 or CD_2Cl_2 δ 5.32). Carbon chemical shifts are reported in ppm (δ) (CDCl_3 , δ 77.16 or CD_3COCD_3 , δ 29.8 and CD_2Cl_2 δ 53.5). Infrared spectra (IR) were recorded on a Bruker Tensor 27 Spectrophotometer equipped with a Golden Gate Single Refraction Diamond ATR (Attenuated Total Reflectance) accessory. Peaks are reported in cm^{-1} . HRMS were recorded in an Agilent 6454 Q-TP spectrometer with an Argilent Jetstream Technology (AJT) source, using electrospray ionization (ESI) or electronic impact (EI).

2.2. Synthesis of Monomers

The synthesis of all monomers and their full chemical characterization is fully described in the supporting information, following a synthetic procedure already described in the literature [51,52].

2.3. Polymerization Reactions

2.3.1. Ex Situ Polymerization in Solution

As a general procedure, 1.1 equiv. of a solution of 35 mM of resublimed iodine in EtOH 96% was added dropwise to a ~ 7 mM solution of functional bis-thiol building blocks (**4a**, **4b**, **6a**, and **6b**) in EtOH 96%. The reaction mixture was stirred for 1 h at rt, after which a yellowish solid precipitated. The supernatant was decanted, and the solid washed with fresh EtOH 96% three times, and dried under vacuum.

In all cases, the monomeric bis-thiol building blocks contained 3% of the related catecholic tris-thiol (**2** for the building blocks **4a** and **4b**, **7** for the building blocks **6a** and **6b**). Polymers (yield): **P4a** (34%), **P4b** (39%), **P6a** (29%), and **P6b** (60%). Copolymers bearing fluorescent and hydrophobic building blocks **4a** and **4b**, respectively. Both monomers **4a** and **4b** were dissolved in EtOH 96%, and a 35 mM solution of iodine (1 equiv.) in EtOH 96% was added dropwise. After 1 h of stirring at rt, the precipitated derivatives were isolated, washed several times with fresh EtOH 96%, and dried with a gentle flux of N_2 . Yields were calculated based on the final amount obtained of the resulting copolymer vs. the initial ones used from both starting monomers. Copolymers: **C(4a-4b)a** [20% **4a**, 80% **4b**; 64% yield]; **C(4a-4b)b** [40% **4a**, 60% **4b**; 64% yield]; **C(4a-4b)c** [40% **4a**, 40% **4b**; 64% yield]; and **C(4a-4b)d** [30% **4a**, 60% **4b**; 65% yield].

2.3.2. In Situ Polymerization

A total of 50 mg of resublimed iodine was placed at the bottom of a 20 mL vial. Test slides coated with the C_{18} -functionalised monomer was placed face-down on top of the vials, and left standing overnight. The slides were then washed three times in EtOH 96% (3×3 mL) to remove the excess of adsorbed iodine, and dried in a gentle flux of Ar.

2.4. Polymers Characterisation

The products obtained from polymerization reactions were characterized by different techniques, such as ^1H NMR, DOSY NMR experiments and gel permeation chromatography (GPC). The ^1H NMR and DOSY experiments were performed in THF-d_8 , whereas the GPC analyses were performed in THF. A first rough value of the polymerization degree in the material was determined by ^1H NMR, calculating the ratio of the thiol peak of the

starting monomer and the resulting product from the polymerization reaction. For some of the materials, their polymerization degrees were also determined by calculating the corresponding molecular weights by means of GPC and DOSY NMR techniques. To prepare the GPC samples, the derivatives obtained after polymerization were dissolved in THF (1 or 2 mg/mL) and filtered through 0.22 μm nylon filters. To determine the polymerization degree by DOSY NMR experiments, firstly a calibration curve was needed. Hence, a pattern of 1-octadecene was used. Its diffusion coefficients were measured, and the diffusion coefficients of the products obtained from the polymerization reactions were interpolated into the calibrate curve to obtain the approximate values of their molecular weights.

The molecular weight distribution of all polymers was determined by gel permeation chromatography (GPC) using an Agilent Technologies 1260 Infinity chromatograph and THF as a solvent. The instrument is equipped with three gel columns: PLgel 5 μm Guard/50 \times 7.5 mm², PLgel 5 μm 10,000 Å MW 4 K–400 K, and PL Mixed gel C 5 μm MW 200–3 M. Calibration was carried out by using polystyrene standards. In each experiment, the freshly prepared polymer-sample of interest was dissolved in THF (1–2 mg/mL), and immediately analyzed using GPC (1 mL/min flow; 30 °C column temperature). The values obtained for M_n are an approximation.

The contact angle of the Milli-Q water droplets (ca. 5 μL) on the coated substrates was used to evaluate the hydrophobicity of the coated samples at rt, using the sessile-drop technique. An Easy Drop Standard analyzer and the Drop Shape Analysis DSA 10 software (KR Ü SS GmbH, Hamburg, Germany) were used throughout. The reported values arise from averaging CA measurements on three different spots of each sample. Energy-dispersive X-ray (EDX) line-scan profiles were obtained at rt and 200 kV on a FEI Tecnai G2 F20 coupled to an EDAX detector. Surface-topography imaging of the different samples was carried out in ambient air, in tapping mode using beam-shaped silicon cantilevers (Nanosensors, nominal force constant: 5 N·m⁻¹, tip radius: ~7 nm) on an Agilent 5500 AFM/SPM microscope (Keysight Technologies, Santa Clara, CA, USA) combined with PicoScan5 version 1.20 (Keysight Technologies) software. An external X-Y positioning system (closed loop, NPXY100E from nPoint, USA) was used. Image processing was carried out using open-source software: WSxM version 3.1 (Nanotec Electronica, Madrid, Spain) and Gwyddion version 2.46 (CMI, Brno, Czech Republic). Scanning-electron-microscopy (SEM) measurements were carried out on a Quanta FEI 200 FEG-ESEM microscope operating at 20 kV. All samples were fixed on SEM holders. Prior to observation with SEM, all samples were metallized with a thin 15 nm layer of platinum using a sputter coater (Leica). Optical and fluorescence images were recorded on a Zeiss Axio Observer Z-1 inverted optical/fluorescence microscope, equipped with five different magnification lenses (5 \times , 10 \times , 20 \times , 50 \times and 100 \times), a motorized XY stage, Hg-lamp excitation source (HBO 103/2, 100 W), AxioCam HRC digital camera, and standard filters in fluorescence mode with an Alexa Fluor 488 filter.

2.5. Coating Experiments

Coating of solid macroscopic substrates. All substrates were cut into 1.5 \times 1.5 cm square slides. Aluminum, copper, and stainless-steel slides were cleaned by sonicating successively in HPLC-grade acetone, EtOH 96% and Milli-Q water (10 min each), and dried in a gentle flux of Ar. Glass slides were cleaned with a plasma cleaner machine (400 W, 5 min). Clean slides were submerged in a ~7 mM solution of the corresponding derivatives in HPLC-grade CH₂Cl₂ (for **P4b** and **P6b**), or HPLC-grade acetone (4 mL) (for **P4a** and **P6a**), and left overnight without stirring. Finally, the slides were washed three times with fresh HPLC-grade solvent (CH₂Cl₂ or acetone), and dried in a gentle flux of argon.

Coating of cotton and polyester cloths. A piece of ca. 1.5 \times 1.5 cm of cotton and polyester cloths (σ = 25 mg/cm) were submerged in a ~7 mM solution of the corresponding derivative in HPLC-grade acetone (for **P4a**), or HPLC-grade CH₂Cl₂ (**P4b** and **P6b**) (4 mL), and left overnight without stirring. The coated textiles were then washed with fresh HPLC solvent (CH₂Cl₂ or acetone) (3 \times 2 mL), and dried in a gentle flux of Ar.

Static contact-angle (WCA) measurements on coated substrates (metals, glass, cotton, and polyester) were carried out at rt with Milli-Q water droplets (ca. 5 μ L), by means of the sessile-drop technique. Reported values arise from averaging the CA measurements on three different spots of each sample.

Oil absorption in an oil-in-water (*o/w*) mixture. TDC, or olive oil (4 g) colored with Disperse Red 13 (200 ppm) was mixed with distilled water (15 mL). A piece of 1.5 \times 1.5 cm cotton cloth (σ = 25 mg/cm, either pristine or coated with the C₁₈-functionalised derivative **P4b**) was submerged in the *o/w* mixture for 15 s, taken out, and left hanging until the excess of liquid drained completely.

Filtration of an *o/w* mixture. A round piece (\varnothing ~ 2 cm) of cotton cloth (σ = 25 mg/cm), either pristine or coated with the C₁₈-functionalised derivative **P4b**, was carefully placed on the mouth of a glass vial and folded slightly inwards. A 1:1 (*v/v*) hand-shaken mixture of distilled water and a solution of Disperse red 13 in Miglyol[®] 840 was carefully added dropwise on the textile, until liquid started to filter through it.

Emulsion-breaking test. A solution of Disperse Red 13 (200 ppm) in Miglyol[®] 840 (5 g) was mixed with a solution of sodium dodecyl sulphate (SDS) (150 mg) in distilled water (15 mL), and stirred with a Turrax[®] homogeniser at 5000 rpm for 10 min at rt, yielding a homogeneous, milky, pink stock-emulsion. A piece of 1 \times 1 cm of cotton cloth (σ = 25 mg/cm², either pristine or coated with alkylated **P4b**), was submerged in a 10 \times diluted aliquot of the stock emulsion, gently stirred by hand for 5 min, and subsequently taken out of the treated emulsion and left to dry in air.

3. Results and Discussion

3.1. Synthesis and Characterization of Monomers

The modular synthetic strategy used to obtain the constitutive monomeric building blocks is depicted in the supporting information. In brief, starting from the pivotal tetrathiol pentaerythritol tetrakis(3-mercaptopropionate), **1**, the functional fragments of the monomers were sequentially introduced to obtain the catecholic functional monomers **4a** and **4b**, along with model monomers **6a** and **6b** (more information about the synthetic procedure in Supporting Information, S1 and S2 and characterization in S4).

3.2. Synthesis and Characterization of Polymers

Afterwards, the polymerization of monomers **4a** or **4b**, through the formation of disulfide bonds between the remaining thiol groups using mild and simple oxidative reaction conditions, was carried out (Scheme 1). For this, a 7 mM solution of a given monomer in EtOH 96% was reacted with two equivalents of iodine (35 mM in EtOH 96%) for 3 h. at rt. It is worth mentioning that, to favor the crosslinking of the monomers, the reaction was also doped with a 5% of trithiol **2**, affording the corresponding uncolored precipitates **P4a** or **P4b**, in moderate yield.

Following a similar procedure, the blank oligomers **P6a** and **P6b** were also synthesized as blank models. For details of the characterization and experimental conditions used in the all the synthetic steps, see Supporting Information. To determine the degree of polymerization, two techniques were used. Gel-permeation-chromatography (GPC) experiments in THF allowed for the determination of the apparent M_n and M_w , while diffusion-ordered-spectroscopy (DOSY) experiments were used to determine the diffusion coefficients of the polymerization products in THF-d₈; from there, the corresponding M_n or M_w was determined, using a calibration-curve interpolation. Both techniques converged on similar and consistent values, indicating that the resulting polymerization products comprise oligomers of around 2–7 monomeric units (for more information about the synthetic procedure see Supporting Information Sections S3, S5 and S6 for the characterization).

3.3. Hydrophobic Coatings Experiments

3.3.1. Hydrophobic Coating and Characterization of Different Material Surfaces

Once the polymeric materials were prepared and characterized, the first coating experiments were carried out by immersing 1.5×1.5 cm glass slides, previously cleaned with plasma (400 W, 5 min), in a ~ 7 mM CH_2Cl_2 solution of **P4b** overnight, without stirring. After this period, the substrates were removed from the solution and dried in a gentle flux of argon. The wettability of such surfaces was evaluated from WCA measurements, using Milli-Q water droplets (ca. $5 \mu\text{L}$) by means of the sessile-drop technique. These measurements showed a contact-angle value of 95° (5° for the pristine glass). It is worth mentioning that the **P4b** robustness was challenged with intensive cleaning three times, with fresh CH_2Cl_2 , in which the oligomer is soluble, in the presence of ultrasounds. After such a strong cleaning process, the substrate extraordinarily still retained a hydrophobic character, with a contact-angle close to 80° . For this reason, and to reinforce the viability of our approach, from now on all the substrates of this work were cleaned under these drastic conditions. For comparison purposes, the same procedure was now repeated using the precursor monomer **4b**, previous polymerization. In this case, even though the initial WCA value was relatively high (84°), it immediately dropped down to 55° , confirming that the monomer self-assembly coatings are less stable (for more information about the coating-procedure see Supporting Information S7).

AFM surface-topography imaging of a standard **P4b** glass coating in ambient (air) conditions revealed a consistent average thickness of $1.5 \mu\text{m}$ and a roughness of 435 ± 32 nm, as measured upon scratching a section of the substrate (see Figure 1b). Other experimental factors such as substrate orientation and time evolution were also studied. For this, four cleaned glass-slides were submerged in a **P4b** HPLC-grade CH_2Cl_2 solution for 1 h, 4 h, 8 h, and overnight. Afterwards, they were washed three times with fresh CH_2Cl_2 , dried in a gentle flux of argon, and the WCA was measured. It is worth mentioning that the WCA values after 4 h were comparable with the ones obtained after 8 h, or even overnight (the WCA values ranged between 71° and 76° in all cases). Therefore, and since it is the shortest experimental time used, experiments at 4 h were now repeated, depositing the slides into the solution with two different orientations, one lying on the bottom of the vial (parallel) and the second one resting on the wall (perpendicular). Afterwards, they were washed with fresh CH_2Cl_2 , and dried with a flux of argon, resulting in comparable hydrophobic values (73° vs. 76° , respectively).

Beyond the glass, three additional surfaces (aluminum, copper, and stainless steel), were also studied, for comparison purposes. As a general procedure, 1.5×1.5 cm slides were cleaned by sonicating in acetone, EtOH 96% and Milli-Q water for 10 min, and dried in a gentle flux of argon. Afterwards, coating with **P4b** was achieved, following the same formula used for the glass surfaces, and characterized by EDX, showing in all cases signals around 2.3 KeV, characteristic of sulphur atoms (see Supporting Information, S8). Furthermore, carbon and oxygen were also identified, and the measured percentages of these were around the expected ones ($\pm 10\%$).

Afterwards, the WCAs were measured, and from there, two main deductions can be extracted (Figure 1). First, in all the cases our coating clearly improves the hydrophobic character, even if the pristine material already exhibits considerable WCA values (see Figure 1a). Second, the WCA differences before and after washing are even less remarkable than for glass, endorsing the robustness of our coating. In fact, once more, coating of the three substrates with the styrene derivative **P6b** revealed WCA values remarkably reduced, in comparison with **P4b**, except for copper substrates, most likely due to the affinity of unreacted terminal thiol-groups for this material. Finally, and regardless of the surface, no color modification was detected upon coating.

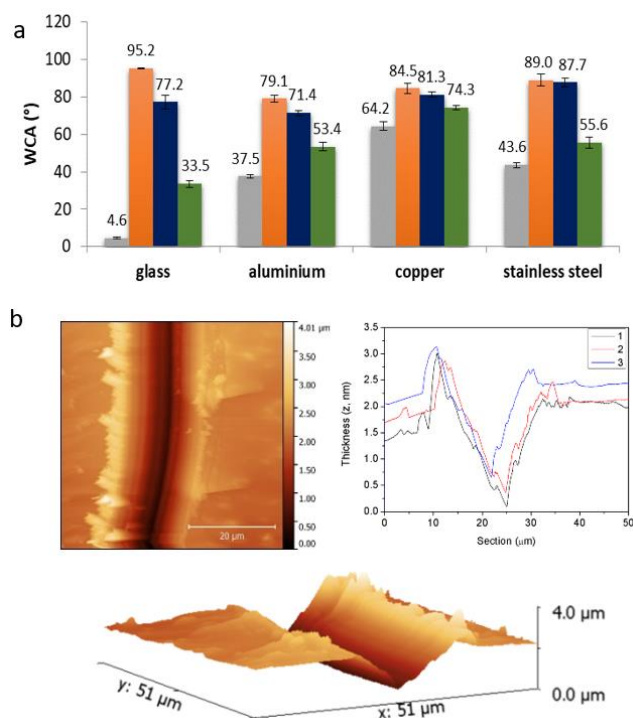


Figure 1. (a) WCA values of four different substrates (glass, aluminum, copper, and stainless steel) coated with **P4b** before (orange) and after (blue) extensive washing, and **P6b** (green) after being rinsed. WCA of the corresponding pristine material is shown in grey. (b) Surface topography imaging of **P4b** coating onto glass in ambient (air) conditions, using tapping mode and beam-shaped silicon cantilevers, with AFM/SPM microscope. The measurements revealed an average thickness of 1.5 µm and an average roughness of 435 ± 32 nm, as measured using scratching techniques. A 3D representation of the scratched sample is shown at the bottom of the Figure.

The polymerization protocol was also tested in situ. For this, the four substrates (including glass) were initially coated by submerging them in a ~ 7 mM CH_2Cl_2 solution of **4b**, and afterwards placing them on closed vials overnight with iodine, ensuring sublimation. Afterwards, surfaces were washed three times with fresh EtOH 96% to remove the excess of iodine, and dried in a gentle flux of argon. At first sight, the area in contact with iodine had already become scattered, pointing to a polymerization reaction. Accordingly, in all cases there was a considerable increase of WCA values, compared with the corresponding blanks (iodine sublimation in the absence of the **P4b** coating), and even for the corresponding coating obtained in solution. This did not apply for aluminum and especially stainless-steel, a fact attributed to the iodine effects (the direct interaction of stainless steel with iodine reduces its WCA from 44° to 12°). An EDX analysis of all samples showed the presence of sulphur at 2.3 keV, carbon at 0.27 keV, and oxygen at 0.52 keV.

3.3.2. Hydrophobic Coating and Characterization of Textile Pieces

After testing the flat surfaces, the next objective was to confer hydrophobic features onto the textile pieces. As a general procedure, pieces of ca. 1.5×1.5 cm of cotton or polyester cloths, without previous treatment, were submerged in a ~ 7 mM **P4b** CH_2Cl_2 solution for four hours, without stirring. The coated textiles were then washed with fresh CH_2Cl_2 (3×2 mL), and dried in a gentle flux of argon. Analysis of the cotton and polyester fibers before and after coating using scanning-electron-microscopy (SEM) images, revealed remarkable differences between them, attributed to the formation of a coating around each one of the individual fibers. It is worth mentioning that no noticeable color nor flexibility and breathability changes of the textiles were macroscopically detected. On top of this, the WCA of Milli-Q water droplets at rt by means of the sessile-drop technique revealed values of 120° (137° before strong washing) for cotton@**P4b**, and 127° (163° before strong washing)

for polyester@**P4b** (WCA values for pristine cotton and polyester were below 10° after a few seconds). Moreover, water droplets stand for a long period without remarkable changes. On the contrary, styrene derivative **P6b**-coatings of both cotton fibers and polyester were completely removed with washes, showing final WCAs close to 0° (for more information see Supporting Information S9).

3.3.3. Oil-Absorbance and Oil/Water-Separation Experiments with Hydrophobic Coated Cotton-Textile

Because of its remarkable water-repellent performance, **P4b**-coated textiles were then used for oil-absorbance tests and oil/water-separation experiments, simulating the removal of oily pollutants from aqueous phases. Two oily phases, tetradecane (TDC) and olive oil, colored with Disperse red 13, were used as non-volatile model pollutants upon the addition of 15 mL of distilled water. Afterwards, **P4b**-coated cotton fibers of known weight (dry) were soaked in the oil phase for 15 s, taken out, allowed to drain for 3 h, and weighted again. The coated fibers showed a 127% weight increase with TDC (25% for pristine cotton), and a 172% weight increase with olive oil (94% for pristine cotton). In accordance with this, SEM images of the fibers before and after absorbing TDC and olive oil reveal differences. A piece (1×2 cm) of cotton@**P4b** was also placed on top of a 20 mL vial, and used as a filter for phase separation of a Miglyol[®] 840 colored with a red-Disperse-13 and distilled-water mixture (1:1). Immediately after deposition with a syringe, oil quickly saturated the coated-cotton passing through, while water was retained at the top. Another piece of cotton@**P4b** (1×1 cm) was also successfully used to recover a microemulsion (20 μ m average droplet-size) of Miglyol[®] 840 colored with Disperse red 13 in water stabilized with sodium dodecyl sulfate (SDS). For this, the textile was submerged in a $10\times$ diluted aliquot of the stock emulsion, gently stirred by hand for 5 min, and subsequently taken out of the treated emulsion and left to dry in air. The coated cotton absorbed up to 97% of its own weight, and therefore acquired a remarkable red color, whereas the weight increase for the uncoated cotton was only 8% (Figure 2).

3.3.4. Fluorescent Coating and Characterization of Glass Surface and Textile Pieces

We also tested our approach by replacing the alkyl chains with the fluorescein derivatives **4a**, **P4a** and **P6a**, using the experimental procedure previously described, but replacing the CH_2Cl_2 with acetone. After rinsing the slides well, the fluorescent images of an inverted microscope using an Alexa Fluor 488 filter revealed that only the **P4a**-coated glass showed continuous intense fluorescence on the whole surface. The **4a**-coated glass slide showed low fluorescent intensity concentrated in some aggregates, while the styrenic derivative **P6a** was completely removed, as the final surfaces did not show fluorescence. Similar results were obtained by repeating the protocol with cotton and textiles, as shown in Figure 3.

3.3.5. Dual-Modulated Hydrophobic and Fluorescent Coating of Textile Pieces

In addition to a multifunctional character, the fluorescent groups also provided higher polarity (WCAs of 31° and 34° for cotton and textiles, respectively), a fact that was then used to modulate the hydrophobic/hydrophilic balance of the textiles. For this, oligomers with different and defined **4a/4b** monomer ratios (80:20, 60:40, 40:60 and 20:80) were obtained in good yields (close to 65% in all the cases) following the same protocol previously described for **P4a** and **P4b** (see Supporting Information for experimental details and characterization). Afterwards, cotton fibers were coated with the resulting **C(4a-4b)** oligomers from different ratios upon immersion in ~ 7 mM solutions in CH_2Cl_2 HPLC-grade for 4 h. Once removed from the solution, they were washed three times with fresh acetone/ CH_2Cl_2 , and dried in a gentle flux of argon. Interestingly, WCAs systematically increased from 0° to 120° , with the amount of the aliphatic derivative **4b** present in the **C(4a-4b)** oligomer (see Figure 3).

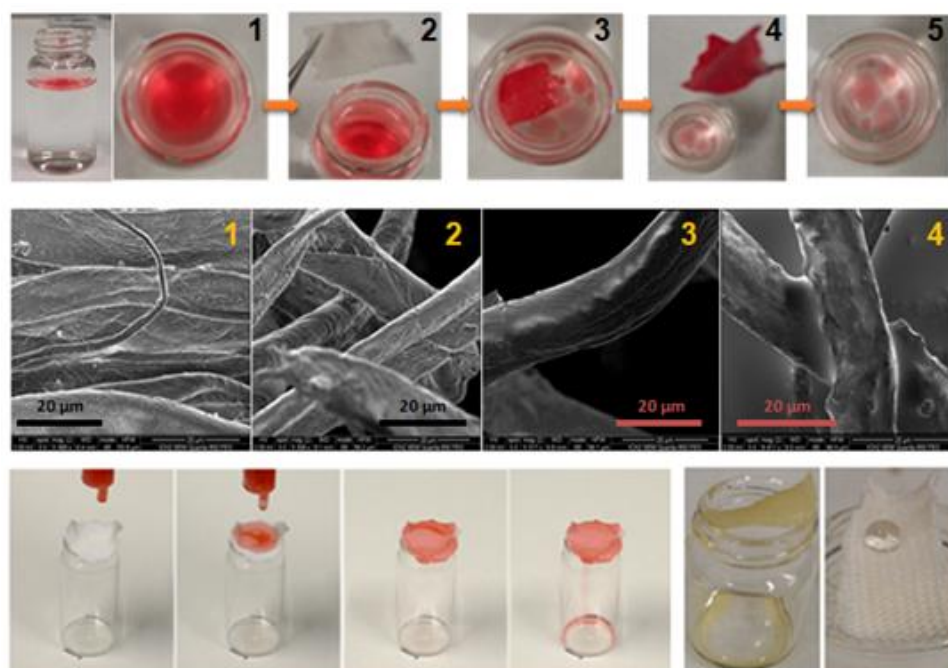


Figure 2. Top: Selective oil removal: (1) olive oil/water separation-phases; (2–5) soaking of a cotton@P4b. Middle: SEM images of pristine cotton weaves (1), cotton@P4b (2), and after absorption of TDC (3) and olive oil (4). Bottom: (Left) Sequence of an oil/water-phase separation by filtration with cotton@P4b. Water phase is retained on the top, whereas oil phase (in red) passes through our household filter into the vial. (Right) Oil-phase saturation onto coated cotton weaves (left), and water-repellent character (right).

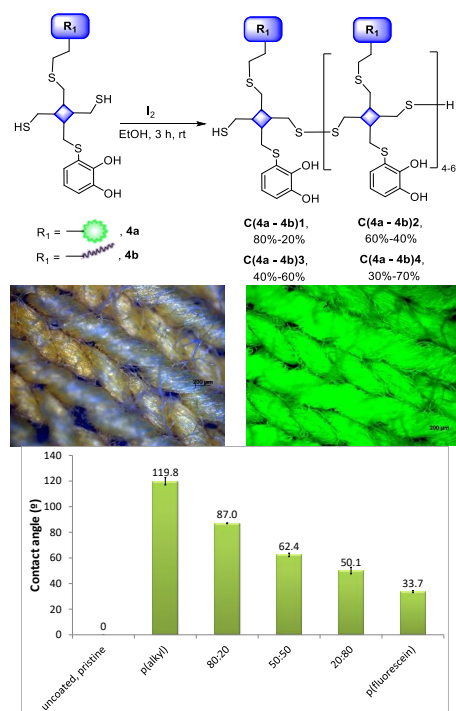


Figure 3. Top: Polymerization with the synthesized monomers 4a and 4b, to obtain final copolymers with two main properties: fluorescence and hydrophobicity (Scale bar: 200 μ m). Middle: images from an optical/fluorescence microscope of cotton fibers coated with copolymer 80:20 (4b:4a) (left), and homopolymer p4a (right). Bottom: WCA values of coated cotton weaves with some copolymers C8-9.

4. Conclusions

We designed a novel catechol-based modular synthetic approach to control the wettability of surfaces in a straightforward and systematic manner, using colorless coatings. For this, we used a unique basic scaffold, pentaerythritol tetrakis(3-mercaptopropionate) **1**, conjugated with both a catechol unit and a functional group of two thiol groups, while leaving the two additional free thiols available for polymerization, through the formation of disulfide bridges. As a proof of concept, we synthesized oligomers that confer a hydrophobic and/or fluorescent character to the surface of glass slides and cotton/textile weaves. Hydrophobic fabrics were, in fact, successfully tested on simulated oil-spill and emulsion samples. Moreover, the proper selection and combination of building block units combining both functionalities allowed us to systematically fine-tune at will the wettability of surfaces. All in all, the modular character of our synthetic approach and its rich and flexible chemistry open new opportunities for the development of colorless coatings with tailored properties. This is so thanks to the presence of the catechol moiety, which plays an important role in the adhesion processes, resulting in robust coatings even after vigorous washing processes.

Supplementary Materials: The following supporting information can be downloaded at: <https://www.mdpi.com/article/10.3390/biomimetics8010003/s1>.

Author Contributions: Conceptualization, J.M.-A., D.R.-M., F.B. and R.A.; methodology, J.M.-A., D.R.-M. and R.A.; formal analysis, C.C., J.M.-A. and M.M.-V.; investigation, C.C., A.L.-M. and M.M.-V.; resources, D.R.-M., F.B. and R.A.; data curation, C.C. and A.L.-M.; writing—original draft preparation, C.C., D.R.-M. and F.B.; writing—review and editing, all the team; supervision, D.R.-M., F.B. and R.A.; project administration, D.R.-M., F.B. and R.A.; funding acquisition, D.R.-M., F.B. and R.A. All authors have read and agreed to the published version of the manuscript.

Funding: The authors would like to acknowledge the funding support from grants: PID2019-106403RB-I00 and PID2021-127983OB-C21 funded by MCIN/AEI/10.13039/501100011033, co-financed with the European Fund for Regional Development (FEDER). and by ERDF's A way of making Europe. The ICN2 is funded by the CERCA programme/Generalitat de Catalunya. The ICN2 is supported by the Severo Ochoa Centres of Excellence programme, and grant SEV-2017-0706 is funded by MCIN/AEI/10.13039/501100011033.

Institutional Review Board Statement: Not applicable.

Data Availability Statement: Not applicable.

Acknowledgments: We thank Salvio Suárez for AFM images.

Conflicts of Interest: The authors declare no conflict of interest.

References

- Zhu, T.; Jiang, C.; Wang, M.; Zhu, C.; Zhao, N.; Xu, J. Skin-Inspired Double-Hydrophobic-Coating Encapsulated Hydrogels with Enhanced Water Retention Capacity. *Adv. Funct. Mater.* **2021**, *31*, 202102433. [CrossRef]
- Jeon, Y.; Nagappan, S.; Li, X.-H.; Lee, J.-H.; Shi, L.; Yuan, S.; Lee, W.-K.; Ha, C.-S. Highly Transparent, Robust Hydrophobic, and Amphiphilic Organic–Inorganic Hybrid Coatings for Antifogging and Antibacterial Applications. *ACS Appl. Mater. Interfaces* **2021**, *13*, 6615–6630. [CrossRef] [PubMed]
- Balkenende, D.W.R.; Winkler, S.M.; Li, Y.; Messersmith, P.B. Supramolecular Cross-Links in Mussel-Inspired Tissue Adhesives. *ACS Macro Lett.* **2020**, *9*, 1439–1445. [CrossRef] [PubMed]
- Inoue, A.; Yuk, H.; Lu, B.; Zhao, X. Strong adhesion of wet conducting polymers on diverse substrates. *Sci. Adv.* **2020**, *6*, eaay5394. [CrossRef] [PubMed]
- Wang, G.; Chen, C.; Chen, Y.; Kang, X.; Yang, C.; Wang, F.; Liu, Y.; Xiong, X. Self-Stabilized and Strongly Adhesive Supramolecular Polymer Protective Layer Enables Ultrahigh-Rate and Large-Capacity Lithium-Metal Anode. *Angew. Chem.* **2020**, *132*, 2071–2076. [CrossRef]
- Sánchez-Bodón, J.; del Olmo, J.A.; Alonso, J.M.; Moreno-Benítez, I.; Vilas-Vilela, J.L.; Pérez-Álvarez, L. Bioactive Coatings on Titanium: A Review on Hydroxylation, Self-Assembled Monolayers (SAMs) and Surface Modification Strategies. *Polymers* **2021**, *14*, 165. [CrossRef]
- Liu, Y.; Tao, X.; Wang, Y.; Jiang, C.; Ma, C.; Sheng, O.; Lu, G.; Lou, X.W. Self-assembled monolayers direct a LiF-rich interphase toward long-life lithium metal batteries. *Science* **2022**, *375*, 739–745. [CrossRef]

8. Mainali, B.P.; Pattadar, D.K.; Zamborini, F.P. Reverse Size-Dependent Electrooxidation of Gold Nanoparticles Coated with Alkanethiol Self-Assembled Monolayers. *J. Phys. Chem. C* **2021**, *125*, 2719–2728. [CrossRef]
9. Yi, R.; Mao, Y.; Shen, Y.; Chen, L. Self-Assembled Monolayers for Batteries. *J. Am. Chem. Soc.* **2021**, *143*, 12897–12912. [CrossRef]
10. Kumar, M.; Sreedhar, N.; Thomas, N.; Mavukkandy, M.; Ismail, R.A.; Aminabhavi, T.M.; Arafat, H.A. Polydopamine-coated graphene oxide nanosheets embedded in sulfonated poly(ether sulfone) hybrid UF membranes with superior antifouling properties for water treatment. *Chem. Eng. J.* **2021**, *433*, 133526. [CrossRef]
11. Zhang, H.; Ou, J.; Fang, X.; Lei, S.; Wang, F.; Li, C.; Li, W.; Hu, Y.; Amirfazli, A.; Wang, P. Robust superhydrophobic fabric via UV-accelerated atmospheric deposition of polydopamine and silver nanoparticles for solar evaporation and water/oil separation. *Chem. Eng. J.* **2022**, *429*, 132539. [CrossRef]
12. Shi, P.; Qin, J.; Wu, X.; Wang, L.; Zhang, T.; Yang, D.; Zan, X.; Appelhans, D. A Facile and Universal Method to Efficiently Fabricate Diverse Protein Capsules for Multiple Potential Applications. *ACS Appl. Mater. Interfaces* **2019**, *11*, 39209–39218. [CrossRef]
13. Wang, H.; Lin, C.-C.; Zhang, X.; Lin, K.; Wang, X.; Shen, S.G. Mussel-Inspired Polydopamine Coating: A General Strategy to Enhance Osteogenic Differentiation and Osseointegration for Diverse Implants. *ACS Appl. Mater. Interfaces* **2019**, *11*, 7615–7625. [CrossRef]
14. Nador, F.; Guisasola, E.; Baeza, A.; Villaecija, M.A.M.; Vallet-Regí, M.; Ruiz-Molina, D. Synthesis of Polydopamine-Like Nanocapsules via Removal of a Sacrificial Mesoporous Silica Template with Water. *Chem. A Eur. J.* **2016**, *23*, 2753–2758. [CrossRef]
15. Lee, H.; Dellatore, S.M.; Miller, W.M.; Messersmith, P.B. Mussel-Inspired Surface Chemistry for Multifunctional Coatings. *Science* **2007**, *318*, 426–430. [CrossRef] [PubMed]
16. Wu, H.; He, Q.; Li, L.; Li, L.; Zhou, Z.; Chen, N.; Yang, M.; Luo, Q.; Zhang, B.; Luo, R.; et al. A facile and versatile superhydrophilic coating on biodegradable PLA stent with stepwise assembly of metal/phenolic networks for mimicking endothelium function. *Chem. Eng. J.* **2021**, *427*, 130932. [CrossRef]
17. Chen, J.; Pan, S.; Zhou, J.; Seidel, R.; Beyer, S.; Lin, Z.; Richardson, J.J.; Caruso, F. Metal-Phenolic Networks as Tunable Buffering Systems. *Chem. Mater.* **2021**, *33*, 2557–2566. [CrossRef]
18. Guo, Z.; Xie, W.; Lu, J.; Guo, X.; Xu, J.; Xu, W.; Chi, Y.; Takuya, N.; Wu, H.; Zhao, L. Tannic acid-based metal phenolic networks for bio-applications: A review. *J. Mater. Chem. B* **2021**, *9*, 4098–4110. [CrossRef]
19. Liu, P.; Shi, X.; Zhong, S.; Peng, Y.; Qi, Y.; Ding, J.; Zhou, W. Metal-phenolic networks for cancer theranostics. *Biomater. Sci.* **2021**, *9*, 2825–2849. [CrossRef]
20. Liu, Y.; Jia, J.; Liu, Z.; Pu, N.; Ye, G.; Wang, W.; Hu, T.; Qi, T.; Chen, J. Competitive Binding-Modulated Metal-Phenolic Assemblies for Adaptable Nanofilm Engineering. *Chem. Mater.* **2021**, *33*, 4733–4744. [CrossRef]
21. Nador, F.; Novio, F.; Ruiz-Molina, D. Coordination Polymer Particles with ligand-centred pH-responses and spin transition. *Chem. Commun.* **2014**, *50*, 14570–14572. [CrossRef] [PubMed]
22. Papov, V.V.; Diamond, T.V.; Biemann, K.; Waite, J.H. Hydroxyarginine-containing Polyphenolic Proteins in the Adhesive Plaques of the Marine Mussel *Mytilus edulis*. *J. Biol. Chem.* **1995**, *270*, 20183–20192. [CrossRef] [PubMed]
23. Poseu, J.S.; Mancebo-Aracil, J.; Nador, F.; Busque, F.; Ruiz-Molina, D. The Chemistry behind Catechol-Based Adhesion. *Angew. Chem. Int. Ed.* **2018**, *58*, 696–714. [CrossRef]
24. Correia, C.; Sousa, R.O.; Vale, A.C.; Peixoto, D.; Silva, T.H.; Reis, R.L.; Pashkuleva, I.; Alves, N.M. Adhesive and biodegradable membranes made of sustainable catechol-functionalized marine collagen and chitosan. *Colloids Surf. B Biointerfaces* **2022**, *213*, 112409. [CrossRef] [PubMed]
25. Ni, X.; Gao, Y.; Zhang, X.; Lei, Y.; Sun, G.; You, B. An eco-friendly smart self-healing coating with NIR and pH dual-responsive superhydrophobic properties based on biomimetic stimuli-responsive mesoporous polydopamine microspheres. *Chem. Eng. J.* **2020**, *406*, 126725. [CrossRef]
26. Zhang, Y.; Hasegawa, K.; Kamo, S.; Takagi, K.; Ma, W.; Takahara, A. Enhanced Adhesion Effect of Epoxy Resin on Metal Surfaces Using Polymer with Catechol and Epoxy Groups. *ACS Appl. Polym. Mater.* **2020**, *2*, 1500–1507. [CrossRef]
27. Zhu, G.; Gao, T.; Si, S.; Zhang, Z.; Liu, Q.; Zhou, G. Mussel-inspired polymerization of catechol and 1,6-hexamethylenediamine for material-independent surface chemistry. *Appl. Surf. Sci.* **2019**, *507*, 145080. [CrossRef]
28. Zhang, Y.; Chu, C.-W.; Ma, W.; Takahara, A. Functionalization of Metal Surface via Thiol-Ene Click Chemistry: Synthesis, Adsorption Behavior, and Postfunctionalization of a Catechol- and Allyl-Containing Copolymer. *ACS Omega* **2020**, *5*, 7488–7496. [CrossRef]
29. Li, M.; Schlaich, C.; Kulka, M.W.; Donskyi, I.S.; Schwerdtle, T.; Unger, W.E.S.; Haag, R. Mussel-inspired coatings with tunable wettability, for enhanced antibacterial efficiency and reduced bacterial adhesion. *J. Mater. Chem. B* **2019**, *7*, 3438–3445. [CrossRef]
30. Nam, S.; Mooney, D. Polymeric Tissue Adhesives. *Chem. Rev.* **2021**, *121*, 11336–11384. [CrossRef]
31. Zhang, J.; Zhang, L.; Gong, X. Design and fabrication of polydopamine based superhydrophobic fabrics for efficient oil-water separation. *Soft Matter* **2021**, *17*, 6542–6551. [CrossRef]
32. Bhat, S.I.; Ahmadi, Y.; Ahmad, S. Recent Advances in Structural Modifications of Hyperbranched Polymers and Their Applications. *Ind. Eng. Chem. Res.* **2018**, *57*, 10754–10785. [CrossRef]
33. Suárez-García, S.; Sedó, J.; Saiz-Poseu, J.; Ruiz-Molina, D. Copolymerization of a Catechol and a Diamine as a Versatile Polydopamine-Like Platform for Surface Functionalization: The Case of a Hydrophobic Coating. *Biomimetics* **2017**, *2*, 22. [CrossRef] [PubMed]

34. Zhou, Q.; Chen, G.; Xing, T. Facile construction of robust superhydrophobic tea polyphenol/Fe@ cotton fabric for self-cleaning and efficient oil–water separation. *Cellulose* **2018**, *25*, 1513–1525. [CrossRef]
35. Lee, W.; Ahn, Y. Separation of Oil/Water Mixtures Using Water-Repellent Particles Coated by a Bioinspired Catechol-based Polymer. *Bull. Korean Chem. Soc.* **2017**, *38*, 1503–1506. [CrossRef]
36. Watanabe, H.; Fujimoto, A.; Nishida, J.; Ohishi, T.; Takahara, A. Biobased Polymer Coating Using Catechol Derivative Urushiol. *Langmuir* **2016**, *32*, 4619–4623. [CrossRef]
37. García, B.; Saiz-Poseu, J.; Gras-Charles, R.; Hernando, J.; Alibés, R.; Novio, F.; Sedó, J.; Busqué, F.; Ruiz-Molina, D. Mussel-Inspired Hydrophobic Coatings for Water-Repellent Textiles and Oil Removal. *ACS Appl. Mater. Interfaces* **2014**, *6*, 17616–17625. [CrossRef]
38. Saiz-Poseu, J.; Sedó, J.; García, B.; Benaiges, C.; Parella, T.; Alibés, R.; Hernando, J.; Busqué, F.; Ruiz-Molina, D. Versatile Nanostructured Materials via Direct Reaction of Functionalized Catechols. *Adv. Mater.* **2013**, *25*, 2066–2070. [CrossRef]
39. Neto, A.I.; Vasconcelos, N.L.; Oliveira, S.M.; Ruiz-Molina, D.; Mano, J.F. High-Throughput Topographic, Mechanical, and Biological Screening of Multilayer Films Containing Mussel-Inspired Biopolymers. *Adv. Funct. Mater.* **2016**, *26*, 2745–2755. [CrossRef]
40. Neto, A.I.; Cibrão, A.C.; Correia, C.R.; Carvalho, R.R.; Luz, G.M.; Ferrer, G.G.; Botelho, G.; Picart, C.; Alves, N.M.; Mano, J.F. Nanostructured Polymeric Coatings Based on Chitosan and Dopamine-Modified Hyaluronic Acid for Biomedical Applications. *Small* **2014**, *10*, 2459–2469. [CrossRef] [PubMed]
41. Payra, D.; Naito, M.; Fujii, Y.; Yamada, N.L.; Hiromoto, S.; Singh, A. Bioinspired adhesive polymer coatings for efficient and versatile corrosion resistance. *RSC Adv.* **2015**, *5*, 15977–15984. [CrossRef]
42. Han, H.; Wu, J.; Avery, C.W.; Mizutani, M.; Jiang, X.; Kamigaito, M.; Chen, Z.; Xi, C.; Kuroda, K. Immobilization of Amphiphilic Polycations by Catechol Functionality for Antimicrobial Coatings. *Langmuir* **2011**, *27*, 4010–4019. [CrossRef]
43. Yang, J.; Stuart, M.A.C.; Kamperman, M. Jack of all trades: Versatile catechol crosslinking mechanisms. *Chem. Soc. Rev.* **2014**, *43*, 8271–8298. [CrossRef]
44. Alfieri, M.L.; Cariola, A.; Panzella, L.; Napolitano, A.; D’Ischia, M.; Valgimigli, L.; Crescenzi, O. Disentangling the Puzzling Regiochemistry of Thiol Addition to *o*-Quinones. *J. Org. Chem.* **2022**, *87*, 4580–4589. [CrossRef]
45. Krüger, J.M.; Börner, H.G. Accessing the Next Generation of Synthetic Mussel-Glue Polymers via Mussel-Inspired Polymerization. *Angew. Chem. Int. Ed.* **2021**, *60*, 6408–6413. [CrossRef]
46. Iacomino, M.; Mancebo-Aracil, J.; Guardingo, M.; Martín, R.; D’Errico, G.; Perfetti, M.; Manini, P.; Crescenzi, O.; Busqué, F.; Napolitano, A.; et al. Replacing Nitrogen by Sulfur: From Structurally Disordered Eumelanins to Regioregular Thiomelanin Polymers. *Int. J. Mol. Sci.* **2017**, *18*, 2169. [CrossRef] [PubMed]
47. Hoyle, C.E.; Bowman, C.N. Thiol-Ene Click Chemistry. *Angew. Chem. Int. Ed.* **2010**, *49*, 1540–1573. [CrossRef]
48. Cespedes, S.; Hand, R.A.; Chmel, N.; Moad, G.; Keddie, D.J.; Schiller, T.L. Enhanced properties of well-defined polymer networks prepared by a sequential thiol-Michael—radical thiol-ene (STMRT) strategy. *Eur. Polym. J.* **2021**, *151*, 110440. [CrossRef]
49. Gao, H.; Sun, Y.; Wang, M.; Wu, B.; Han, G.; Jin, L.; Zhang, K.; Xia, Y. Self-healable and reprocessable acrylate-based elastomers with exchangeable disulfide crosslinks by thiol-ene click chemistry. *Polymer* **2020**, *212*, 123132. [CrossRef]
50. Ruiz-Molina, D.; Sedo-Vegara, J.; Mancebo-Aracil, J. Catechol Derivative Compounds and their Use. *Patent EP343 8093B1*, 2017.
51. Mancebo-Aracil, J.; Casagualda, C.; Moreno-Villaécija, M.A.; Nador, F.; Garcia-Pardo, J.; Franconetti-García, A.; Busqué, F.; Alibés, R.; Esplandiú, M.J.; Ruiz-Molina, D.; et al. Bioinspired Functional Catechol Derivatives through Simple Thiol Conjugate Addition. *Chem. Eur. J.* **2019**, *25*, 12367–12379. [CrossRef] [PubMed]
52. Nador, F.; Mancebo-Aracil, J.; Zanutto, D.; Ruiz-Molina, D.; Radivoy, G. Thiol-yne click reaction: An interesting way to derive thiol-provided catechols. *RSC Adv.* **2021**, *11*, 2074–2082. [CrossRef] [PubMed]

Disclaimer/Publisher’s Note: The statements, opinions and data contained in all publications are solely those of the individual author(s) and contributor(s) and not of MDPI and/or the editor(s). MDPI and/or the editor(s) disclaim responsibility for any injury to people or property resulting from any ideas, methods, instructions or products referred to in the content.



Article

States of Aggregation and Phase Transformation Behavior of Metallosurfactant Complexes by Hexacyanoferrate(II): Thermodynamic and Kinetic Investigation of ETR in Ionic Liquids and Liposome Vesicles

Karuppiyah Nagaraj ^{1,*}, Subramanian Sakthnathan ², Te-Wei Chiu ², Subramaniam Kamalesu ³, Snehal Lokhandwala ⁴, Nikhil M. Parekh ¹ and Chelladurai Karuppiyah ^{5,*}

- ¹ SRICT, Institute of Science and Research, UPL University of Sustainable Technology, Block No. 402, Valia Rd., Vataria, Ankleshwar 393135, Gujarat, India
- ² Department of Materials and Mineral Resources Engineering, National Taipei University of Technology, No. 1, Section 3, Chung-Hsiao East Road, Taipei 106, Taiwan
- ³ Department of Chemistry, University Institute of Science, Chandigarh University, Gharuan, Mohali 140413, Punjab, India
- ⁴ SRICT, Department of Environmental Science & Technology, UPL University of Sustainable and Technology, Block No. 402, Valia Rd., Vataria, Ankleshwar 393135, Gujarat, India
- ⁵ Battery Research Center of Green Energy, Ming Chi University of Technology, New Taipei City 24301, China
- * Correspondence: k.nagaraj@sriect.in (K.N.); kcdurai.rmd@gmail.com (C.K.)

Citation: Nagaraj, K.; Sakthnathan, S.; Chiu, T.-W.; Kamalesu, S.; Lokhandwala, S.; Parekh, N.M.; Karuppiyah, C. States of Aggregation and Phase Transformation Behavior of Metallosurfactant Complexes by Hexacyanoferrate(II): Thermodynamic and Kinetic Investigation of ETR in Ionic Liquids and Liposome Vesicles. *Biomimetics* **2022**, *7*, 221. <https://doi.org/10.3390/biomimetics7040221>

Academic Editors: Stanislav N. Gorb, Giuseppe Carbone, Thomas Speck and Andreas Taubert

Received: 4 November 2022

Accepted: 23 November 2022

Published: 30 November 2022

Publisher's Note: MDPI stays neutral with regard to jurisdictional claims in published maps and institutional affiliations.



Copyright: © 2022 by the authors. Licensee MDPI, Basel, Switzerland. This article is an open access article distributed under the terms and conditions of the Creative Commons Attribution (CC BY) license (<https://creativecommons.org/licenses/by/4.0/>).

Abstract: Electronic absorption spectroscopy was used to study the ETR of surfactant–cobalt(III) complexes containing imidazo[4,5-f][1,10]phenanthroline, dipyrido[3,2-d:2'-3'-f]quinoxaline and dipyrido[3,2-a:2',4'-c](6,7,8,9-tetrahydro)phenazine ligands by using ferrocyanide ions in unilamellar vesicles of dipalmitoylphosphatidylcholine (DPPC) and 1-butyl-3-methylimidazolium bromide ((BMIM)Br), at different temperatures under pseudo-first-order conditions using an excess of the reductant. The reactions were found to be second-order and the electron transfer is postulated as occurring in the outer sphere. The rate constant for the electron transfer reactions was found to increase with increasing concentrations of ionic liquids. Besides these, the effects of surfactant complex ions on liposome vesicles in these same reactions have also been studied on the basis of hydrophobicity. We observed that, below the phase transition temperature, there is an increasing amount of surfactant–cobalt(III) complexes expelled from the interior of the vesicle membrane through hydrophobic effects, while above the phase transition temperature, the surfactant–cobalt(III) complexes are expelled from the interior to the exterior surface of the vesicle. Kinetic data and activation parameters are interpreted in respect of an outer-sphere electron transfer mechanism. By assuming the existence of an outer-sphere mechanism, the results have been clarified based on the presence of hydrophobicity, and the size of the ligand increases from an ip to dpqc ligand and the reactants become oppositely charged. In all these media, the ΔS^\ddagger values are recognized as negative in their direction in all the concentrations of complexes employed, indicative of a more ordered structure of the transition state. This is compatible with a model in which these complexes and $[\text{Fe}(\text{CN})_6]^{4-}$ ions bind to the DPPC in the transition state. Thus, the results have been interpreted based on the self-aggregation, hydrophobicity, charge densities of the co-ligand and the reactants with opposite charges.

Keywords: liposome; ionic liquids; phase transition; metallosurfactants; hydrophobic effect; outer-sphere electron transfer

1. Introduction

During the last few decades, rapid advances in our understanding of surface phenomena have taken place. However, the significance of surface science has been recognized

for more than a century. Surfactants are used as ligands [1] that dramatically decrease the interfacial free energy of solids and liquids [2]. Surfactants are amphiphilic molecules, i.e., they possess hydrophilic and hydrophobic regions [3], with a long hydrocarbon tail and moderately small ionic or polar head group. Surface-active agents play major roles in chemistry, biology, and pharmaceuticals [4]. It has been observed that both the oxidation and reduction of micellar medium can be influenced by hydrophobic and electrostatic forces and, for a given set of reactions, the observed rate depends on the extent of the association between the micellar aggregation and the reactants [5]. In recent times, there have been reports on surfactant metal complexes of various natures and their micellar aggregation properties [6].

The electron transfer based on the outer sphere among first-row metal complexes plays a vital role both in vivo [5] and in the treatment of molecular-scale devices, such as logic gates and molecular wires [7]. The alterations of the electron transfer reactions on the outer-sphere environment complex are attributable to the variation of counter ion concentrations [8]. Gaswick et al. have reported that the $[\text{Fe}(\text{CN})_6]^{4-}$ can reduce some pentamminecobalt(III) complexes to cobalt(II) via an outer-sphere electron transfer step [9] and they have also reported that the substituted pentamminecobalt(III) complexes could be reduced by $[\text{Fe}(\text{CN})_6]^{4-}$ with the development of an ion pair [10]. There are many reports available on electron transfer between metal complexes and ferrocyanide ions [11–14]. A. R. Mustafina et al. [15] have studied the electron transfer reaction of outer-sphere combination of p-sulfanototalix[4]arene and some cobalt-based metal complexes. The ion pairing of the complexes with macrocycle STCA accelerates the $[\text{Fe}(\text{CN})_6]^{4-}$ cobalt(III) electron transfer reactions. A. J. Miralles et al. [16] have explored the outer-sphere reductions of cobalt and ruthenium-based pyridinepentamine complexes by $[\text{Fe}(\text{CN})_6]^{4-}$. A. A. Holder has reported the mechanistic investigation of the reduction of the molybdopentamminecobalt(III) ion by aqueous $[\text{Fe}(\text{CN})_6]^{4-}$ and aqueous sulfite [17]. A. P. Szecsy and A. Haim [18] have studied the mechanism of the reaction which takes place in the imidazolate bridges intramolecular electron transfer between pentacyanoferrate(II) and pentammine cobalt(III) complexes containing imidazole and its conjugate base. Jing-Jer Jwo et al. [19] have performed intramolecular electron transfer between the same reactant and pentammine cobalt(III) mediated by various 4,4'-bipyridines. M. Martinez et al. [20] have reported the outer-sphere reactions of (N)₅-macrocyclic cobalt(III) complexes. Several studies have been conducted to resolve the dependence of electron transfer on different environments, such as DNA vesicles and micelles [21–25], and have received plenty of interest over the last several decades. An amount of research has been devoted to the interaction of amphiphilic molecules with phospholipid vesicles membrane models due to the partition equilibrium between the bilayers and the aqueous phase; this integration involves complex perturbations in the physical properties of vesicle membranes, which pertain to the type and amount of surfactant [26]. It is evident that surfactant complexes are marked by their dual nature consisting of the hydrocarbon component (hydrophobic) and the ionic component (hydrophilic), which is responsible for the self-aggregation process in solution [27].

Vesicles are used for gene therapy in preclinical and clinical trials and have also proven to be beneficial carriers for the delivery of genes to cultured cells [28]. Surfactant-vesicle systems are good models for cell membrane solubilization studies [29]. In the past few years, ionic liquids (ILs) have generated substantial interest as potential new media for nanostructure construction materials, electrochemistry, organic synthesis and catalyst supports [30,31]. From a fundamental prospect, ionic liquids facilitate solvophobic interactions, which are present among ionic liquids and surfactants, enhancing the solvation characteristics of the ionic liquid-surfactant system [32–34]. The outer-sphere electron transfer reactions of innumerable metallomicelles have been developed in our laboratory [35–38]. We have reported that both the oxidant and reductant are cations on the electron transfer between surfactant complexes with iron(II) in DPPC [35–39]. In the present work, we present our results on the influence of phase transition behavior in ionic

liquids and liposome vesicles on the outer-sphere electron transfer between surfactant complexes containing aromatic diimine ligands and ferrocyanide ions.

2. Experimental Section

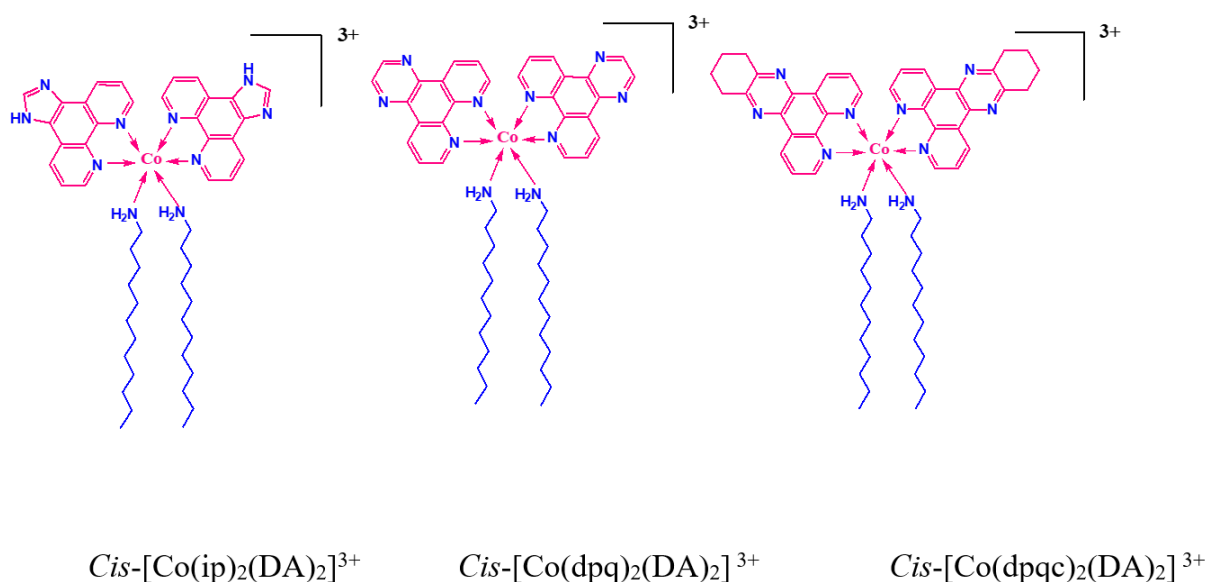
2.1. Materials

The Disodium salt of EDTA, sodium nitrate and potassium ferrocyanide were acquired from Fluka, Germany, and were used without further purification. All the solvents used were of analytical grade only. The liposome vesicles and ionic liquids were acquired from Sigma–Aldrich, India, and were used as such. Phosphate buffer solutions were prepared with the help of sodium phosphate and sodium dihydrogen orthophosphate. All solvents used were of analytical grade. To prepare buffer solutions, sodium phosphate and sodium dihydrogen orthophosphate were used.

2.2. Methods

2.2.1. Preparation of Reductant/Oxidant

The surfactant–cobalt(III) complexes, $\text{cis-}[\text{Co}(\text{ip})_2(\text{C}_{12}\text{H}_{25}\text{NH}_2)_2]^{3+}$, $\text{cis-}[\text{Co}(\text{dpq})_2(\text{C}_{12}\text{H}_{25}\text{NH}_2)_2]^{3+}$ and $\text{cis-}[\text{Co}(\text{dpqc})_2(\text{C}_{12}\text{H}_{25}\text{NH}_2)_2]^{3+}$ used as oxidants were synthesized as reported in our earlier work [40]. The structure of complexes is shown in Scheme 1.



Scheme 1. The structure of surfactant–cobalt(III) complexes.

2.2.2. Nature of the Reaction

On mixing $[\text{Fe}(\text{CN})_6]^{4-}$ and our surfactant–cobalt(III) complexes in the aqueous solution, a precipitate was formed and, therefore, homogeneous kinetic measurements were precluded. However, when $\text{Na}_2\text{H}_2\text{EDTA}$ was present in the solution, no precipitate was formed during the reaction and therefore all the experiments were carried out in the presence of $\text{Na}_2\text{H}_2\text{EDTA}$. A disodium salt of ethylenediamine tetra acetic acid acted as a sequestering agent to eradicate cobalt(II) and prevented the precipitation of the cobalt(II) ion as a hexacyanoferrate salt.

2.2.3. Liposome Preparation

In the present study, unilamellar vesicles (ULV) were used and these were prepared by ethanol injection [41]. A solution of the lipid in ethanol was injected promptly into the buffer with the help of a fine needle and sustained at 50 °C under optimized conditions. The volume of ethanol injected was always <1% *v/v* in order to avoid any damage to the

liposome. This method gave rise to a small unilamellar vesicle (SUV) in the size range of ~15–25 nm [42].

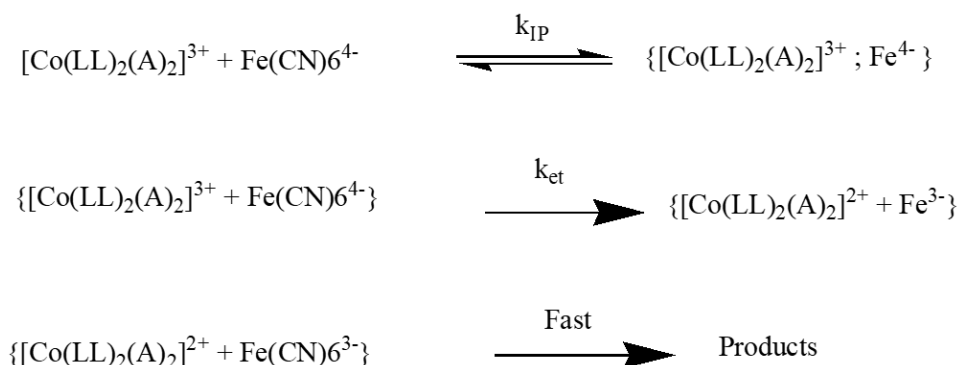
2.2.4. Kinetic Measurements

The rate of the reaction was measured spectrophotometrically using a Shimadzu-1800 UV–Vis. spectrophotometer equipped with a water Peltier system (PCB 150). The temperature was controlled within ± 0.01 °C. A solution containing the desired concentration of potassium ferrocyanide, sodium nitrate, disodium ethylenediamine tetraacetate ($\text{Na}_2\text{H}_2\text{EDTA}$), liposome/ionic liquids in oxygen-free water was placed in a 1 cm cell, which was then covered with a serum cap fitted with a syringe needle. This cell was placed in a thermostated compartment in the spectrophotometer and then the solution containing surfactant–cobalt(III) complexes was added anaerobically using the syringe, and then all increases in the absorbance of the oxidant observed at 470 nm were recorded as a function of time. The ionic strength was maintained at 1.0 mol dm^{-3} in all runs using NaNO_3 . The second-order rate constant, k , for the $[\text{Fe}(\text{CN})_6]^{4-}$ reduction of the cobalt(III) complexes defined by $-\text{d}[\text{Co}(\text{III})]/\text{dt} = k[\text{Co}(\text{III})][\text{Fe}(\text{CN})_6]^{4-}$ was calculated from the concentration of $[\text{Fe}(\text{CN})_6]^{4-}$ and the slope of the pseudo-first-order plot of $\log(A_t - A_\infty)$ versus time plot, which is equal to $-k[\text{Fe}(\text{CN})_6]^{4-}/2.303$, where A_t is the absorbance at time t , A_∞ is the absorbance after all the cobalt(III) complexes have been reduced to cobalt(II), and k is the second-order rate constant. Generally, the value of A_∞ was measured at times corresponding to ten half-lives. All the first-order plots were significantly linear for at least five half-lives, with a correlation coefficient of >0.999 . Each rate constant declared is the average result of triplicate runs. Rate constants attained from consecutive half-life values within a single run agreed to within $\pm 5\%$.

3. Results and Discussion

3.1. Kinetics of Outer-Sphere Electron Transfer Reaction

The reduction of the surfactant–cobalt(III) complexes, $\text{cis-}[\text{Co}(\text{ip})_2(\text{C}_{12}\text{H}_{25}\text{NH}_2)_2]^{3+}$, $\text{cis-}[\text{Co}(\text{dpq})_2(\text{C}_{12}\text{H}_{25}\text{NH}_2)_2]^{3+}$ and $\text{cis-}[\text{Co}(\text{dpqc})_2(\text{C}_{12}\text{H}_{25}\text{NH}_2)_2]^{3+}$ using ferrocyanide ions proceeds to produce aqueous cobalt. This reaction is to be outer-sphere, by comparing the pathway of similar electron transfer reactions reported in the literature [43–46]. In the present study, these cobalt(III) complexes cannot be substituted, due to the non-availability of a coordination site for an inner-sphere precursor complex. The most favorable mechanism for the second-order reaction is an outer-sphere electron transfer process which consists of three elementary steps: ion pair formation (k_{IP}), electron transfer (k_{et}), and product dissociation in Scheme 2.



Scheme 2. Electron transfer reaction of surfactant complexes by ferrocyanide ions. LL = ip, dpq and dpqc; A = Dodecylamine.

3.2. Effect of Electron Transfer Reaction in Vesicles and Ionic Liquid Media

The electron transfer reaction of surfactant–cobalt(III) complexes, $\text{cis-}[\text{Co}(\text{ip})_2(\text{C}_{12}\text{H}_{25}\text{NH}_2)_2]^{3+}$, $\text{cis-}[\text{Co}(\text{dpq})_2(\text{C}_{12}\text{H}_{25}\text{NH}_2)_2]^{3+}$ and $\text{cis-}[\text{Co}(\text{dpqc})_2(\text{C}_{12}\text{H}_{25}\text{NH}_2)_2]^{3+}$ and

ferrocyanide ions in the presence of DPPC and ionic liquid mediums have been examined at different temperatures. The rate constants are provided in Table 1 and Supplementary Information (SI) Tables S1 and S2, and the plots of k against various concentrations of DPPC are shown in Figure 1 and SI Figures S1 and S2. Comparing previous studies of electron transfer in the same liposome vesicles media, results are rather different where some of the reactants had the same charges. In the present system, comprising those of opposite charges, we have ascertained two propensities in the characteristics of the reaction with an increase in the concentration of liposome vesicles as shown in Scheme 3.

Table 1. Second-order rate constants for the reduction of cobalt(III) complex ion by Fe^{2+} in DPPC medium under various temperatures; $\text{cis-}[\text{Co}(\text{ip})_2(\text{C}_{12}\text{H}_{25}\text{NH}_2)_2](\text{ClO}_4)_3 = 4 \times 10^{-4} \text{ mol dm}^{-3}$, $\mu = 1.0 \text{ mol dm}^{-3}$, $[\text{Fe}(\text{CN})_6]^{4-} = 0.01 \text{ mol dm}^{-3}$.

[DPPC] $\times 10^5$ (mol dm^{-3})	$k \times 10^2, \text{ dm}^3 \text{ mol}^{-1} \text{ s}^{-1}$					
	298 K	303 K	308 K	323 K	328 K	333 K
2.0	15.0	15.2	15.5	16.4	16.8	17.3
3.0	14.7	15.0	15.4	17.0	17.5	18.0
4.0	14.0	14.4	15.0	17.2	17.8	18.2
5.0	13.5	13.9	14.1	17.7	18.3	18.7
6.0	12.7	13.0	13.4	18.3	18.6	19.1
7.0	11.3	11.7	12.5	18.7	19.1	19.5

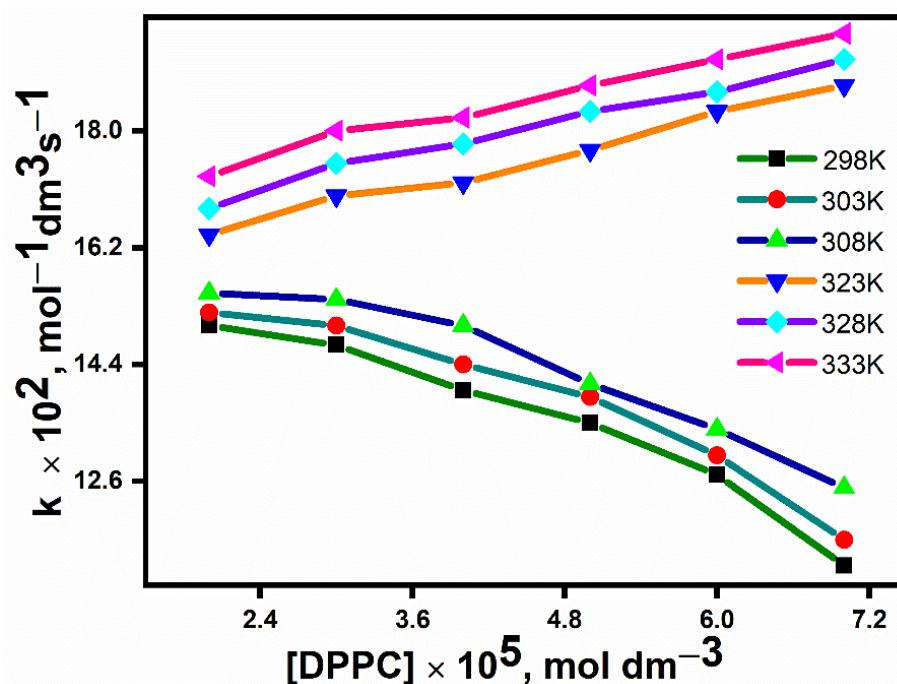
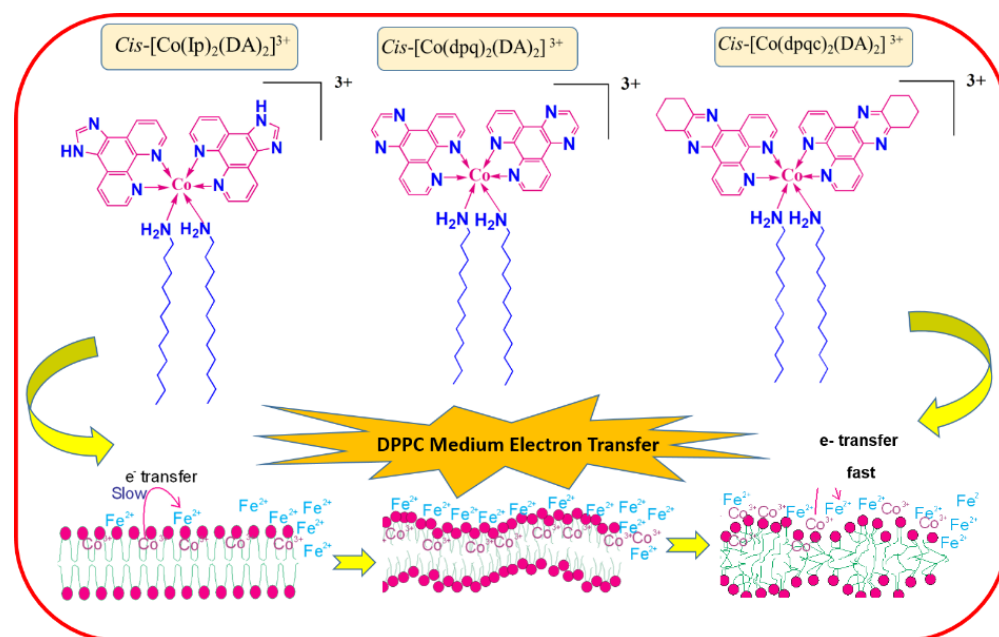


Figure 1. Plot of k against DPPC for $\text{cis-}[\text{Co}(\text{ip})_2(\text{C}_{12}\text{H}_{25}\text{NH}_2)_2](\text{ClO}_4)_3$ under various temperatures; $\text{cis-}[\text{Co}(\text{ip})_2(\text{C}_{12}\text{H}_{25}\text{NH}_2)_2](\text{ClO}_4)_3 = 4 \times 10^{-4} \text{ mol dm}^{-3}$, $\mu = 1.0 \text{ mol dm}^{-3}$, $[\text{Fe}(\text{CN})_6]^{4-} = 0.01 \text{ mol dm}^{-3}$.



Scheme 3. DDPC-mediated ETR of surfactant–cobalt(III) complexes.

3.2.1. Effect of DPPC

Because of its amphiphilic nature, DPPC undergoes spontaneous aggregation in aqueous solutions. This leads to the formation of a three-dimensional closed bilayer structure known as a vesicle [47]. When the temperature is increased, these vesicles of DPPC undergo phase transitions at 40 °C [48], from the gel phase to the liquid crystalline phase. The effect of DPPC vesicles (2.0×10^{-5} to 7.0×10^{-5} mol dm⁻³) on the kinetics of outer-sphere electron transfer between the surfactant–cobalt(III) complexes *cis*-[Co(ip)₂(C₁₂H₂₅NH₂)₂]³⁺, *cis*-[Co(dpq)₂(C₁₂H₂₅NH₂)₂]³⁺ and *cis*-[Co(dpqc)₂(C₁₂H₂₅NH₂)₂]³⁺ and [Fe(CN)₆]⁴⁻ has been investigated at various temperatures. As we have used the ethanol injection method, the reaction medium of these electron transfer reactions should contain only unilamellar vesicles. We observed two trends in the behavior of the rate constants with varying concentrations of DPPC. Below the phase transition temperature, the rate constants decrease with increasing DPPC, whereas above this temperature the rate constants increase with DPPC. These trends were observed for both the surfactant–cobalt(III) complexes used in the present study. It is well known that when a surfactant is added to an aqueous medium containing lipid membranes, the interaction between surfactant and lipids takes place in three ways: part of the added surfactant is inserted into the outer membrane leaflet; the surfactant molecules equilibrate between the outer and inner leaflets of the vesicle; and the inner leaflet equilibrates with the interior of the vesicle [49,50]. Below the phase transition temperature, the lipid is very rigid (Scheme 3), so our surfactant–metal complexes are tightly bound to the membrane DPPC, mostly at the inner membrane leaflet. As the concentration of DPPC is increased, more of the surfactant–cobalt(III) complex will be accumulated into the DPPC interior, whereas [Fe(CN)₆]⁴⁻ will be at the outer surface, so the rate constant decreases (Table 1 and SI Tables S1 and S2). However, beyond the phase transition temperature, the rigidity of the DPPC membrane is low; so when the concentration of DPPC is increased, more of the surfactant–cobalt(III) complex molecules will move from the membrane interior to the outer surface where the concentration of [Fe(CN)₆]⁴⁻ is also high, causing the rate constant to increase. Additionally, the phase transition may favorably affect the reorganization energies and the free energy barrier associated with electron transfer [51]. As a result, the higher hydrophobicity of complex *Cis*-[Co(ip)₂(C₁₂H₂₅NH₂)₂]³⁺ gives a higher second-order rate constant compared to *Cis*-[Co(dpq)₂(C₁₂H₂₅NH₂)₂]³⁺ which is, in turn, higher than that of *Cis*-[Co(dpqc)₂(C₁₂H₂₅NH₂)₂]³⁺.

3.2.2. Effect of Ionic Liquids

The electron transfer reaction of the same complexes in the presence of ionic liquids has been studied. The effect of ionic liquid mediums on the kinetics of electron transfer regarding the oxidants and ferrocyanide ions has been examined at different temperatures. The observed second-order rate constants are given in Table 2 and SI Tables S3 and S4 and the plot of k against various concentrations of ionic liquids is shown in Figure 2 and SI Figures S3 and S4 for the above reaction, at various temperatures. As seen from these tables, the rate constant of the reaction continues to increase with an increase in the concentration of ionic liquids from 1.4×10^{-3} to 2.6×10^{-3} mol dm⁻³. As the cation of the ionic liquid used has an inherent amphiphilicity, it can interact with the long aliphatic double chain of the surfactant–cobalt(III) complexes, meaning that the specific structures before and after aggregation consist of well-aligned cation–anion aggregates. In the initial aggregation, the surfactant complexes and [Fe(CN)₆]⁴⁻ ions were far apart from the ionic liquid pool, so the rate constant did not increase significantly. After aggregation, the surfactant complexes and [Fe(CN)₆]⁴⁻ ions moved toward the “ionic liquids pool” surface. As a result of charge neutralization or charge creation, a marginal contribution to the activation volume is expected. Thus, the ionic liquids consisting of charged ions should be energetically favored, which could lead to an increase in the reaction rate with increasing concentrations of ionic liquid reactants existing in small volumes, leading to a higher rate and lower activation energy. This aggregation leads to higher local concentration of reactants leading to an increase in the rate of the reaction. Hence, the rate of the outer-sphere electron transfer reaction of the present study increases with an increase in the concentration of the ionic liquid. As changes in amphiphilicity of the transition state can cause large effects in terms of electrostriction/solvation in ionic liquids [52], the ionic liquid mediums facilitates more aggregation of the surfactant–cobalt(III) complexes, which increases with an increase in the concentration of the ionic liquid. As seen from Table 2 and SI Tables S3 and S4, the rate constant values of the surfactant–cobalt(III) complexes (Figure 2 and SI Figures S3 and S4) of the present study are very much different from one another. This difference in the rate constant values between the surfactant–cobalt(III) complexes of the present study are explained as follows: the rate constant value of the surfactant–cobalt(III) complexes containing ip and dpq ligands is lower than that of the corresponding surfactant–cobalt(III) complexes containing dpqc ligands in all the initial concentrations studied. Due to high hydrophobicity of dpqc-ligands-containing complex, the numbers of micelles formed from these complex molecules are more than those of ip- and dpq-containing complexes at the same concentration values. Hence, dpqc-containing complexes enhance the overall rate of the reaction. Among these surfactant–cobalt(III) complexes containing ip, dpq and dpqc ligands, the rate constant values of the dpqc complexes are the highest due to the greater hydrophobicity of the ligand. In the previous reports [36] of the electron transfer reaction in this media with Fe²⁺, it was established that amphiphilicity influenced the reaction rates. On comparing the previous reports of rate constant to those of the present study, the reaction rate is increased due to the increase in size of the amine ligand which increases the amphiphilicity of the oxidants which speeds up aggregation, leading to higher reaction rates of the outer sphere.

Table 2. Second-order rate constants for the reduction of cobalt(III) complex ion by Fe^{2+} in the presence of [BMIM]Br under various temperatures; $\text{cis-}[\text{Co}(\text{ip})_2(\text{C}_{12}\text{H}_{25}\text{NH}_2)_2](\text{ClO}_4)_3 = 4 \times 10^{-4} \text{ mol dm}^{-3}$, $\mu = 1.0 \text{ mol dm}^{-3}$, $[\text{Fe}(\text{CN})_6]^{4-} = 0.01 \text{ mol dm}^{-3}$.

[BMIM]Br $\times 10^3$, mol dm $^{-3}$	$k \times 10^2$, dm $^{-3}$ mol $^{-1}$ s $^{-1}$					
	298 K	303 K	308 K	313 K	318 K	323 K
1.4	4.0	4.2	6.5	8.9	14.7	23.0
1.6	5.2	5.5	7.7	12.0	20.6	27.4
1.8	6.1	7.4	8.5	25.5	31.5	33.7
2.0	6.5	9.4	15.5	28.6	34.8	55.4
2.2	10.5	15.2	21.3	32.1	45.3	63.7
2.4	11.4	20.2	24.2	35.2	58.2	77.2
2.6	11.6	21.2	25.6	36.2	59.6	80.4

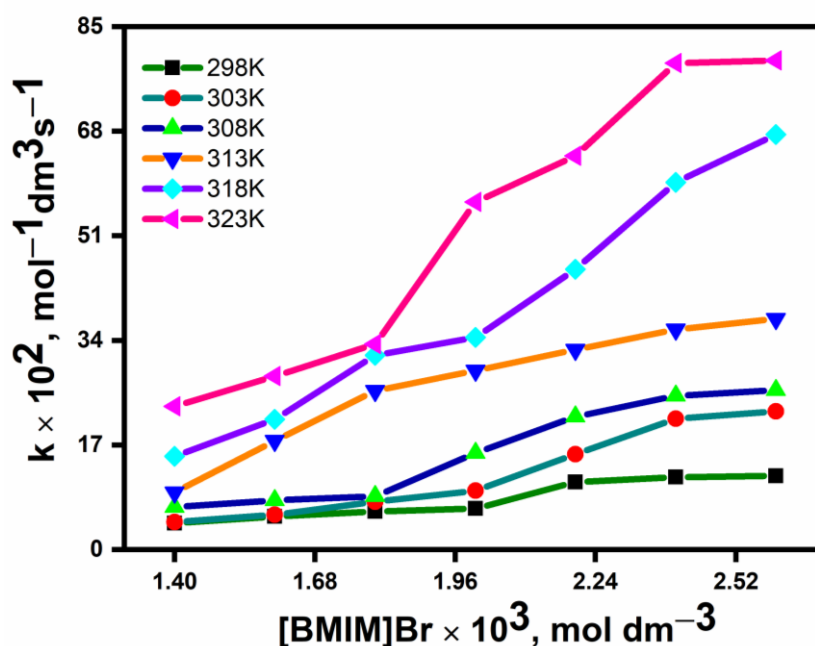


Figure 2. Plot of k against [BMIM]Br for $\text{cis-}[\text{Co}(\text{ip})_2(\text{C}_{12}\text{H}_{25}\text{NH}_2)_2](\text{ClO}_4)_3$ at various temperatures; $\text{cis-}[\text{Co}(\text{ip})_2(\text{C}_{12}\text{H}_{25}\text{NH}_2)_2](\text{ClO}_4)_3 = 4 \times 10^{-4} \text{ mol dm}^{-3}$, $\mu = 1.0 \text{ mol dm}^{-3}$, $[\text{Fe}(\text{CN})_6]^{4-} = 0.01 \text{ mol dm}^{-3}$.

3.3. Oxidants with Self-Aggregation-Forming Capacity

The self-aggregation of each complex indicates its respective self-aggregation forming capacity. Lower critical micelle concentration value indicates higher aggregation-forming capacity. The difference in the self-aggregation between various surfactant–cobalt(III) complexes in the present study (Table 2 and SI Tables S3 and S4) are explained as follows: for all types of complexes, it has been observed that the critical micelle concentration value of each double-chain oxidant is lower than the respective single-chain surfactant complexes. The CMC value of each of the surfactant–cobalt(III) complex is lower than the respective single-chain surfactant complexes. Because of these extending the aromaticity of ligands, the oxidants become more aggregated, which increases the possibility of these oxidants forming self-aggregation. The order of aggregation-forming capacity of the oxidants is as follows: $\text{Cis-}[\text{Co}(\text{ip})_2(\text{C}_{12}\text{H}_{25}\text{NH}_2)_2]^{3+} < \text{Cis-}[\text{Co}(\text{dpq})_2(\text{C}_{12}\text{H}_{25}\text{NH}_2)_2]^{3+} < \text{Cis-}[\text{Co}(\text{dpqc})_2(\text{C}_{12}\text{H}_{25}\text{NH}_2)_2]^{3+}$.

3.4. Activation Parameters

The effect of temperature on the rate was studied at 298, 303, 308, 313, 318, and 323 K for all rate constant tables for DPPC and ionic liquid mediums in order to obtain the activation parameters for the reaction of oxidants and the reductant of ferrocyanide ions. Figure 2 and SI Figures S3 and S4 show that increasing the temperature rate constant increases in ionic liquids, and Figure 1 and SI Figures S1 and S2 show that increasing the temperature (above phase transition) increases the reaction rate, while it decreases the reaction rate of electron transfer reactions in DPPC at below-phase-transition temperatures.

3.5. Isokinetic Plots

In order to investigate the change in the mechanistic pathway of the OET with respect to the change in the concentration of liposome vesicles and ionic liquids at different phase transitions of oxidants, from the transition state theory [53,54], the values of entropy and enthalpy were determined by plotting $\ln(k/T)$ versus $1/T$, and the plots are shown in Figures 3 and 4 and SI Figures S5–S8. The ΔS^\ddagger and ΔH^\ddagger values obtained are shown in Tables 3 and 4 and SI Tables S5–S8. As seen from these tables, the value of entropy is positive for all the reactions in both media, testifying that the formation of activated complexes is endothermic. In ionic liquids and liposome media, the entropy values are found to be negative in directions and in all the concentrations of oxidants used, indicative of a more ordered structure of the transition state. This is consistent with a model in which the oxidant and reductant bind to the liposome in the transition state. In such a case, the transition state complex attracts the surrounding water molecules, with the positive and negative charges of the ion pair leading to loss of freedom of the solvent molecules in the transition state [31]. In order to check for any change in the mechanism occurring during the electron transfer reaction with respect to the change in concentration of liposome and ionic liquids of oxidants, we have calculated the entropy and enthalpy and made isokinetic plots for the electron transfer reactions of the oxidants under study. The linearity of the plot of entropy of activation versus enthalpy of activation (Figures 5 and 6 and SI Figures S9–S12) establishes the existence of a common mechanism with respect to the change in the initial concentration of oxidants.

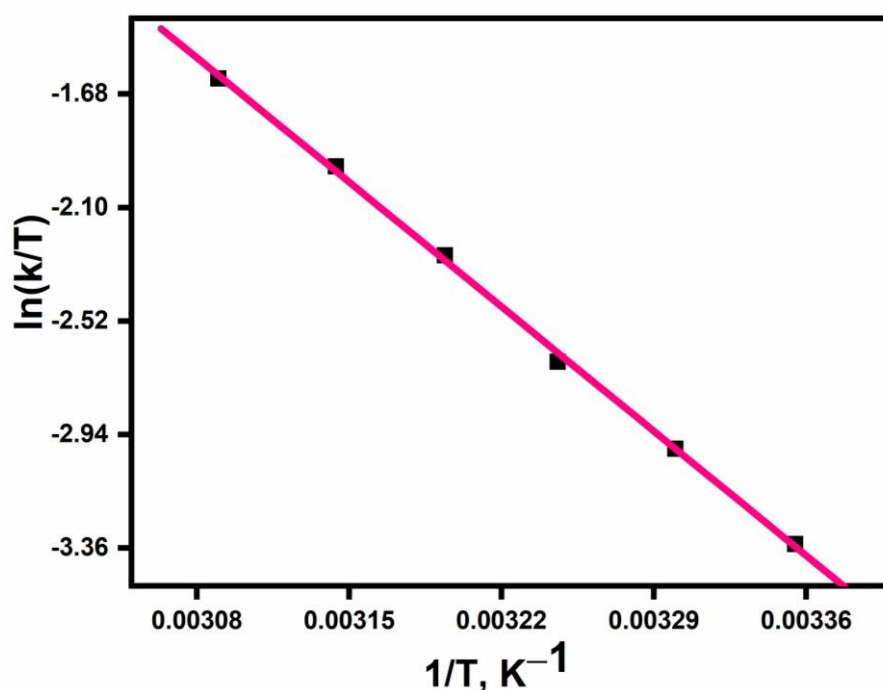


Figure 3. Eyring plot for $\text{cis-}[\text{Co}(\text{ip})_2(\text{C}_{12}\text{H}_{25}\text{NH}_2)_2](\text{ClO}_4)_3$ in DPPC medium. $[\text{Complex}] = 4 \times 10^{-4} \text{ mol dm}^{-3}$; $[\text{Fe}^{2+}] = 0.01 \text{ mol dm}^{-3}$; $[\mu] = 1.0 \text{ mol dm}^{-3}$.

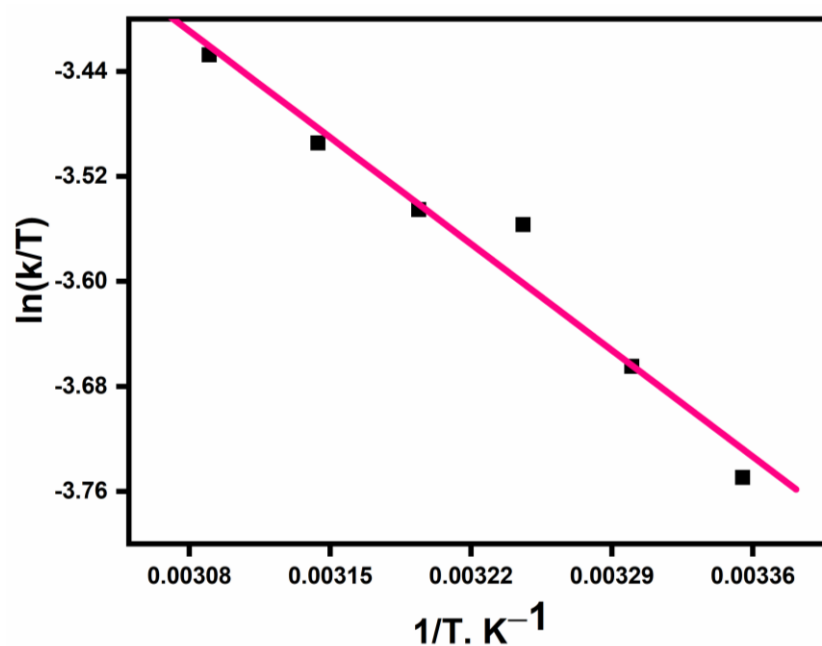


Figure 4. Eyring plot for $\text{cis-}[\text{Co}(\text{ip})_2(\text{C}_{12}\text{H}_{25}\text{NH}_2)_2](\text{ClO}_4)_3$ in $[\text{BMIM}]\text{Br}$ medium. $[\text{Complex}] = 4 \times 10^{-4} \text{ mol dm}^{-3}$; $[\text{Fe}(\text{CN})_6]^{4-} = 0.01 \text{ mol dm}^{-3}$; $[\mu] = 1.0 \text{ mol dm}^{-3}$.

Table 3. Activation parameters for the reduction of $\text{cis-}[\text{Co}(\text{ip})_2(\text{C}_{12}\text{H}_{25}\text{NH}_2)_2](\text{ClO}_4)_3$, $\mu = 1.0 \text{ mol dm}^{-3}$ in DPPC medium.

$[\text{DPPC}] \times 10^5$ (mol dm^{-3})	ΔH^\ddagger	$-\Delta S^\ddagger$
2.0	0.14	218.2
3.0	0.37	212.1
4.0	0.67	204.3
5.0	0.99	195.7
6.0	1.38	185.6
7.0	2.03	168.4

Entropy and Enthalpy of activation is symbolized ΔS^\ddagger and ΔH^\ddagger .

Table 4. Activation parameters for the reduction of $\text{cis-}[\text{Co}(\text{ip})_2(\text{C}_{12}\text{H}_{25}\text{NH}_2)_2](\text{ClO}_4)_3$, $\mu = 1.0 \text{ mol dm}^{-3}$ in $[\text{BMIM}]\text{Br}$ medium.

$[\text{BMIM}]\text{Br} \times 10^3$, mol dm^{-3}	ΔH^\ddagger	$-\Delta S^\ddagger$
1.4	6.62	50.2
1.6	6.56	49.7
1.8	6.57	42.1
2.0	6.67	35.0
2.2	6.79	34.7
2.4	7.26	24.2
2.6	7.96	7.3

Entropy and Enthalpy of activation is symbolized ΔS^\ddagger and ΔH^\ddagger .

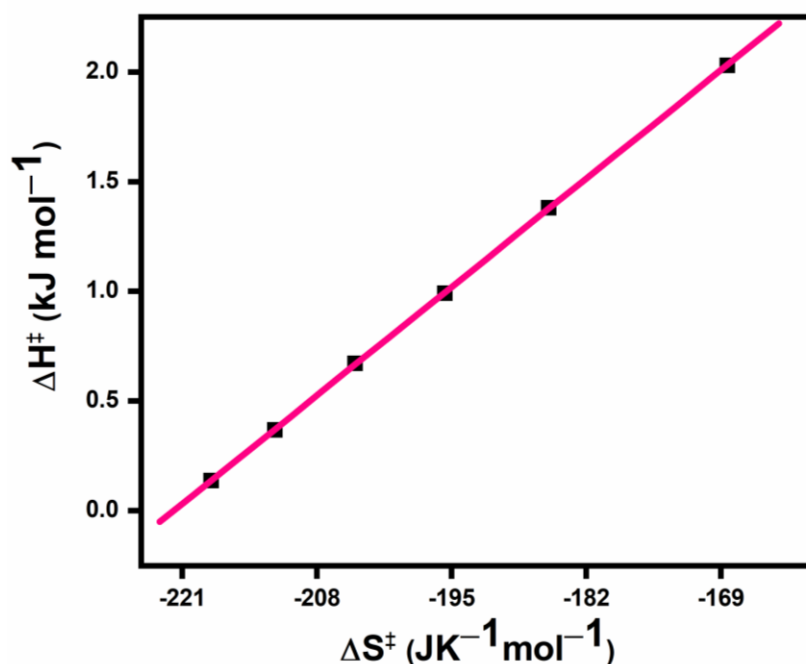


Figure 5. Isokinetic plot of the activation parameters for the reduction of cis-[Co(ip)₂(C₁₂H₂₅NH₂)₂](ClO₄)₃ by ion(II) in DPPC medium. [Complex] = 4×10^{-4} mol dm⁻³; [Fe²⁺] = 0.01 mol dm⁻³; [μ] = 1.0 mol dm⁻³. (Entropy and Enthalpy of activation is symbolized ΔS^\ddagger and ΔH^\ddagger).

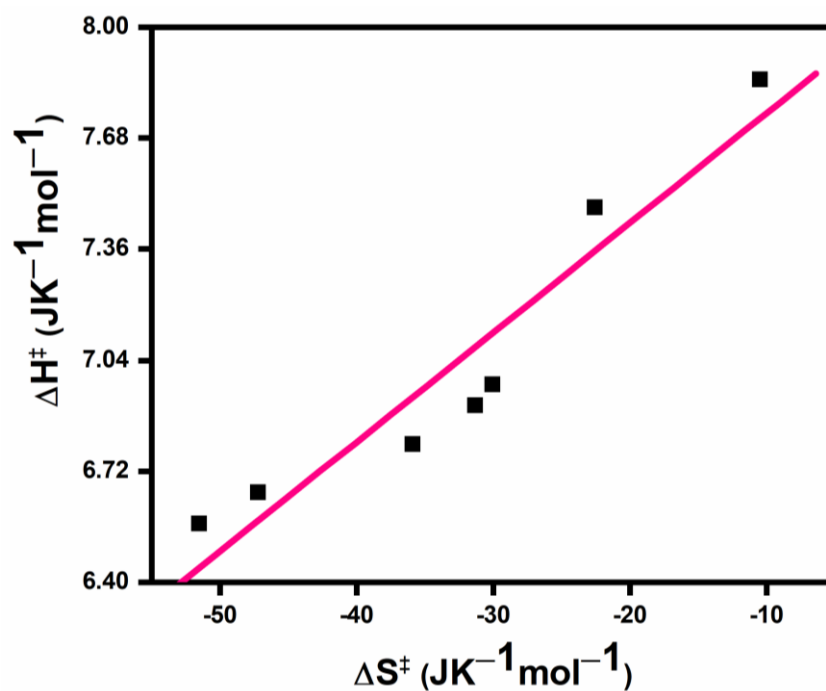


Figure 6. Isokinetic plot of the activation parameters for the reduction of cis-[Co(ip)₂(C₁₂H₂₅NH₂)₂](ClO₄)₃ by ion(II) in [BMIM]Br medium. [Complex] = 4×10^{-4} mol dm⁻³; [Fe(CN)₆]⁴⁻ = 0.01 mol dm⁻³; [μ] = 1.0 mol dm⁻³. (Entropy and Enthalpy of activation is symbolized ΔS^\ddagger and ΔH^\ddagger).

4. Conclusions

In this report, the kinetics of the outer-sphere electron transfer reaction between surfactant–cobalt(III) complexes and [Fe(CN)₆]⁴⁻ in DPPC and ionic liquids were studied.

In DPPC liposome media, it was revealed that below the phase transition temperature, the rate decreases with increasing concentration of DPPC, which is explained by the accumulation of these surfactant–cobalt(III) complexes inside the vesicles through hydrophobic effects. Above the phase transition temperature, the rate increased with increasing concentration of DPPC, which may be due to the release of the cobalt(III) complexes from the interior to the exterior surface of the DPPC membrane. In ionic liquids media, the corresponding increase in rate constant with the increase in the concentration of ionic liquids is due to inherent amphiphilicity of (BMIM)Br which can interact with the long aliphatic chain of the surfactant–cobalt(III) complexes, therefore, the ionic liquids facilitate some aggregation of the surfactant–cobalt(III) complexes. On comparative study of the electron transfer involving ferrocyanide anion and iron(II) as reductants with the same oxidants, the rate constants involving ferrocyanide anion are higher for each of the surfactant–cobalt(III) complexes due to the good π -accepting character of ferrocyanide anion compared to iron(II). We provided the isokinetic plots for the *Cis*-[Co(ip)₂(C₁₂H₂₅NH₂)₂]³⁺, [Co(dpq)₂(C₁₂H₂₅NH₂)₂]³⁺ and [Co(dpqc)₂(C₁₂H₂₅NH₂)₂]³⁺ complexes regarding ionic liquids and DPPC vesicles.

Supplementary Materials: The following supporting information can be downloaded at: <https://www.mdpi.com/article/10.3390/biomimetics7040221/s1>, Figure S1: Plot of k against DPPC for *Cis*-[Co(dpq)₂(C₁₂H₂₅NH₂)₂](ClO₄)₃ under various temperatures; *cis*-[Co(ip)₂(C₁₂H₂₅NH₂)₂](ClO₄)₃ = 4 × 10^{−4} mol dm^{−3}, μ = 1.0 mol dm^{−3}, [Fe(CN)₆^{4−}] = 0.01 mol dm^{−3}; Figure S2: Plot of k against DPPC for *Cis*-[Co(dpqc)₂(C₁₂H₂₅NH₂)₂](ClO₄)₃ under various temperatures; *cis*-[Co(ip)₂(C₁₂H₂₅NH₂)₂](ClO₄)₃ = 4 × 10^{−4} mol dm^{−3}, μ = 1.0 mol dm^{−3}, [Fe(CN)₆^{4−}] = 0.01 mol dm^{−3}; Figure S3: Plot of k against [BMIM]Br for *Cis*-[Co(dpq)₂(C₁₂H₂₅NH₂)₂](ClO₄)₃ at various temperatures; *Cis*-[Co(ip)₂(C₁₂H₂₅NH₂)₂](ClO₄)₃ = 4 × 10^{−4} mol dm^{−3}, μ = 1.0 mol dm^{−3}, [Fe(CN)₆^{4−}] = 0.01 mol dm^{−3}; Figure S4: Plot of k against [BMIM]Br for *Cis*-[Co(dpqc)₂(C₁₂H₂₅NH₂)₂](ClO₄)₃ at various temperatures; *Cis*-[Co(ip)₂(C₁₂H₂₅NH₂)₂](ClO₄)₃ = 4 × 10^{−4} mol dm^{−3}, μ = 1.0 mol dm^{−3}, [Fe(CN)₆^{4−}] = 0.01 mol dm^{−3}; Figure S5: Eyring plot for *Cis*-[Co(dpq)₂(C₁₂H₂₅NH₂)₂](ClO₄)₃ in DPPC medium. [complex] = 4 × 10^{−4} mol dm^{−3}; [Fe(CN)₆^{4−}] = 0.01 mol dm^{−3}; [μ] = 1.0 mol dm^{−3}; Figure S6: Eyring plot for *Cis*-[Co(dpqc)₂(C₁₂H₂₅NH₂)₂](ClO₄)₃ in DPPC medium. [complex] = 4 × 10^{−4} mol dm^{−3}; [Fe(CN)₆^{4−}] = 0.01 mol dm^{−3}; [μ] = 1.0 mol dm^{−3}; Figure S7: Eyring plot for *Cis*-[Co(dpq)₂(C₁₂H₂₅NH₂)₂](ClO₄)₃ in [BMIM]Br medium. [complex] = 4 × 10^{−4} mol dm^{−3}; [Fe(CN)₆^{4−}] = 0.01 mol dm^{−3}; [μ] = 1.0 mol dm^{−3}; Figure S8: Eyring plot for *Cis*-[Co(dpqc)₂(C₁₂H₂₅NH₂)₂](ClO₄)₃ in [BMIM]Br medium. [complex] = 4 × 10^{−4} mol dm^{−3}; [Fe(CN)₆^{4−}] = 0.01 mol dm^{−3}; [μ] = 1.0 mol dm^{−3}; Figure S9: Isokinetic plot of the activation parameters for the reduction of *Cis*-[Co(dpq)₂(C₁₂H₂₅NH₂)₂](ClO₄)₃ by ion(II) in DPPC medium. [complex] = 4 × 10^{−4} mol dm^{−3}; [Fe²⁺] = 0.01 mol dm^{−3}; [μ] = 1.0 mol dm^{−3}; Figure S10: Isokinetic plot of the activation parameters for the reduction of *Cis*-[Co(dpqc)₂(C₁₂H₂₅NH₂)₂](ClO₄)₃ by ion(II) in aqueous solutions. [complex] = 4 × 10^{−4} mol dm^{−3}; [Fe(CN)₆^{4−}] = 0.01 mol dm^{−3}; [μ] = 1.0 mol dm^{−3}; Figure S11: Isokinetic plot of the activation parameters for the reduction of *Cis*-[Co(dpq)₂(C₁₂H₂₅NH₂)₂](ClO₄)₃ by ion(II) in [BMIM]Br medium. [complex] = 4 × 10^{−4} mol dm^{−3}; [Fe(CN)₆^{4−}] = 0.01 mol dm^{−3}; [μ] = 1.0 mol dm^{−3}; Figure S12: Isokinetic plot of the activation parameters for the reduction of *Cis*-[Co(dpqc)₂(C₁₂H₂₅NH₂)₂](ClO₄)₃ by ion(II) in [BMIM]Br medium. [complex] = 4 × 10^{−4} mol dm^{−3}; [Fe(CN)₆^{4−}] = 0.01 mol dm^{−3}; [μ] = 1.0 mol dm^{−3}; Table S1: Second-order rate constants for the reduction of cobalt(III) complex ion by Fe²⁺ in DPPC under various temperatures. *Cis*-[Co(dpq)₂(C₁₂H₂₅NH₂)₂](ClO₄)₃ = 4 × 10^{−4} mol dm^{−3}, μ = 1.0 mol dm^{−3}, [Fe(CN)₆^{4−}] = 0.01 mol dm^{−3}; Table S2: Second-order rate constants for the reduction of cobalt(III) complex ion by Fe²⁺ in DPPC under various temperatures. *Cis*-[Co(dpqc)₂(C₁₂H₂₅NH₂)₂](ClO₄)₃ = 4 × 10^{−4} mol dm^{−3}, μ = 1.0 mol dm^{−3}, [Fe(CN)₆^{4−}] = 0.01 mol dm^{−3}; Table S3: Second-order rate constants for the reduction of cobalt(III) complex ion by Fe²⁺ in the presence of [BMIM]Br medium under various temperatures. *Cis*-[Co(dpq)₂(C₁₂H₂₅NH₂)₂](ClO₄)₃ = 4 × 10^{−4} mol dm^{−3}, μ = 1.0 mol dm^{−3}, [Fe(CN)₆^{4−}] = 0.01 mol dm^{−3}; Table S4: Second-order rate constants for the reduction of cobalt(III) complex ion by Fe²⁺ in the presence of [BMIM]Br medium under various temperatures. *Cis*-[Co(dpqc)₂(C₁₂H₂₅NH₂)₂](ClO₄)₃ = 4 × 10^{−4} mol dm^{−3}, μ = 1.0 mol dm^{−3}, [Fe(CN)₆^{4−}] = 0.01 mol dm^{−3}; Table S5: Activation parameters for the reduction of *Cis*-[Co(dpq)₂(C₁₂H₂₅NH₂)₂](ClO₄)₃, μ = 1.0 mol dm^{−3} in DPPC medium; Table S6: Activation parameters for the reduction of *Cis*-[Co(dpqc)₂(C₁₂H₂₅NH₂)₂](ClO₄)₃, μ = 1.0 mol dm^{−3} in DPPC medium; Table S7: Activation pa-

rameters for the reduction of Cis-[Co(dpq)₂(C₁₂H₂₅NH₂)₂](ClO₄)₃, $\mu = 1.0 \text{ moldm}^{-3}$ in [BMIM]Br medium; Table S8: Activation parameters for the reduction of Cis-[Co(dpqc)₂(C₁₂H₂₅NH₂)₂](ClO₄)₃, $\mu = 1.0 \text{ moldm}^{-3}$ in [BMIM]Br medium.

Author Contributions: All the authors have contributed equally. All authors have read and agreed to the published version of the manuscript.

Funding: This research received no external funding.

Institutional Review Board Statement: Not applicable.

Data Availability Statement: Not applicable.

Acknowledgments: The authors are grateful to the Ankleshwar Rotary Education Society, are managing Shroff S R Rotary Institute of Chemical Technology (SRICT) and SRICT-Institute of Science and Research (SRICT-ISR) for providing lab facilities and equipment to perform this study. K. Nagaraj thanks to Provost, Dean and UPL University (SRICT-Institute of Science and Research) Management.

Conflicts of Interest: The authors declare no conflict of interest financial or otherwise.

References

- Rosen, M.J. *Surfactants and Interfacial Phenomena*; Wiley: New York, NY, USA, 1978.
- McBain, J.W.; Heath, D.C. *Handbook of Surface and Colloid Chemistry*; CRC Press: Boca Raton, FL, USA, 2003.
- Tanford, C. *The Hydrophobic Effect: Formation of Micelles and Biological Membranes*; Wiley-Interscience: New York, NY, USA, 1973.
- Fendler, J.H.; Fendler, E.J. *Catalysis in Micellar and Macromolecular Systems*; Academic Press: New York, NY, USA, 1975.
- Babich, O.A.; Gould, E.S. Electron transfer. Part 148. Reactions of corrin-bound cobalt(III) with s² metal-ion reducing centers. *Inorg. Chim. Acta* **2002**, *336*, 80–86. [CrossRef]
- Walker, G.W.; Geue, R.J.; Sargeson, A.M.; Behm, C.A. Surface-active cobalt cage complexes: Synthesis, surface chemistry, biological activity, and redox properties. *J. Chem. Soc. Dalton Trans.* **2003**, *15*, 2992. [CrossRef]
- Szaciłowski, K. Molecular Logic Gates Based on Pentacyanoferrate Complexes: From Simple Gates to Three-Dimensional Logic Systems. *Eur. J.* **2004**, *10*, 2520. [CrossRef] [PubMed]
- Pfeiffer, J.; Kirchner, K.; Wherland, S. Extensive inhibition by ion pairing in a bimolecular, outer-sphere electron transfer reaction, reduction of a cobalt clathrochelate by ferrocene in methylene chloride. *Inorg. Chim. Acta* **2001**, *313*, 37. [CrossRef]
- Gaswick, D.; Haim, A. Direct measurement of a first-order rate constant for an elementary electron transfer step. *J. Am. Chem. Soc.* **1971**, *93*, 7347–7348. [CrossRef]
- Miralles, A.J.; Szecsy, A.P.; Haim, A. Electron-transfer reactions of ion pairs: Reductions of various substituted pyridinepentaaminocobalt(III) complexes by hexacyanoferrate(II). *Inorg. Chem.* **1982**, *21*, 697–699. [CrossRef]
- Rillema, P.; Endicott, J.F.; Patel, R.C. Outer-sphere electron-transfer reactions of macrocyclic complexes of cobalt(III). Critical assessment of linear free energy relations. *J. Am. Chem. Soc.* **1972**, *94*, 394–401. [CrossRef]
- van Eldik, R.; Kelm, H. Concerning the pressure dependence of outer-sphere electron-transfer reactions: The reduction of Co(NH₃)₅OH³⁺ by Fe(CN)₆⁴⁻ in aqueous acidic solution. *Inorg. Chim. Acta.* **1982**, *73*, 91. [CrossRef]
- Kustin, K.; Epstein, I.R.; Simoyi, R.H. Systematic design of chemical oscillators. Part 56. Kinetics and mechanism of the oxidation of hexacyanoferrate(II) by aqueous bromine. *J. Chem. Soc. Dalton Trans.* **1990**, 971–975. [CrossRef]
- Larsson, R. Classification of glyceride crystal forms. *Acta. Chem. Scand.* **1967**, *21*, 257. [CrossRef]
- Mustafina, A.R.; Shtyrin, V.G.; Zakharova, L.Y.; Skripacheva, V.V.; Zairov, R.R.; Soloreva, S.E.; Antipen, I.S.; Kononov, A.I. The outer-sphere association of p-sulfonatothiacalix[4]arene with some Co(III) complexes: The effect on their redox activity in aqueous solutions. *J. Incl. Phenom. Macrocycl. Chem.* **2007**, *29*, 25. [CrossRef]
- Miralles, A.J.; Armstrong, R.E.; Haim, A. The outer-sphere reductions of pyridinepentaaminocobalt(III) and pyridinepentaamineruthenium(III) by hexacyanoferrate(II). *J. Am. Chem. Soc.* **1977**, *99*, 1416–1420. [CrossRef]
- Holder, A.A.; Dasgupta, T.P. Kinetics and mechanism of the reduction of the molybdato-pentaaminocobalt(III) ion by aqueous sulfite and aqueous potassium hexacyanoferrate(II). *Inorg. Chim. Acta* **2002**, *331*, 279. [CrossRef]
- Szecsy, A.P.; Haim, A.J. Intramolecular electron transfer from pentacyanoferrate(II) to pentaaminocobalt(III) via an imidazolate bridge. The role of distance in inner-sphere reactions. *Am. Chem. Soc.* **1981**, *103*, 1679.
- Jwo, J.J.; Gaus, P.L.; Haim, A. Intramolecular electron transfer from pentacyanoferrate(II) to pentaaminocobalt(III) mediated by various 4,4'-bipyridines. *J. Am. Chem. Soc.* **1979**, *101*, 6189–6197. [CrossRef]
- Martinez, M.; Pitarque, M.A.; Eldik, R.V. Outer-sphere redox reactions of (N)5-macrocyclic cobalt(III) complexes. A temperature and pressure dependence kinetic study on the influence of size and geometry of different macrocycles. *Inorg. Chim. Acta* **1997**, *256*, 51. [CrossRef]
- Tavernier, H.L.; Barzykin, A.V.; Tachiya, M.; Fayer, M.D. Solvent reorganization energy and free energy change for donor/acceptor electron transfer at micelle surfaces: Theory and experiment. *J. Phys. Chem. B* **1998**, *102*, 6078–6088. [CrossRef]

22. Hammarstrom, L.; Norrby, T.; Stenhangen, G.; Martensson, J.; Akermark, B.; Almgren, M.J. Two-dimensional emission quenching and charge separation using a Ru(II)-photosensitizer assembled with membrane-bound acceptors. *Phys. Chem. B* **1997**, *101*, 7494. [CrossRef]
23. Wang, X.L.; Chao, H.; Li, H.; Hong, X.L.; Liu, Y.J.; Tan, L.F.; Ji, L.N. DNA interactions of cobalt(III) mixed-polypyridyl complexes containing asymmetric ligands. *J. Inorg. Biochem.* **2004**, *98*, 1143. [CrossRef]
24. Ji, L.N.; Zou, X.H.; Liu, J.G. Shape and enantioselective interaction of Ru(II)/Co(III) polypyridyl complexes with DNA. *Coord. Chem. Rev.* **2001**, *513*, 216–217. [CrossRef]
25. Srinivasan, S.; Annaraj, J.; Athappan, P.R. Spectral and redox studies on mixed ligand complexes of cobalt(III) phenanthroline/bipyridyl and benzoylhydrazones, their DNA binding and antimicrobial activity. *J. Inorg. Biochem.* **2005**, *99*, 876–882. [CrossRef] [PubMed]
26. Predo-Gotor, R.; Jimenez, R.; Lopez, P.; Perez, C.; Gomez-Herrera, F.; Sanchez, F. Micellar effects upon the reaction between acetonitrile pentacyanoferrate(II) and Bi s(ethylenediammine)(2-pyrazinecarboxylato)cobalt(III). *Langmuir* **1998**, *14*, 1539. [CrossRef]
27. Cameron, P.J.; Peter, L.M.; Zakeeruddin, S.M.; Gratzel, M. Electrochemical studies of the Co(III)/Co(II)(dbbip) 2 redox couple as a mediator for dye-sensitized nanocrystalline solar cells. *Coord. Chem. Rev.* **2004**, *248*, 1447–1453. [CrossRef]
28. Chonn, A.; Cullis, P.R. Recent advances in liposomal drug-delivery systems. *Cur. Opi. Biotech.* **1995**, *6*, 698–708. [CrossRef]
29. Pignatello, R.; Musumeci, T.; Basile, L.; Carbone, C.; Puglisi, G.J. Biomembrane models and drug-biomembrane interaction studies: Involvement in drug design and development. *Pharm. Bioallied Sci.* **2011**, *3*, 4. [CrossRef] [PubMed]
30. Paternostre, M.T.; Roux, M.; Rigaud, J.L. Mechanisms of Membrane Protein Insertion into Liposomes during Reconstitution Procedures Involving the Use of Detergents. 1. Solubilization of Large Unilamellar Liposomes (Prepared by Reverse-Phase Evaporation) by Triton X-100, Octyl Glucoside, and Sodium Cholate. *Biochemistry* **1998**, *27*, 2667–2668.
31. Almog, S.; Litman, B.J.; Wimley, W.; Cohen, J.; Wachtel, E.J.; Barenholz, Y.; Ben-Shaul, A.; Lichtenberg, D. States of Aggregation and Phase Transformations in Mixtures of Phosphatidylcholine and Octyl Glucoside. *Biochemistry* **1990**, *29*, 4582–4592. [CrossRef]
32. Javadian, S.; Ruhi, V.; Heydari, A.; Shahir, A.A.; Yousefi, A.; Akbari, J. Self-Assembled CTAB Nanostructures in Aqueous/Ionic Liquid Systems: Effects of Hydrogen Bonding. *Ind. Eng. Chem. Res.* **2013**, *52*, 4517–4526. [CrossRef]
33. Blesic, M.; Marques, M.H.; Plechkova, N.V.; Seddon, K.R.; Rebelo, L.P.N.; Lopes, A. Self-aggregation of ionic liquids: Micelle formation in aqueous solution. *Green Chem.* **2007**, *9*, 481–490. [CrossRef]
34. Kristin, A.; Siddharth, F.; Pandey, M. Surfactant Aggregation within Room-Temperature Ionic Liquid 1-Ethyl-3-methylimidazolium Bis (trifluoromethylsulfonyl) imide. *Langmuir* **2004**, *20*, 33–36.
35. Nagaraj, K.; Arunachalam, S. Studies on outer-sphere electron transfer reactions of surfactant cobalt(III) complexes with iron(II) in liposome (dipalmitoylphosphatidylcholine) vesicles. *Trans. Met. Chem.* **2012**, *37*, 423–429. [CrossRef]
36. Nagaraj, K.; Arunachalam, S. Synthesis and electron transfer kinetics of a surfactant cobalt(III) complex: Effects of micelles, b-cyclodextrin, and ionic liquids. *Trans. Met. Chem.* **2013**, *38*, 649–657. [CrossRef]
37. Nagaraj, K.; Arunachalam, S. Synthesis, CMC Determination, and Outer Sphere Electron Transfer Reaction of the Surfactant] Complex Ion, cis-[Co(en)₂(4CNP)(DA)]³⁺ with [Fe(CN)₆]⁴⁻ in Micelles, b-cyclodextrin, and Liposome (Dipalmitoylphosphatidylcholine) Vesicles. *Aust. J. Chem.* **2013**, *66*, 930–937. [CrossRef]
38. Nagaraj, K.; Arunachalam, S. Kinetics of reduction of cis-bis(dodecylamine)bis(1,10-phenanthroline)cobalt(III) perchlorate and cis-bis(dodecylamine)bis(2,2'-bipyridine)cobalt(III) perchlorate by Fe(II) in dipalmitoylphosphatidylcholine vesicle. *Monatsh. Chem.* **2014**, *145*, 427–433. [CrossRef]
39. Cannon, R.D.; Gardiner, J.J. Kinetics of electron transfer: The reaction of acetatopenta-amminecobalt(III) with Nmethyliminodiacetatoiron(II). *J. Chem. Soc. Dalton. Trans.* **1972**, *89*, 887–890. [CrossRef]
40. Influence of self-assembly on intercalative DNA binding interaction of double-chain surfactant Co(III) complexes containing imidazo[4,5-f][1,10]phenanthroline and dipyrido [3,2-d:2'-3'-f]quinoxaline ligands: Experimental and theoretical study. *Dalton Trans.* **2014**, *43*, 18074–18086. [CrossRef]
41. Kipp, E.B.; Haines, R.A. Infrared studies of cis- and trans-bis(halogenoacetato)bis(ethylenediamine)-cobalt(III) complexes. *Can. J. Chem.* **1969**, *47*, 1073–1078. [CrossRef]
42. Morris, M.L.; Busch, D.H. Infrared Spectra Studies on the cis and trans Isomers of Diacidobis-(ethylenediamine)-cobalt(III) Complexes. *J. Am. Chem. Soc.* **1960**, *82*, 1521–1526. [CrossRef]
43. Miyashita, O.; Wolynes, P.G.; Onuchic, J.N. Simple Energy Landscape Model for the Kinetics of Functional Transitions in Proteins. *J. Phys. Chem. B* **2005**, *109*, 1959–1969. [CrossRef]
44. Yamamura, H.; Yamada, S.; Kohno, K.; Okuda, N.; Araki, S.; Kobayashi, K.; Katakai, R.; Kano, K.; Kawai, M. Preparation and guest binding of novel β-cyclodextrin dimers linked with various sulfur-containing linker moieties. *J. Chem. Soc. Perkin Trans.* **1999**, *1*, 2943–2948. [CrossRef]
45. Hak, S.C.; Tooru, O.; Shintrao, S.; Nobukiko, Y. Control of rapid phase transition induced by supramolecular complexation of b-cyclodextrin-conjugated poly (e-lysine) with a specific guest. *Macromolecules* **2003**, *36*, 5342.
46. Ghosh, S.; Barve, A.C.; Kumbhar, A.A.; Kumbhar, A.S.; Puranik, V.G.; Datar, P.A.; Sonawane, U.B.; Joshi, R.R. Synthesis, characterization, X-ray structure and DNA photocleavage by cis-dichloro bis(diimine) Co(III) complexes. *J. Inorg. Biochem.* **2006**, *100*, 331–343. [CrossRef] [PubMed]
47. *New RRC 1990 Liposomes a Practical Approach*; Oxford University Press: London, UK, 1990.

48. Subuddhi, U.; Mishra, A.K. Prototropism of 1-hydroxypyrene in liposome suspensions: Implications towards fluorescence probing of lipid bilayers in alkaline medium. *Photochem. Photobiol. Sci.* **2006**, *5*, 283–290. [CrossRef] [PubMed]
49. Leonenko, Z.V.; Finot, E.; Ma, H.; Dahms, T.E.S.; Cramb, D.T. Investigation of temperature-induced phase transitions in DOPC and DPPC phospholipid bilayers using temperature-controlled scanning force microscopy. *Biophys. J.* **2004**, *86*, 3783–3793. [CrossRef] [PubMed]
50. Tumuli, M.S.; Fandler, J.H. Aspects of artificial photosynthesis. Photosensitized electron transfer across bilayers, charge separation, and hydrogen production in anionic surfactant vesicles. *J. Am. Chem. Soc.* **1981**, *103*, 2507–2513. [CrossRef]
51. Batzri, S.; Korn, E.D. Single bilayer liposomes prepared without sonication. *Biochim. Biophys. Acta.* **1973**, *298*, 1015–1019. [CrossRef]
52. Benson, P.; Haim, A. Preparation and Reaction with Nucleophiles. *J. Am. Chem. Soc.* **1965**, *87*, 3656–3691.
53. Arulsamy, N.; Bohle, D.S.; Goodson, P.A.; Jaeger, D.A.; Reddy, V.B. Synthesis, Structure, and Stereochemistry of Double-Chain Surfactant Co(III) Complexes. *Inorg. Chem.* **2001**, *40*, 836–842. [CrossRef]
54. Ismail, A.M. Kinetics and mechanism of amine-catalysed solvolysis of azlactone in water-dioxan mixtures. *Indian J. Chem.* **2008**, *47*, 49.



Article

Biomimetic and Bioactive Small Diameter Tubular Scaffolds for Vascular Tissue Engineering

Elisabetta Rosellini *, Nicoletta Barbani, Luigi Lazzeri and Maria Grazia Cascone

Department of Civil and Industrial Engineering, University of Pisa, Largo Lucio Lazzarino, 56122 Pisa, Italy

* Correspondence: elisabetta.rosellini@unipi.it; Tel.: +39-050-2217908

Abstract: The present work aimed at the production and characterization of small caliber biomimetic and bioactive tubular scaffolds, which are able to favor the endothelialization process, and therefore potentially be suitable for vascular tissue engineering. The tubular scaffolds were produced using a specially designed mold, starting from a gelatin/gellan/elastin (GGE) blend, selected to mimic the composition of the extracellular matrix of native blood vessels. GGE scaffolds were obtained through freeze-drying and subsequent cross-linking. To obtain systems capable of promoting endothelialization, the scaffolds were functionalized using two different bioactive peptides, Gly-Arg-Gly-Asp-Ser-Pro (GRGSDP) and Arg-Glu-Asp-Val (REDV). A complete physicochemical, mechanical, functional, and biological characterization of the developed scaffolds was performed. GGE scaffolds showed a good porosity, which could promote cell infiltration and proliferation and a dense external surface, which could avoid bleeding. Moreover, developed scaffolds showed good hydrophilicity, an elastic behavior similar to natural vessels, suitability for sterilization by an ISO accepted treatment, and an adequate suture retention strength. In vitro cell culture tests showed no cytotoxic activity against 3T3 fibroblasts. The functionalization with the REDV peptide favored the adhesion and growth of endothelial cells, while GRGDSP-modified scaffolds represented a better substrate for fibroblasts.

Keywords: gelatin; gellan; elastin; endothelialization; functionalization; peptide

Citation: Rosellini, E.; Barbani, N.; Lazzeri, L.; Cascone, M.G.

Biomimetic and Bioactive Small Diameter Tubular Scaffolds for Vascular Tissue Engineering.

Biomimetics **2022**, *7*, 199. <https://doi.org/10.3390/biomimetics7040199>

Academic Editors: Stanislav N. Gorb, Giuseppe Carbone, Thomas Speck and Andreas Taubert

Received: 10 October 2022

Accepted: 7 November 2022

Published: 14 November 2022

Publisher's Note: MDPI stays neutral with regard to jurisdictional claims in published maps and institutional affiliations.



Copyright: © 2022 by the authors. Licensee MDPI, Basel, Switzerland. This article is an open access article distributed under the terms and conditions of the Creative Commons Attribution (CC BY) license (<https://creativecommons.org/licenses/by/4.0/>).

1. Introduction

Vascular diseases, including peripheral arterial occlusive diseases and coronary heart diseases, remain a leading cause of patient mortality and disability worldwide. Surgical repair is an indispensable treatment option in patients with advanced vascular disease, and vascular grafts are generally used to replace or bypass diseased vessels.

Synthetic vascular grafts have been found to be adequate in replacing large and medium caliber vessels. In contrast, small synthetic grafts have poor patency rates due to thrombus formation and intimal hyperplasia. Therefore, while having limitations, autologous vascular grafts are currently the only clinically viable options for the replacement of small caliber vessels [1].

An interesting alternative to traditional vascular prostheses implant is represented by vascular tissue engineering, whose purpose is to develop vascular grafts that integrate with the patient tissue and behave in a similar way to native vascular vessels.

The wall of native vessels is composed of three layers: an inner layer, called intima; a middle layer, called media; and an outer one, called adventitia. The intima is made up of connective tissue and a monolayer of endothelial cells (ECs), that lines the luminal surface of the wall in contact with the blood. The media consists of connective tissue (rich in collagen, elastin, and elastic fibers) and smooth muscle cells. The adventitia is made up of fibrous tissue, consisting of elastin and collagen fibers, and fibroblasts [2]. ECs of the intima play an important role in antithrombogenicity, by suppressing the activation of platelets and subsequent coagulation cascade [3,4]. Therefore, the formation of an endothelial layer

on the inner surface of a TEVG is of fundamental importance to avoid thrombosis, which leads to stenosis and occlusion of the vascular lumen [5].

The materials selected to produce tissue engineered vascular grafts (TEVGs) must be biocompatible and not provoke an immune response. TEVGs should be able to mimic the native extracellular matrix (ECM), supporting the growth of cells and guiding tissue regeneration [4,6]. Moreover, they should exhibit long-term patency, an antithrombotic surface, and the ability to remodel in response to different stimuli [7].

Both natural and synthetic polymers have been used in literature to produce scaffolds for vascular tissue engineering [8]. A great advantage of synthetic polymers, such as biodegradable synthetic polyesters, is that their mechanical properties and degradation rate are adjustable [9]; however, they are unable to provide useful signals affecting cell adhesion and proliferation [10]. On the other hand, natural polymers present properties similar to those of the native ECM in terms of functional groups [8] and exhibit natural domains that are recognized by cells and able to influence their behavior. In numerous studies, mixtures of collagen and elastin have been used for the production of scaffolds, which are able to mimic the ECM composition of natural vessels [11–14]. However, collagen is potentially immunogenic due to its animal origin and it presents high costs. To overcome these limitations, an alternative could be represented by gelatin, which is obtained from collagen denaturation. Gelatin is biocompatible, biodegradable, non-immunogenic, easy to process, and inexpensive. Furthermore, it does not activate platelets, which is an important property for a material envisioned for vascular tissue engineering applications. Another limitation of collagen/elastin scaffolds is that they only reproduce the protein components of vascular ECM, which instead contains also glycosaminoglycans.

Therefore, the use of a blend based on natural polymers, of both protein and polysaccharide type, could represent a valid solution to produce a scaffold more closely mimicking the composition of the natural vascular ECM [15]. Moreover, the inclusion in the blend of a polysaccharide component could increase the number of functional groups available for subsequent scaffold functionalization.

Another crucial requirement in the development of a scaffold for vascular tissue engineering is in fact the ability to promote the formation of an endothelial layer on the inner surface, given that surface endothelialization is fundamental to guarantee the patency of the vessel.

Several strategies have been proposed in literature to promote endothelialization, inducing ECs migration, adhesion, and proliferation, or favoring the homing and directional differentiation of endothelial progenitor cells.

Different surface modification methods, controlling scaffold microstructure [16–20] and physicochemical properties [21–24], have been investigated. Alternatively, endothelialization was promoted by loading the scaffold with biological factors, such as antibodies [25], growth factors [26], adhesive proteins [27], or short peptide sequences derived from them [28].

This last strategy is one of the most promising. Specific amino acid sequences, derived from ECM proteins, can mediate cell adhesion, proliferation, and differentiation by binding to integrins or other membrane protein receptors. The most widely investigated peptide sequence is the arginine-glycine-aspartic acid (RGD) sequence from fibronectin, which is recognized by integrin receptors that are present on the surface of all cell types [29]. Additionally, longer sequences are widely used for scaffold functionalization containing the RGD sequence, such as the sequence Gly-Arg-Gly-Asp-Ser-Pro (GRGDSP) derived from fibronectin, which has a demonstrated affinity toward integrin receptors that are present on the surface of various cells types, including ECs, fibroblasts, and smooth muscle cells [30,31]. Another peptide sequence proposed for the functionalization of scaffolds intended for the regeneration of blood vessels is the Arg-Glu-Asp-Val (REDV) sequence, from fibronectin. In contrast to the GRGDSP sequence, the REDV sequence specifically promotes the adhesion of ECs and endothelial progenitor cells. This sequence binds the

$\alpha v\beta 3$ integrin of ECs and several studies have shown that a highly uniform cell layer can be obtained [32,33].

In the present work, innovative scaffolds for the engineering of small diameter blood vessels have been developed. These scaffolds are based on the combination of: (i) biomimicry, given by the use as scaffold material of a protein/polysaccharide blend, mimicking native ECM composition; (ii) bioactivity, obtained by peptide coupling on scaffold surface, to induce endothelialization.

Small diameter tubular scaffolds were produced, using a specially designed mold, starting from a polymer blend of gelatin, gellan, and elastin, through a freeze-drying process.

Two different bioactive peptides were investigated for scaffold functionalization: the GRGSDP sequence, recognized by integrin receptors present on the surface of different cell types, and the REDV sequence, specifically recognized by integrin receptors present on the surface of ECs.

A complete characterization of the produced materials (GRGDSP- and REDV-modified scaffolds and unmodified scaffolds) was performed by carrying out morphological analysis, infrared analysis, thermal analysis, biomechanical characterization (including dynamic mechanical analysis, burst pressure strength, and suture retention strength), swelling and degradation tests. The suitability of the material to sterilization by an ISO accepted treatment was also verified. Finally, a biological *in vitro* characterization of the scaffolds was carried out, including cytotoxicity test with 3T3 fibroblasts and adhesion and proliferation tests with human umbilical vein endothelial cells (HUVEC) and human dermal fibroblasts (HDF).

2. Materials and Methods

2.1. Materials

Gelatin (type B from bovine skin), gellan, soluble elastin from bovine neck ligament, 1-(3-dimethylaminopropyl)-3-ethylcarbodiimide hydrochloride (EDC), N-hydroxysuccinimide (NHS), and phosphate buffered saline (PBS) were supplied by Sigma-Aldrich (Milan, Italy). The peptide sequences Gly-Gly-Gly-Arg-Glu-Asp-Val (GGGREDV) and Gly-Gly-Gly-Gly-Arg-Gly-Asp-Ser-Pro (GGGGRGDSP) were synthesized and provided by Cambridge Research Biochemicals (Billingham, Cleveland, UK). Moreover, calcium chloride and acetone were purchased from Carlo Erba Reagenti (Milan, Italy). All the other reagents were commercially available and used as received.

2.2. Mold Design

To produce tubular scaffolds, an appropriate mold was designed. The mold was mechanized by the company Brusa srl, established in Livorno, Italy.

The mold was composed of two main parts: an internal mandrel and an external chamber, made by two semi-shells with four screws (Figure 1).

The materials selected for mold fabrication were: Teflon for the internal mandrel, thanks to its chemical inertness, insolubility in water and organic solvents and excellent surface smoothness; aluminum for the external chamber, thanks to its high corrosion resistance and good temperature conductivity.

An aluminum bush was also used for maintaining the mandrel centered in the external chamber.

The mold was designed to permit the production of tubular scaffolds with an internal diameter of 4 mm, a thickness of 1 mm, and a length of 7 cm.

2.3. Scaffold Fabrication Procedure

Biomimetic tubular scaffolds were produced by freeze-drying, starting from the preparation of a gelatin/gellan/elastin (GGE) blend. A 2% (*w/v*) GGE solution (with a weight ratio of 50/35/15 among the three components, respectively) was prepared in bi-distilled water at 50 °C. Then, the blend was introduced in the orifice of the blood vessel mold, frozen at −25 °C and lyophilized using a ΔT of 10 °C.

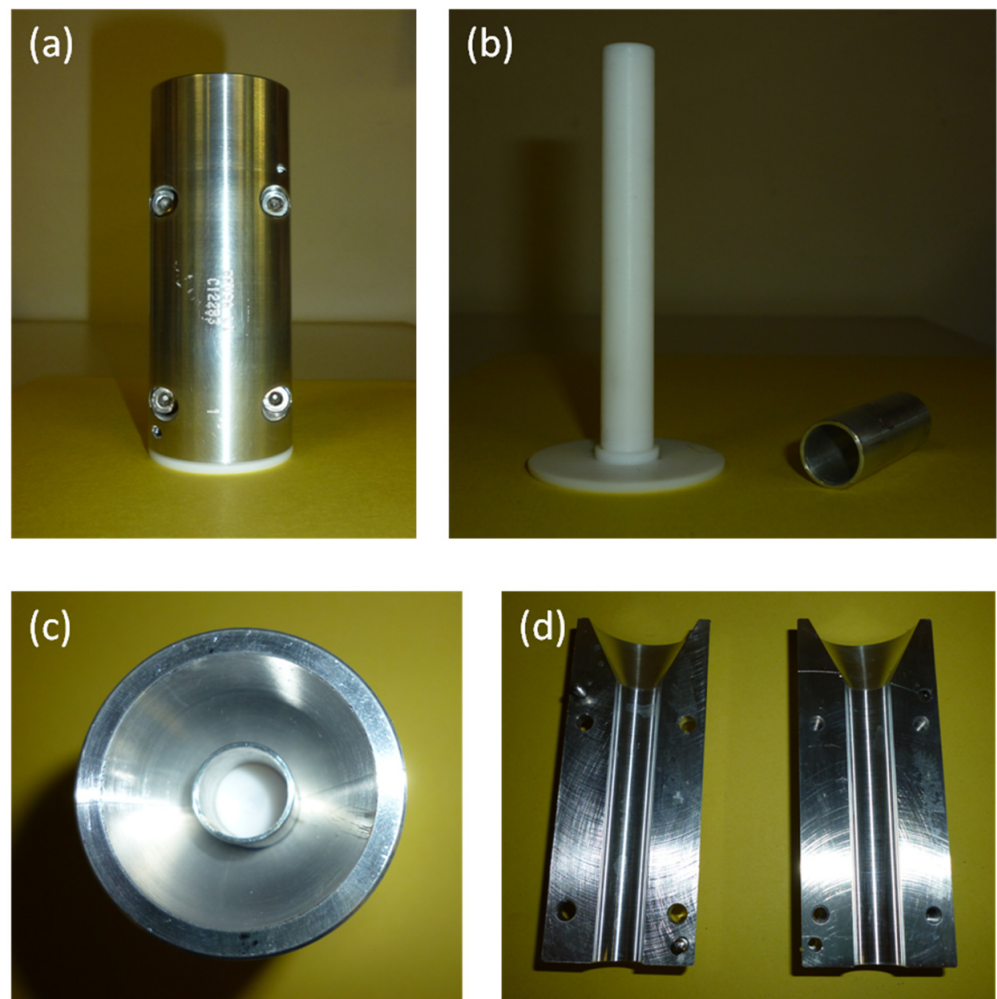


Figure 1. Mold designed for the production of tubular scaffolds by freeze-drying. (a) Complete mold; (b) internal mandrel and bush; (c) view from the top; (d) external chamber, open.

Since all the three biopolymers are soluble in water, scaffolds were cross-linked by treatment with EDC, for the stabilization of both protein components, and with a CaCl_2 solution, for the ionic cross-linking of the polysaccharide component.

Preformed scaffolds were first immersed under stirring for 24 h at room temperature into an EDC/NHS solution in acetone/water = 90/10 (*v/v*), using an amount of EDC corresponding to 30% of protein content in the scaffold and a sufficient amount of NHS to have a 1/1 molar ratio between EDC and NHS. Then, samples were immersed, under stirring for 2 h at room temperature, in a 2% (*w/v*) CaCl_2 solution. Thereafter, cross-linked scaffolds were washed three times with bi-distilled water, to remove unreacted compounds, and then freeze-dried.

2.4. Functionalization Procedure

As a further step toward the development of bioactive scaffolds, functionalization by immobilization of bioactive peptides was performed.

For this purpose, scaffolds were prepared into Petri dishes, rather than using the blood vessel mold.

EDC/NHS, used as cross-linking agents, are also coupling reagents which are able to activate the carboxylic groups contained in the blend, for subsequent amide bond formation with amine groups of bioactive peptides used for functionalization.

Both peptide sequences (GRGDSP and REDV) were synthesized by Cambridge Research Biochemicals (Billingham, Cleveland, UK), introducing a spacer, made by three

residues of glycine, to increase their flexibility and thus favoring their interaction with the cell membrane integrin receptors.

After the cross-linking process, scaffolds were introduced for 12 h, at 4 °C, in the coupling solution, made by GRGDSP or REDV peptide dissolved in PBS (pH = 7.4), at a concentration of 3.6 µmol/mL.

Peptide-modified scaffolds were finally washed three times in bi-distilled water to remove unreacted compounds and avoid any potential cytotoxic effect, as already demonstrated in our previous paper in which surface coupling through EDC/NHS chemistry was investigated on different scaffold substrates [34,35]. Thoroughly rinsed scaffolds were then freeze-dried. GRGDSP- and REDV-modified scaffolds were subsequently compared with not functionalized ones.

2.5. Morphological Analysis

Morphological properties of the scaffolds, especially in terms of porosity (pores dimension and interconnection among them), were investigated by scanning electron microscopy, using the microscope JSM 5600 (Jeol Ltd., Tokyo, Japan). Before analysis, samples were mounted on metal stubs and sprayed with gold to a thickness of 200–500 Å using a gold sputter. Images were acquired at different magnifications, reported on the micrographs. The percentage of porosity was calculated by analyzing SEM images through the ImageJ software (version 1.53a, National Institutes of Health), as the ratio between pores area and total scaffold area.

2.6. Infrared Chemical Imaging Analysis

The scaffolds were subjected to infrared analysis to investigate: (i) the presence of interactions among components; (ii) the chemical homogeneity at the end of the fabrication process; (iii) the secondary structure of protein components; and (iv) the occurrence of the coupling reaction.

A Fourier transformed infrared (FT-IR) spectrometer (Spectrum Spotlight 350 FT-NIR imaging system, Perkin Elmer, Waltham, MA, USA) was used.

To test the chemical homogeneity of the samples, spectral images were acquired using an infrared imaging system in the 4000–600 cm⁻¹ range. From the chemical map, the medium spectrum (which is the most representative spectrum) was recorded. Then, using the instrument software, the correlation map was elaborated as the correlation among the chemical map and the medium spectrum. A correlation index close to one on all the investigated samples indicated the chemical homogeneity of the sample.

2.7. Thermal Analysis

The thermal behavior of the GGE scaffolds was investigated by a Perkin–Elmer DSC 7 differential scanning calorimeter (DSC), using aluminum pans. The scans were performed at a rate of 10 °C/min, from 20 to 250 °C.

2.8. Swelling Tests

The swelling properties of cross-linked scaffolds were evaluated both by exposure to aqueous vapor at 37 °C and by immersion in PBS, following standard procedures [15]. At appointed times, swelling percentage was evaluated according to the following equation:

$$\text{Swelling \%} = \frac{W_s - W_d}{W_d} \times 100 \quad (1)$$

where W_d is the starting dry weight and W_s is the swollen weight.

2.9. Degradation Tests

Degradation test was performed in agreement with the ISO norm 10993-13 “Biological evaluation of medical devices. Part 13: Identification and quantification of degradation products from polymeric medical devices” [36].

The *in vitro* hydrolytic degradation properties of cross-linked GGE scaffolds were evaluated in PBS (pH = 7.4).

The weight loss of the scaffolds during degradation was determined by measuring changes in dry weight after specific incubation times. All experiments were performed in triplicate; the results are the mean (\pm SE) of three determinations carried out by keeping the samples in separate containers.

Test samples were prepared by cutting scaffolds into squares of 1 cm². Samples were dried at room temperature to a constant mass and the starting dry weight, W_0 , was determined for each sample using a balance with adequate precision. Then, the samples were placed in containers, added with PBS in order to be completely immersed, closed, and placed in a stirring bath at 37 ± 1 °C for the entire duration of the degradation test.

At appointed times, samples were removed from the degradation solution using a weighted filter and rinsed in bi-distilled water. The filter and its content were dried at room temperature to a constant mass and the dry weight at time t of degradation, W_t , was determined for each sample. Percentage weight loss was evaluated according to the following equation:

$$\text{Weight loss \%} = \frac{W_0 - W_t}{W_0} \times 100 \quad (2)$$

In addition to the determination of percentage weight loss during degradation, degraded samples were characterized by infrared analysis, to understand the mechanism of hydrolysis.

2.10. Biomechanical Characterization

2.10.1. Dynamic Mechanical Analysis (DMA)

The viscoelastic properties of GGE scaffolds were investigated using a dynamic mechanical analyzer (DMA8000, Perkin-Elmer, Waltham, MA, USA), following the protocol described in our previous paper [15]. Before analysis, samples were equilibrated for 1 h in PBS, at 37 °C, and tests were carried out under wet conditions. Single strain (10 μ m)/multi-frequency (1, 3.5, and 10 Hz) tests were performed and storage modulus (E'), loss modulus (E''), and tangent delta ($\tan \delta$) were determined.

2.10.2. Burst Pressure Strength

The burst pressure for the tubular scaffolds was measured by increasing the pressure of a fluid within them, until failure or leakage occurred. A 9% (w/v) aqueous solution of polyvinylpyrrolidone (PVP) was used, being the viscosity of this solution similar to blood [37]. A peristaltic pump was introduced to test the burst pressure strength. The pressure was gradually increased until failure or leakage occurred and pressure change was recorded through a digital manometer. Triplicate samples were tested and average values were obtained.

2.10.3. Suture Retention Strength

The suture retention strength of the scaffolds was measured according to the guidelines of the American National Standard Institute for the Advancement of Medical Instruments 7198, 2016 [38]. Rectangular samples of 20 \times 10 mm were prepared. Samples were immersed in PBS for 1 h prior to testing to simulate the hydrated condition at the implant site. One end of the sample was fixed to the stage clamp of the Instron tensile tester (Instron 5542 dynamometer, Instron, Turin, Italy). The opposite end was connected to another clamp of the testing device by polypropylene suture, creating a single loop, 2 mm from the short edge.

The tests were carried out at room temperature by setting a deformation speed of 50 mm/min to pull the suture and using a load cell of 50 N. The samples were subjected to a longitudinal tension force.

The maximum load prior to pull-through of the suture was recorded as the suture retention strength.

2.11. Determination of Peptide Surface Density

High performance liquid chromatography (HPLC, 200 Series HPLC system, Perkin Elmer, with a UV/VIS detector) was used to determine the peptide surface density, by measuring the corresponding concentration in the coupling solution after coupling reaction (C_f), as well as in the wash waters (C_w). An HP Prosphere C4 300A 5u column (250 mm length \times 4.5 mm internal diameter, Alltech Associates, Deerfield, IL) was used. The mobile phase was: A = 0.085% trifluoroacetic acid (w/v) in acetonitrile; B = 0.1% trifluoroacetic acid (w/v) in water. The elution condition was a linear binary gradient at a flow rate of 1 mL/min and the gradient was from 30% A and 70% B to 60% A and 40% B in 15 min. The injection volume was 50 μ L. The detector wavelength was set at $\lambda = 280$ nm. Knowing the concentration of the coupling solution before the reaction (C_i), the volume of the coupling solution and of the wash waters (V) and the area (A) of the treated surface, the peptide surface density was calculated according to the following equation:

$$\text{Density} = \frac{V(C_i - C_f - C_w)}{A} \quad (3)$$

2.12. Suitability for Sterilization

GGE samples were sterilized by Gamma irradiation, which is a sterilization procedure accepted by the ISO norm [39]. To investigate the suitability of the material to the sterilization process, infrared and mechanical analysis were carried out on the sterilized samples, according to the procedures already described under Sections 2.6 and 2.10.1. Results were compared with those obtained before sterilization.

2.13. In Vitro Biological Characterization

2.13.1. Cytotoxicity Tests

GGE scaffolds were tested for cytotoxicity using a 3T3 embryonic mouse fibroblast cell line (European Collection of Cell Culture, London, UK), according to the ISO norm 10993-5 "Biological evaluation of medical devices—Test for cytotoxicity: in vitro methods" [40]. The cytotoxicity test was performed by direct contact; 3T3 fibroblasts (about 10^6 cells/mL) suspended in DMEM containing 10% (v/v) fetal bovine serum (FBS), 2 mM glutamine, penicillin (100 U/mL), and streptomycin (100 μ g/mL), were seeded in 24-well plates, using 1 mL for each well. After 24 h of seeding, the medium was replaced with fresh medium and a sterilized unmodified GGE sample was placed in the center of each well. Polystyrene (culture dish surface) was used as the negative control, while 2,4-dinitrophenol (70 μ g/mL) was added to the positive control wells. Cell culture was carried out for 72 h inside an incubator at 37 $^{\circ}$ C in a humidified atmosphere containing 5% CO₂. After 72 h of incubation, cell viability was measured by (3-(4,5-dimethylthiazol-2-yl)-2,5-diphenyltetrazolium bromide (MTT) assay as follows. MTT solution was added to the wells in an amount equal to 10% (v/v) of the culture volume, followed by incubation at 37 $^{\circ}$ C for 4 h. At the end of the incubation time, the resulting formazan precipitate was dissolved by the addition of MTT solvent in an amount equal to the original culture volume. An UV spectrophotometer (Shimadzu, UV-2100) was used to measure the absorbance at 570 nm.

2.13.2. Cell Adhesion and Proliferation Tests

Both HUVEC and HDF were used to perform cell adhesion and proliferation tests. HUVEC were used to study the capability of peptide-modified scaffolds to promote endothelialization; HDF were used to investigate the effect on a different cell type which is present in native vessels. REDV-modified GGE scaffolds, GRGDSP-modified GGE scaffolds and unmodified GGE scaffolds ($n = 3$ for each sample type) were first sterilized by the following protocol: washing in water/ethanol with 70% ethanol, drying under a sterile hood, and UV exposure for 15 min on each side. Prior to cell seeding, the scaffolds were placed in 96-well plates, washed 3 times with sterile 2x Pen-Strep (#P0781, Sigma-Aldrich, Milan, Italy)/Diflucan (Pfizer, Rome, Italy) saline, and rinsed with PBS. HUVEC and HDF

were seeded on the scaffolds at a density of 2×10^5 cells/sample in a volume of 15 μ L of complete culture medium. Endothelial Cell Growth Medium (ECGM, #211-500, Cell application inc, Sand Diego, CA, US) was used for HUVEC and Dulbecco's Modified Eagle Medium (DMEM, #11054-020, Gibco, Milan, Italy) for HDF, both added with fetal bovine serum (10%), 2 mM glutamine, penicillin (100 U/mL), and streptomycin (100 μ g/mL). The plates were placed for 1 h in the incubator, for cell adhesion, then complete medium was added and the cells were cultured for 11 days, providing media changes every 3 days.

The Alamar Blue assay (#BUF012A, Serotec Ltd., Oxford, UK) was used to test the viability and proliferation of cells seeded onto the GGE samples. This bioassay uses a redox indicator, which causes the culture media to change color in response to cell metabolism. The low toxicity of this assay allows it to be repeated numerous times on the same samples. In accordance with the manufacturer's instructions, samples and controls—including scaffolds devoid of cells used as blank controls—were incubated with the dye for 3 h. To determine cell viability, samples were analyzed at three different culture times: 3, 7, and 11 days after seeding. At the appointed times, the culture supernatants were taken out and fresh culture media was added. A spectrophotometer (Victor3, PerkinElmer, Waltham, MA, USA) was used to analyze supernatants under a double wavelength reading of 570 and 600 nm. Finally, the manufacturer's recommended absorbance calculations and dye molar extinction coefficients were used to obtain the dye reduction percentage.

2.13.3. Statistical Analysis

Statistical significance in Alamar Blue assay was evaluated using the 2-tailed *t*-test for paired data, followed by Bonferroni's correction.

3. Results and Discussion

3.1. Morphological Analysis

SEM micrographs of GGE tubular scaffolds were acquired before and after cross-linking.

The morphological analysis of untreated scaffolds (Figure 2a–c) showed the presence of a good porosity in sample section, which could promote cell infiltration and proliferation. Pore diameter increased from the external surface (where the average pore diameter was around 100 μ m) to the internal lumen (where the average pore diameter was around 250 μ m); the wall thickness of dried samples was 800 μ m. The external surface appeared dense, which is a desired property to avoid bleeding.

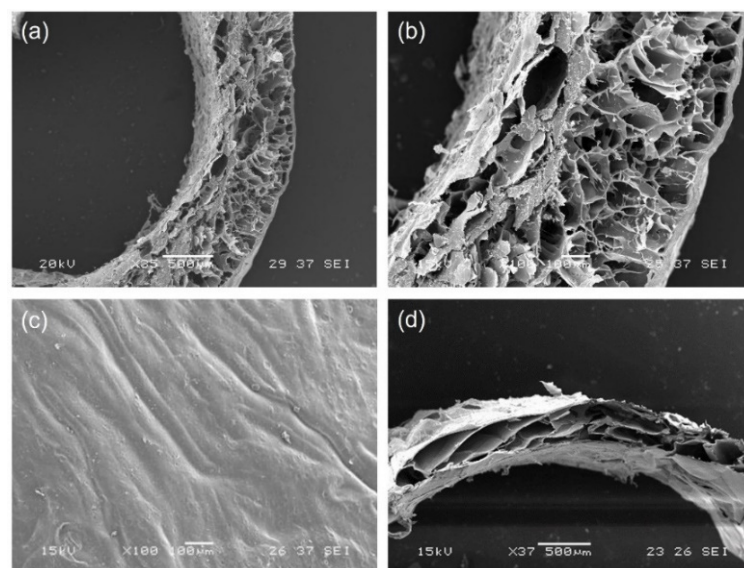


Figure 2. SEM micrographs of: (a,b) section and (c) external surface of untreated GGE tubular scaffold; (d) section of cross-linked GGE tubular scaffold.

After cross-linking, we observed a contraction of scaffold material, with a decrease in wall thickness of dried scaffolds to 600 μm (Figure 2d). However, the section of the scaffold maintained a high degree of porosity.

The percentage of porosity, as calculated by ImageJ analysis of SEM images, was 43%.

SEM micrographs of tubular scaffolds prepared in different times were also compared to evaluate the reproducibility of the preparation procedure (see Supplementary Figure S1). The images acquired showed only small differences in pore dimensions, imputable to the intrinsic variability of the freeze-drying process.

3.2. Infrared Chemical Imaging Analysis

Infrared chemical imaging analysis was carried out on the scaffolds. The chemical map was acquired and the medium spectrum, which is the most representative of the chemical map, was recorded. The medium spectrum (Figure 3a) was compared with those of pure polymers (see Supplementary Figure S2). The two proteins are characterized by absorption bands at 1650 cm^{-1} , due to the stretching of C=O group in Amide I, and at 1538 cm^{-1} , due to the N-H bending in Amide II. Gellan is characterized by an absorption band at 1024 cm^{-1} , due to the C-O-C group of the polysaccharide ring. The FT-IR medium spectrum of the scaffold showed the presence of all the absorption peaks typical of both protein and polysaccharide components, even if band displacements were observed. In particular, the Amide II band moved to 1550 cm^{-1} and the C-O-C band moved to 1035 cm^{-1} . These band displacements were explained by the establishment of interactions among the protein and the polysaccharide components [41]. It was supposed that these interactions are due to the formation of hydrogen bonds between the N-H group of the proteins and glycosidic group of gellan, as already observed in similar protein/polysaccharide blends [15,42].

The correlation map between the chemical map and the medium spectrum was elaborated to investigate sample homogeneity. The correlation map (Figure 3b) revealed correlation values close to 1 on all the analyzed sample, demonstrating the high chemical homogeneity of the scaffold. The high chemical homogeneity can be considered a consequence of the interactions among the protein and the polysaccharide components, demonstrated by the displacement of the adsorption bands due to Am II and C-O-C of polysaccharide ring, as previously discussed.

Furthermore, the protein secondary structure was investigated by acquiring second derivative spectra (Figure 3c). It is well known that the deconvolution of Amide I band is relevant for the identification of polypeptide conformation [43]. Second derivative spectra of GGE scaffolds showed the presence of typical peaks, due to β -sheet (1663 cm^{-1}), α -helix (1650 cm^{-1}), β -unordered (1630 cm^{-1}), and triple helix (1638 cm^{-1}) structures. In particular, the presence of this last band suggested a partial reorganization of protein material, probably due to the interactions established among blend components [44]. However, the triple helix band was less evident than in other protein/polysaccharide blends [15,42]. This could be explained by milder interactions between components in the GGE blend developed in this work, with respect to alginate/gelatin [15] and alginate/gelatin/elastin [42] blends investigated in previous works.

Chemical imaging analysis was also performed after GGE scaffold functionalization (Figure 4). The band ratio between Amide II absorption peak (of protein material) and C-O-C absorption peak (of gellan) was used to verify the functionalization of scaffold surfaces with peptides. Chemical maps, in function of Am II/C-O-C band ratio, were acquired before and after functionalization.

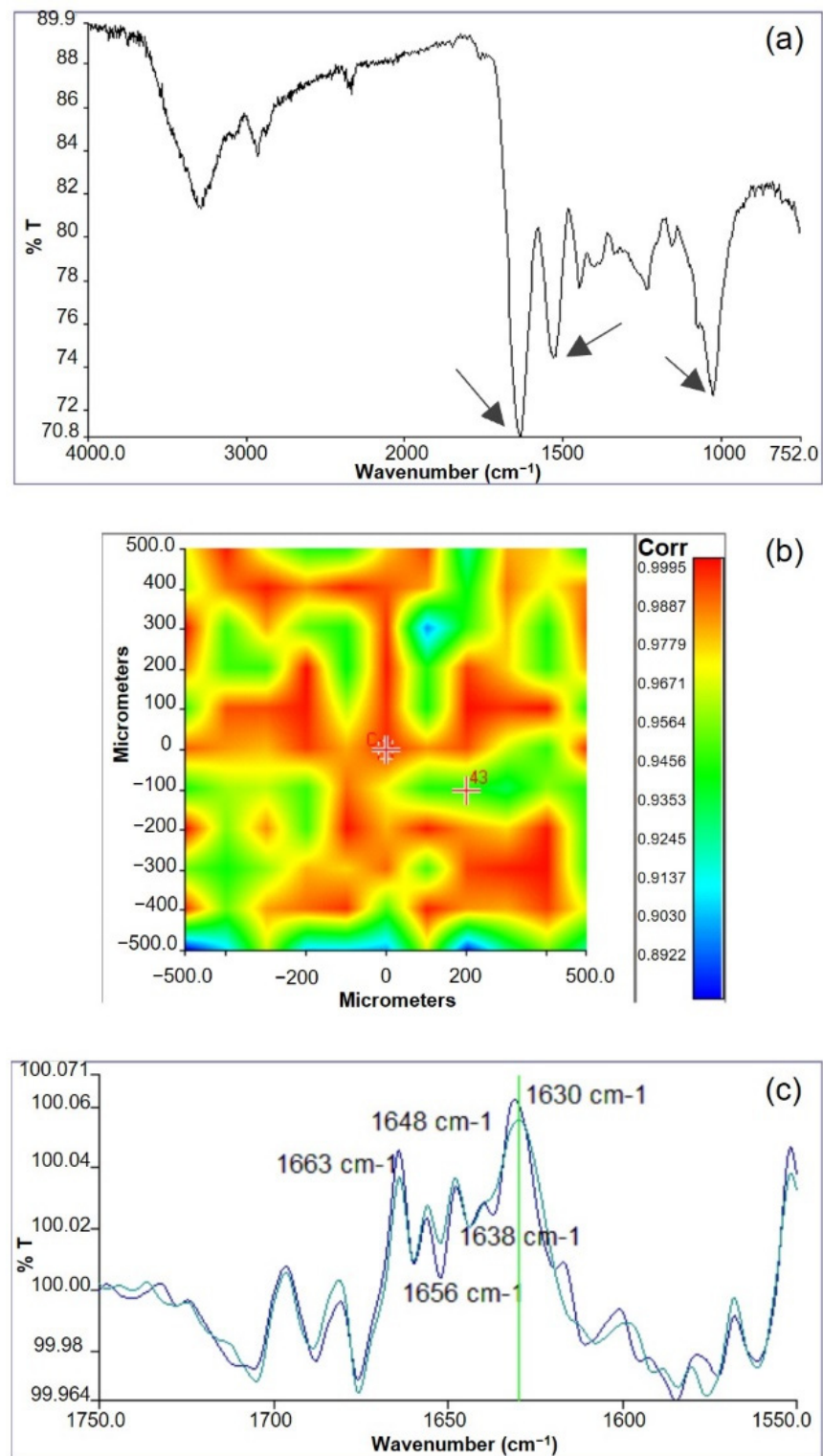


Figure 3. Infrared analysis of GGE scaffolds: (a) Medium spectrum recorded from the chemical map; (b) correlation map between the chemical map and the medium spectrum; (c) second derivative spectra.

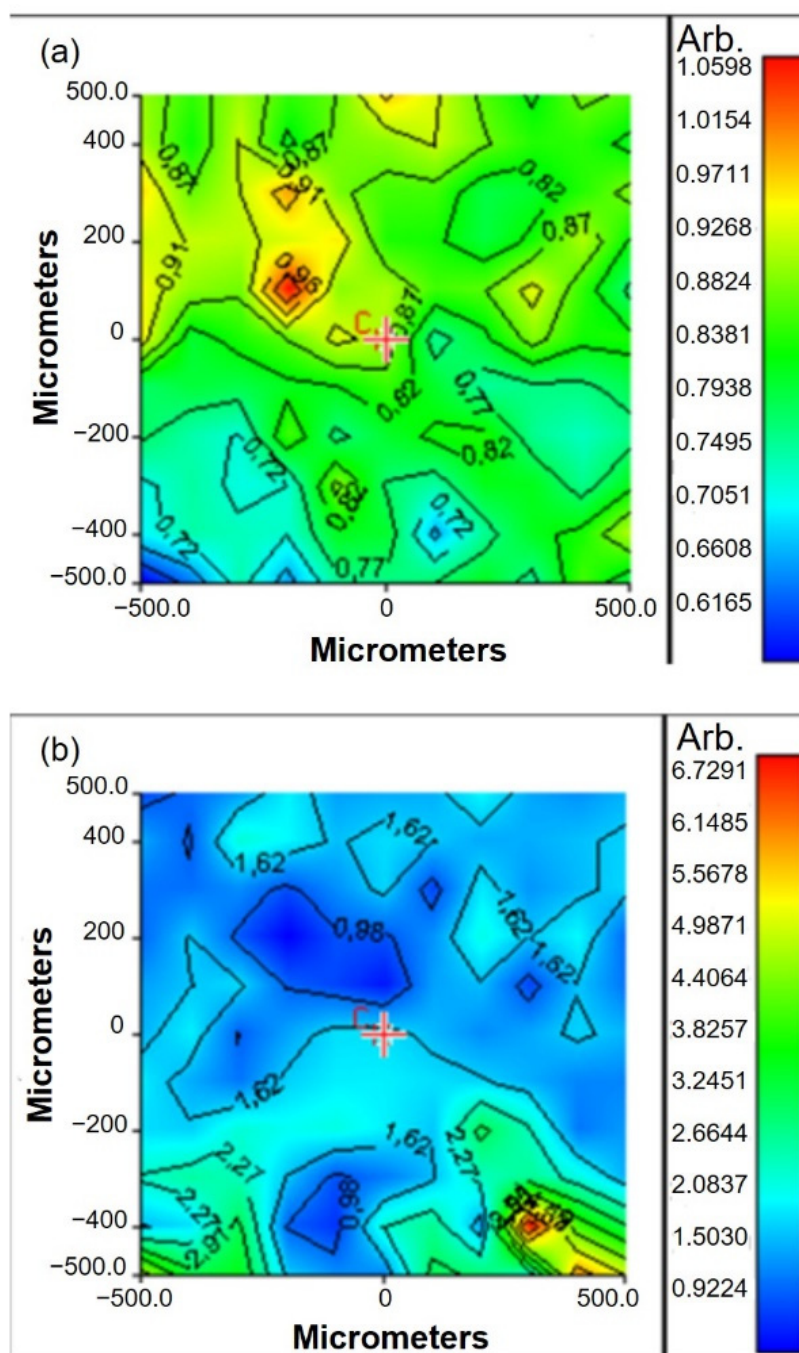


Figure 4. Chemical maps, in function of Am II/C-O-C band ratio, acquired: (a) before functionalization; (b) after functionalization.

The value of band ratio before functionalization was in the interval 0.6–1 (Figure 4a). After functionalization, a significant increase in the band ratio was observed, which could be explained by the increase in protein content after peptide binding (Figure 4b).

3.3. Thermal Analysis

Thermal analysis was carried out by DSC to investigate the presence of interactions between blend components [41].

Thermograms of GGE scaffolds (Figure 5b), before and after cross-linking, were compared with those of pure components (Figure 5a). Gellan thermogram showed a first endothermic event between 50 and 130 °C, due to the evaporation of residual water,

and a second exothermic event at 260 °C, due to the polysaccharide degradation. Elastin thermogram showed a variation of the baseline, between 160 and 190 °C, attributable to the glass transition event. Gelatin showed a glass transition event at 220 °C, superimposed to an endothermic event, due to the denaturation of residual triple helix.

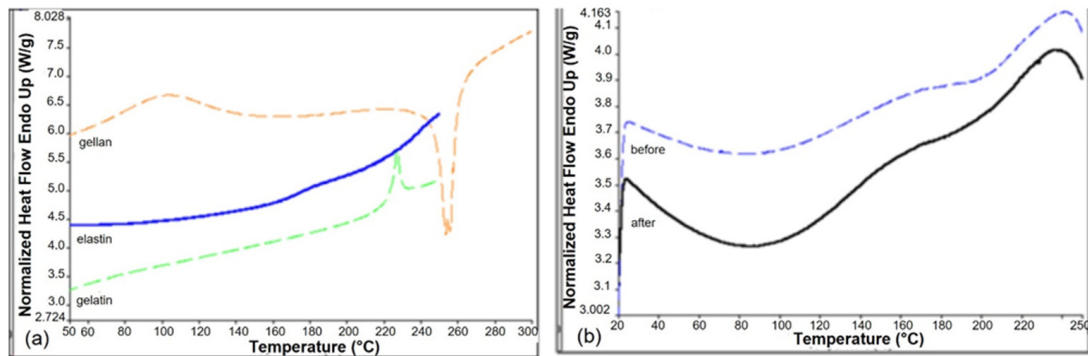


Figure 5. DSC thermograms of pure components (a) and of GGE tubular scaffolds, before and after cross-linking (b).

In the thermogram of the GGE blend we observed only one thermal event, between 130 and 190 °C, which can be attributed to the glass transition of the protein components. The presence in the blend of only one glass transition event could be explained by the establishment of strong interactions between gelatin and elastin.

The thermogram of cross-linked scaffolds was identical to non-cross-linked ones, suggesting that the cross-linking process did not alter the interactions between components.

3.4. Swelling Tests

Swelling tests were carried out to investigate the ability of the material to absorb water. This property is related to the degree of hydrophilicity and depends on the chemical characteristics of blend components, the degree of cross-linking, the interactions between the components, and the morphological properties of the produced materials.

GGE cross-linked samples were first exposed to water vapours and the percentage of swelling was calculated using the formula reported in Section 2.8, obtaining the trend over time, as represented in Figure 6a. The swelling percentage of absorbed water increased, until it reached the equilibrium swelling value of 42%.

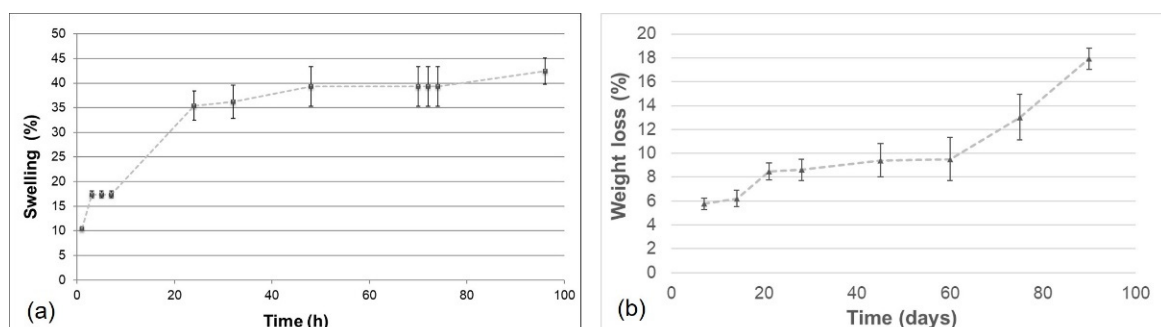


Figure 6. Swelling kinetic for cross-linked GGE scaffold exposed to water vapours (a) and weight loss kinetic during the hydrolysis of cross-linked GGE scaffolds (b).

The obtained value of swelling degree was only slightly lower than that obtained in a previous work [42] for alginate/gelatin/elastin scaffolds and this difference can be explained by the different polysaccharides used (gellan rather than alginate) and by the different weight ratios between components.

Swelling tests were also performed by immersion in PBS solution at 37 °C. The cross-linked GGE sample reached an equilibrium swelling percentage of $145 \pm 7\%$, only after 1 h of immersion.

Overall, these results demonstrated a good hydrophilicity of the prepared scaffolds.

3.5. Degradation Tests

Degradation tests were performed maintaining the cross-linked GGE samples in PBS, at 37 °C, into an agitating bath. At appointed times, the percentage of weight loss was evaluated.

The weight loss kinetic showed a rapid release of material during the first week; then the sample continued to release material more slowly up to 60 days, when a recovery of the hydrolysis process was observed (Figure 6b). After 90 days, 80% of scaffold material was still present.

Infrared analysis of degraded samples was carried out. Spectra of degraded materials showed the same absorption peaks of non-degraded samples. However, a decrease in the intensity for the absorption band at 1050 cm^{-1} (due to gellan) was observed. Therefore, to verify whether the weight loss during hydrolysis was mainly due to the release of the polysaccharide component, the band ratio between the absorption peaks of the protein materials (Am I + Am II, between 1727 and 1485 cm^{-1}) and the absorption peak of the polysaccharide (C-O-C, between 1181 and 945 cm^{-1}) was calculated. An increase in the band ratio was found during hydrolysis, from 1.22 before hydrolysis, to 1.43 after one month of hydrolysis and 1.69 after 3 months of hydrolysis. These results suggested that the weight loss during hydrolysis was mainly due to gellan release.

3.6. Biomechanical Characterization

3.6.1. Dynamic Mechanical Analysis (DMA)

In Table 1, the results of the mechanical analysis, performed by DMA, are shown. Values of storage modulus (E'), loss modulus (E''), and tan delta were determined at three different frequencies (1, 3.5, and 10 Hz), corresponding to healthy human heart rate, pathological human heart rate, and a fatigue condition with a supraphysiological pulse rate, respectively [15].

Table 1. Storage modulus (E'), loss modulus (E''), and tan delta of GGE scaffolds, measured by DMA at three different frequencies (1, 3.5, and 10 Hz).

	E' (Pa)	E'' (Pa)	Tan δ
1 Hz	$(5.30 \pm 0.07) \times 10^4$	$(5.10 \pm 0.17) \times 10^3$	0.10 ± 0.02
3.5 Hz	$(5.49 \pm 0.08) \times 10^4$	$(5.52 \pm 0.09) \times 10^3$	0.10 ± 0.01
10 Hz	$(5.69 \pm 0.11) \times 10^4$	$(5.63 \pm 0.07) \times 10^3$	0.10 ± 0.01

Values of E' were one order of magnitude higher than values of E'' , with E' on the order of 10^4 Pa, over the entire frequency range, indicating the elastic behavior of the developed scaffolds [45].

As expected, increasing the oscillation frequency, an increase was observed for values of E' and E'' . This result demonstrated that the stiffness of GGE scaffolds increased with frequency increase, as typically occurs for hydrogel scaffolds [46]. This stiffening involves both an increase in elasticity (E') and an increase in heat dissipation (E'').

Values of tan δ were around 0.1 and did not show variations by increasing frequency, suggesting that E' and E'' increased with frequency at the same proportion.

DMA was used in literature to evaluate the viscoelastic properties of blood vessels and their substitutes [47]. The storage modulus measured for GGE scaffold in this work is lower than reported by Khosravi et al. for autologous graft (1.55 MPa for small saphenous vein and 5.79 MPa for internal thoracic artery [48]). However, native vessels showed a similar elastic behavior (with E' around an order of magnitude above E'') and values of tan

delta close to 0.1 [48], as found in this work for GGE scaffolds. Moreover, the viscoelastic characterization by DMA of scaffolds for vascular tissue engineering application carried out by Liu et al. [49] reported values of storage modulus on the order of 10^4 Pa and values of loss modulus on the order of 10^3 Pa, similarly to what is obtained in this work.

3.6.2. Burst Pressure Strength

The burst pressure strength is one of the most important properties for blood vessel scaffolds. To evaluate whether GGE tubular scaffolds had sufficient strength to withstand physiological forces, burst pressure tests were performed to determine the maximum pressure that GGE vascular scaffolds could endure before failure. Six GGE tubular scaffolds were used and a burst pressure strength of 150 ± 27 mmHg was measured.

As the normal blood pressure in the human body is 90–120 mmHg [50] and the ideal burst pressure for blood vessel scaffolds is 2000 mmHg [51], the value measured for GGE scaffolds can be considered sufficient but not optimal.

To improve this property, we tested the dipping of the developed scaffolds in a gellan solution. Gellan was dissolved in bi-distilled water, at a concentration of 2% (*w/v*). GGE scaffolds were mounted on the mandrel of the mold, immersed in the gellan solution for 5 min, and then dried. This procedure was carried out three times. Burst pressure tests were repeated after dipping, showing a significant increase in the burst pressure strength up to 320 ± 23 mmHg, which is a value closer to what is reported in literature for other blood vessel scaffolds based only on natural polymers [47].

3.6.3. Suture Retention Strength

The ability of a scaffold to withstand forces due to suturing is a crucial parameter in the fabrication of scaffold for blood vessel tissue engineering, as it determines the success of the graft implantation procedure. Experiments carried out in this work showed a suture retention strength of 2.2 ± 0.1 N for hydrated GGE scaffolds. Reference values reported in literature show a suture retention strength of 1.96 N for human arteries [52]. Therefore, the obtained results suggest that the suture retention strength of GGE scaffolds was more than adequate for suturing during implantation.

3.7. Determination of Peptide Surface Density

The peptide surface density on functionalized scaffold was determined by quantifying, through HPLC analysis, the amount of residual peptide in the coupling solution after the coupling process.

Considering the molecular weight of the peptide sequences, the immobilized peptide density resulted in 0.17 ± 0.02 $\mu\text{mol}/\text{cm}^2$ for scaffolds modified with GRGDSP and 0.24 ± 0.03 $\mu\text{mol}/\text{cm}^2$ for scaffolds modified with REDV. It is well known in literature that there is a relationship between cell response and the surface concentration of immobilized peptides [53]. In particular, surface modification with GRGDSP and REDV peptides has been investigated in literature on materials different from GGE scaffold [32,54]. According to the results reported in these studies, a peptide density on the order of pmol/cm^2 is sufficient to promote cell adhesion and proliferation. Although cell attachment is influenced not only by peptide density, but also by other parameters, such as the surface properties of the material used as substrate [55], the peptide density obtained on functionalized GGE scaffolds is several orders of magnitude above these reference values. Therefore, it should be adequate to affect cell response.

3.8. Suitability for Sterilization

Checking suitability for sterilization is of paramount importance in the characterization of scaffolds for tissue engineering applications. Materials intended to come into contact with biological tissues must necessarily be sterilized to avoid contamination, through an ISO norm-approved sterilization method, and the sterilization procedure must not change their properties.

The sterilization of GGE scaffolds was performed by Gamma irradiation, a procedure that is in agreement with the ISO norms on sterilization of medical devices [39]. The suitability for sterilization of the prepared scaffolds was investigated by comparing the physicochemical and mechanical characteristics of the materials, after the sterilization process, with those observed before sterilization.

The infrared and mechanical tests performed on the sterilized scaffolds did not reveal any significant variation with respect to the results obtained for non-sterilized samples (see Supplementary Figure S3 and Supplementary Table S1), demonstrating that the polymeric scaffolds developed in this work can be sterilized by ISO recommended treatments.

3.9. In Vitro Biological Characterization

3.9.1. Cytotoxicity Tests

In vitro cytotoxicity tests were performed according to ISO norm 10993-5. Cytotoxicity was tested by direct contact, using murine fibroblast 3T3. Cell viability was measured 72 h after seeding by MTT assay, and reading absorbance at 570 nm.

The results were expressed in terms of percentage of cell viability, which was calculated as follows:

$$\text{Cell viability \%} = \frac{\text{Absorbance (570 nm) test product}}{\text{Absorbance (570 nm) negative control}} \times 100 \quad (4)$$

Reduction in cell viability by more than 50% with respect to negative control was considered a cytotoxic effect.

The results are collected in Figure 7. No cytotoxic activity against murine fibroblast 3T3 was detected for GGE unmodified scaffolds.

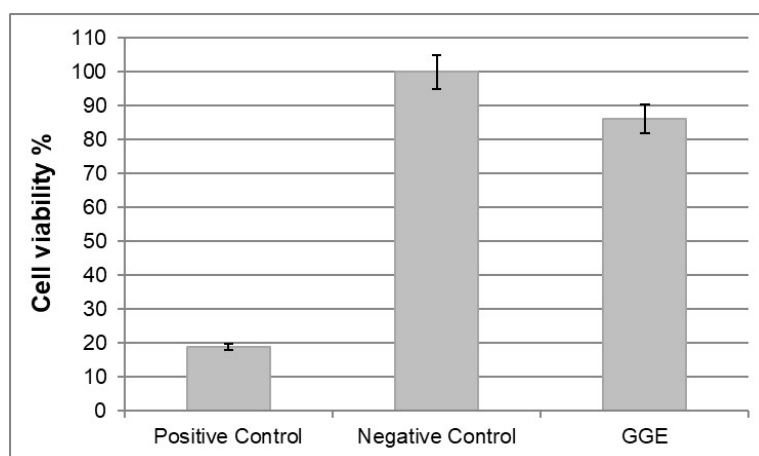


Figure 7. Results of cytotoxicity test on GGE scaffolds.

3.9.2. Cell Adhesion and Proliferation Tests

The in vitro Alamar Blue assay was performed to evaluate the viability and proliferation of HUVEC and HDF seeded onto the scaffolds. Samples were analyzed at three different culture times, 3, 7, and 11 days after seeding. The spectrophotometric analysis of culture supernatants was performed under a double wavelength reading of 570 and 600 nm. The results, expressed in terms of percentage of dye reduction, showed that the functionalization of the scaffolds promoted cell adhesion and proliferation. With regard to HUVEC (Figure 8a), the highest percentage of reduction (corresponding to a higher cell viability and therefore to a higher number of cells on the scaffold) was observed for the REDV-modified samples. On the other hand, with respect to HDF (Figure 8b), the highest percentage of reduction was observed for the GRGDSP-modified samples.

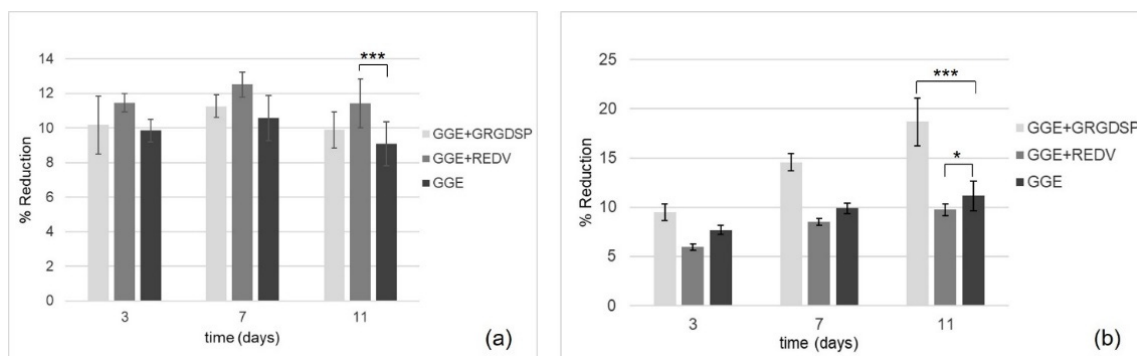


Figure 8. Alamar Blue reduction percentage as a function of culture times for scaffolds seeded with HUVEC (a) and HDF (b). GRGDSP-modified scaffolds (GGE+GRGDSP) and REDV-modified scaffolds (GGE+REDV) were compared with unmodified scaffolds (GGE). The data ($n = 9$; error bars \pm SD) were compared using Student's t -test and differences were considered significant when * $p < 0.05$, *** $p < 0.001$.

In both cases, an increase in the percentage of reduction was observed as a function of time, suggesting the ability of the cells which are adhered to the materials to proliferate.

4. Conclusions

Novel biomimetic and bioactive small diameter tubular scaffolds were produced by freeze-drying and subsequent cross-linking, starting from a polymer blend of gelatin, gellan, and elastin, which are able to mimic the protein/polysaccharide components that are present in the ECM of native vessels.

The scaffolds were functionalized using two different bioactive peptides: GRGDSP, recognized by integrin receptors present on the surface of different cell types, and REDV, specifically recognized by integrin receptors present on the surface of ECs.

A complete physicochemical, mechanical, functional, and biological characterization of the produced materials (GRGDSP- and REDV-modified scaffolds and unmodified scaffolds) was performed.

The produced GGE scaffolds showed a good porosity, which could promote cell infiltration and proliferation, and a dense external surface that could avoid bleeding. The infrared chemical imaging analysis pointed out a high chemical homogeneity of the material and the establishment of interactions between components, which produced a partial reorganization of protein material. In addition, this analysis confirmed the occurrence of the coupling reaction with the peptide sequences. Peptide surface density was quantified by HPLC analysis and resulted higher than reference values reported in literature to promote a biological response. The GGE scaffolds showed good hydrophilicity, and suitability for sterilization by an ISO accepted treatment. The material showed an elastic behavior similar to natural vessels. The measured burst pressure strength of 150 mmHg was well below the ideal value of 2000 mmHg. However, it was demonstrated that it can be easily increased above physiological and pathological pressure values, by simply dipping the scaffold in a gellan solution. Suture retention strength resulted adequate to withstand a surgical implantation procedure.

No cytotoxic activity against 3T3 murine fibroblast was detected for GGE unmodified scaffolds. Cell adhesion and proliferation tests were carried out with HUVEC and HDF, comparing peptide-modified scaffolds with unmodified ones. The functionalization of the scaffolds promoted cell adhesion and proliferation. The best substrates for HUVEC were the GGE scaffolds functionalized with the REDV peptide. In the case of samples seeded with HDF, the best results were obtained with scaffolds functionalized with GRGDSP, while samples functionalized with REDV behave worse than unmodified control. An increase in the number of cells was also observed as a function of time, indicating the ability of adhered cells to proliferate.

Overall, the obtained results look promising and suggest a potential use of the developed GGE scaffolds for in vitro vascular tissue engineering, while their application for in situ strategies would request a further improvement in mechanical properties, especially in terms of burst pressure strength. Results of biological characterization indicate that functionalization of the GGE scaffolds with the REDV peptide favors the adhesion and growth of ECs and therefore could be advantageous for the endothelialization of the internal surface of an engineered vessel, while that with GRGDSP promotes the adhesion of fibroblasts, which are present in the external layer of blood vessel. Therefore, as a further step toward the development of a biomimetic and bioactive scaffold for vascular tissue engineering, a bi-functionalized tubular scaffold could be developed. REDV could be grafted on the luminal side of the scaffold, to promote specifically endothelial cell adhesion, while GRGDSP could be used for the functionalization of the external side, to promote fibroblasts and smooth muscle cells adhesion. This bi-functionalized scaffold could be able to promote the regeneration of a layered tissue, resembling the native structure of small-caliber arteries.

Supplementary Materials: The following supporting information can be downloaded at: <https://www.mdpi.com/article/10.3390/biomimetics7040199/s1>. Figure S1: SEM micrographs of three different prototypes; Figure S2: Comparison between the infrared spectrum of GGE (in black) and the infrared spectrum of pure components, gelatin (in red) and gellan (in blue); Figure S3: Infrared spectra of GGE scaffolds, before and after sterilization by Gamma irradiation; Table S1: Storage modulus (E'), loss modulus (E''), and tan delta of GGE scaffolds, measured by DMA at three different frequencies (1, 3.5, and 10 Hz), after scaffold sterilization by Gamma irradiation.

Author Contributions: Conceptualization, E.R.; methodology, E.R., N.B., L.L. and M.G.C.; formal analysis, E.R., N.B., L.L. and M.G.C.; investigation, E.R. and N.B.; resources, E.R.; data curation, E.R. and N.B.; writing—original draft preparation, E.R. and M.G.C.; writing—review and editing, E.R. and M.G.C.; visualization, E.R.; supervision, E.R. and M.G.C.; project administration, E.R.; funding acquisition, E.R. All authors have read and agreed to the published version of the manuscript.

Funding: This research was partially funded by European Commission FP7 Programme, grant number 214539.

Institutional Review Board Statement: Not applicable.

Data Availability Statement: The data presented in this study are available within the article.

Acknowledgments: The authors gratefully acknowledge Claudio Ricci for performing the Alamar Blue assay.

Conflicts of Interest: The authors declare no conflict of interest.

References

1. Leal, B.B.J.; Wakabayashi, N.; Oyama, K.; Kamiya, H.; Braghirolli, D.I.; Pranke, P. Vascular Tissue engineering: Polymers and methodologies for small caliber vascular grafts. *Front. Cardiovasc. Med.* **2021**, *7*, 592361. [CrossRef] [PubMed]
2. Devillard, C.D.; Marquette, C.A. Vascular Tissue Engineering: Challenges and Requirements for an Ideal Large Scale Blood Vessel. *Front. Bioeng. Biotechnol.* **2021**, *9*, 721843. [CrossRef] [PubMed]
3. Braghirolli, D.; Helfer, V.; Chagastelles, P.; Dalberto, T.; Gamba, D.; Pranke, P. Electrospun scaffolds functionalized with heparin and vascular endothelial growth factor increase the proliferation of endothelial progenitor cells. *Biomed. Mater.* **2017**, *12*, 025003. [CrossRef] [PubMed]
4. Jia, W.; Li, M.; Weng, H.; Gu, G.; Chen, Z. Design and comprehensive assessment of a biomimetic tri-layer tubular scaffold via biodegradable polymers for vascular tissue engineering applications. *Mat. Sci. Eng. C* **2020**, *110*, 110717. [CrossRef]
5. McGuigan, A.; Sefton, M. The influence of biomaterials on endothelial cell thrombogenicity. *Biomaterials* **2007**, *28*, 2547–2571. [CrossRef]
6. Gao, J.; Jiang, L.; Liang, Q.; Shi, J.; Hou, D.; Tang, D.; Chen, S.; Kong, D.; Wang, S. The grafts modified by heparinization and catalytic nitric oxide generation used for vascular implantation in rats. *Regen. Biomater.* **2018**, *5*, 105–114. [CrossRef]
7. Benrashid, E.; McCoy, C.; Youngwirth, L.; Kim, J.; Manson, R.; Otto, J.; Lawson, J.H. Tissue engineered vascular grafts: Origins, development, and current strategies for clinical application. *Methods* **2016**, *99*, 13–19. [CrossRef]
8. Wang, Z.; Mithieux, S.; Weiss, A. Fabrication techniques for vascular and vascularized tissue engineering. *Adv. Healthc. Mater.* **2019**, *8*, 1900742. [CrossRef]

9. Ercolani, E.; Gaudio, C.; Bianco, A. Vascular tissue engineering of small diameter blood vessels: Reviewing the electrospinning approach. *J. Tissue. Eng. Regen. Med.* **2015**, *9*, 861–888. [CrossRef]
10. Carrabba, M.; Madeddu, P. Current strategies for the manufacture of small size tissue engineering vascular grafts. *Front. Bioeng. Biotechnol.* **2018**, *6*, 41. [CrossRef]
11. Boland, E.D.; Matthews, J.A.; Pawlowski, K.J.; Simpson, D.G.; Wnek, G.E.; Bowlin, G.L. Electrospinning collagen and elastin: Preliminary vascular tissue engineering. *Front. Biosci.* **2004**, *9*, 1422–1432. [CrossRef] [PubMed]
12. Buttafoco, L.; Engbers-Buijtenhuijs, P.; Poot, A.A.; Dijkstra, P.J.; Daamen, W.F.; van Kuppevelt, T.H.; Vermes, I.; Feijen, J. First steps towards tissue engineering of small-diameter blood vessels: Preparation of flat scaffolds of collagen and elastin by means of freeze drying. *J. Biomed. Mater. Res. B* **2006**, *77*, 357–368. [CrossRef] [PubMed]
13. Koens, M.J.; Faraj, K.A.; Wismans, R.G.; van der Vliet, J.A.; Krasznai, A.G.; Cuijpers, V.M.; Jansen, J.A.; Daamen, W.F.; van Kuppevelt, T.H. Controlled fabrication of triple layered and molecularly defined collagen/elastin vascular grafts resembling the native blood vessel. *Acta Biomater.* **2010**, *6*, 4666–4674. [CrossRef] [PubMed]
14. Chen, Q.; Bruyneel, A.; Carr, C.; Czernuszka, J. Biomechanical properties of novel bi-layer collagen-elastin scaffolds for heart valve tissue engineering. *Proc. Eng.* **2013**, *59*, 247–254. [CrossRef]
15. Rosellini, E.; Zhang, Y.S.; Migliori, B.; Barbani, N.; Lazzeri, L.; Shin, S.R.; Dokmeci, M.R.; Cascone, M.G. Protein/polysaccharide-based scaffolds mimicking native extracellular matrix for cardiac tissue engineering applications. *J. Biomed. Mater. Res. Part A* **2018**, *106*, 769–781. [CrossRef] [PubMed]
16. Han, C.; Luo, X.; Zou, D.; Li, J.; Zhang, K.; Yang, P.; Huang, N. Nature-inspired extracellular matrix coating produced by micro-patterned smooth muscle and endothelial cells endows cardiovascular materials with better biocompatibility. *Biomater. Sci.* **2019**, *7*, 2686–2701. [CrossRef]
17. Schieber, R.; Lasserre, F.; Hans, M.; Fernandez-Yague, M.; Diaz-Ricart, M.; Escolar, G.; Ginebra, M.P.; Mucklich, F.; Pegueroles, M. Direct laser interference patterning of CoCr alloy surfaces to control endothelial cell and platelet response for cardiovascular applications. *Adv. Healthc. Mater.* **2017**, *6*, 1700327. [CrossRef]
18. Cortella, L.R.X.; Cestari, I.A.; Guenther, D.; Lasagni, A.F.; Cestari, I.N. Endothelial cell responses to castor oil-based polyurethane substrates functionalized by direct laser ablation. *Biomed. Mater.* **2017**, *12*, 065010. [CrossRef]
19. Kang, I.G.; Park, C.I.; Seong, Y.J.; Lee, H.; Kim, H.E.; Han, C.M. Bioactive and mechanically stable hydroxyapatite patterning for rapid endothelialization of artificial vascular graft. *Mater. Sci. Eng. C* **2020**, *106*, 110287. [CrossRef]
20. Chun, Y.; Kealey, C.P.; Levi, D.S.; Ridberg, D.A.; Chen, Y.; Tillman, B.W.; Mohanchandra, K.P.; Shayan, M.; Carman, G.P. An in vivo pilot study of a microporous thin film nitinol-covered stent to assess the effect of porosity and pore geometry on device interaction with the vessel wall. *J. Biomater. Appl.* **2017**, *31*, 1196–1202. [CrossRef]
21. Liu, T.; Liu, S.; Zhang, K.; Chen, J.; Huang, N. Endothelialization of implanted cardiovascular biomaterial surfaces: The development from in vitro to in vivo. *J. Biomed. Mater. Res. A* **2014**, *102*, 3754–3772. [CrossRef] [PubMed]
22. Chang, H.; Zhang, H.; Hu, M.; Chen, J.Y.; Li, B.C.; Ren, K.F.; Martins, M.C.L.; Barbosa, M.A.; Ji, J. Stiffness of polyelectrolyte multilayer film influences endothelial function of endothelial cell monolayer. *Colloids Surf. B Biointerfaces* **2017**, *149*, 379–387. [CrossRef] [PubMed]
23. Zhang, L.; Wei, F.; Bai, Q.; Song, D.; Zheng, Z.; Wang, Y.; Liu, X.; Abdulrahman, A.A.; Bian, Y.; Xu, X.; et al. Oscillating magnetic field regulates cell adherence and endothelialization based on magnetic nanoparticle-modified bacterial cellulose. *ACS Appl. Mater. Interfaces* **2020**, *12*, 52467–52478. [CrossRef] [PubMed]
24. Zhang, H.; Chang, H.; Wang, L.M.; Ren, K.F.; Martins, M.C.L.; Barbosa, M.A.; Ji, J. Effect of polyelectrolyte film stiffness on endothelial cells during endothelial-to-mesenchymal transition. *Biomacromolecules* **2015**, *16*, 3584–3593. [CrossRef]
25. Zhang, M.; Wang, Z.; Wang, Z.; Feng, S.; Xu, H.; Zhao, Q.; Wang, S.; Fang, J.; Qiao, M.; Kong, D. Immobilization of anti-CD31 antibody on electrospun poly(ϵ -caprolactone) scaffolds through hydrophobins for specific adhesion of endothelial cells. *Colloid. Surface. B* **2011**, *85*, 32–39. [CrossRef]
26. Duan, Y.; Yu, S.; Xu, P.; Wang, X.; Feng, X.; Mao, Z.; Gao, C. Co-immobilization of CD133 antibodies, vascular endothelial growth factors, and REDV peptide promotes capture, proliferation, and differentiation of endothelial progenitor cells. *Acta Biomater.* **2019**, *96*, 137–148. [CrossRef]
27. Yu, C.; Guan, G.; Glas, S.; Wang, L.; Li, Z.; Turng, L.S. A biomimetic basement membrane consisted of hybrid aligned nanofibers and microfibers with immobilized collagen IV and laminin for rapid endothelialization. *Bio. Des. Manuf.* **2021**, *4*, 171–189. [CrossRef]
28. Liu, Y.; Munisso, M.C.; Mahara, A.; Kambe, Y.; Yamaoka, T. Anti-platelet adhesion and in situ capture of circulating endothelial progenitor cells on ePTFE surface modified with poly(2-ethylacryloyloxyethyl phosphorylcholine) (PMPC) and hemocompatible peptide 1 (HCP-1). *Colloids Surf. B Biointerfaces* **2020**, *193*, 111113. [CrossRef]
29. Hersel, U.; Dahmen, C.; Kessler, H. RGD modified polymers: Biomaterials for stimulated cell adhesion and beyond. *Biomaterials* **2003**, *24*, 4385–4415. [CrossRef]
30. Hasan, A.; Memic, A.; Annabi, N.; Hossain, M.; Paul, A.; Dokmeci, M.R.; Dehghani, F.; Khademhosseini, A. Electrospun scaffolds for tissue engineering of vascular grafts. *Acta Biomater.* **2014**, *10*, 11–25. [CrossRef]
31. Zhang, X.; Chen, X.; Hong, H.; Hu, R.; Liu, J.; Liu, C. Decellularized extracellular matrix scaffolds: Recent trends and emerging strategies in tissue engineering. *Bioact. Mater.* **2022**, *10*, 15–31. [CrossRef] [PubMed]

32. Butruk-Raszeja, B.A.; Dresler, M.S.; Kuźmińska, A.; Ciach, T. Endothelialization of polyurethanes: Surface silanization and immobilization of REDV peptide. *Colloids Surf. B Biointerfaces* **2016**, *144*, 335–343. [CrossRef] [PubMed]
33. Cai, Q.; Liao, W.; Xue, F.; Wang, X.; Zhou, W.; Li, Y.; Zeng, W. Selection of different endothelialization modes and different seed cells for tissue-engineered vascular graft. *Bioact. Mater.* **2021**, *6*, 2557–2568. [CrossRef] [PubMed]
34. Rai, R.; Tallawi, M.; Barbani, N.; Frati, C.; Madeddu, D.; Cavalli, S.; Graiani, G.; Quaini, F.; Roether, J.A.; Schubert, D.W.; et al. Biomimetic poly(glycerol sebacate) (PGS) membranes for cardiac patch application. *Mater. Sci. Eng. C-Mater. Biol. Appl.* **2013**, *33*, 3677–3687. [CrossRef] [PubMed]
35. Rosellini, E.; Cristallini, C.; Guerra, G.D.; Barbani, N. Surface chemical immobilization of bioactive peptides on synthetic polymers for cardiac tissue engineering. *J. Biomater. Sci. Polym. Ed.* **2015**, *26*, 515–533. [CrossRef] [PubMed]
36. *ISO 10993-13; Biological Evaluation of Medical Devices Identification and Quantification of Degradation Products from Polymeric Medical Devices*. International Organization for Standardization: Geneva, Switzerland, 1998.
37. Denniss, S.; Rush, J. Polyvinylpyrrolidone can be used to cost-effectively increase the viscosity of culture media. *FASEB J.* **2015**, *29*, 1029. [CrossRef]
38. *ISO 7198; Cardiovascular Implants and Extracorporeal Systems—Vascular Prostheses—Tubular Vascular Grafts and Vascular Patches*. International Organization for Standardization: Geneva, Switzerland, 2016.
39. *ISO 11137-2; Sterilization of Health Care Products—Radiation—Part 2: Establishing the Sterilization Dose*. International Organization for Standardization: Geneva, Switzerland, 2013.
40. *ISO 10993-5; Biological Evaluation of Medical Devices—Part 5: Tests for In Vitro Cytotoxicity*. International Organization for Standardization: Geneva, Switzerland, 2009.
41. Daniliuc, L.; De Kasel, C.; David, C. Intermolecular interactions in blends of poly(vinyl alcohol) with poly(acrylic acid)-1. FTIR and DSC studies. *Eur. Polym. J.* **1992**, *28*, 1365–1371. [CrossRef]
42. Rosellini, E.; Madeddu, D.; Barbani, N.; Frati, C.; Graiani, G.; Falco, A.; Lagrasta, C.; Quaini, F.; Cascone, M.G. Development of biomimetic alginate/gelatin/elastin sponges with recognition properties toward bioactive peptides for cardiac tissue engineering. *Biomimetics* **2020**, *20*, 67. [CrossRef]
43. Segtnan, V.H.; Isaksson, T. Temperature, sample and time dependant structural characteristics of gelatin gels studied by near infrared spectroscopy. *Food Hydrocoll.* **2004**, *18*, 1–11. [CrossRef]
44. Debelle, L.; Alix, A.J.P.; Jacobi, M.P.; Huvenne, J.P.; Berjot, M.; Sombret, B.; Legrand, P. Bovine Elastin and k-Elastin Secondary Structure Determination by Optical Spectroscopies. *J. Biol. Chem.* **1995**, *270*, 26099–26103. [CrossRef]
45. Fleury, G.; Schlatter, G.; Brochon, C.; Hadziioannou, G. From high molecular weight precursor polyrotaxanes to supramolecular sliding networks. The ‘sliding gels’. *Polymer* **2005**, *46*, 8494–8501. [CrossRef]
46. Celli, J.P.; Turner, B.S.; Afdhal, N.H.; Ewoldt, R.H.; McKinley, G.H.; Bansil, R.; Erramilli, S. Rheology of gastric mucin exhibits a pH-dependent sol-gel transition. *Biomacromolecules* **2007**, *8*, 1580–1586. [CrossRef] [PubMed]
47. Camasao, D.B.; Mantovani, D. The mechanical characterization of blood vessels and their substitutes in the continuous quest for physiological-relevant performances. A critical review. *Mater. Today* **2021**, *10*, 100106. [CrossRef] [PubMed]
48. Khosravi, A.; Salimi Bani, M.; Bahreinizad, H.; Karimi, A. Viscoelastic properties of the autologous bypass grafts: A comparative study among the small saphenous vein and internal thoracic artery. *Artery Res.* **2017**, *19*, 65–71. [CrossRef]
49. Liu, Y.; Chan-Park, M.B. Hydrogel based on interpenetrating polymer networks of dextran and gelatin for vascular tissue engineering. *Biomaterials* **2009**, *30*, 196–207. [CrossRef]
50. Kim, H.M.; Kokubo, T.; Fujibayashi, S.; Nishiguchi, S.; Nakamura, T. Bioactive macroporous titanium surface layer on titanium substrate. *J. Biomed. Mater. Res. Part A* **2000**, *52*, 553–557. [CrossRef]
51. L’Heureux, N.; Dusserre, N.; Konig, G.; Victor, B.; Keire, P.; Wight, T.N.; Chronos, N.A.F.; Kyles, A.E.; Gregory, C.R.; Hoyt, G.; et al. Human tissue-engineered blood vessels for adult arterial revascularization. *Nat. Med.* **2006**, *12*, 361–365. [CrossRef]
52. Soletti, L.I.; Hong, Y.; Guan, J.; Stankus, J.J.; El-Kurdi, M.S.; Wagner, W.R.; Vorp, D.A. A bilayered elastomeric scaffold for tissue engineering of small diameter vascular grafts. *Acta Biomater.* **2010**, *6*, 110–122. [CrossRef]
53. Shin, H.; Jo, S.; Mikos, A.G. Biomimetic materials for tissue engineering. *Biomaterials* **2003**, *24*, 4353–4364. [CrossRef]
54. Patel, S.; Tsang, J.; Harbers, G.M.; Healy, K.E.; Li, S. Regulation of endothelial cell function by GRGDSP peptide grafted on interpenetrating polymers. *J. Biomed. Mater. Res.* **2007**, *83A*, 423–433. [CrossRef]
55. Massia, S.P.; Hubbell, J.A. An RGD spacing of 440 nm is sufficient for integrin alpha V beta 3-mediated fibroblast spreading and 140 nm for focal contact and stress fiber formation. *J. Cell Biol.* **1991**, *114*, 1089–1100. [CrossRef] [PubMed]



Article

The Mechanics of Bioinspired Stiff-to-Compliant Multi-Material 3D-Printed Interfaces

Dolev Frenkel [†], Eran Ginsbury [†] and Mirit Sharabi *

Department of Mechanical Engineering and Mechatronics, Ariel University, Ariel 407000, Israel

* Correspondence: miritsh@ariel.ac.il; Tel.: +972-3-6453159

[†] These authors contributed equally to this work.

Abstract: Complex interfaces that involve a combination of stiff and compliant materials are widely prevalent in nature. This combination creates a superior assemblage with strength and toughness. When combining two different materials with large stiffness variations, an interfacial stress concentration is created, decreasing the structural integrity and making the structure more prone to failure. However, nature frequently combines two dissimilar materials with different properties. Additive manufacturing (AM) and 3D printing have revolutionized our engineering capabilities concerning the combination of stiff and compliant materials. The emergence of multi-material 3D-printing technologies has allowed the design of complex interfaces with combined strength and toughness, which is often challenging to achieve in homogeneous materials. Herein, we combined commercial 3D-printed stiff (PETG) and compliant (TPU) polymers using simple and bioinspired interfaces using a fused deposition modeling (FDM) printer and characterized the mechanical behaviors of the interfaces. Furthermore, we examined how the different structural parameters, such as the printing resolution (RES) and horizontal overlap distance (HOD), affect the mechanical properties. We found that the bioinspired interfaces significantly increased the strain, toughness, and tensile modulus compared with the simple interface. Furthermore, the more refined printing resolution elevated the yield stress, while the increased overlap distance mostly elevated the strain and toughness. Additionally, 3D printing allows the fabrication of other complex designs in the stiff and compliant material interface, allowing various tailor-designed and bioinspired interfaces. The importance of these bioinspired interfaces can be manifested in the biomedical and robotic fields and through interface combinations.

Keywords: interface; bioinspired materials; stiffness; strength; biomimetics; 3D printing; mechanical testing; stiff-to-compliant

Citation: Frenkel, D.; Ginsbury, E.; Sharabi, M. The Mechanics of Bioinspired Stiff-to-Compliant Multi-Material 3D-Printed Interfaces. *Biomimetics* **2022**, *7*, 170. <https://doi.org/10.3390/biomimetics7040170>

Academic Editors: Stanislav N. Gorb, Giuseppe Carbone, Thomas Speck and Andreas Taubert

Received: 14 September 2022

Accepted: 17 October 2022

Published: 18 October 2022

Publisher's Note: MDPI stays neutral with regard to jurisdictional claims in published maps and institutional affiliations.



Copyright: © 2022 by the authors. Licensee MDPI, Basel, Switzerland. This article is an open access article distributed under the terms and conditions of the Creative Commons Attribution (CC BY) license (<https://creativecommons.org/licenses/by/4.0/>).

1. Introduction

The combination of dissimilar materials in a single structure is an effective approach to improve the mechanical performance. The emergence of 3D printing technologies has enabled and facilitated the design of these multi-material structures while highlighting the diverse interfacial possibilities [1,2]. These multi-material 3D printing technologies hold potential in many areas, such as in biomedical, soft electronics, optoelectronics, aerospace, and robotics applications [3,4].

Bioinspired interfaces combining stiff-to-compliant materials can improve these multi-material structures, as widely prevalent in natural materials. This combination creates a superior assemblage with strength and toughness [5,6]. For example, in the insertion site, the binding between the tendon and bone allows proper load transfer between the stiff bone (with an elastic modulus of ~20 GPa) and compliant tendon, whose elastic stiffness is 2–3 orders of magnitude lower [7,8]. Moreover, in bone and nacre, a compliant protein matrix is one of the mechanisms that allow damage tolerance and superior toughness [9,10]. In fish armor and sea sponges, interlocking mechanisms, fractal designs, and sutures enhance the interfacial stiffness and strength and increase the resistance to crack propagation [11–13].

When combining two different materials with large stiffness variations, an interfacial stress concentration is created, decreasing the structural integrity and making the structure more prone to failure. However, nature frequently combines two dissimilar materials with different properties [5].

Furthermore, the fracture toughness of brittle materials can be improved using interfacial engineering. i.e., the presence of soft and compliant materials in the interface between stiff constituents can significantly increase the fracture toughness through structural mechanisms such as the fractal design and crack deflection [14].

Bone–tendon and bone–ligament interfaces are responsible for attaching muscles to bones to transfer muscle forces and provide joint stability, respectively. These multi-material interfaces (entheses) carry large loads using diverse structural mechanisms. One of these mechanisms includes the overlap of the collagen fibers that intrude into the bone, providing a firmer hold between the stiff bone and compliant tendon or ligament while allowing an effective transition between materials with different mechanical properties at several length scales [7].

Biomimetics and bioinspiration have brought about numerous advances in the design of materials and interfaces. Using traditional processing techniques, mimicking the stiff-to-compliant native interfaces based on their complex structure, functional gradient, and composition is a genuine engineering challenge. However, additive manufacturing (AM) and 3D printing have revolutionized our engineering capabilities relating to the combination of stiff and compliant materials [15]. The emergence of multi-material 3D printing technologies allows the design of complex interfaces with combined strength and toughness, which is often challenging to achieve in homogeneous materials [6,16]. Although restricted to polymers, the latter is a unique approach for combining materials with elastic properties varying over three orders of magnitude. This combination demonstrated increased toughness similar to natural materials [14,16–20].

Different 3D printing technologies have been established over the last few years [15,21]. However, multi-material 3D printing is often achieved using state-of-the-art polyjet printers [14,18,20,22]. In this method, photocurable polymeric inks are pre-blended to fabricate polymeric materials using specific tailor-designed polymers [18].

The more common and affordable fused deposition modeling (FDM) 3D printers are not commonly used for 3D-printed multi-material interfaces.

In this study, we combined commercial 3D-printed stiff (PETG) and compliant (TPU) polymers using simple and bioinspired interfaces using an FDM printer and characterized the mechanical behavior of these interfaces. We used digital image correlation (DIC) to quantify the displacements and strains of the multi-material printed samples. Moreover, we examined how the different structural parameters, such as the printing resolution (RES) and horizontal overlap distance (HOD), affect the different mechanical properties in tailor-designed stiff–compliant 3D-printed interfaces.

2. Materials and Methods

2.1. Sample Preparation

All samples were designed using Solidworks (Dassault Systemes, France) and printed with a single printing head using an FDM Ender 5 printer (Creality 3D; Shenzhen, China). The 3D printer has a resolution of 50 μm in the z-direction (thickness) and 100 μm in the x and y-direction.

Polyethylene terephthalate glycol (PETG, eSUN, Shenzhen, China) was used for the stiff material and thermoplastic polyurethane (TPU, eSUN, Shenzhen, China), a rubber-like compliant material, was used for the compliant material. The CAD file was saved as a stereolithography (STL) file and sliced using Ultimaker Cura (Ultimaker B.V., Utrecht, The Netherlands) software to obtain the G code for the printer. The printing was performed in an enclosed chamber in a temperature-controlled environment with 100% infill.

The interface was controlled via the resolution (RES, layer thickness) and the horizontal overlap distance (HOD, Figure 1). The G-codes for layer 1 and G layer 2 (different materials)

were merged into a single file to get a sequence of alternated layers (Supplementary Materials, File S1). The overlap distance included the same amount of layers of each material, and the resolution was affected by the applied pressure by the printer (Figure 1). The 3D-printed sample dimensions were 1 mm in thickness, 5 mm in width, and 16.6 mm in gage length (Figure 2).

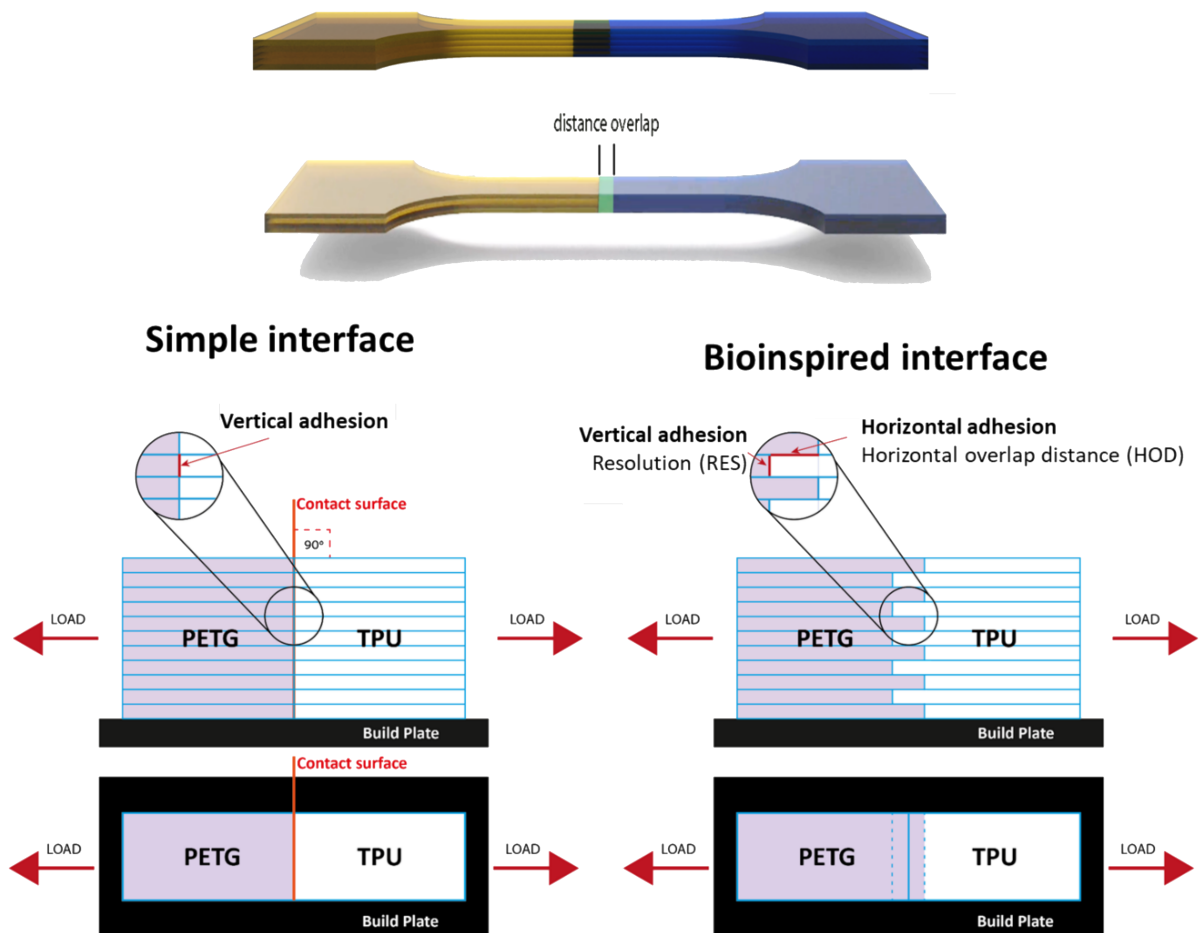


Figure 1. Schematic illustration of 3D-printed stiff-to-compliant interface samples. Simple interface (left) vs. bioinspired interface (right) with the effects of the resolution (RES) and horizontal overlap distance (HOD).

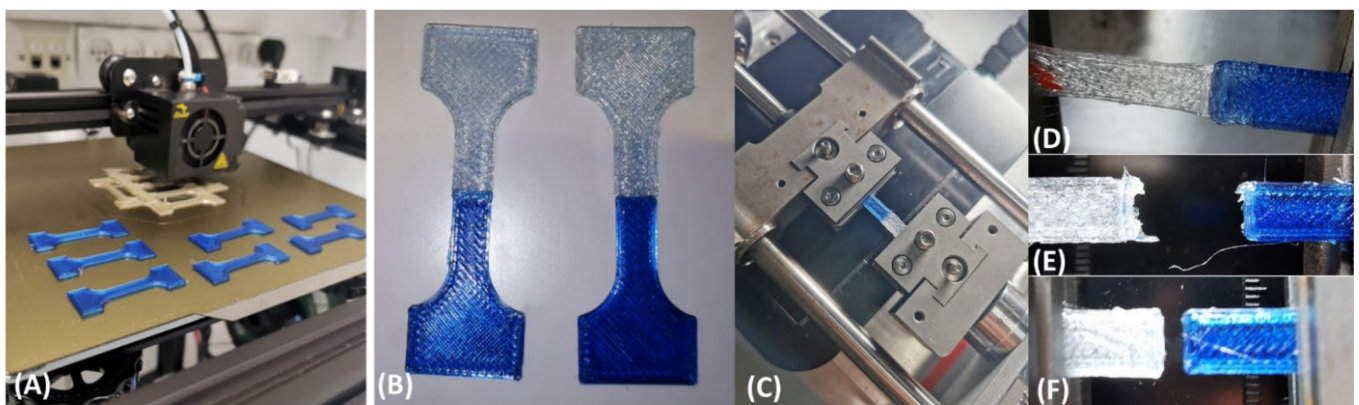


Figure 2. (A) The 3D printing of dog bones. (B–F) Combined stiff (PETG, blue) and compliant (TPU, white) samples after printing (B) under tensile testing and failure testing (C–F).

2.2. Mechanical Testing

The tensile testing was performed using the μ TS load frame (PsysloTech, Evanston, IL, USA) using 222 N and 1600 N load cells. The samples were stretched to failure at a rate of $3 \text{ mm} \cdot \text{min}^{-1}$ under displacement control. The 1600 N load cell was used for the PETG samples and the 222 N load cell was used for the TPU and combined material specimens. The sample dimensions were measured using a digital caliper and a micrometer.

Here, 2D digital image correlation (DIC) was applied initially to examine the behavior of the combined interface. Due to the large deformations of the TPU, it was applied only to representative samples. DIC measurements and analyses were employed using 12-bit CCD digital camera (MER-503-20GM-P, Daheng, China) with a macro lens (100 mm F2.8, Nikon) and GOM Correlate software 2019 (GOM GmbH, Braunschweig, Germany). The 12-bit CCD camera consisted of a trigger that was connected to the PsysloTech load frame for load data synchronization between the tensile machine and the camera. The test data were recorded using a camera rate of 15 Hz and were synchronized with the loading frame measurements. The sample preparation included spraying a very delicate thin layer of white paint and then black paint on top of the white one to achieve adequate contrast and a random speckle pattern to get a good contrast for the DIC post-processing algorithm (Figure 3).

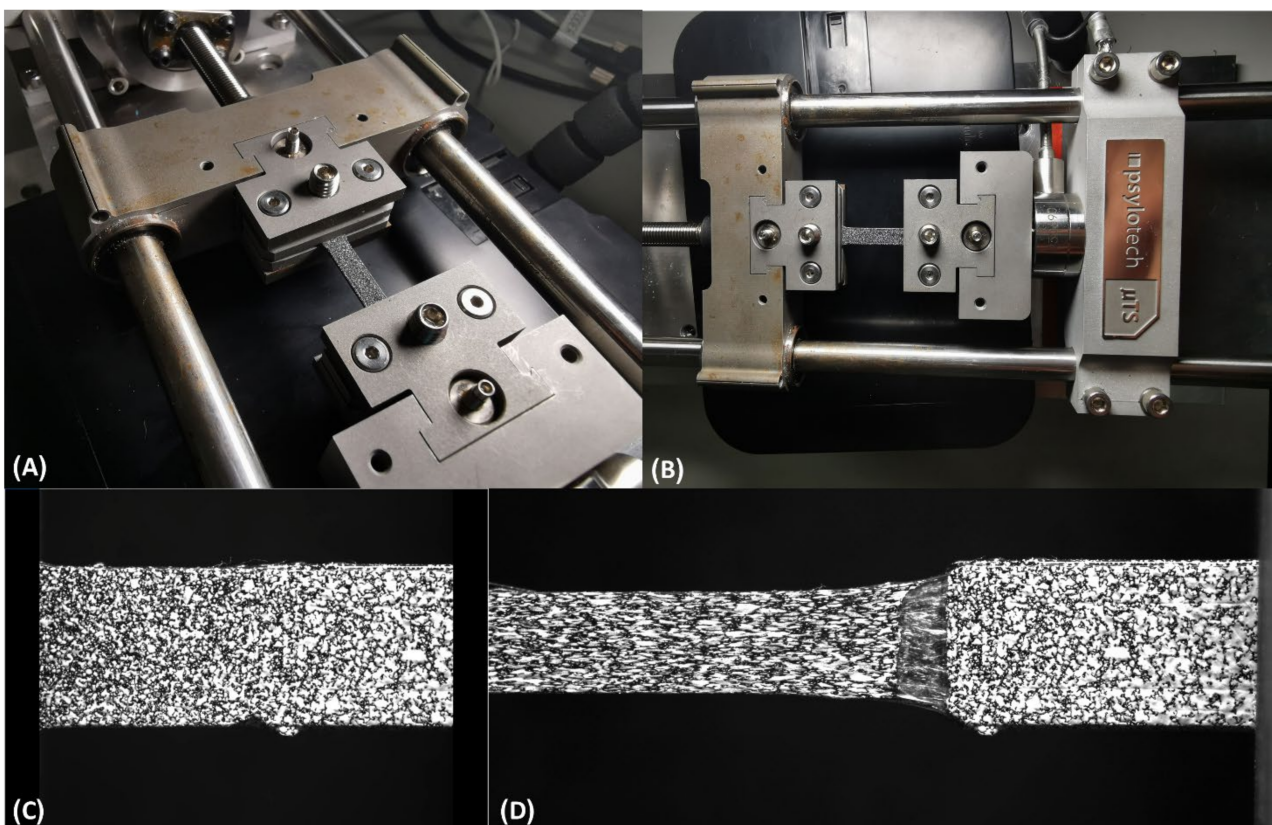


Figure 3. Combined stiff and compliant samples under tensile test with DIC. (A,B) Random-colored samples under tensile test for DIC post-processing. Speckle pattern of the TPU-PETG sample- before (C) and after (D) tension test.

2.3. Mechanical Measurements

We used engineering stresses and strains, whereby stress was defined as the force divided by the initial cross-sectional area and strain as the displacement divided by the initial gage length. The yield stress was calculated at a strain of 0.05 mm/mm. The ultimate stresses and strains were defined as the maximum stresses and strains, respectively. The moduli were calculated as the slope of the curve up to 0.025 strain. The maximal strain

was taken as the failure strain. The tensile toughness was calculated as the area under the stress–strain curve up to failure using the trapezoid method.

2.4. Statistical Analysis

For each measurement, the mean and standard deviation were calculated. GraphPad Prism 9[®] was used to perform a one-way ANOVA with multiple comparisons and with a Fisher LSD test analysis or unpaired *t*-tests. Statistical significance was defined as $p < 0.05$.

3. Results

The TPU, PETG, simple, and bioinspired interfaces were 3D-printed and tested mechanically. Three resolutions (RES = 0.10, 0.20, and 0.25 mm), three horizontal overlap distances (HOD, D = 1, 2, and 3 mm), and their combinations were printed and tested (Figures 1 and 2, Table 1).

Table 1. Sample description and geometry.

Sample Name	N	Thickness [mm]	Width [mm]	Gage Length [mm]	Layer Thickness [RES] [mm]	Horizontal Overlap Distance [HOD,D] [mm]
PETG	4	1.02 ± 0.01	4.98 ± 0.01	18.59 ± 0.86	0.2	-
TPU	3	1.10 ± 0.13	5.24 ± 0.36	18.59 ± 0.86	0.2	-
Simple interface	4	1.27 ± 0.09	5.43 ± 0.21	18.74 ± 0.38	0.2	0
Bioinspired interface_0.1_1	3	1.20 ± 0.12	5.26 ± 0.07	17.72 ± 1.29	0.1	1
Bioinspired interface_0.1_2	3	1.23 ± 0.02	5.35 ± 0.13	14.95 ± 2.30	0.1	2
Bioinspired interface_0.1_3	3	1.20 ± 0.01	5.22 ± 0.02	16.58 ± 0.08	0.1	3
Bioinspired interface_0.2_1	3	1.28 ± 0.01	5.25 ± 0.06	17.87 ± 0.34	0.2	1
Bioinspired interface_0.2_2	3	1.20 ± 0.06	5.24 ± 0.02	16.54 ± 0.46	0.2	2
Bioinspired interface_0.2_3	3	1.21 ± 0.01	5.22 ± 0.05	16.53 ± 0.58	0.2	3
Bioinspired interface_0.25_1	3	1.30 ± 0.09	5.25 ± 0.02	16.17 ± 2.47	0.25	1
Bioinspired interface_0.25_2	3	1.40 ± 0.05	5.30 ± 0.09	16.81 ± 0.69	0.25	2
Bioinspired interface_0.25_3	3	1.35 ± 0.05	5.27 ± 0.02	16.79 ± 0.93	0.25	3

The samples with multi-material interfaces demonstrated a minor increase in thickness and width compared with single material 3D printing due to the accuracy of the printer.

Representative samples with bioinspired interfaces were captured and measured using the DIC method (Figure 3). The displacements and strains of a representative sample with a bioinspired interface were measured at $t = 0, 55,$ and 135 s (with corresponding stresses of 0, 7.3 and 8.5 MPa, respectively) (Figure 4). As expected, the TPU was mainly deformed, while the PETG stayed stiff. The failure started at the interface, which was subjected to large deformations (up to ~25% strain). The transition between the stiff and compliant materials can be clearly seen in the DIC results (Figure 4). However, the DIC algorithm we used was limited to deformation and strain of approximately 5 mm and 25%, respectively. Above these values, the DIC algorithm could trace the speckle pattern changes.

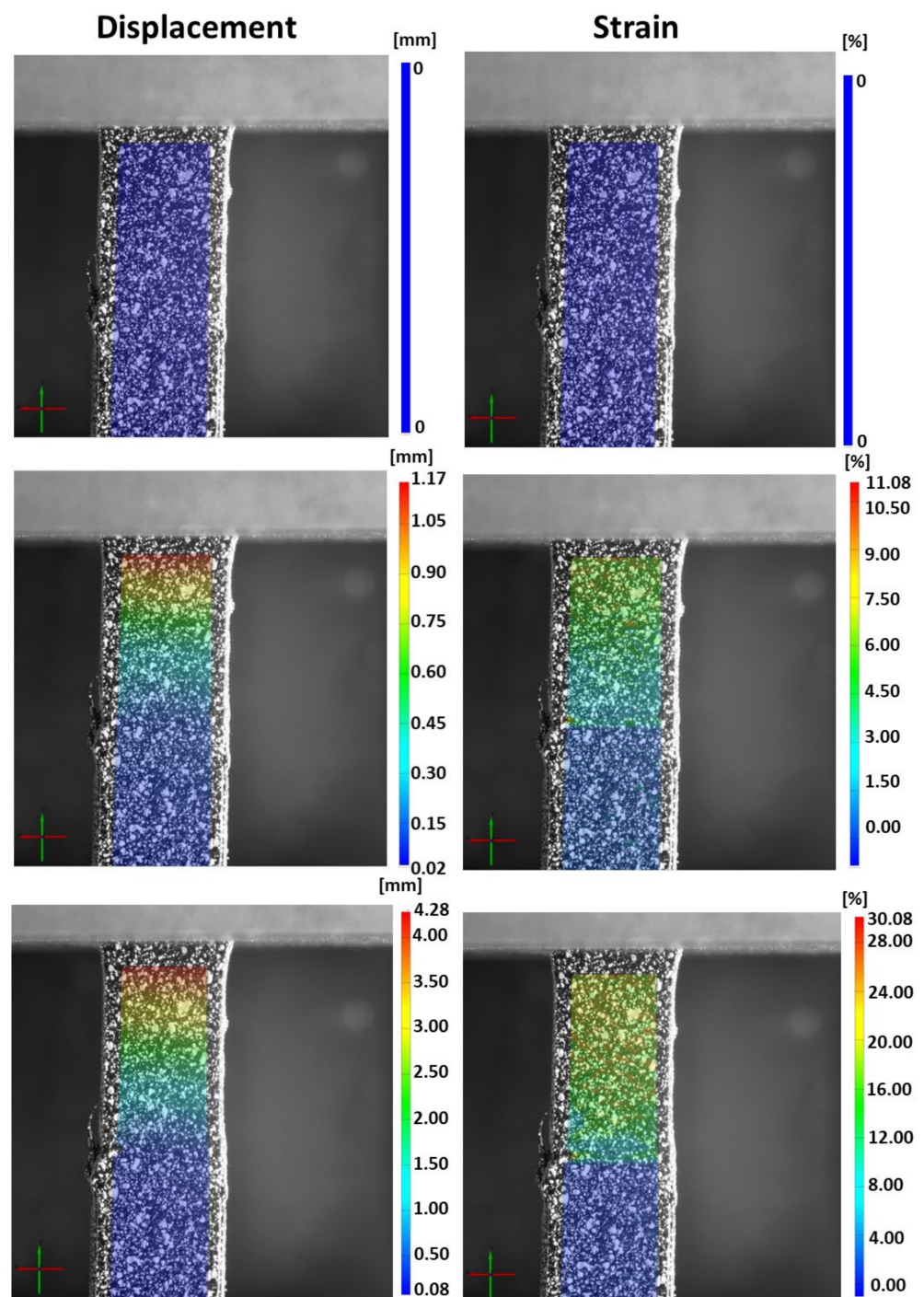


Figure 4. DIC measurements (strains and displacements) for of a sample with a bioinspired interface at $t = 0, 55,$ and 135 s.

The overall mechanical behavior results of the PETG, TPU, and combined samples with the simple and bioinspired interfaces are presented in Figure 5. The 3D-printed TPU samples demonstrated large deformations and toughness and relatively small tensile moduli. The PETG samples demonstrated a large tensile modulus and small deformations (Figures 5 and 6). When combining these materials, the stress concentration in the interface and the failure started in the binding area.

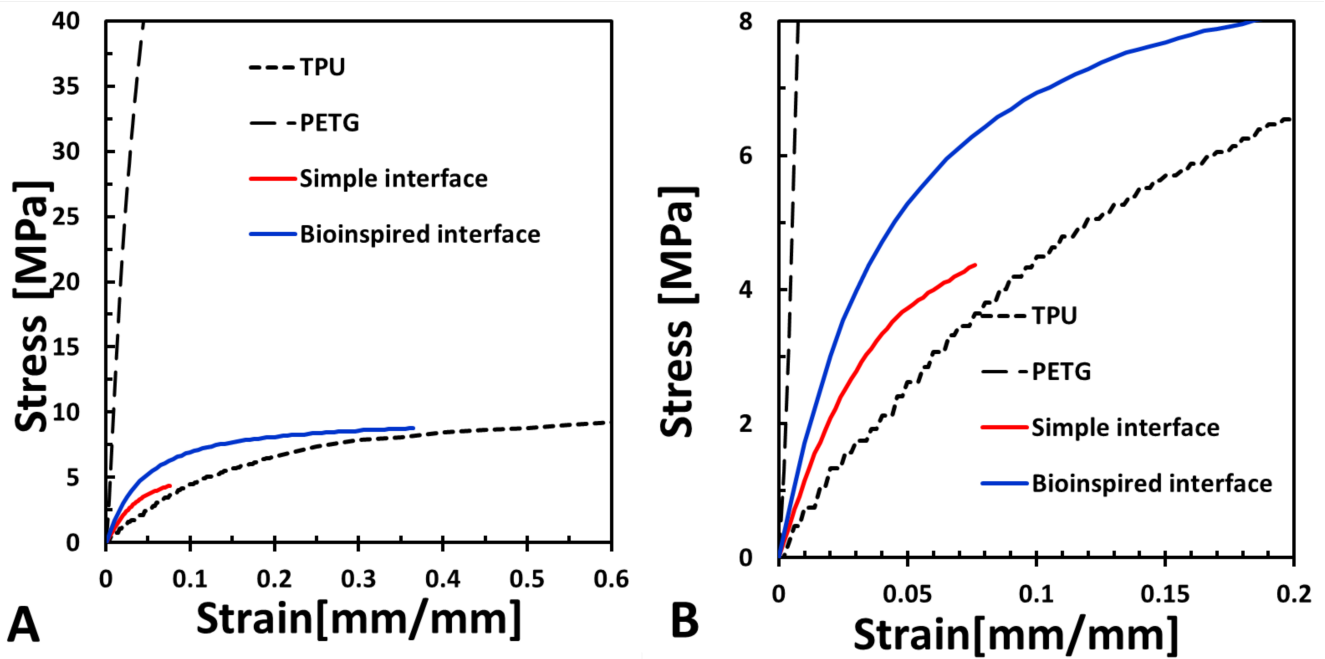


Figure 5. (A,B) Mechanical behavior for 3D-printed PETG, TPU, and combined samples with simple and bioinspired interfaces. (B) is the enlarged representation of (A).

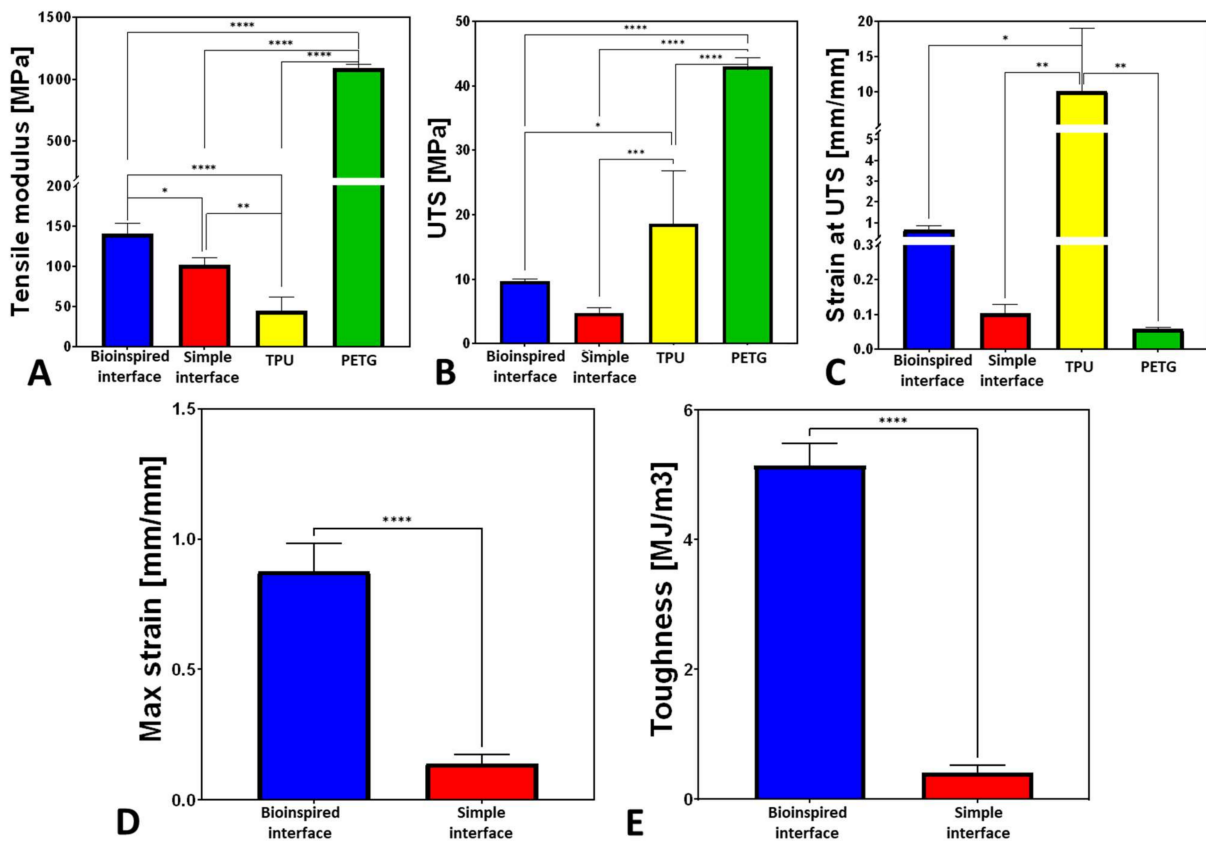


Figure 6. Mechanical properties of 3D-printed PETG, TPU, and combined samples with simple and bioinspired interfaces: (A) tensile modulus; (B) UTS; (C) strain at UTS; (D) maximal strain; (E) tensile toughness. Note: * stands for $p < 0.05$, ** for $p < 0.005$, *** $p < 0.0005$, and **** $p < 0.0001$.

The simple interface was stiffer by 230% than the TPU sample ($p < 0.005$) but less stiff than the PETG sample by an order of magnitude ($p < 0.0001$, Figure 6). The maximal strain in the simple interface was larger by 177% than the PETG.

The bioinspired interface (HOD2, RES0.2) demonstrated significantly improved mechanical properties than the simple interface; the tensile toughness and maximum strain increased by 1259% and 626%, respectively ($p < 0.0001$), the tensile modulus increased by 137% ($p < 0.05$), the UTS increased by 202%, and the strain at UTS increased by 646% (Figure 6).

For all of the tested conditions (with different RES and HOD settings), the bioinspired interfaces demonstrated improved mechanical properties compared with the simple interface. The least influence was seen on the tensile modulus. However, the toughness and strain at UTS demonstrated an increasing trend with the increase in RES for HODs of $D = 2$ and $D = 3$ mm (Figure 7).

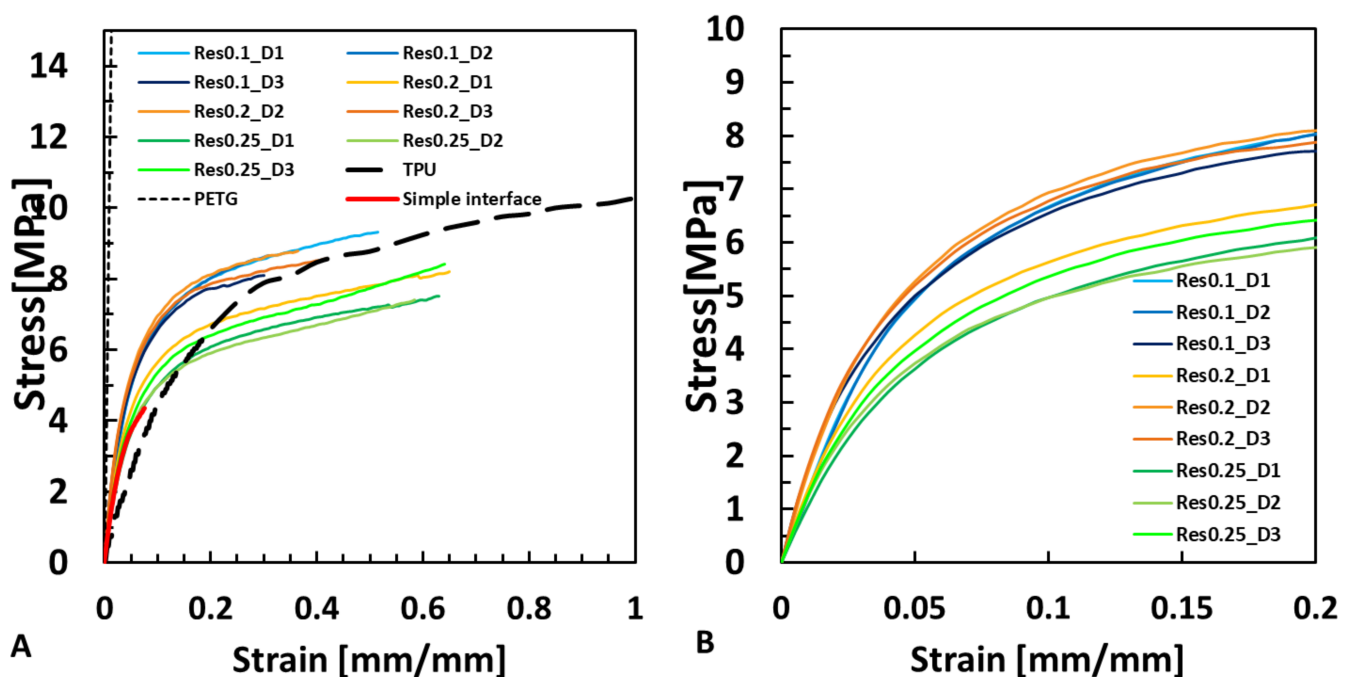


Figure 7. (A) The influence of the resolution (RES) and horizontal overlap distance (HOD, D) parameters on the mechanical behavior in comparison to the TPU, PETG and Simple interface. (B) The influence of RES and HOD in the mechanical behavior up to 0.2 strain.

The influence of the resolution (RES) on the mechanical properties was tested at three different resolutions, 0.1, 0.2, and 0.25 mm, as shown in Figure 8.

More specifically, in the elastic region of the stress–strain curves, there was no major difference between the different samples (Figure 7A,B). However, with larger strains, the simple interface failed (~0.1 mm/mm).

For the same printing resolution (RES), the change in HOD presented significantly increased UTS, toughness, and strain at UTS values compared with the simple interface (Figure 8). For all HODs at RES0.1, the yield stress increased significantly ($p < 0.0005$) compared with the simple interface but not for RES0.25 (Figures 7 and 8E).

The tensile modulus changes did not demonstrate a specific trend and seemed similar for all tested samples at RES0.25. For RES0.2, significant changes in the tensile modulus were observed between HOD2, HOD3, and HOD1 ($p < 0.005$) and between HOD2, HOD3, and the simple interface ($p < 0.0005$, Figure 8B). The bioinspired interface significantly influenced the toughness, with an opposite trend between RES0.1 and RES0.25 (Figure 8C). For RES0.1, the strain at UTS significantly decreased with the increase in HOD ($p < 0.005$). A similar trend was seen for RES0.2 ($p < 0.005$) but not for RES0.25 (Figure 8D).

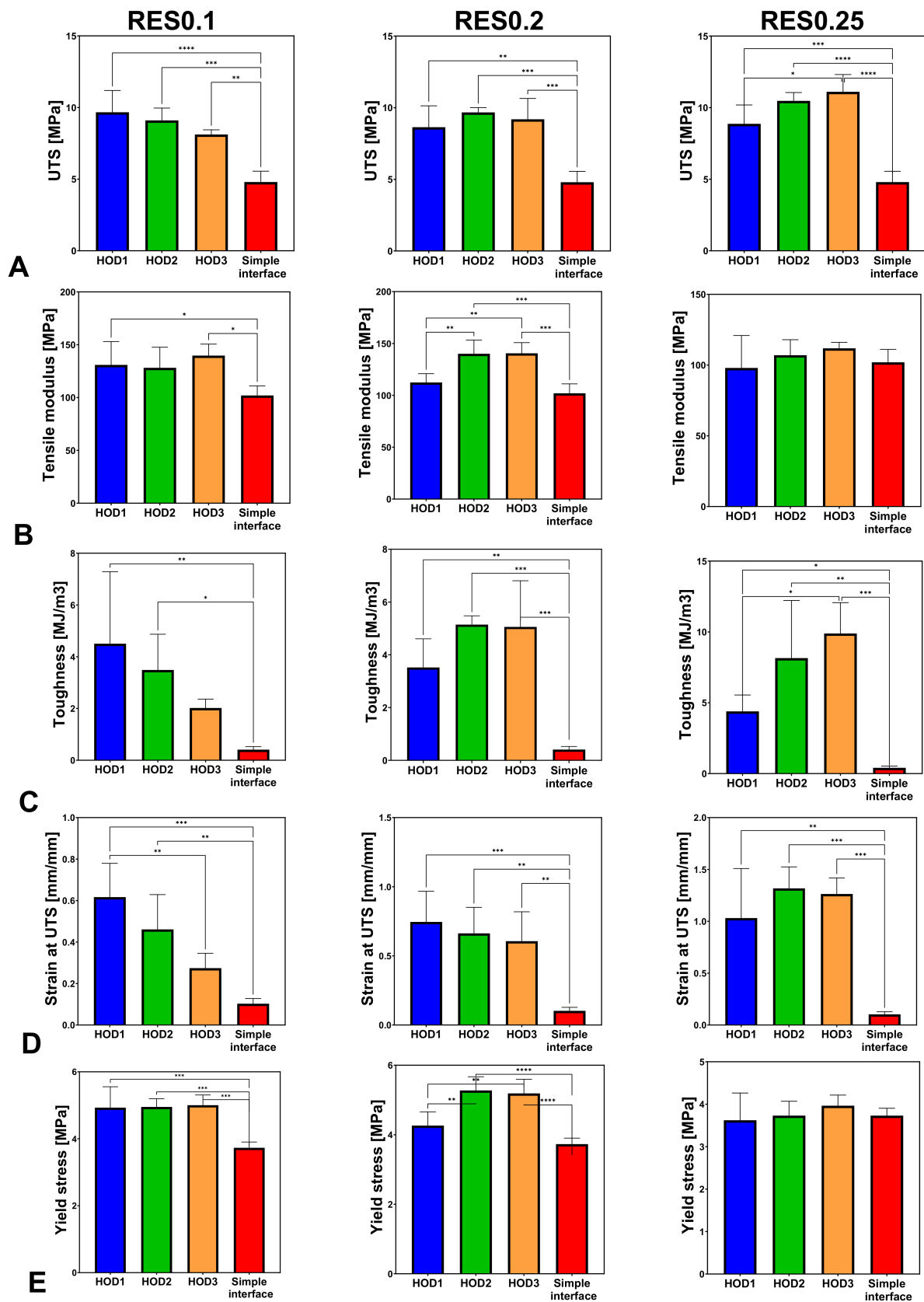


Figure 8. Effect of the horizontal distance (HOD) on the mechanical properties of stiff-to-compliant samples: (A) UTS; (B) tensile modulus; (C) tensile toughness; (D) strain at UTS; (E) yield stress (* stands for $p < 0.05$, ** for $p < 0.005$, *** $p < 0.0005$, and **** $p < 0.0001$).

For the UTS, toughness, and strain at UTS, the effect of the resolution also caused significant changes compared with the simple interface (Figure 9). For RES0.1 (e.g., more printed layers), increased yield stress was observed compared with RES0.25 ($p < 0.005$) (Figure 9E).

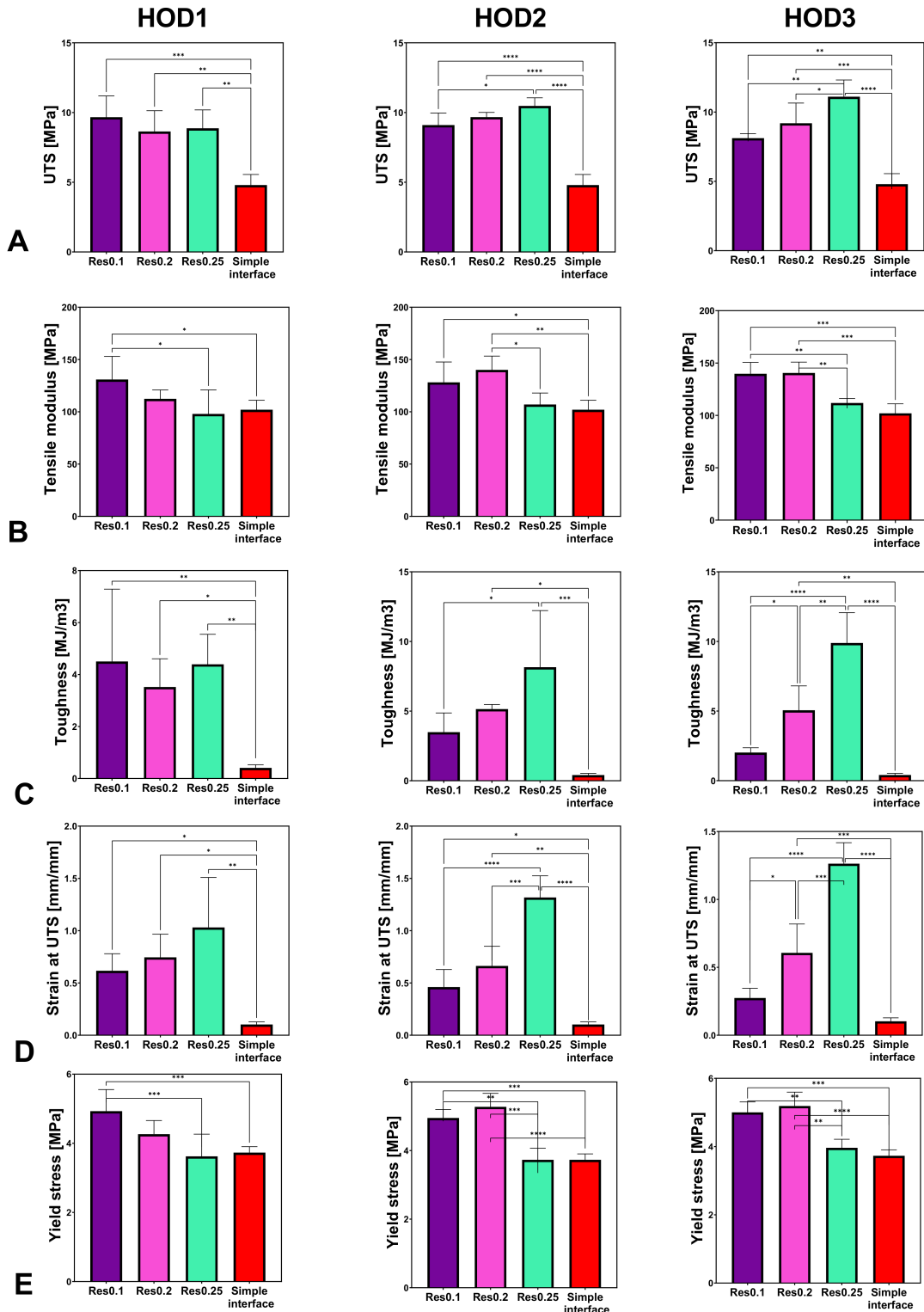


Figure 9. Effect of the resolution (RES) on the mechanical properties of stiff-to-compliant samples: (A) UTS; (B) tensile modulus; (C) tensile toughness; (D) strain at UTS; (E) yield stress (* stands for $p < 0.05$, ** for $p < 0.005$, *** for $p < 0.0005$, and **** for $p < 0.0001$).

A significant increase in UTS was seen for RES0.25 for HOD3 as compared with HOD1 (Figure 9A). Larger moduli were seen for the smaller RES values (RES0.1, RES0.2) (Figure 9B). For HOD2 and HOD3, increases in toughness and strain at UTS were observed when the RES was changed from 0.1 to 0.25 (fewer printed layers) (Figure 9C,D).

The resolution was more influential when the HOD was larger (3 mm). Thus, for the UTS, at $D = 3$ mm, RES0.25 demonstrated a significantly stronger interface than RES0.1 ($p < 0.05$).

4. Discussion

The interface is essential to allow a stiff-to-compliant transition with minimal stress and maximal energy absorbance and toughness. The current research investigated the effect of a bioinspired interface design, i.e., a penetrating design, in the interface between 3D-printed combined stiff (PETG) and compliant (TPU) samples. These interfaces are widely distributed in natural materials, such as in tendon-to-bone insertion sites, which combine the stiff and hard bone with the soft and stretchable ligament. In this study, we investigated how the bioinspired interface behaves mechanically compared with its constituents and how the bioinspired design principles affect the overall tensile behavior using a simple and affordable 3D FDM printer. Unlike conventional fabrication methods, 3D printing can enable the control of the interface.

The mechanical behavior of the interface resulted from the combination of the TPU and PETG materials. TPU provides large strains, ductility, and toughness but is neither strong nor stiff, while PETG is stiff and strong but not tough and ductile. For the simple interface, involving binding between the PETG and TPU in a sharp transition, there is a plane that is subjected to stress concentrations due to a sharp transition between the stiff and compliant materials. As a composite material, the simple interface specimen demonstrated increased strains compared with the PETG and an increased tensile modulus compared with the TPU. However, its failure started in the interface, demonstrating inferior UTS, strain, and toughness values. Unlike the simple interface, the bioinspired interface, which also demonstrated a combination of these two materials, exhibited significantly improved stiffness compared with the TPU, showing even larger strains and increased toughness compared with the PETG.

Thus, the bioinspired interface was far superior to the simple interface for all tested mechanical properties, including the maximal strain, tensile modulus, UTS, strain at UTS, and tensile toughness.

The DIC results demonstrated that the TPU was mainly strained and not the PETG. The bioinspired interface increased the adhesion between the materials and carried large deformations (Figure 3). The DIC algorithm could capture up to 25% strain, which was insufficient to capture the large strains that the interface carried before sample failure (Figures 5 and 7).

The 3D printing technique allowed the bioinspired design of the interface between the TPU and PETG. Inspired by natural designs, in this study we tested the influence of the printing resolution, accounting for the layer thickness and the overlap distance of the 3D-printed materials, as well as their influence on the mechanical properties. We found that all tested bioinspired interfaces significantly increased the strain, toughness, and modulus compared with the simple interface. Furthermore, the more refined printing resolution elevated the yield stress, while the increased overlap distance mostly elevated the strains and toughness. For all tested designs, the mechanical properties were influenced but the ductility and plasticity were the most affected; thus, the toughness, strains, and UTS demonstrated most of the differences compared with the simple interface.

Surprisingly, the most refined resolution (RES0.1) did not always result in the most improved mechanical properties but mostly increased the yield stress (Figure 7). The larger resolutions elevated the strains, UTS, and toughness (Figure 9). Therefore, a refined resolution is not always necessary for the interface. Regarding the overlap distances (HODs) between the materials, a distance of 2 mm resulted in improved results, but an HOD of

1 mm was not enough (Figure 8). The overlapping distance strongly influenced the strain at UTS and toughness, i.e., their values increased with the increasing distance. Therefore, the printing method that included pressure-driven extrusion and an increased interfacial surface area strengthened the binding of the materials, using a toughening mechanism similar to the one observed in the tendon-to-bone enthesis. The enthesis is optimized to reduce the peak stresses and improve the failure resistance [23]. Here, the failure of the bioinspired interfaces was jagged as it is in natural materials, unlike the straight and blunt failure in the simple interface sample (Figure 2E,F).

Different additive manufacturing techniques are used for multi-material printing, mostly state-of-the-art polyjet printing with photocurable polymers. They demonstrate improved mechanical properties of bioinspired interfaces but different results than our FDM results. However, it is important to note that different materials, interfaces, and mechanical properties were investigated. For example, Roach et al. (2019) [24] developed a new novel multi-material multi-method (m4) 3D printer and combined direct ink writing (DIW) and inkjet (IJ) methods. Using that method, they demonstrated an opposite trend to our results, since the samples with overlap interfaces demonstrated inferior toughness compared to the blunt interface samples. This difference could stem from the pressure-driven extrusion during the FDM elevating the attachments between the different materials. Furthermore, Zorzetto et al. (2020) [18] investigated the mechanical properties of polyjet 3D-printed interfaces, including blurred and sharp interfaces. They found that blending stiff and compliant materials does not lead to a homogenous blend but has a biphasic nature. This method is different from FDM; therefore, the resulting interface properties are different. The printing technology, method, and materials strongly influence the interface properties. Thus, the interface optimization is case-dependent. FDM 3D printing is well-distributed and affordable. Therefore, multi-material interface 3D printing designs can affect many industries.

These multi-material interfaces are valuable in many areas, such as biomedical, soft electronics, optoelectronics, aerospace, and robotics applications [3,4]. For example, multi-material 3D printing is used for bone and soft-tissue grafts [25,26], soft actuators [27], medical prostheses [28], soft robotics [28,29], artificial muscles [30], electronics [28,29], and even 3D-printed multi-material wheels [24].

Our main focus in this paper was to investigate the effects of bioinspired interfaces on the interfaces of stiff and compliant 3D-printed materials and the parameters that influence the different mechanical properties. Additional 3D-printed bioinspired mechanisms such as graded transitions [18,22], staggered structures [14,15,20,31–33], and sutures [16] can be further designed to provide superior mechanical properties to the multi-material systems. Improved technologies involving affordable FDM printers would allow nature's complex structures to be replicated in our daily life, profiting from superior mechanical properties.

5. Conclusions

In this study, we demonstrated the mechanical behavior of combined TPU and PETG 3D-printed samples using a simple and affordable FDM printer. The combined samples showed mechanical behavior in between their separate constituents. The interface design significantly influenced the mechanical properties, mainly the stiffness, strain, UTS, and toughness. The simple interface was significantly inferior to the bioinspired interfaces, which included horizontal overlap between the printed layers. We found that to improve the yield stress, a more refined resolution is needed. Moreover, to increase the strain and toughness, an elevated overlap distance is required.

The importance of bioinspired interface designs can be seen in the different applications in the biomedical and robotic fields and through interface combinations.

Supplementary Materials: The following supporting information can be downloaded at: <https://www.mdpi.com/article/10.3390/biomimetics7040170/s1>, File S1: Gcode-PETG and TPU print_0.1mm_1mm.gcode.

Author Contributions: Conceptualization, M.S.; methodology, M.S., D.F. and E.G.; software, D.F. and E.G.; validation, D.F. and E.G.; formal analysis, M.S., D.F. and E.G.; investigation, M.S., D.F. and E.G.; resources, M.S.; data curation, D.F. and E.G.; writing—original draft preparation, M.S., D.F. and E.G.; writing—review and editing, M.S.; visualization, M.S., D.F. and E.G.; supervision, M.S.; project administration, M.S. All authors have read and agreed to the published version of the manuscript.

Funding: This research received no external funding.

Data Availability Statement: Not applicable.

Conflicts of Interest: The authors declare no conflict of interest.

References

- Lopes, L.R.; Silva, A.F.; Carneiro, O.S. Multi-Material 3D Printing: The Relevance of Materials Affinity on the Boundary Interface Performance. *Addit. Manuf.* **2018**, *23*, 45–52. [CrossRef]
- Skylar-Scott, M.A.; Mueller, J.; Visser, C.W.; Lewis, J.A. Voxelated Soft Matter via Multimaterial Multinozzle 3D Printing. *Nature* **2019**, *575*, 330–335. [CrossRef] [PubMed]
- Muralidharan, A.; Uzcatogui, A.C.; McLeod, R.R.; Bryant, S.J. Stereolithographic 3D Printing for Deterministic Control over Integration in Dual-Material Composites. *Adv. Mater. Technol.* **2019**, *4*, 1900592. [CrossRef] [PubMed]
- Rafiee, M.; Farahani, R.D.; Therriault, D. Multi-Material 3D and 4D Printing: A Survey. *Adv. Sci.* **2020**, *7*, 1902307. [CrossRef]
- Wegst, U.G.K.; Bai, H.; Saiz, E.; Tomsia, A.P.; Ritchie, R.O. Bioinspired Structural Materials. *Nat. Mater.* **2015**, *14*, 23–36. [CrossRef]
- Ritchie, R.O. The Conflicts between Strength and Toughness. *Nat. Mater.* **2011**, *10*, 817–822. [CrossRef]
- Pitta Kruize, C.; Panahkhahi, S.; Putra, N.E.; Diaz-Payno, P.; Van Osch, G.; Zadpoor, A.A.; Mirzaali, M.J. Biomimetic Approaches for the Design and Fabrication of Bone-to-Soft Tissue Interfaces. *ACS Biomater. Sci. Eng.* **2021**. [CrossRef] [PubMed]
- Rossetti, L.; Kuntz, L.A.; Kunold, E.; Schock, J.; Müller, K.W.; Grabmayr, H.; Stolberg-Stolberg, J.; Pfeiffer, F.; Sieber, S.A.; Burgkart, R.; et al. The Microstructure and Micromechanics of the Tendon–Bone Insertion. *Nat. Mater.* **2017**, *16*, 664–670. [CrossRef]
- Barthelat, F.; Yin, Z.; Buehler, M.J. Structure and Mechanics of Interfaces in Biological Materials. *Nat. Rev. Mater.* **2016**, *1*, 1–16. [CrossRef]
- Launey, M.E.; Buehler, M.J.; Ritchie, R.O. On the Mechanistic Origins of Toughness in Bone. *Annu. Rev. Mater. Res.* **2010**, *40*, 25–53. [CrossRef]
- Dunlop, J.W.C.; Weinkamer, R.; Fratzl, P. Artful Interfaces within Biological Materials. *Mater. Today* **2011**, *14*, 70–78. [CrossRef]
- Fratzl, P.; Weinkamer, R. Nature’s Hierarchical Materials. *Prog. Mater. Sci.* **2007**, *52*, 1263–1334. [CrossRef]
- Yang, W.; Chen, I.H.; Gludovatz, B.; Zimmermann, E.A.; Ritchie, R.O.; Meyers, M.A. Natural Flexible Dermal Armor. *Adv. Mater.* **2013**, *25*, 31–48. [CrossRef]
- Libonati, F.; Gu, G.X.; Qin, Z.; Vergani, L.; Buehler, M.J. Bone-Inspired Materials by Design: Toughness Amplification Observed Using 3D Printing and Testing. *Adv. Eng. Mater.* **2016**, *18*, 1354–1363. [CrossRef]
- Bandyopadhyay, A.; Traxel, K.D.; Bose, S. Nature-Inspired Materials and Structures Using 3D Printing. *Mater. Sci. Eng. R Reports* **2021**, *145*, 100609. [CrossRef] [PubMed]
- Lin, E.; Li, Y.; Ortiz, C.; Boyce, M.C. 3D Printed, Bio-Inspired Prototypes and Analytical Models for Structured Suture Interfaces with Geometrically-Tuned Deformation and Failure Behavior. *J. Mech. Phys. Solids* **2014**, *73*, 166–182. [CrossRef]
- Libonati, F.; Vergani, L. Understanding the Structure–Property Relationship in Cortical Bone to Design a Biomimetic Composite. *Compos. Struct.* **2016**, *139*, 188–198. [CrossRef]
- Zorzetto, L.; Andena, L.; Briatico-Vangosa, F.; De Noni, L.; Thomassin, J.-M.; Jérôme, C.; Grossman, Q.; Mertens, A.; Weinkamer, R.; Rink, M.; et al. Properties and Role of Interfaces in Multimaterial 3D Printed Composites. *Sci. Rep.* **2020**, *10*, 1–17. [CrossRef]
- Tran, P.; Ngo, T.D.; Ghazlan, A.; Hui, D. Bimaterial 3D Printing and Numerical Analysis of Bio-Inspired Composite Structures under in-Plane and Transverse Loadings. *Compos. Part B Eng.* **2017**, *108*, 210–223. [CrossRef]
- Grezzana, G.; Loh, H.C.; Qin, Z.; Buehler, M.J.; Masic, A.; Libonati, F. Probing the Role of Bone Lamellar Patterns through Collagen Microarchitecture Mapping, Numerical Modeling, and 3D-Printing. *Adv. Eng. Mater.* **2020**, *22*, 2000387. [CrossRef]
- Ngo, T.D.; Kashani, A.; Imbalzano, G.; Nguyen, K.T.Q.; Hui, D. Additive Manufacturing (3D Printing): A Review of Materials, Methods, Applications and Challenges. *Compos. Part B Eng.* **2018**, *143*, 172–196. [CrossRef]
- Mirzaali, M.J.; Herranz de la Nava, A.; Gunashekar, D.; Nouri-Goushki, M.; Veeger, R.P.E.; Grossman, Q.; Angeloni, L.; Ghatkesar, M.K.; Fratila-Apachitei, L.E.; Ruffoni, D.; et al. Mechanics of Bioinspired Functionally Graded Soft-Hard Composites Made by Multi-Material 3D Printing. *Compos. Struct.* **2020**, *237*, 111867. [CrossRef]
- Tits, A.; Ruffoni, D. Joining Soft Tissues to Bone: Insights from Modeling and Simulations. *Bone Reports* **2021**, *14*, 100742. [CrossRef] [PubMed]
- Roach, D.J.; Hamel, C.M.; Dunn, C.K.; Johnson, M.V.; Kuang, X.; Qi, H.J. The M4 3D Printer: A Multi-Material Multi-Method Additive Manufacturing Platform for Future 3D Printed Structures. *Addit. Manuf.* **2019**, *29*, 100819. [CrossRef]

25. Sears, N.; Dhavalikar, P.; Whitely, M.; Cosgriff-Hernandez, E. Fabrication of Biomimetic Bone Grafts with Multi-Material 3D Printing. *Biofabrication* **2017**, *9*, 025020. [CrossRef]
26. Idaszek, J.; Volpi, M.; Paradiso, A.; Nguyen Quoc, M.; Górecka, Ż.; Klak, M.; Tymicki, G.; Berman, A.; Wierzbicki, M.; Jaworski, S.; et al. Alginate-Based Tissue-Specific Bioinks for Multi-Material 3D-Bioprinting of Pancreatic Islets and Blood Vessels: A Step towards Vascularized Pancreas Grafts. *Bioprinting* **2021**, *24*, e00163. [CrossRef]
27. Chan, V.; Jeong, J.H.; Bajaj, P.; Collens, M.; Saif, T.; Kong, H.; Bashir, R. Multi-Material Bio-Fabrication of Hydrogel Cantilevers and Actuators with Stereolithography. *Lab Chip* **2011**, *12*, 88–98. [CrossRef]
28. Zhou, L.Y.; Gao, Q.; Fu, J.Z.; Chen, Q.Y.; Zhu, J.P.; Sun, Y.; He, Y. Multimaterial 3D Printing of Highly Stretchable Silicone Elastomers. *ACS Appl. Mater. Interfaces* **2019**, *11*, 23573–23583. [CrossRef]
29. Soomro, A.M.; Memon, F.H.; Lee, J.W.; Ahmed, F.; Kim, K.H.; Kim, Y.S.; Choi, K.H. Fully 3D Printed Multi-Material Soft Bio-Inspired Frog for Underwater Synchronous Swimming. *Int. J. Mech. Sci.* **2021**, *210*, 106725. [CrossRef]
30. Zhang, Z.; Fan, W.; Chen, G.; Luo, J.; Lu, Q.; Wang, H. A 3D Printable Origami Vacuum Pneumatic Artificial Muscle with Fast and Powerful Motion. In *Proceedings of the 2021 IEEE 4th International Conference on Soft Robotics, New Haven, CT, USA, 12–16 April 2021, RoboSoft 2021*; Institute of Electrical and Electronics Engineers Inc.: New Haven, CT, USA, 2021; pp. 551–554. [CrossRef]
31. Slesarenko, V.; Kazarinov, N.; Rudykh, S. Distinct Failure Modes in Bio-Inspired 3D-Printed Staggered Composites under Non-Aligned Loadings. *Smart Mater. Struct.* **2017**, *26*, 035053. [CrossRef]
32. Jia, Z.; Wang, L. 3D Printing of Biomimetic Composites with Improved Fracture Toughness. *Acta Mater.* **2019**, *173*, 61–73. [CrossRef]
33. Dimas, L.S.; Bratzel, G.H.; Eylon, I.; Buehler, M.J. Tough Composites Inspired by Mineralized Natural Materials: Computation, 3D Printing, and Testing. *Adv. Funct. Mater.* **2013**, *23*, 4629–4638. [CrossRef]

Article

Neodymium Selenide Nanoparticles: Greener Synthesis and Structural Characterization

Abu A. Ansary¹, Asad Syed^{2,*}, Abdallah M. Elgorban² , Ali H. Bahkali², Rajender S. Varma³ 
and Mohd Sajid Khan^{4,*} 

¹ Unique Sixth Form, 1-19 Wakefield Street, London N18 2BZ, UK

² Botany and Microbiology Department, College of Science, King Saud University, P.O. Box 2455, Riyadh 11451, Saudi Arabia

³ Regional Centre of Advanced Technologies and Materials, Czech Advanced Technology and Research Institute, Palacký University in Olomouc, Šlechtitelů 27, 783 71 Olomouc, Czech Republic

⁴ Nanomedicine & Nanobiotechnology Lab, Department of Biosciences, Integral University, Lucknow 226026, India

* Correspondence: assyed@ksu.edu.sa (A.S.); research.sajid@gmail.com (M.S.K.)

Abstract: This investigation presents the greener biomimetic fabrication of neodymium selenide nanoparticles (Nd_2Se_3 NPs) deploying nitrate-dependent reductase as a reducing (or redox) agent, extracted from the fungus, *Fusarium oxysporum*. The Nd_2Se_3 NPs, with an average size of 18 ± 1 nm, were fabricated with the assistance of a synthetic peptide comprising an amino acid sequence (Glu-Cys)_n-Gly, which functioned as a capping molecule. Further, the NPs were characterized using multiple techniques such as UV-Vis spectroscopy, fluorescence, dynamic light scattering (DLS), and XRD. The hydrodynamic radii of biogenic polydispersed Nd_2Se_3 NPs were found to be 57 nm with PDI value of 0.440 under DLS. The as-made Nd_2Se_3 NPs were water-dispersible owing to the existence of hydrophilic moieties ($-\text{NH}_2$, $-\text{COOH}$, $-\text{OH}$) in the capping peptide. Additionally, these functionalities render the emulsion highly stable (zeta potential -9.47 mV) with no visible sign of agglomeration which bodes well for their excellent future prospects in labeling and bioimaging endeavors.

Keywords: biomimetic synthesis; Nd_2Se_3 ; synthetic peptide; structural characterization

Citation: Ansary, A.A.; Syed, A.; Elgorban, A.M.; Bahkali, A.H.; Varma, R.S.; Khan, M.S. Neodymium Selenide Nanoparticles: Greener Synthesis and Structural Characterization. *Biomimetics* **2022**, *7*, 150. <https://doi.org/10.3390/biomimetics7040150>

Academic Editors: Stanislav N. Gorb, Giuseppe Carbone, Thomas Speck and Andreas Taubert

Received: 11 September 2022

Accepted: 29 September 2022

Published: 3 October 2022

Publisher's Note: MDPI stays neutral with regard to jurisdictional claims in published maps and institutional affiliations.



Copyright: © 2022 by the authors. Licensee MDPI, Basel, Switzerland. This article is an open access article distributed under the terms and conditions of the Creative Commons Attribution (CC BY) license (<https://creativecommons.org/licenses/by/4.0/>).

1. Introduction

Chalcogenides (compounds and alloys of sulfur, selenium, and tellurium) are known for their splendid physical properties as they have phenomenal magnetic, electronic, catalytic, sensing, thermal, optical, and superconductivity properties. The conversions of chalcogenides into nanocrystalline metal chalcogenides have revolutionized the importance of these materials [1]. In particular, semiconductor nanocrystals have attracted global consideration owing to their distinctive optical features, such as great resistance to photo bleaching, an enormous absorption cross-section, extended fluorescence lifetimes, good quantum yield, and a luminescence emission with a large Stokes shift [2]. Furthermore, their perceived properties make them a subject of study for biologically relevant applications, which extend to medicine and bioimaging [3]. Highly functional nanostructured materials are grown using a biological system (including silica via diatoms, and magnetic nanomaterials using magnetotactic bacteria) [4], among numerous ongoing efforts to assemble inorganic nanoparticles (NPs) by biological means thus mimicking such phenomena at a laboratory scale. Various organisms (such as bacteria, fungi, and actinomycetes) have been studied for the generation of NPs over a range of chemical compositions that include metals, semiconductors, and oxides [5–9].

Generally, semiconductor materials are defined by their composition-dependent band gap energy (E_g), which is the minimal energy needed to stimulate an electron from the valence band (VB) into the vacant conduction energy (CE) band [10]. Band gaps play

substantial role in determining the purity of nanomaterials as well as in designing the fabrication of devices (sensors and photocatalysts) [11]. Other vital factors that may also affect the development of nanostructures in semiconductor NPs, include the comparative surface energies of the constituent metals, their corresponding rates of surface diffusion, and the conditions prevailing during or after deposition, whereas the large surface area enhances the surface properties. Additionally, these factors make whole-structure characterization important for these systems; moreover, they provide a more effective way to tune the structural morphology, and its corresponding properties. The relative differences between the energetic and fundamental structural parameters of a constituent's metal and nonmetal vary considerably between elemental systems. For the last two decades, the applications of nano-chalcogenides have garnered worldwide attention and their nanocrystalline forms have received immense significance in various applications [12]. Therefore, different routes for the synthesis of nanocrystalline metal chalcogenides have evolved for the preparation of nano-chalcogenides of desired physical properties [13–15]. Metal chalcogenides can easily be tuned, and their optoelectronic, physicochemical, magnetic, and biological properties can conversely manipulate for energy to biomedical applications. Neodymium oxides nanomaterials are being extensively used in optical, antireflection coatings, gate insulators, protective coatings photonic, catalytic, and many special applications [9]. Inner transition metals nanomaterials have attractive luminescent properties. The promising utilities in time resolved luminescence bioassays of lanthanide compounds propose exceptional sharp fluorescence with highly distinguishable long lasting emission bands and large Stoke shifts [16]. Their luminescence is created by transition within 4f shell. To the best of our knowledge, this is the first ever fungal-derived protein-mediated biosynthesis of Nd_2Se_3 NPs which may help open new dimensions of fluorescence applications in nanomedicine.

Chemical and physical methods produce highly toxic, unsafe, environmental unfriendly, cumbersome, unstable colloidal NPs that also require tedious derivatization protocols. In this regard, it is highly necessary to develop high-quality semiconductor nanomaterials via cost-effective, convenient, and less toxic methods. Therefore, nanotechnologists are looking toward greener machineries to produce nontoxic, stable, and long-lasting nanomaterials that function under ambient conditions. To that end, various methodologies have been designed to produce biogenic nanomaterials. In addition to this, the green synthesis of Au, Ag, and CdS NPs have also been achieved using enzymes and peptides purified from fungus [17–19]. These synthesized NPs (green synthesis by enzyme) are capped with small metal binding peptides with flanking free carboxyl or amino groups [19]. These readily available functionalities obviate the need for biofunctionalization, which is required for conjugating the NPs to the biomolecules [19]. Particularly, a wide range of templates has been engaged for enzyme immobilization, namely silica nanotubes [20], phospholipid bilayers [21], and self-assembled monolayers [22]. Furthermore, numerous studies have been reported on semiconductor–enzyme conjugates that embrace the development and enzyme-mimicking behavior of NPs complexed with horseradish peroxidase [23], xanthine oxidase [24], and carbonic anhydrase [25].

Herein, our study presents a detailed investigation into the use of enzymes (e.g., nitrate reductase) cleansed from fungus (e.g., *Fusarium oxysporum*) for the fabrication of technically vital, highly stable semiconductor Nd_2Se_3 NPs capped with a synthetic peptide. We have observed that the aqueous Nd^{2+} and Se^{4+} ions were simultaneously oxidized and reduced (redox reaction), respectively with the aid of enzyme nitrate reductase, leading to the creation of stable Nd_2Se_3 NPs in solution; ensued NPs were in the range of 16–27 nm in size, with an average of 18 ± 1 nm. This is an unprecedented use of an enzyme nitrate reductase and capping peptide in the synthesis of Nd_2Se_3 NPs. Lastly, these investigations will help assist in developing a rational enzymatic approach for the fabrication of NPs with a variety of compositions as well as tunable surface morphologies.

2. Materials and Methods

All the chemical reagents were acquired from commercially available sources and were of the highest purity available. The enzyme nitrate reductase was purified as described by Kumar et al. [18].

2.1. Green Synthesis of Nd_2Se_3 NPs

The reaction mixture (3 mL), containing $NdCl_2$ (1 mM), $SeCl_4$ (1 mM), $NaNO_3$ (5 mM), 100 μg (2.66×10^{-2} mM) of synthetic peptide having the amino acid sequence (Glu-Cys) $_n$ -Gly, 1.0 mM α -NADPH (a reduced form of nicotinamide adenine di-nucleotide phosphate sodium salt), and 1.66 U of nitrate reductase, was incubated under anaerobic conditions at 25 °C. After 12 h, the reaction mixture was exposed to UV-Vis spectrophotometric measurements. On completion of the reaction, Nd_2Se_3 NPs were subjected to treatment with 50% *v/v* of ethanol to eliminate unbound proteins and were then used for further characterization. Eventually, NPs were precipitated at 30,000 g for half an hour.

2.2. Characterization of Green Synthesized Nd_2Se_3 NPs

The confirmation of synthesis was ascertained utilizing UV-Vis spectrophotometer from Shimadzu (UV-1601 PC). Fluorescence was performed by exciting the samples at 330 nm, and the emission spectra were logged from 400 to 700 nm using a spectrofluorometer, FLS920, Edinburgh Instruments, UK at a scan rate of 300 nm/min. X-ray diffraction (XRD) patterns were logged in the 2θ range of 20°–80° with a step size of 0.02° and 5 s per step using a Philips X'PERT PRO armed with X'celerator, a rapid solid-state detector with iron-filtered Cu K α radiation ($\lambda = 1.5406 \text{ \AA}$) as the source. The Nd_2Se_3 NP suspension coated onto carbon coated copper grids was subjected to TEM analysis using an FEI Tecnai 30 TEM operated at 300 kV. The FTIR spectroscopy of bioengineered Nd_2Se_3 NP was performed in KBr pellets using a Perkin-Elmer Spectrum One instrument. The spectrometer was operated in the diffuse reflectance mode at a resolution of 2 cm^{-1} . To obtain good signal to noise ratio, 128 scans of the film were taken in the range of 450–4000 cm^{-1} . The dried powder of bioengineered Nd_2Se_3 NPs was used for thermogravimetric analysis on a Q5000V 2.4 Build 223 instrument by applying a scan rate of 10 °C min^{-1} [26].

3. Results

The schematic representation of biosynthesis and proposed mechanism of Nd_2Se_3 NPs is depicted in Figure 1.

The present study examined the modified and advanced processes for the greener production of nanomaterials using enzyme nitrate reductase purified from the extra cellular broth of *Fusarium oxysporum*, as reported by Kumar et al. [18]. After incubation at 25 °C for 12 h under anaerobic circumstances, the reaction mixture (3 mL) in 200 mM phosphate buffer (pH 7.2) containing freshly prepared $NdCl_2$, $SeCl_4$, $NaNO_3$, synthetic peptide (Glu-Cys) $_n$ -Gly, NADPH, and nitrate reductase resulted in the creation of Nd_2Se_3 NPs (Figure 1). The synthesis was monitored by following the attendance of the absorption band centered at 330 nm, which indicated the formation of Nd_2Se_3 NPs [27]. The absorption band at 270–280 nm is visible in Figure 2a, which is attributable to the proteins and α -NADPH used in the reaction. The suspension was very stable, with no sign of aggregation of the NPs even after one month. No absorption band at 330 nm was found without or denatured nitrate reductase or NADPH (data not shown). This observation confirmed the involvement of the enzyme in the oxidation of neodymium (from Nd^{2+} to Nd^{3+}) and reduction of selenium (Se^{4+} to Se^{2+}) to produce Nd_2Se_3 NPs utilizing nitrate as a substrate and NADPH as a cofactor. We used the fungus *Fusarium oxysporum* for the extracellular biosynthesis of Nd_2Se_3 NPs; the same had been used in earlier studies to purify the nitrate reductase (18).

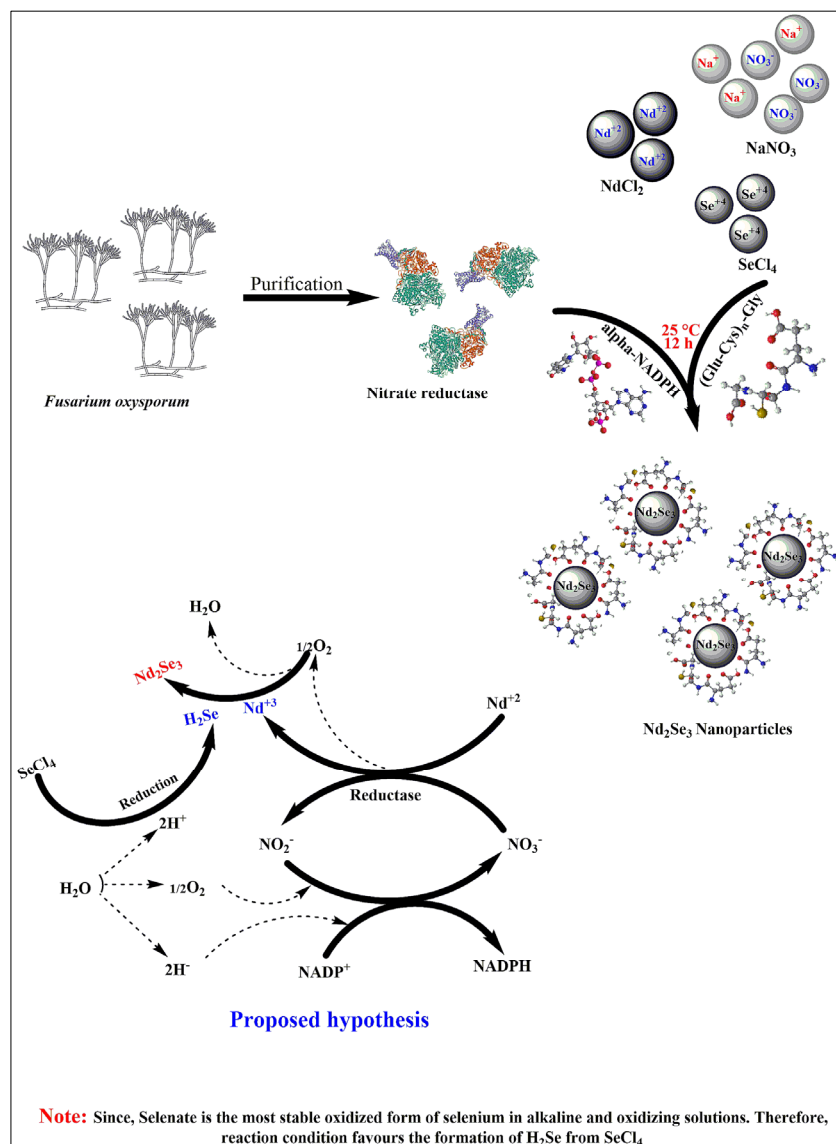


Figure 1. Schematic representation for synthesis of neodymium nanoparticles and proposed mechanism.

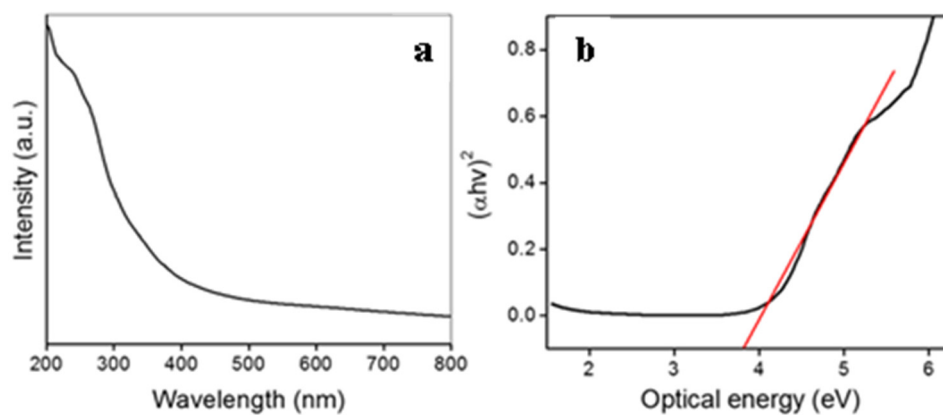


Figure 2. (a) UV/Visible absorption spectrum and (b) Tauc plot of neodymium selenide nanoparticles.

Eventually, the optical energy band gap of Nd₂Se₃ NPs was estimated via the Tauc Equation (1) shown below

$$\alpha h\nu = A (h\nu - E_g)^{1/n} \quad (1)$$

where α , A , h , and ν are absorption co-efficient, arbitrary constant, Plank constant, and light frequency, respectively. Further, on the basis of electronic transition, the n -parameter could be 1/2 (direct allowed), 2 (indirect allowed), or 3 (indirect forbidden) [28].

The absorption co-efficient (α) was estimated from the UV-Vis absorbance parameters via the following Equation (2),

$$\alpha = 2.303 (A_b/t) \quad (2)$$

where A_b is the absorbance of nanocrystals and t is the thickness of the cuvette used for measurements. The optical band gap of a nanocrystals was obtained by extrapolation of the linear region of the plot $(\alpha h\nu)^2$ vs. $h\nu$ to the point $(\alpha h\nu)^2 = 0$ [29]. The calculated band gap for Nd_2Se_3 NPs was found to be 3.75 eV, and is shown in Figure 2b.

Fluorescence spectrum of Nd_2Se_3 NPs was obtained at 330 nm excitation, as depicted in Figure 2. Whereas emission spectra revealed a band at 421 nm with red shift (Figure 3). The emission band at 421 nm is considerably red shifted compared to its absorption onset, which is credited to the band-gap or near-band-gap emission. The small shift in the peak suggests that the NPs possess a continuous surface with most surface atoms exhibiting the coordination and oxidation states of their bulk counterparts. The full width at half maximum (FWHM), which is the extent of the spread of peak, is 88.9 nm.

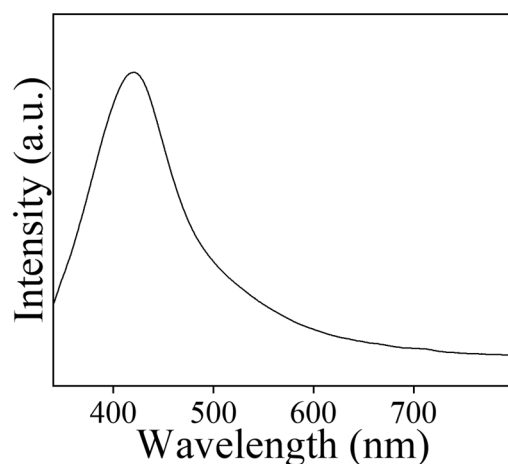


Figure 3. Fluorescence measurement of neodymium selenide nanoparticles.

The spherical shape and size (18 ± 1 nm) of the Nd_2Se_3 NPs were confirmed by TEM (Figure 4a) and the spherical formation of the nanocrystals may have been due to their dynamic nature. To further verify the crystallinity of Nd_2Se_3 nanoparticles, the diffraction patterns of X-ray was recorded from drop cast films of biogenic Nd_2Se_3 nanoparticles. The as-synthesized Nd_2Se_3 nanoparticles were found to reveal the crystalline nature owing to well-defined Bragg's reflections. The peak position and 2θ values agree with those reported for Nd_2Se_3 nanoparticles, almost all peaks in the pattern could be indexed to cubic phase cell parameters, $a = b = c = 8.85$, $\alpha = \beta = \gamma = 90^\circ$ [JCPDF # 190823]. The given investigation has confirmed the first ever synthesis of Nd_2Se_3 nanoparticles under ambient conditions. The XRD pattern of the Nd_2Se_3 NPs showed intense peaks at (211), (220), (310), (321), (420), (422), (521) (611), (620), and (444) in the 2θ range of 20° – 80° (Figure 4b) and agrees with those reported for the Nd_2Se_3 nanocrystals. The size of particles under XRD was found to be ~ 16 nm (Figure 4b). Further, the confirmation of encapsulation of proteins over the surface of particles was realized through FTIR. Therefore, the peak at 1635.56 cm^{-1} corresponds to characteristic of C=O of amide group of the amide I linkage confirmed the presence of protein. Further, the peak at 3320.62 cm^{-1} confirms the N-H stretching vibration. The C-N stretching of aliphatic amines associated with peptide bond was affirmed by extra characteristic peak at 1044.54 cm^{-1} (Figure 4c).

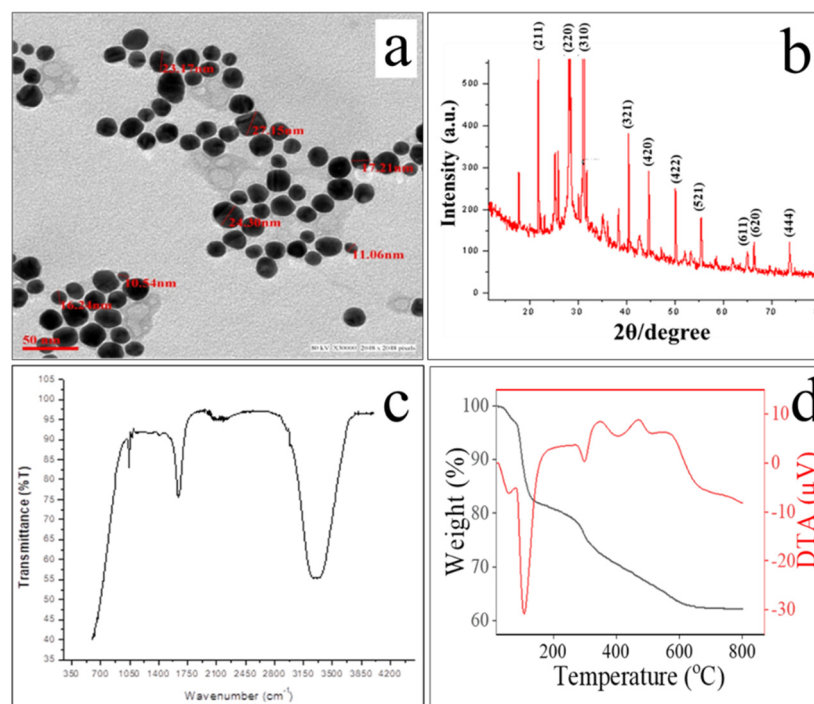


Figure 4. (a) TEM, (b) XRD, (c) FTIR and (d) TGA/DTA analysis of biogenic Nd_2Se_3 NPs.

The gravimetric analyses were performed to check the thermal stability of capping agents. TGA was performed on as-synthesized Nd_2Se_3 NPs in a nitrogen gas environment at temperatures ranging from 20 °C to 800 °C to calculate the amount of proteins present on the nanoparticles. As pointed out earlier, the as-synthesized nanoparticles are capped with proteins that stabilize them against aggregation. As a result, it degrades in two stages. Weight loss occurs up to 120 °C due to the evaporation of adsorbed water. In the second stage, loss is attributed to the decomposition of proteins bound on the surfaces of nanoparticles. The coating was found to contribute almost up to 18% which can be inferred via weight-loss when the particles were heated up to 600 °C. A further increase in the temperature shows a loss of weight that can be accounted for the decomposition of nanoparticles (Figure 4d).

The DTA study was also performed on the same particles. The endothermic weight loss was found to be around 110 °C which indicated the elimination of adsorbed water molecules on the surface of nanoparticles. Again, endothermic weight loss was found around 300 to 400 °C due to the decomposition of proteins (Figure 4d).

Additionally, DLS and zeta potential were performed to check the hydrodynamic radii along with different populations of particles and stability of nanoemulsion. The hydrodynamic radii of particles under DLS were found to be ~57 nm with PDI value of 0.440 (Figure 5A). Zeta potential was found to be -9.47mV (Figure 5B) which indicated the substantially high stability due to low value of Hamaker constant; TEM revealed only the size of the inorganic core, whereas DLS offered the hydrodynamic radii (inorganic core plus hydration layers). The suspension was found to be stable up to 3 months and there were no significant changes in DLS and Zeta potential.

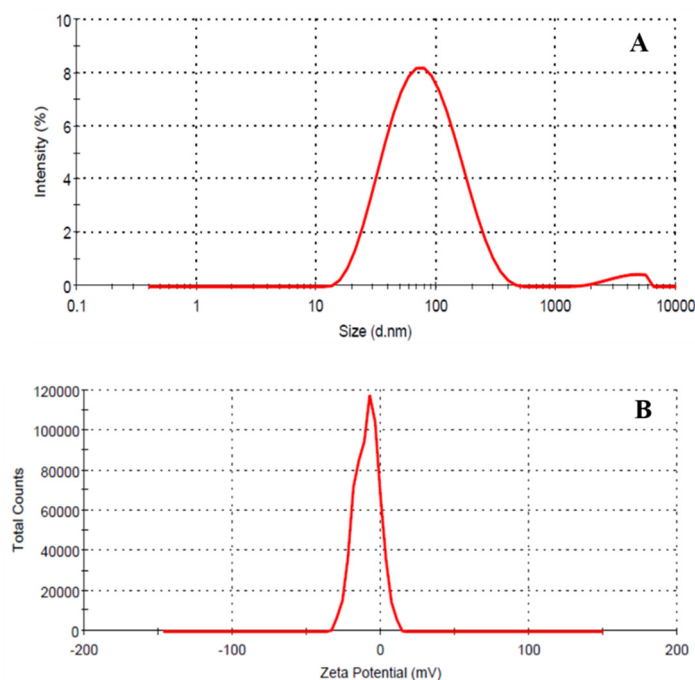


Figure 5. (A) DLS and (B) zeta potential for Nd_2Se_3 NPs.

Possible Mechanism

There are several methods to produce semiconductor NPs, but biological methods are rarely used. In the present study, a very simple and effective greener synthesis method for semiconductor NPs was developed. Nd_2Se_3 semiconductor NPs were synthesized by the instantaneous oxidation of a metal (from Nd^{2+} to Nd^{3+}) and the reduction of nonmetal ions (Se^{4+} to Se^{2+}) using purified nitrate reductase enzyme in the presence of the synthetic peptide (Glu-Cys) $_n$ -Gly (where $n = 5-7$), as a capping and stabilizing agent containing repetitive glutamate and cysteine amino acids.

Nitrate reductase has a strong reducing property [30] due to its moderate reduction potential (+0.44 V), which participated in the redox reaction where oxidation of Nd^{2+} into Nd^{3+} took place and simultaneously reduction of selenium from Se^{4+} into Se^{2+} occurred with the synthesis of nano sized materials (Figure 1). During the synthesis, the synthetic peptide [(Glu-Cys) $_n$ -Gly, where $n = 5-7$] served as a stabilizing agent, which not only reduced steric hindrance and static-electronic repulsive forces between metal and non-metal, but also served as a capping agent responsible for attaining the required sizes and shapes. Synthetic peptides comprising repetitive units of glutamate [31] and cysteine [32] amino acids were designed by virtue of their tendency to interact with inorganic NPs. The designed peptides stabilize semiconductor Nd_2Se_3 NPs and enable them to interact with various molecules due to the existence of different functional groups. The interaction of peptides and NPs depends upon the chemical properties of NPs, peptides, and reaction parameters and the dynamics of their interaction is responsible for the long-term stability of peptide-capped NPs. The electronic properties of NPs can be perfectly determined by UV-Vis spectroscopy, and their absorption peak and its width is directly correlated to the chemical composition and size of the particles. The energy of far-UV light is sufficient to excite the electrons of Nd_2Se_3 NPs. Therefore, the size and concentration of the Nd_2Se_3 NPs were determined by UV-Vis spectroscopy and were further confirmed by DLS (hydrodynamic radii) and TEM (inorganic core) [33].

The overall NP and peptide interaction is a multifunctional phenomenal process, and its properties are determined not only by the characteristics of the NPs, but also by the interacting peptides and the reaction parameters. Particularly, the rate of specific association and dissociation of the involved peptide will determine its longevity in the interaction with

the NP surface. Moreover, the synthetic conditions determine the morphological nature and miscibility of a metal and a nonmetal in semiconductor NPs. Generally, semiconductor NPs comprising two dissimilar elements (metal and non-metal) has received greater attention than metallic NPs, both scientifically as well as technologically [34,35]. The blending of two different constituting elements can result in morphological changes in the semiconductor NPs, wherein an extra degree of freedom is developed [36]. However, the constituting elements (metal and nonmetal) and the size determine the behavior of the semiconductor NPs. Mostly, composition and size generally provide the tendency to optimize the energy of the plasmon absorption band of the metal and non-metal blend, which delivers a multipurpose tool for biological applications. Lastly, by means of semiconductor formation, the catalytic nature of the resultant NPs can be enhanced to a reasonable extent, which may not be achievable when employing its corresponding monometallic NPs.

The energy of the incident photon at a wavelength of 300 nm is 4.136 eV, which is responsible for the electronic transitions of Nd₂Se₃ NPs. The spectrum obtained describes the chemical composition and particle size. It also confirms the synthesis of the NPs, and their difference from bulk counterparts.

The dependency of the optical nature on particle size is mostly an effect of the internal structure of the nanocrystals. However, as the crystals become smaller, the quantity of involved atoms on the surface increases, which greatly influences optical behaviors. If these surface energy states are for nanocrystal band gaps, they can trap charge carriers at the surface and decrease the overlap between the electron and the hole. The number of electrons excited in the conduction band (CB) is a function of the temperature and magnitude of the energy band gap (E_g), defined as the separation between the maximum energy in the valence band and the minimum energy in the CB. As our biogenic material Nd₂Se₃ revealed, the optical intensity at 330 nm correlates with 3.75 eV (band gap), it can also be calculated by the following Equations (3) and (4).

$$E_g = 1240/(\lambda \text{ (nm)}) \quad (3)$$

$$E_g = 1240/330 = 3.75 \text{ eV} \quad (4)$$

The roles of nano-chalcogenide have been exploited in a variety of newer and emerging technologies. Their applications in broad categories are derived from their unique tunable chemical and physical properties, which give rise to their potential uses in the fields of biomedical, nonlinear optics, luminescence, electronics, catalysis, solar energy conversion, optoelectronics, among others. With decrease in size of nano-chalcogenides, the percent of surface atoms and the value of band gaps increase leading to the surface properties playing an important role in the properties of the materials (14). The transition metal nano-chalcogenides have specific applications. The group II–VI chalcogenide semiconductors have their role in optoelectronic light-emitting diodes and optical devices owing to their wide-bandgap. Additionally, V–VI main-group nano-chalcogenides due to their semiconductor nature have applications in television cameras with photoconducting targets, thermoelectric devices, and electronic and optoelectronic devices and in IR spectroscopy (16). The inner transition metal nano-chalcogenides are very rare and their synthesis ought to be exploited in detail because of their non-toxic nature (9) which can be explored for their fluorescence properties toward biomedical applications.

4. Conclusions

The present study enabled the development of environmentally friendly biogenic methodology to produce Nd₂Se₃ NPs utilizing biologically relevant molecules. Neodymium selenide NPs were synthesized using enzyme nitrate reductase. They were orthorhombic with a size distribution of 18 ± 1 nm (under TEM); the chemical formula was found to be Nd₂Se₃ based on the crystal structure of the fabricated NPs. Our ability to fabricate these NPs via a non-toxic, eco-friendly method presents a significant advancement in developing “greener” technique to produce NPs. Lastly, this study offers an alternative approach for

the environmentally friendly, cost-efficient, and commercial fabrication of water dispersible Nd_2Se_3 NPs. These Nd_2Se_3 NPs have favorable bio-medical application potential without any additional requirements for further functionalization.

Author Contributions: R.S.V.: write-up, editing and revision; A.A.A. and A.S.: Conceptualization, investigation, revision; A.A.A. and A.S.: Methodology, Data curation, resources; A.M.E.: Software, validation, review and editing; A.H.B.: Methodology, Writing-original draft preparation; M.S.K.: Conceptualization, methodology, supervision, project administration. All authors have read and agreed to the published version of the manuscript.

Funding: This research was funded by Researchers Supporting Project number (RSP-2021/ 56), King Saud University, Riyadh, Saudi Arabia.

Institutional Review Board Statement: Not applicable.

Informed Consent Statement: Not applicable.

Data Availability Statement: Not applicable.

Acknowledgments: The authors acknowledge Integral University and Department of Biosciences for providing facilities and support for the research. The authors extend their appreciation to the Researchers Supporting Project number (RSP-2021/ 56), King Saud University, Riyadh, Saudi Arabia.

Conflicts of Interest: The authors declare no conflict of interest. The funders had no role in the design of the study; in the collection, analyses, or interpretation of data; in the writing of the manuscript; or in the decision to publish the results.

References

1. Furdyna, J.K.; Dong, S.-N.; Lee, S.; Liu, X.; Dobrowolska, M. The Ubiquitous Nature of Chalcogenides in Science and Technology. In *Chalcogenide*; Elsevier: Amsterdam, The Netherlands, 2020; pp. 1–30.
2. Bera, D.; Qian, L.; Tseng, T.-K.; Holloway, P.H. Quantum Dots and Their Multimodal Applications: A Review. *Materials* **2010**, *3*, 2260–2345. [CrossRef]
3. Abbasi, E.; Kafshdooz, T.; Bakhtiary, M.; Nikzamir, N.; Nikzamir, N.; Nikzamir, M.; Mohammadian, M.; Akbarzadeh, A. Biomedical and Biological Applications of Quantum Dots. *Artif. Cells Nanomed. Biotechnol.* **2016**, *44*, 885–891. [CrossRef] [PubMed]
4. Sarikaya, M. Biomimetics: Materials Fabrication through Biology. *Proc. Natl. Acad. Sci. USA* **1999**, *96*, 14183–14185. [CrossRef] [PubMed]
5. Klaus, T.; Joerger, R.; Olsson, E.; Granqvist, C.G. Silver-Based Crystalline Nanoparticles, Microbially Fabricated. *Proc. Natl. Acad. Sci. USA* **1999**, *96*, 13611–13614. [CrossRef] [PubMed]
6. Sweeney, R.Y.; Mao, C.; Gao, X.; Burt, J.L.; Belcher, A.M.; Georgiou, G.; Iverson, B.L. Bacterial Biosynthesis of Cadmium Sulfide Nanocrystals. *Chem. Biol.* **2004**, *11*, 1553–1559. [CrossRef] [PubMed]
7. Ahmad, A.; Mukherjee, P.; Mandal, D.; Senapati, S.; Khan, M.I.; Kumar, R.; Sastry, M. Enzyme Mediated Extracellular Synthesis of CdS Nanoparticles by the Fungus, *Fusarium Oxysporum*. *J. Am. Chem. Soc.* **2002**, *124*, 12108–12109. [CrossRef] [PubMed]
8. Kowshik, M.; Deshmukh, N.; Vogel, W.; Urban, J.; Kulkarni, S.K.; Paknikar, K.M. Microbial Synthesis of Semiconductor CdS Nanoparticles, Their Characterization, and Their Use in the Fabrication of an Ideal Diode. *Biotechnol. Bioeng.* **2002**, *78*, 583–588. [CrossRef] [PubMed]
9. Iram, S.; Khan, S.; Ansary, A.A.; Arshad, M.; Siddiqui, S.; Ahmad, E.; Khan, R.H.; Khan, M.S. Biogenic Terbium Oxide Nanoparticles as the Vanguard against Osteosarcoma. *Spectrochim. Acta Part A Mol. Biomol. Spectrosc.* **2016**, *168*, 123–131. [CrossRef]
10. Brus, L.E. Electron–Electron and Electron-hole Interactions in Small Semiconductor Crystallites: The Size Dependence of the Lowest Excited Electronic State. *J. Chem. Phys.* **1984**, *80*, 4403–4409. [CrossRef]
11. Khan, S.B.; Faisal, M.; Rahman, M.M.; Akhtar, K.; Asiri, A.M.; Khan, A.; Alamry, K.A. Effect of Particle Size on the Photocatalytic Activity and Sensing Properties of CeO_2 Nanoparticles. *Int. J. Electrochem. Sci.* **2013**, *8*, 7284–7297.
12. Yanchatuña Aguayo, O.P.; Mouheb, L.; Villota Revelo, K.; Vásquez-Ucho, P.A.; Pawar, P.P.; Rahman, A.; Jeffryes, C.; Terencio, T.; Dahoumane, S.A. Biogenic Sulfur-Based Chalcogenide Nanocrystals: Methods of Fabrication, Mechanistic Aspects, and Bio-Applications. *Molecules* **2022**, *27*, 458. [CrossRef]
13. Feng, Y.; Marusak, K.E.; You, L.; Zauscher, S. Biosynthetic Transition Metal Chalcogenide Semiconductor Nanoparticles: Progress in Synthesis, Property Control and Applications. *Curr. Opin. Colloid Interface Sci.* **2018**, *38*, 190–203. [CrossRef]
14. Zhu, J.-J.; Wang, H. Synthesis of Metal Chalcogenide Nanoparticles. In *Encyclopedia of Nanoscience and Nanotechnology*; American Scientific Publishers: Stevenson Ranch, CA, USA, 2004; Volume 10, pp. 347–367.

15. Asuigui, D.R.; Atif, R.; Swanson, J.; Glaser, P.; Garskaite, E.; Žarkov, A.; Stoll, S.L. Synthesis of Lanthanide Chalcogenide Nanoparticles. *Nanomater. Single-Source Precursors* **2022**, 219–243. [CrossRef]
16. Zawadzki, M.; Kępiński, L. Synthesis and Characterization of Neodymium Oxide Nanoparticles. *J. Alloys Compd.* **2004**, *380*, 255–259. [CrossRef]
17. Kumar, S.A.; Abyaneh, M.K.; Gosavi, S.W.; Kulkarni, S.K.; Ahmad, A.; Khan, M.I. Sulfite Reductase-mediated Synthesis of Gold Nanoparticles Capped with Phytochelatin. *Biotechnol. Appl. Biochem.* **2007**, *47*, 191–195.
18. Kumar, S.A.; Abyaneh, M.K.; Gosavi, S.W.; Kulkarni, S.K.; Pasricha, R.; Ahmad, A.; Khan, M.I. Nitrate Reductase-Mediated Synthesis of Silver Nanoparticles from AgNO₃. *Biotechnol. Lett.* **2007**, *29*, 439–445. [CrossRef]
19. Ansary, A.A.; Kumar, S.A.; Krishnasastri, M.V.; Abyaneh, M.K.; Kulkarni, S.K.; Ahmad, A.; Khan, M.I. CDS Quantum Dots: Enzyme Mediated in vitro Synthesis, Characterization and Conjugation with Plant Lectins. *J. Biomed. Nanotechnol.* **2007**, *3*, 406–413. [CrossRef]
20. Mitchell, D.T.; Lee, S.B.; Trofin, L.; Li, N.; Nevanen, T.K.; Söderlund, H.; Martin, C.R. Smart Nanotubes for Bioseparations and Biocatalysis. *J. Am. Chem. Soc.* **2002**, *124*, 11864–11865. [CrossRef]
21. Hamachi, I.; Fujita, A.; Kunitake, T. Enhanced N-Demethylase Activity of Cytochrome c Bound to a Phosphate-Bearing Synthetic Bilayer Membrane. *J. Am. Chem. Soc.* **1994**, *116*, 8811–8812. [CrossRef]
22. Fang, J.; Knobler, C.M. Phase-Separated Two-Component Self-Assembled Organosilane Monolayers and Their Use in Selective Adsorption of a Protein. *Langmuir* **1996**, *12*, 1368–1374. [CrossRef]
23. Stonehuerner, J.G.; Zhao, J.; O'Daly, J.P.; Crumbliss, A.L.; Henkens, R.W. Comparison of Colloidal Gold Electrode Fabrication Methods: The Preparation of a Horseradish Peroxidase Enzyme Electrode. *Biosens. Bioelectron.* **1992**, *7*, 421–428. [CrossRef]
24. Zhao, J.; O'daly, J.P.; Henkens, R.W.; Stonehuerner, J.; Crumbliss, A.L. A Xanthine Oxidase/Colloidal Gold Enzyme Electrode for Amperometric Biosensor Applications. *Biosens. Bioelectron.* **1996**, *11*, 493–502. [CrossRef]
25. Crumbliss, A.L.; Perine, S.C.; Stonehuerner, J.; Tubergen, K.R.; Zhao, J.; Henkens, R.W.; O'Daly, J.P. Colloidal Gold as a Biocompatible Immobilization Matrix Suitable for the Fabrication of Enzyme Electrodes by Electrodeposition. *Biotechnol. Bioeng.* **1992**, *40*, 483–490. [CrossRef] [PubMed]
26. Uddin, I.; Poddar, P.; Ahmad, A. Extracellular Biosynthesis of Water Dispersible, Protein Capped Mn₅O₈ Nanoparticles Using the Fungus *Fusarium Oxysporum* and Study of Their Magnetic Behavior. *J. Nanoeng. Nanomanufacturing* **2013**, *3*, 91–97. [CrossRef]
27. Li, Q.; Jin, X.; Yang, Y.; Wang, H.; Xu, H.; Cheng, Y.; Wei, T.; Qin, Y.; Luo, X.; Sun, W. Nd₂ (S, Se, Te)₃ Colloidal Quantum Dots: Synthesis, Energy Level Alignment, Charge Transfer Dynamics, and Their Applications to Solar Cells. *Adv. Funct. Mater.* **2016**, *26*, 254–266. [CrossRef]
28. Li, X.; Hou, Y.; Zhao, Q.; Wang, L. A general, one-step and template-free synthesis of sphere-like zinc ferrite nanostructures with enhanced photocatalytic activity for dye degradation. *J. Colloid Interface Sci.* **2011**, *358*, 102–108. [CrossRef] [PubMed]
29. Soltani, T.; Entezari, M.H. Photolysis and Photocatalysis of Methylene Blue by Ferrite Bismuth Nanoparticles under Sunlight Irradiation. *J. Mol. Catal. A Chem.* **2013**, *377*, 197–203. [CrossRef]
30. Lacey, D.L.; Timms, E.; Tan, H.L.; Kelley, M.J.; Dunstan, C.R.; Burgess, T.; Elliott, R.; Colombero, A.; Elliott, G.; Scully, S. Osteoprotegerin Ligand Is a Cytokine That Regulates Osteoclast Differentiation and Activation. *Cell* **1998**, *93*, 165–176. [CrossRef]
31. Brancolini, G.; Kokh, D.B.; Calzolari, L.; Wade, R.C.; Corni, S. Docking of Ubiquitin to Gold Nanoparticles. *ACS Nano* **2012**, *6*, 9863–9878. [CrossRef]
32. Battocchio, C.; Porcaro, F.; Mukherjee, S.; Magnano, E.; Nappini, S.; Fratoddi, I.; Quintiliani, M.; Russo, M.V.; Polzonetti, G. Gold Nanoparticles Stabilized with Aromatic Thiols: Interaction at the Molecule–Metal Interface and Ligand Arrangement in the Molecular Shell Investigated by SR-XPS and NEXAFS. *J. Phys. Chem. C* **2014**, *118*, 8159–8168. [CrossRef]
33. Sharma, G.; Gupta, V.K.; Agarwal, S.; Kumar, A.; Thakur, S.; Pathania, D. Fabrication and Characterization of Fe@ MoPO Nanoparticles: Ion Exchange Behavior and Photocatalytic Activity against Malachite Green. *J. Mol. Liq.* **2016**, *219*, 1137–1143. [CrossRef]
34. Vinayagam, R.; Varadavenkatesan, T.; Selvaraj, R. Evaluation of the Anticoagulant and Catalytic Activities of the Bridelia Retusa Fruit Extract-Functionalized Silver Nanoparticles. *J. Clust. Sci.* **2017**, *28*, 2919–2932. [CrossRef]
35. Toshima, N.; Yonezawa, T. Bimetallic Nanoparticles—Novel Materials for Chemical and Physical Applications. *New J. Chem.* **1998**, *22*, 1179–1201. [CrossRef]
36. Sharma, G.; Naushad, M.; Kumar, A.; Devi, S.; Khan, M.R. Lanthanum/Cadmium/Polyaniline Bimetallic Nanocomposite for the Photodegradation of Organic Pollutant. *Iran. Polym. J.* **2015**, *24*, 1003–1013. [CrossRef]



Article

Novel Motion Sequences in Plant-Inspired Robotics: Combining Inspirations from Snap-Trapping in Two Plant Species into an Artificial Venus Flytrap Demonstrator

Falk J. Tauber ^{1,2,*}, Philipp Auth ^{1,†}, Joscha Teichmann ¹, Frank D. Scherag ^{2,3} and Thomas Speck ^{1,2,4}

¹ Plant Biomechanics Group, Botanic Garden, University of Freiburg, 79110 Freiburg, Germany; ph.auth@gmx.de (P.A.); joscha.teichmann@studmail.w-hs.de (J.T.); thomas.speck@biologie.uni-freiburg.de (T.S.)

² Cluster of Excellence livMatS @ FIT-Freiburg Center for Interactive Materials and Bioinspired Technologies, University of Freiburg, 79110 Freiburg, Germany; scherag@imtek.de

³ Laboratory for Chemistry and Physics of Interfaces CPI, Department of Microsystems Engineering-IMTEK, University of Freiburg, 79110 Freiburg, Germany

⁴ Freiburg Materials Research Center (FMF), University of Freiburg, 79110 Freiburg, Germany

* Correspondence: falk.tauber@biologie.uni-freiburg.de; Tel.: +49-761-203-95152

† These authors contributed equally to this work.

Abstract: The field of plant-inspired robotics is based on principles underlying the movements and attachment and adaptability strategies of plants, which together with their materials systems serve as concept generators. The transference of the functions and underlying structural principles of plants thus enables the development of novel life-like technical materials systems. For example, principles involved in the hinge-less movements of carnivorous snap-trap plants and climbing plants can be used in technical applications. A combination of the snap-trap motion of two plant species (*Aldrovanda vesiculosa* and *Dionaea muscipula*) has led to the creation of a novel motion sequence for plant-inspired robotics in an artificial Venus flytrap system, the Venus Flyflap. The novel motion pattern of Venus Flyflap lobes has been characterized by using four state-of-the-art actuation systems. A kinematic analysis of the individual phases of the new motion cycle has been performed by utilizing precise pneumatic actuation. Contactless magnetic actuation augments lobe motion into energy-efficient resonance-like oscillatory motion. The use of environmentally driven actuator materials has allowed autonomous motion generation via changes in environmental conditions. Measurement of the energy required for the differently actuated movements has shown that the Venus Flyflap is not only faster than the biological models in its closing movement, but also requires less energy in certain cases for the execution of this movement.

Keywords: plant-inspired robotics; artificial Venus flytrap; motion sequence; biomimetics; bioinspiration

Citation: Tauber, F.J.; Auth, P.; Teichmann, J.; Scherag, F.D.; Speck, T. Novel Motion Sequences in Plant-Inspired Robotics: Combining Inspirations from Snap-Trapping in Two Plant Species into an Artificial Venus Flytrap Demonstrator. *Biomimetics* **2022**, *7*, 99. <https://doi.org/10.3390/biomimetics7030099>

Academic Editor: Jinyou Shao

Received: 15 June 2022

Accepted: 15 July 2022

Published: 22 July 2022

Publisher's Note: MDPI stays neutral with regard to jurisdictional claims in published maps and institutional affiliations.



Copyright: © 2022 by the authors. Licensee MDPI, Basel, Switzerland. This article is an open access article distributed under the terms and conditions of the Creative Commons Attribution (CC BY) license (<https://creativecommons.org/licenses/by/4.0/>).

1. Introduction

Within the last decade, plant-inspired robotics has become established as a new emerging field of soft robotic science. One outstanding example is represented by the plant-inspired growing robots developed by the group at the Italian Institute of Technology; these robots have roots, tendrils, and leaves like their biological models and are able to grow, forage, and harvest energy from the environment [1–5]. A focus area within this field is the development of artificial systems with certain characteristics that are able (1) to exist autonomously, (2) to sense, adapt, and react to the environment, (3) to sustain their homeostasis by harvesting energy, (4) to sense damage, and (5) to possess self-repair functions. Such systems are currently still in their infancy but should revolutionize the technical world in the future.

The Venus flytrap (*Dionaea muscipula*) provides a suitable biological model for plant-inspired robotics. These plants perceive their environment and adapt and react to it, all

of which are features required by robots. In addition, Venus flytraps carry out one of the most complex decentralized controlled process sequences in nature, namely a fast snap-buckling prey capture movement, which includes an upstream mechanical memory and several subsequent processes depending on successful prey capture [6]. The Venus flytrap can be considered as a bi-stable system, with the lobes being stable in a convex and concave configuration [6–8], changing through a snap-buckling motion similar to technical bistable systems [9–12]. The transference and combination of the basic principles of the Venus flytrap movement sequence has enabled the production of life-like artificial Venus flytraps (AVF) [13]. However, artificial Venus flytraps have so far been produced more as a by-product of the development of new actuation systems. AVFs have been used as suitable demonstrators of the capabilities of actuators in the development of novel pneumatic systems utilizing instabilities in elastic energy storage [14], magnetically driven bi-stable prepregs [15,16], ionic electroactive polymer metal composites (IPMCs) [17,18], light responsive liquid crystalline elastomers (LCEs) [19,20], and hygroscopic bistable systems (HBS) reacting to changes in humidity [21]. However, none of these AVF systems incorporates all the functions of the biological model *D. muscipula*. Most of them only exhibit a reasonably fast (sometimes without snapping) closure mechanism following an external stimulus, as Esser et al. [13] have shown in their review of the current state of AVFs. Nevertheless, a simple and low cost AVF with a novel motion pattern inspired by two carnivorous plants has been developed, inspired by those AVF systems: the Venus Flyflap (VFf). It uses various actuation modes and allows the investigation and characterization of the energy needed for actuation [22]. In addition, for the first time, this system combines motion features of two closely related snap-trapping carnivorous plants into one system, namely the snap-buckling of *D. muscipula* (Figure 1A,B) and the kinematic coupling and motion amplification of the Waterwheel plant (*Aldrovanda vesiculosa*) (Figure 1C,D) [6,7,23,24]. The trap closure movements based on these motion principles are among the fastest movements in the plant kingdom: *A. vesiculosa* needs 0.02 to 0.1 s [23] and *D. muscipula* 0.1 to 0.5 s [6] to close their trap lobes.

The compliant foil structure used in the VFf is based on a shape inspired by the biological models. A rectangle forms the base (analogous to the leaf midribs of *A. vesiculosa* and *D. muscipula*); attached to its long sides, two triangles represent the trap lobes, and two circles ('ears') at the short ends of the rectangle allow the actuation of the system through kinematic coupling (Figure 1E–G) [14]. A downwardly directed motion of the 'ears' results in motion amplification causing the fast closure of the system by a continuous motion, as found in *A. vesiculosa*. To be able to snap, the foil 'midrib' is reinforced with a plastic microscopic slide as a backbone. When force is applied centrally, the backbone changes its curvature, and the VFf opens its lobes in a fast snapping motion similar, but inverse in direction, to the snapping by curvature inversion in *D. muscipula*. Thus, a new motion sequence has been achieved by combining the motion principles of the two snap-trap plants into one artificial system. A fast (continuous) closing step, followed by a sudden release of the stored potential elastic energy in the system, causes a snap opening, as soon as the input energy exceeds a certain threshold.

The present study aims to answer the following questions. Is it possible to build a biomimetic system that combines and utilizes two movement principles in one cost-efficient structure, that mimics the biological models, and that can be triggered by environmental stimuli?

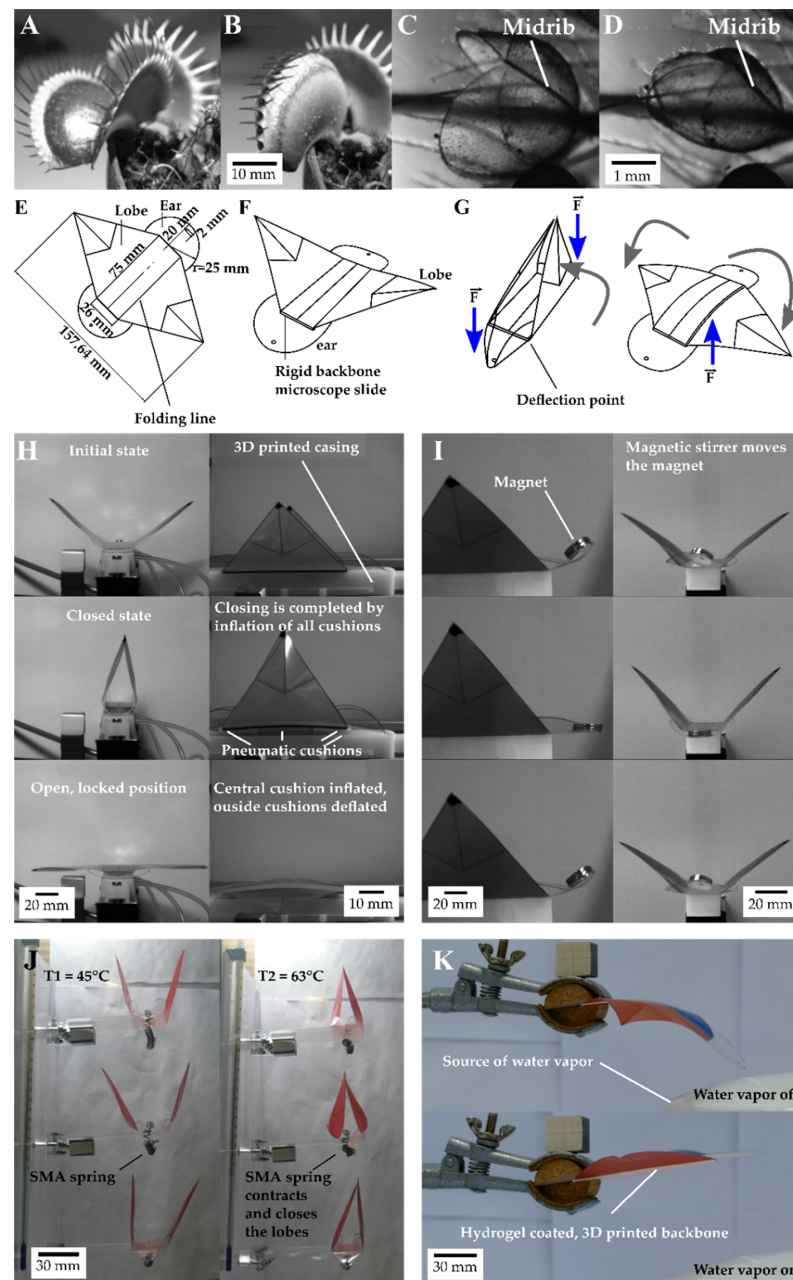


Figure 1. After being triggered, the Venus flytrap (*Dionaea muscipula*) closes its lobes by inverting the curvature of the lobes from, as viewed from the outside, concave (A) to convex (B) through the release of stored elastic energy. In the waterwheel plant (*Aldrovanda vesiculosa*) (C), water displacement in turgescent cells lying along the midrib combined with the release of stored elastic energy results in bending of the midrib, which is kinematical amplified and causes trap closure (D). The compliant foil demonstrator, the Venus Flyflap (Vff) (E), combines both mechanisms to close and open its artificial lobes. When force is applied to the ears (F,G), the lobes close via a kinematic coupling mechanism. Force applied to the backbone triggers a fast-snapping opening movement similar to the closing movement of the Venus flytrap. These mechanisms have been incorporated into various actuation scenarios. Pneumatic cushions drive the motion and enable the characterization of each phase of the motion sequence (H). A resonance-like, rapidly oscillating, flapping motion is achieved by a magnet that is attached to the ears and that responds to a rotating magnetic field (I). The Vff can also be actuated by environmental stimuli, when fitted with shape memory alloy (SMA) springs (J) or a combination of environmentally sensitive materials such as SMA and polymers in combination with hydrogels reacting only to a change in humidity and temperature (K).

Direct actuation by means of pneumatic cushions enables the opening and closing movements of the VFf to be controlled in a targeted manner (Figure 1H). Thereby, specific aspects of the motion and system as a whole can be investigated separately. This should provide new insight into the motion behavior (closing and opening times and speeds), the kinematics, and the elastic energy storage of the system. Contactless actuation via a magnet varying the actuation speed is used to achieve and investigate a uniform energy-effective oscillation or resonance-like motion (Figure 1I). Concerning autonomous systems, the VFf can be also actuated by environmental stimuli such as heat and humidity or a combination of both, by using environmentally sensitive materials such as shape memory alloys and polymers in combination with hydrogels. Furthermore, a comparison of our system with the biological models and the state of the art in artificial Venus flytraps allows an evaluation of its biomimetic potential.

2. Materials and Methods

2.1. Setups for Movement Analysis of *Dionaea Muscipula* and the Artificial Venus Flyflap (VFf)

In order to enable a valid comparison of the motion characteristics of the *D. muscipula* plant with the pneumatically and magnetically actuated VFf, a kinematic analysis was performed using a video chamber fitted with two 1000 fps high-speed cameras (Baumer matrix monochrome camera VCXU 13 M/Imaging Solutions Motion traveller 1000) (Figure 2A). Videos were recorded at a constant frame-rate of 1000 fps with a resolution of 512×512 pix, and the recordings were synchronized using NorPix-StreamPix 8.0.0.0 (x64) Software. During actuation, the path of motion, movement speed, and kinematic parameters (speed and acceleration) were tracked and analyzed using the open-source software Kinovea (version 0.9.1). During the testing period of three weeks, 28 traps from four different *D. muscipula* plants were tested repeatedly. The tests were performed on three different dates with one week of “rest” in between to minimize the stress for the plants. Tracking markers were applied to the lobe tips of the pneumatic VFf and the magnetic VFf and to the magnets. The video and picture-based analysis of the thermally driven VFf actuated with shape memory alloy (SMA) springs (Figure 2B) and of the hydrogel actuated VFf (Figure 2C) required only a lower framerate because of the lower motion speed. Therefore, a digital camera (Panasonic Lumix DMC-FZ1000, Figure 2(C3)) with a recording framerate of 25 fps was used. In the case of the thermally driven VFf, the lobe tips and the spring length were tracked. Statistical data analysis was performed with the open-source software RStudio (version 1.2.5042).

The setup of the actuator systems is described in detail in Esser et al. [14] and shown in Figure 1. Further information is provided in the supplementary material section “Materials and Methods: 2.1 Standardized production of the compliant foil demonstrators”.

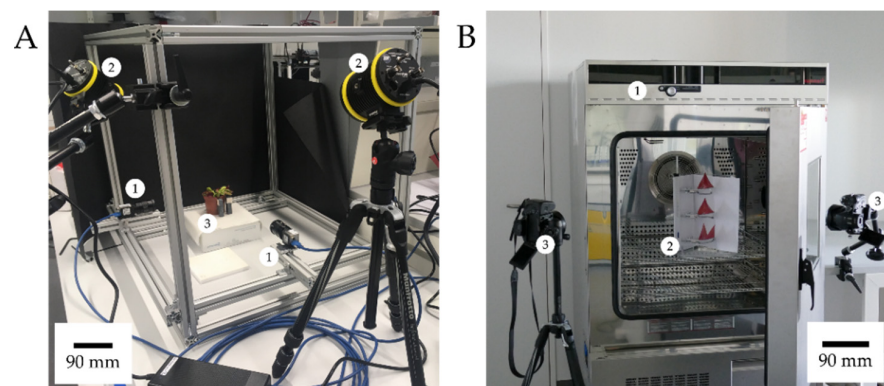


Figure 2. Cont.

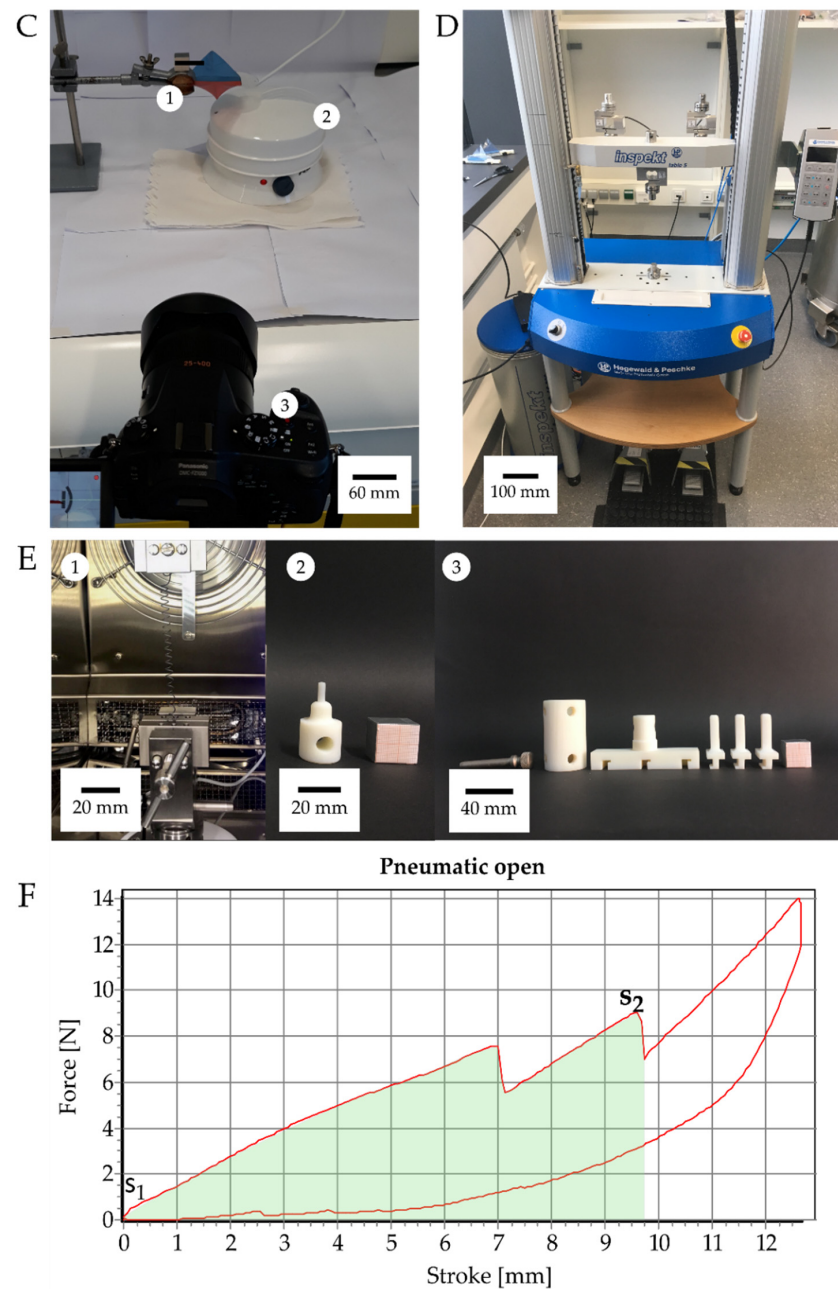


Figure 2. Characterization setups. High-speed videos were recorded in a specifically build recording chamber (A) with two highspeed cameras (A1) positioned at a 90° angle to each other. Light is provided by two high-power flicker-free LED light sources (A2) that point at the object of interest (A3). The Venus flytrap and the pneumatic and the magnetic demonstrators were recorded using this setup. The SMA actuated demonstrators were tested by placing them in a temperature chamber (B1). Three demonstrators were tested simultaneously (B2). The movement of the springs and the lobes of the demonstrator were recorded by two cameras (B3) for later analysis. For actuation of the hydrogel-based demonstrator (C1), a hot water vapour source (C2) provided enough humidity to unlock the demonstrator, which was filmed by a camera for kinematic analysis (C3). Force-displacement measurements were performed with specific test mounts by the Hegewald and Peschke Inspekt Table 5 (D). The output force for each SMA spring was measured (E1) at 63 °C. To mimic the actuation procedure, specific mounts were designed to apply pressure in the direction of actuation in the demonstrator (magnetic (E2) and pneumatic (E3)). An exemplary force displacement curve of an opening event of the pneumatic system is shown in (F). S₁ and S₂ indicate the lower and upper end, respectively, of the integral (green area) used for calculating the kinetic energy necessary to open the the two lobes (lobe opening indicated in the curve by the two sudden force reductions).

2.2. Energy Measurements

The energy consumption in each experiment was determined by measuring the amount of electricity that was required for actuation. The electricity consumption was determined with an energy-measuring device that was plugged into the socket before the actual electricity consumer, e.g., the pneumatic test bench, magnetic stirrer, temperature chamber, or steam source. Force-displacement measurements were performed for calculating the necessary work and kinetic energy to drive and trigger the closing and opening movements of the demonstrators (Figure 2F). A specific testing setup to apply force according to the actuation scenario was designed for each VFf system (Figure 2E). The pneumatic VFfs were fixed in an upside-down orientation in the testing machine, and the compression pistons applied force to the backbone through the casing openings for the pneumatic cushions (Figure 2(E3)). In the case of the magnetic VFf, a downward force was applied to the magnets until the lobes closed (Figure 2(E2)) Clamps for the tensile tests held the SMA spring of the thermal VFf inside the thermal chamber of the testing machine. The temperature was increased up to 65 °C, and the output force was measured. All measurements were performed with an Inspect universal testing machine (Hegewald and Peschke Meß- und Prüftechnik GmbH, Nossen, Germany). During all hysteresis measurements, the stroke was adjusted accordingly to achieve a full closing or opening movement. The movement of the machine caused further increasing forces after a complete opening, since the testing machine did not immediately change the direction of movement after opening. These measurement ranges were excluded from the kinetic energy calculations. Since the course of the force was not uniform, it had to be integrated over the entire path until the moment when both trap lobes opened (s_2) (Figure 2F). The area under the force-displacement curve represents the work exerted on the moving object. By measuring the area, the work and thus the required kinetic energy can be calculated by:

$$W = \int_{s_1}^{s_2} \vec{F}(\vec{s}) * d\vec{s}. \quad (1)$$

with W = work/kinetic energy; F = force; s = stroke; s_1 and s_2 indicate the lower and upper end of the integral, respectively. The efficiency calculation and corresponding equations are shown in the supplementary material section “Materials and Methods: 9. Actuation system efficiency calculation”.

2.3. Motion Analysis of Discrete Repetitive Motion Generation by Pneumatic Actuation

Analysis of the complex motion pattern of the VFf was achieved by using directly driven pneumatic actuation of the opening and closing motions, which could be triggered separately. The foil-based VFf was attached to a 3D-printed (RigurTM; Stratasys Ltd., Eden Prairie, MN, USA) ridged case that housed three pneumatic cushions (EcoFlex 0030; KauPo Plankenhorn e.K., Spaichingen, Germany) (Figure S1). Pressurization of the two smaller outside cushions pushed the rigid backbone of the VFf upwards, because its ears were attached to the casing (Figure 1H). This closed the lobes via kinematic amplification, as seen in *A. vesiculosa*. To trigger the opening movement, the central cushion inflated, while the outside cushions deflated. This caused the backbone to bend, leading to a fast “snapping” opening movement accompanied by an inversion of the spatial curvature of the lobes, similar to the snap-buckling principle of *D. muscipula*. Pressurized air was supplied by a pneumatic test bench [25] that enabled measurement and manipulation of the pressure and pressurization time for the closing and opening motions, respectively (see Table S3 for actuation pattern). As pressurization inflated the cushions and actuated the system, we further refer to the duration of pressurization as the actuation time (AT). The actuation times chosen for the characterization were 200 ms, 300 ms, and 400 ms, as the closing time of the biological model was below 500 ms. During actuation, the valves opened depending on the AT pressurizing the cushions. The actuation pressure was determined to be 0.7 bar in preliminary tests. This was the maximum pressure at which complete closure was

guaranteed without the cushions bursting. The system pressure was adjusted accordingly to the AT in order to achieve a pressure of 0.7 bar within the actuators during each AT.

2.4. Motion Analysis of Contactless Actuation of the Demonstrator by a Rotating Magnetic Field

In the magnetic Vff, the foil demonstrator was directly attached to a 3D-printed casing without the rigid microscopy slide backbone. The casing in turn was attached to an aluminum profile in the video chamber (see Figures 1I and S2). A set of two round flat magnets (Neodymium, 15×2 mm, 30 g each, 6 kg holding force) was attached to one of the ears. The Vff was placed 20 mm above a magnetic stirrer (IKA RCT B 5000) with adjustable rotations per minute (rpm) ranging from 100 to 1500 rotations per minute. The rotating magnet pulled and pushed the Vffs magnets, resulting in upwards and downwards movements of the Vff ear, which in turn set the lobes into a flapping motion. To investigate the possibility of reaching the natural frequency and gaining a resonance effect in the oscillating flapping motion of the system, six different actuation speeds were investigated with 400, 700, 800, 900, 1000, and 1300 rpm, respectively. In preliminary tests, the rpm were steadily increased from 0 to 1500 and the behavior of the Vff was observed. From 400 rpm onwards, the first clear movements occurred, at 800 and 900 rpm a uniform movement behavior was observed and for frequencies above 1300 rpm only irregular behavior. Because of this, the focus of the experiments was on the range of 800 and 900 rpm, and additional frequencies 100 rpm higher and lower were investigated. In addition, the extremes of 400 rpm (first clear movements) and 1300 rpm (only irregular erratic motions) were investigated.

2.5. Environmentally Triggerable Systems

2.5.1. Motion Analysis of Thermally Actuated Vff by Using SMA Springs

To introduce autonomy into the system, the Vff was equipped with a temperature-sensitive SMA spring (Nitinol). The critical temperature for the SMA springs to induce contraction was determined by placing five springs in the temperature chamber of the universal testing machine at increasing temperatures, starting at 22 °C, and the length was measured each time that the temperature rose by 2 °C (see Table S2 and Figure S4). An SMA spring was attached to the foil demonstrator by using rivets on each lobe (see Figure 1J). The spring was stretched to a fixed length of 115 mm and then attached to the Vff. Three Vff were tested simultaneously in a climate chamber (Environmental test chamber CTC256, Memmert GmbH + Co. KG) that allowed programmed temperature settings (Figure S5). Three different temperatures were tested (55 °C, 60 °C, 65 °C) (Figure S6). The rising ambient temperature induced a phase transformation in the spring material reversing the deformation of the spring, which then shortened and, hence pulled the ears downwards closing the Vff.

2.5.2. Motion Analysis in Vffs Actuated by Combination of Two Stimuli: Humidity and Temperature

By using a hydrogel-coated 3D-printed shape memory polymer (SMP), an actuator system was created that responded to a combination of two environmental stimuli. The hydrophilic terpolymer (hydrogel) at a concentration of 100 mg/mL was applied manually to the SMP midrib backbones, which had a low T_G of 50 °C (RigurTM; Stratasys Ltd., Eden Prairie, MN, USA) (Figure 1K). After a drying step at 65 °C, the terpolymer was simultaneously cross-linked and surface-attached by UV irradiation at 365 nm. During drying, the surface-attached hydrogel shrank leading to a bent backbone (see Figure S7). This process thus formed a water-sensitive hydrogel network that actuated the demonstrator when exposed to higher (or different) levels of humidity. The bending angle was measured via ImageJ (version 1.53a, [26] (see Figure S9). After being crosslinked, the bent backbone was attached to a snapped-open foil Vff. The Vff full assembly (Figure S8) is described in more detail in the supplementary material section “8. Environmentally triggerable systems: Stimulus combination humidity and temperature”.

In the fully assembled VFf testing scenario, the change in environmental conditions was achieved through a source of hot water vapor (REER FD 1540) that generated a constant flow of hot steam. The VFfs were positioned in the steam at a fixed distance of 5.7 cm to the outlet for 300 s. This caused hydration of the dried hydrogel and led to swelling, which reduced the bend in the now flexible backbone (heated above the T_g by the hot steam). This unlocked the snapped-open VFf, the stored elastic energy was released, and the lobes moved upwards to the resting position. Thereafter, the VFf was ready for manual actuation. Nineteen backbones were tested repeatedly for five dehydration and rehydration cycles. For the identification of the threshold humidity at which the hydrogel-coated backbones straightened, ten were tested in a small climate chamber in which the humidity was raised from 20% to 80% at a constant temperature of 65 °C.

2.6. Statistics

The open-source software RStudio (v. 1.2.5042, R Core Team 2017) and statistic programming language R were used for statistical analysis and calculations. For the pneumatic demonstrator, we used a two-way ANOVA on ranked transformed data, having checked for normal distribution (Shapiro–Wilk test) and homoscedasticity (Bartlett test). The significance levels and correlation between variable actuation times and movement speeds were determined. Post-hoc tests were performed via multiple comparisons by using Tukey’s test. Data from the kinematic analysis of the magnetic demonstrator were checked for normal distribution (Shapiro–Wilk test) and homoscedasticity (Bartlett test). Significant differences between movement speed and actuation rpm were determined using the Wilcoxon signed-rank test. For the hydrogel- and SMA-based demonstrator, we used a paired Wilcoxon signed-rank test, having checked for normal distribution (Shapiro–Wilk test) and variance homogeneity (Kruskal–Wallis test).

3. Results

3.1. Movement Characteristics of the Biological Model *D. muscipula*

The movement of the trap leaves of the biological model *D. muscipula* was observed from two perspectives (Figure 3A), and the leaf rim was tracked in order to calculate movement speed (Figure 3B). The closing time of the five tested plants ranged from 148 ms to 1821 ms with a mean value of 599.1 ms (SD = 487.7 ms). During the three-week testing period, mean closing time increased each week of testing from 549 ms in the first week to 683.9 ms in the third week (Figure 3C). Of the closing events, 56.1% took place in less than 500 ms (Figure 3D). Closing times above 1000 ms were the result of a delay between the initiations of the closing motions of the two lobes (Figure 3). Speed values of the closing motion ranged from 0.016 m/s to 0.245 m/s with an average movement speed of 0.088 m/s. The corresponding raw data is shown in Table S1 in the supplementary material section “Materials and Methods: 3. Kinematic analysis of the biological role model”.

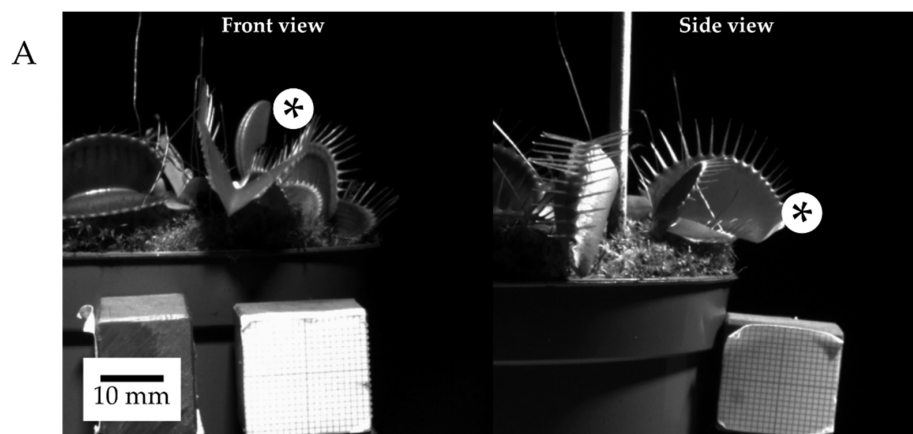


Figure 3. Cont.

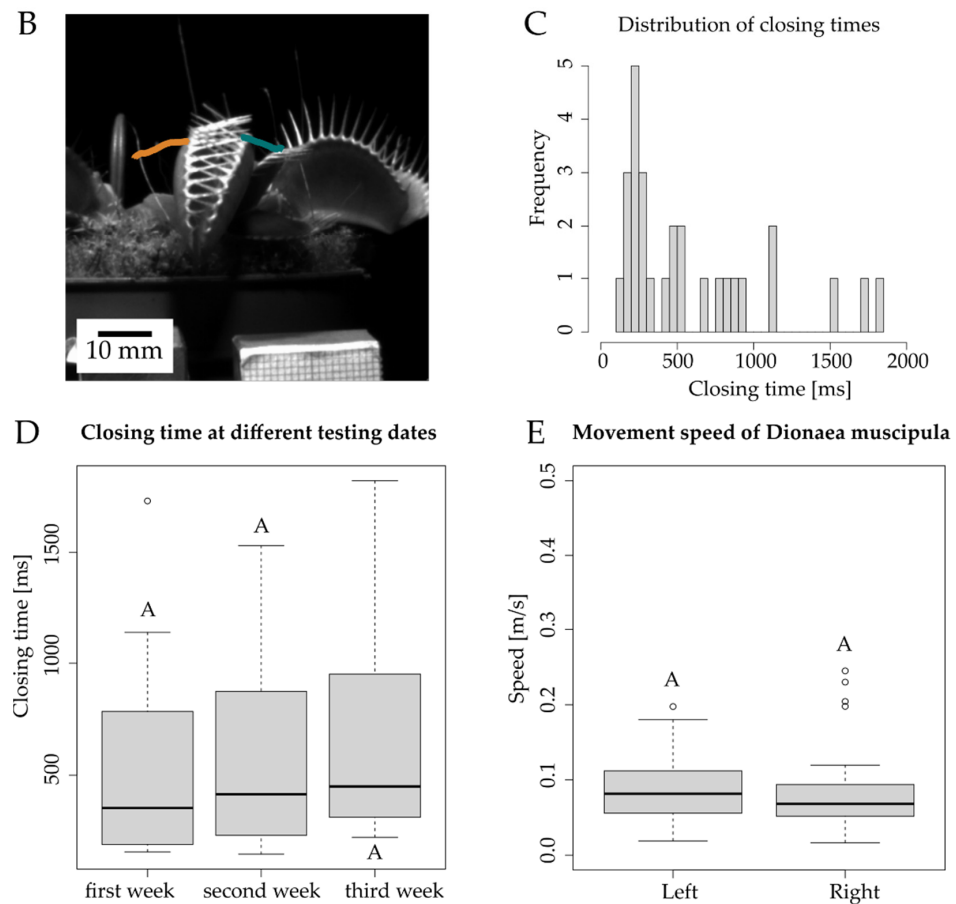


Figure 3. High-speed recording of the Venus flytrap from two angles gave a good impression of the overall movement (A). The path of motion was tracked at the base of the marginal teeth (orange and green lines) (B), and the movement speed was measured for these particular trajectories. Average closing time ranged from 550 to 680 ms for the three weeks of testing (C), whereas over half of the closing events needed less than 500 ms. The box plots represent 12, 8, and 8 measurements for week one, two, and three, respectively (D). Lobe tips reached velocities of between 0.016 and 0.24 m/s during closing. Each plot includes 28 measurements (E).

3.2. Motion Analysis of Generation of Discrete Repetitive Motion by Pneumatic Actuation

The kinematic analysis of three pneumatically actuated VFfs showed that a movement cycle consisting of one closing and opening movement could be separated into five separate phases (Figure 4A), with a curvature inversion and unrolling movement of the lobes during the snap opening of the VFfs (Figure 4B). During actuation, the highest velocities were observed during the opening movement (Figure 4C). The closing movement lasted between 132 ms and 311 ms (Figure 4D). The opening time ranged from 19 ms to 56 ms, depending on the time delay between the opening events of the two lobes. The fastest opening times were observed when both lobes moved simultaneously in parallel. Opening time is defined as the time needed from the first sign of the opening movement to the passing of the horizontal line of the backbone. After opening, with a still-inflated central cushion, the demonstrator remained locked in the open position. When all pressure was released from the system, the VFf returned to its initial position. The closing velocity showed a dependence on actuation time (AT) (a longer AT of 200, 300, and 400 ms gave slower closing) (Figure 4E). In contrast, the AT had almost no significant effect on the opening velocity of each lobe (Figure 4F). The measured speeds of the lobe tips during opening ranged from 3.05 m/s to 4.91 m/s (Figure 4F). Demonstrator three showed faster opening times because of the simultaneous opening of the two lobes (Figure 4F). The applied pressure ranged between 0.75 and 0.79 bar for the outside cushions and 0.66 and 0.69 bar for the single central pneumatic cushion.

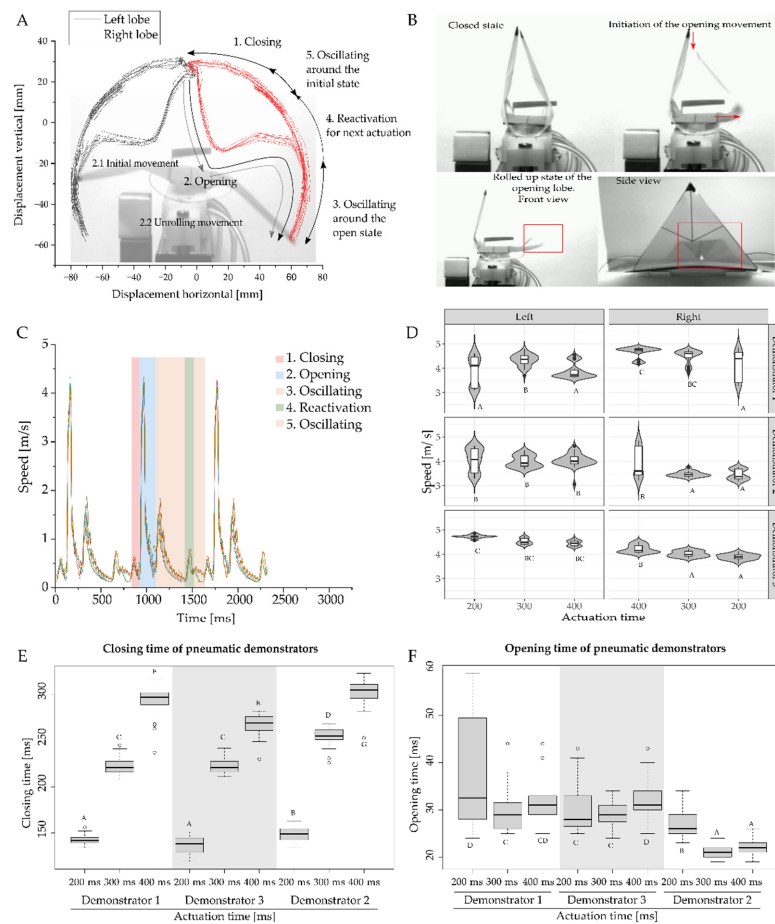


Figure 4. Kinematic analysis of the five phasic motions of the pneumatic VFf. After activation of the outside cushions, the VFf closes, and the opening movement is triggered when the central cushion is inflated. Examination of the lobe movement reveals five phases (A) starting with the closing movement (A1). The second phase is the opening movement (A2) that begins with a slight outward movement of the base of the lobe leading to a rolled-up intermediate state that is followed by a fast-unrolling movement (B). After opening, the lobes oscillate in the locked open position (A3). Following air release, the VFf snaps back into its original position and is ready for the next actuation (A4) with the lobes oscillating around the initial position (A5). In (B), a time-delayed opening of both lobes shows the unrolling movement of one of the lobes. The five phases are characterized by their different movement speeds (C), an example of which is shown here for a motion cycle at 400 ms AT. During actuation, the highest velocities (up to 4.9 m/s) are observed during the opening movement (D). Closing times depend on the overall actuation time (E). Significant differences above 40 ms for opening times are attributable to a delayed and non-parallel opening movement of the two lobes. Faster opening times represent simultaneous opening (F). Each boxplot corresponds to five measurements during which the three demonstrators have each completed eight movement cycles. Significance levels are indicated by the capital letters next to each boxplot. Different letters represent significant differences from other results with p -values below 0.05.

3.3. Motion Analysis of Contactless Demonstrator Actuation by a Rotating Magnetic Field

During actuation at low speed (rounds per minute) of the magnetic stirrer, the VFf lobes showed shivering movements, while the permanent magnet moved up and down depending on the speed of the magnetic stirrer (Figure 5A). The motion accelerated in association with an increase in actuation velocity, transforming into a fast, nearly regular, oscillating flapping motion around 800–900 rpm with a stable motion frequency of 15.6 Hz at 900 rpm (Figure S3 and Table S4). At 1000 rpm, the bent lobes tended to buckle and quickly returned to their original shape thereafter (Figure 5C); the highest observed velocity

at this time was 3.56 m/s (Figure 5B). The average speed of lobe tips increased with rising actuation velocity ranging from 0.33 m/s to 2.37 m/s. In correspondence the motion frequency also increased from 3.67 Hz to 44 Hz, with an observed decrease as the motion became more erratic at higher rpm (Figure S3 and Table S4). The movement of the lobes was delayed compared with the perpendicular motion of the magnet (Figure 5C).

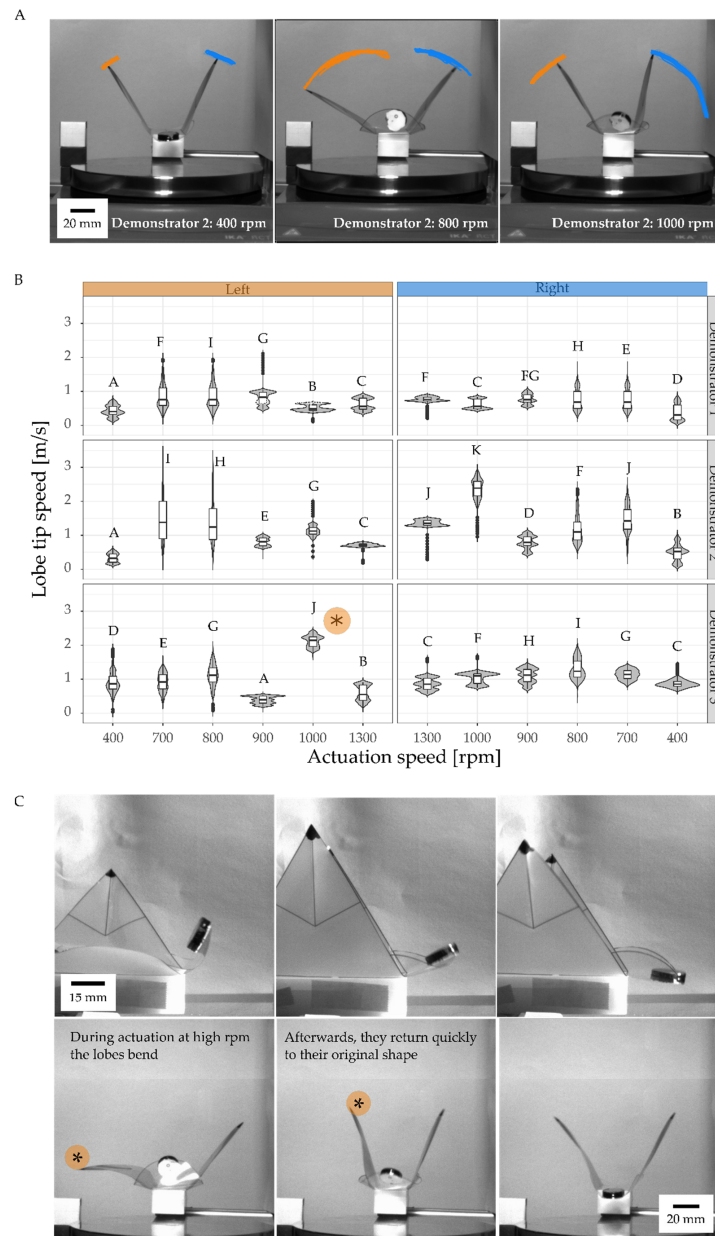


Figure 5. Motion analysis of magnetically driven oscillating VFfs with velocities approximating to natural frequency. With higher actuation velocity (higher rpm), the movement speed and amplitude increase (motion tracks indicated by orange and blue lines) (A). Three VFfs were tested at six different actuation speeds (B). Significance levels are indicated by the capital letters next to each boxplot. Different letters represent significant differences from other results with p -values below 0.05. Recording frame-rate of 1000 fps for a video duration of 3 s resulted in 3000 values for each speed ($n = 3000$) of the movement of the three tested VFfs. Highest velocities were observed when a lobe bent during the outward and downward movement and then snapped back into its original curvature (C). The images illustrate the difference in speed of the left and the right lobe of demonstrator 3 at 1000 rpm. * indicates the fastest snapping lobe in (B,C).

3.4. Environmentally Triggerable Systems

3.4.1. Thermally Driven VFf

When the surrounding air is heated above the critical temperature of the SMA spring, temperature-induced phase transformation takes place, and the spring contracts and generates enough force to pull the ears downwards thereby closing the lobes. To ascertain the critical temperature of the SMA springs, they were stretched to 115 mm and placed in an oven. Between 60 °C and 65 °C, four of the five tested springs reduced their length by at least 50%. The spring that did not contract sufficiently was not tested further (see supplementary materials Figure S3). In some cases, these differences may originate from the production process, as these were commercially available SMA spring. Three springs with comparable contraction behavior were selected for further experiments with the VFf. These were attached to the VFf ears, and the closing behavior was investigated at three different temperatures (55 °C, 60 °C, and 65 °C) via video analysis and motion tracking (Figure 6A,D). No movement was detected at 55 °C, only one demonstrator closed its lobes at 60 °C, whereas all demonstrators performed closing movements at 65 °C (Figure 6B). The closing movement was triggered by a reduction in spring length, which was here measured at the beginning and the end of a heating cycle at the target temperature (Figure 6D lower orange lines). Spring contractions ranged from 0 cm to 5.44 cm (Figure 6B). A minimal spring length reduction of 0.56 cm was needed fully to close the lobes of the demonstrator (Figure 6B red line). The overall time needed from the first sign of movement to the complete closure of the VFf was defined as the closing time. The closing times of the three VFf ranged from 36 to 429 s with an average of 234.7 s (Figure 6C), the fastest closing times being observed at 65 °C. The average closing speed ranged from 0.19×10^{-3} to 1.1×10^{-3} m/s (Figure 6E). The force generated by the spring contraction was measured at 65 °C. Spring two and three showed no significant difference with an average force between 4.17 N and 6.83 N (Figure 6F). The corresponding raw data for spring length change is shown in Table S5 and for demonstrator closing times in Table S6 in the supplementary material section “Materials and Methods: 7. Environmentally triggerable systems: Thermally driven AVF using shape memory alloy (SMA) springs”.

3.4.2. Motion Analysis in VFfs Actuated by a Combination of Two Stimuli: Humidity and Temperature

The change in curvature of the hydrogel-coated backbones under changing environmental conditions was analyzed in a small climatic chamber that allowed controlled changes to be made in air humidity and temperature. Seven hydrogel-coated backbones were tested at a constant temperature of 65 °C, and the bending angle was observed at various humidity levels (Figure 7A). All seven backbones straightened completely at 60% relative humidity. The process started slowly, and minor changes became visible at 25% to 35% humidity. Between 35% and 60%, the decrease in the opening angle accelerated, levelling out at 65% to 80% humidity (Figure 7B).

After attachment of the hydrogel coated backbone to the foil VFf, a higher environmental humidity of about 70% was needed to reduce the curvature of the backbone and thus to unlock the demonstrator. At higher humidity, the hydrogel swelled to a greater extent, as was necessary to overcome the resistance of the foil material. After the VFf had been placed in a stream of hot steam (Figure 7C), it took an average of 64.5 s to unlock and reach the initial resting position for manual actuation (Figure 7D). Out of 95 tests, 62 demonstrators unlocked correctly during the 300 s rehydration time in hot steam. The average time required from the first contact of the steam to the unlocking of the VFf varied from 33.2 s to 126 s during the five cycles, whereas the actual unlocking movement ($n = 19$) required approximately 0.404 s (sd = 81.4 ms).

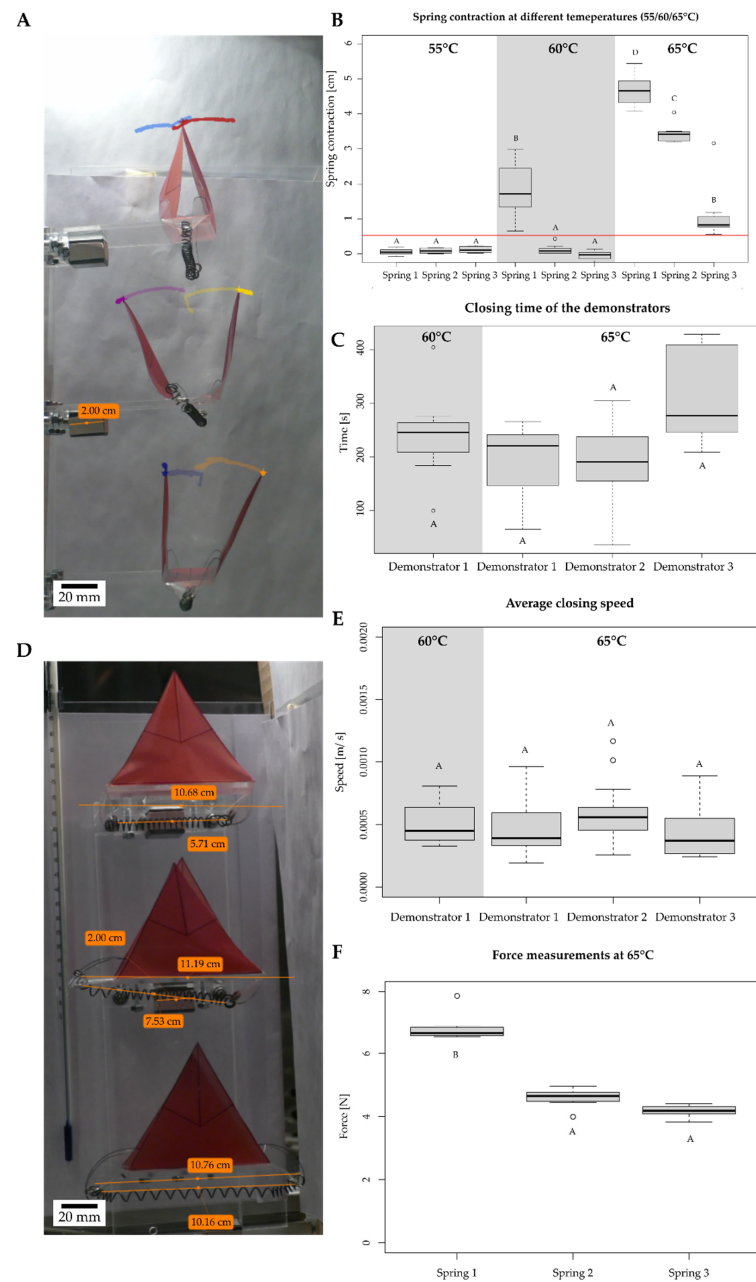


Figure 6. Kinematic motion analysis of the thermally driven Vff. Each demonstrator was actuated by a thermo-responsive SMA spring, which contracted and thus performed a closing motion when a critical temperature was reached. The tested demonstrators were placed in a climate chamber at three different temperatures. Videos were recorded from two perspectives (A,D), and the closing movement was further analyzed via motion tracking. Spring length was determined before and after the heating cycle (D), and the difference in length was calculated for complete closure. In (D), the upper orange line represents the demonstrator length and lower orange line the spring length before actuation. All boxplots above the red line indicate full closure (B). Each boxplot represents seven measurements. Different letters represent significant differences from other results with p -values below 0.05. Closing times (C) and speeds (E) were measured with the help of the motion paths (colored tracks of lobe tips). Closing times ranged from 36 s to 429 s with an average of 234.7 s, whereas average closing speeds ranged from 0.19×10^{-3} m/s up to 1.1×10^{-3} m/s. Each boxplot represents 14 measurements. In order to determine the force that was generated by the springs at closing temperature (65 °C), they were placed in the thermal chamber of the testing machine, and the output force was measured (F).

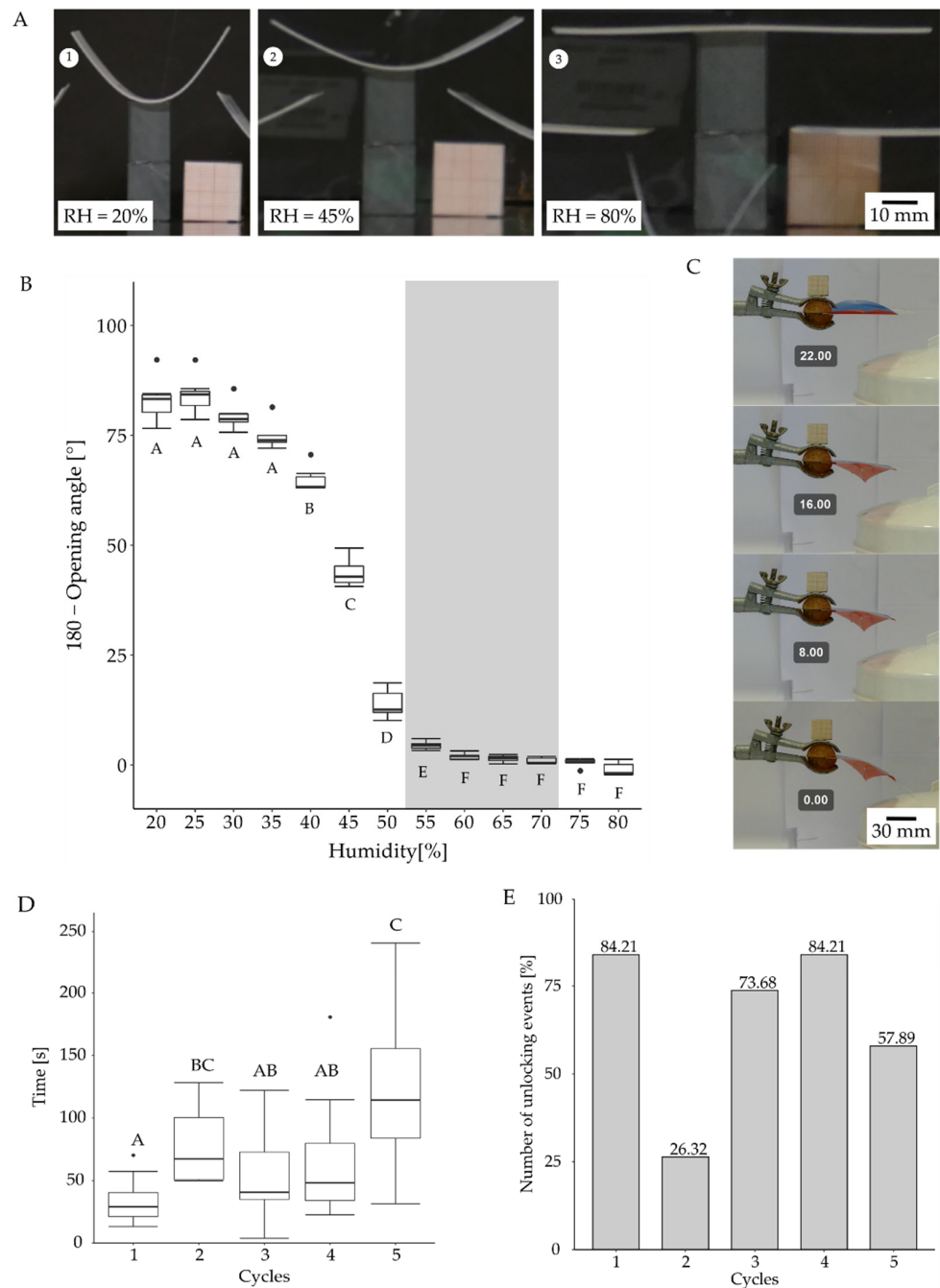


Figure 7. Autonomous environmentally triggered motion of VFf with a hydrogel-coated SMP backbone. In the dried state, the hydrogel-coated backbone is bent ((A1), 20%) but straightens when the level of humidity increases ((A2), 45%; (A3), 80%). At a constant temperature of 65 °C and 60% humidity, the backbone reaches 0° curvature (B) $n = 7$. The straightening process of the locked demonstrator (with foil attached) needs higher levels of humidity to overcome the resistance within the bent foil. Approximately 70% humidity is required to unlock the hydrogel demonstrator. To determine the unlocking time precisely from contact to switching, a stream of hot steam was directed selectively towards only the hydrogel-coated backbone (C). The time needed for the unlocking of the demonstrator ranged from 16.8 s to 241 s after first contact with the stream of hot water vapor (C,D). Significance levels are indicated by the capital letters next to each boxplot. Different letters represent significant differences from other results with p -values below 0.05. In this testing scenario, 19 demonstrators were tested five times. If the demonstrator did not unlock within 300 s, the test was declared unsuccessful (E).

3.5. Energy and Work/Kinetic Energy Requirements and Stored Energy for and during Lobe Movement

The energy consumption of each experiment was determined by measuring the amount of electricity that was required for actuation. The electricity consumption was determined with an energy-measuring device that was plugged into the socket before the actual electricity consumer. Between 0.24 and 0.23 L of compressed air was needed for each actuation cycle of the pneumatic demonstrator, and the pneumatic test bench consumed 1 J per cycle (closing and opening). The magnetic stirrer consumed between 27 J and 39 J for the duration of actuation depending on rotation speed. Unlocking of the heat- and moisture-driven hydrogel actuator through a hot water steam source consumed 129,712 J, whereas the SMA-based actuation through contactless heating in a temperature chamber consumed 5,464,800 J of electric energy (Table 1). The efficiency of the systems is for pneumatic actuation around 3.7%, for magnetic actuation 5.6%, whereas for the SMA spring it is far lower as the temperature chamber used has a very high power consumption (Table 1).

Force-displacement measurements were performed to determine the amount of kinetic energy (work) required either to open or to close the VFfs (Figure 8). The closing movement of the pneumatic VFf needed an average amount of kinetic energy between 19.04 mJ and 30.81 mJ. Most of the time (97.3%), the opening motion of the two lobes was slightly time-shifted, as one lobe opened before the other (Figure 8C,D). For the opening movement of the VFf, an average kinetic energy requirement of 24.42 mJ to 34.65 mJ was needed to trigger the first opening event (Figure 8D,E). Between 38.49 mJ and 79.54 mJ were necessary for the second opening event (Figure 8D,E). A parallel or simultaneous lobe opening demanded less kinetic energy (around 37 mJ), although the force needed was higher (10 N compared with 9 N for the second lobe opening). The overall stroke necessary to achieve the opening movement was less than that for the non-parallel opening (Figure 8F). During opening, this difference was also reflected in the observed force drop, which was lower for non-parallel opening than for parallel simultaneous opening (Figure 8E). The release of the stored energy was reflected in the drop in force after the opening of a lobe. The released stored energy was calculated with Equation (1) to be approximately 0.6 mJ for the opening of one lobe and 2.4 mJ for the opening of both lobes in parallel.

Similar experiments were performed on the magnetic VFfs by applying a downward force on the magnets (Figure 8G,H). The mean kinetic energy requirements ranged between 11.63 mJ and 17.31 mJ. The measured curves for the closing movement of the pneumatically and magnetically driven VFf differed from each other. Both showed a linear increase in force at first, but for the pneumatic demonstrator, the curve became steeper at the end of stroke (B), whereas for the magnetic demonstrator, it flattened, and even decreased (H). The average force generated by the SMA springs at 65 °C ranged from 4.17 N to 6.83 N (Figure 6F) and the change in spring length (Figure 6B) from 5.6 mm to 54.4 mm. Based on these values, the average kinetic energy requirements computed to 48.1 mJ to 315.9 mJ. The energy values of all tested VFf systems in comparison with the biological model are shown in Table 1.

Table 1. Comparison of *D. muscipula* with artificial Venus flytraps.

Schematic	Type	Actuation	Sensing	Snap-Buckling	Closing Time	Maximum Speed	Kinetic Energy Requirements for Actuation	Energy Consumption of the Test Setup	Efficiency of the Actuation	Reversibility
	<i>Dionaea muscipula</i>	Stimulation of trigger hairs lead to active water displacement	Touch sensitive trigger hairs	Yes	0.15 s to 1.8 s Literature: 0.1 s to 0.5 s [27]	0.016–0.245 m/s	Approx. 300 μmol ATP (at standard conditions equals 9.66 J) [27,28]	-	-	Yes
	Pneumatic VFF	Pressurized air (approx. 0.7 bar)	No sensor/actuated manually	Yes	Closing: 0.119 s to 0.311 s Opening: 0.023 s to 0.059 s	Opening movement: 3.26 m/s to 4.94 m/s	Opening: 38.49 mJ to 79.54 mJ Closing: 19.04 mJ to 30.81 mJ	1 J for magnet valves and between 0.24 L and 0.3 L compressed air	3.7%	Yes
	Magnetically driven VFF	Rotating magnetic field	No sensor/actuated manually	No	Lobes do not close completely	0.56 m/s to 3.56 m/s	11.52 to 17.15 mJ for manual closing	Between 27 and 39 J for the magnetic stirrer	5.6%	Yes
	Thermally driven SMA VFF	Increase in temperature	Inherent to the material	No	36.0 s to 429 s with an average of 234.7 s.	0.000254 to 0.00117 m/s	Approx. 48.1 mJ to 315.9 mJ of energy provided by the SMA spring	5,464,800 J for thermal heating	$3.3 \times 10^{-8}\%$	Yes
	Hydrogel coated VFF	Change in humidity	Inherent to the material	No	No real closure but unlocking time: 33.2 s to 126 s	Not determined	Environmental humidity of approx. 77%	129,712.68 J for steam production	-	-

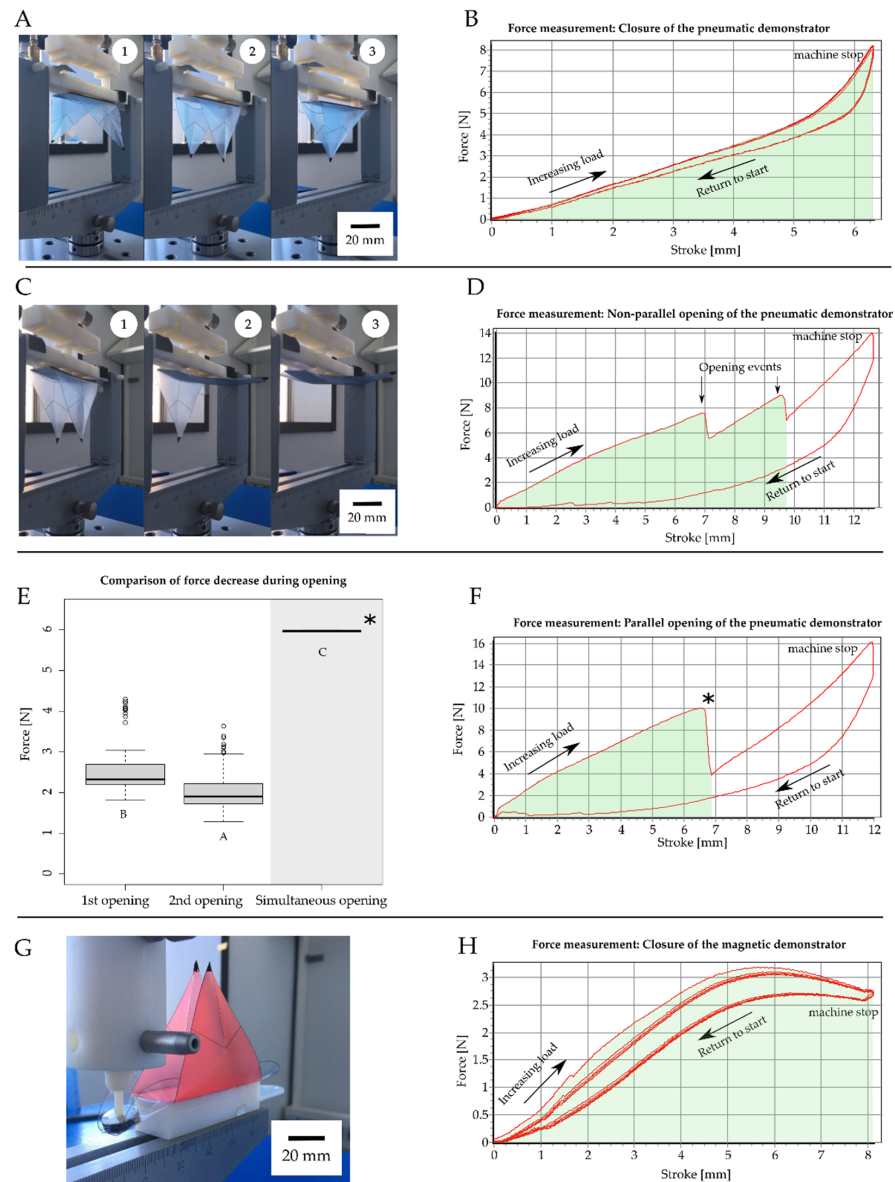


Figure 8. Kinematic energy measurements: examples of force displacement measurements carried out on the pneumatic and magnetic VFfs. Force measurements are used to calculate the energy needed to close and open the system. To imitate the closure of the pneumatic demonstrator, a piston with two pins is used to apply pressure to the backbone until the lobes close (A1–A3). The force (B) necessary to close the lobes is measured repeatedly. The force for the opening movement is measured with a piston designed to apply pressure at the center of the backbone (C1–C3). In most cases, the lobes open one after another (C2,C3) resulting in two distinct sudden drops in the force measured (D). When both lobes open simultaneously (F), the measured decrease in force (indicated by * in (E,F)) is larger compared with the separate opening events (E). Each of the three demonstrators used for video analysis were tested 25 times for opening and closing movements, respectively. The magnetic demonstrator (G,H) needed less force compared with the pneumatic demonstrator and also less energy. The force-displacement curves shown in (B,D–F,H) represent exemplary curves. Significance levels are indicated by the capital letters next to each boxplot. Different letters represent significant differences from other results with *p*-values below 0.05 (B).

4. Discussion

We have created an environmentally triggerable biomimetic system combining two movement principles in one cost-efficient structure mimicking biological models. The

movement characterization with direct and precise pneumatic actuation has revealed that one motion cycle of our VFf system consists of five phases, beginning with a fast closure within 311 ms, followed by an even faster snap opening within 73 ms based on the release of stored elastic energy during opening. Through contactless, magnetically driven actuation, the VFf achieves an oscillating motion of the lobes near to the estimated resonance frequency of the system. The SMA spring and hydrogel-coated SMP backbone actuated VFfs highlight the possibility of an actuation of the system induced by environmental stimuli. Overall, the first combination of two snap-trap motion principles within one compliant system provides the baseline not only for novel artificial Venus flytraps, which are as fast as the biological model (pneumatic VFfs) and which act just as autonomously (3D-printed hydrogel-coated VFfs), but also for application in the fields of bioinspired architecture, autonomous systems, and soft robotic actuation.

High-speed recordings have allowed us to study the complete movement of the capture lobe of *D. muscipula*, an event that lasts on average less than 500 ms, matching well with the literature values (100–500 ms [6,27,29]). We have observed that, during a three-week testing period, the plants tend to take longer and longer to close after an unsuccessful attempt at catching prey, a rest period, and a full reopening. We have been able to record and track the time and speed of the fast snap buckling motions in the biological model and to compare them with measurements of the motions of our VFf systems. With the presented characterization process and setup, it is possible to analyze fast 3D movements with high-resolution videos at 1000 fps frame rate.

4.1. Comparison with the Biological Model

Our VFf systems take less time for closure and generate higher speeds than the biological models (Table 1). Table 1 represents an updated extension of the table published by Esser et al. [13] and compares the individual VFf systems of this study with the biological model. To determine the energy required for closure, the energy consumption of each experiment was determined by measuring the amount of electricity that was required for actuation via an energy-measuring device. Force-displacement measurements were performed to determine the kinetic energy required for closure and the potential energy stored in the system during closure. The VFf systems required less energy (1 J in the case of pneumatic actuation derived from electrical energy consumption) for lobe closure than *D. muscipula*, which needed approximately 300 μmol ATP (ca. 10 J under standard conditions [27,28]). A comparison with other AVF literature values is difficult, since no energy measurements or calculations have been performed for most systems. The SMA spring-driven system of Kim et al. [30] needs 12.4 J for closing and 48 J for reopening, which are lower values than for our thermally driven SMA system and higher for the biological model. Their AVF system is faster in closing than our SMA-driven system. As we use a thermal chamber for heating instead of direct heating via electrical current (joule heating), our system heats up far more slowly than that of Kim et al. [30]. However, the former more clearly reflects heating attributable to a change in ambient temperature and validates the feasibility of our system for its intended use. In contrast to the system of Kim et al., the highest movement speeds in our study were achieved with the pneumatically and magnetically driven VFf systems.

4.2. Combination of Two Snap-Trap Principles Gives a Novel Pneumatically Driven Motion Sequence

The actuation time (AT) significantly influenced the closing time of the pneumatic VFf, with a shorter AT resulting in a shorter closure time. As the necessary actuation pressure inside the cushions was 0.7 bar, the overall system pressure had to be higher to achieve this value during shorter AT. The closed state of the pneumatic VFf represents a high energetic state, where energy is stored by elastic deformation within the backbone and by distortion of the lobe geometry. This energy can only be released suddenly by passing a threshold in pressure and increasing the curvature of the backbone, which thereby transforms the stored elastic energy into kinetic energy causing the observed rapid movement of the lobes.

Thus, the pneumatic cushions are not involved in this opening process; as such, their AT has only marginal to no influence on the opening time. The small differences observed are attributable to variations in the acceleration of the lobe. Significant differences above 40 ms in the opening times are attributable to a delayed and non-parallel opening movement of the two lobes. The observed large differences are probably based on inaccuracies during the manufacturing process, as the demonstrators are produced by hand, which can lead to (small) geometric deviations between the individual demonstrators.

A comparable pneumatic AVF system from Pal et al. [14] consists entirely of silicone and is able to close its trap lobes within 50 ms when using 0.35 to 0.7 bar for actuation, comparable with the pressure used in our pneumatic VFfs. In contrast to Pal's system, our system stores energy during the closure movement within its lobe curvature similar to *D. muscipula* and does not rely on a pre-stretched layer. Therefore, the opening of our system shows actual snap buckling similar to that achieved in the biological model by releasing the stored energy in the lobes and thereby producing a rapid movement.

4.3. Resonance-like Movement and Generation of Contactless Fast Flapping Motion

Driven via a rotating magnetic field, the VFf is able to achieve a uniform oscillation or resonance-like motion depending on the rotational speed. Since the lobe motion is kinematically coupled to the ear motion, a significant influence of the different actuation speeds on the lobe motion in terms of velocity and overall motion has been observed. At 400 and 700 rpm, only minor motion of the VFfs is observed, but as the system approaches its presumed natural frequency at about 800–900 rpm based on acoustic and visual regularity, motion becomes more regular, and high flapping velocities and large amplitudes of motion are achieved. At more than 900 rpm, the movement becomes more irregular, and the lobes undergo kinking. Their movement could no longer follow the movement of the ear, which moves up and down faster than the lobes.

A comparison with the magnetic AVF from Zhang et al. [15,16] is difficult as their system uses an electromagnet to repulse a magnet attached to the AVF lobe, closing the system in 100 ms. Our system does not fully close its lobes and performs a flapping motion instead of closure.

4.4. Environmentally Triggered Motion

The closing of the SMA spring was significantly slower compared with that of the pneumatic VFf presented. Once the transition temperature was reached, the movement was continuous but slow. Notably, the used climate chamber showed effects of inevitable thermal stratification because of the low fan speed used during video recording (Figure S6). This led to the VFf nearest to the ceiling of the chamber reaching the critical transition temperature first. The systems showed no significant difference in closing speed or time (necessary for full closure) once the closing motion was initiated at transition temperature.

A direct comparison with the SMA-powered AVFs by Kim et al. (2014) is impossible, as the latter is based on bi-stable prepreg surfaces, in which the SMA springs are used to overcome the tipping point in the bi-stable system resulting in a fast-snapping motion, which takes from 0.4 s to 1.2 s [30].

Autonomy and environmental triggers are introduced into the system with the incorporation of shape memory materials. The VFf closure movement can be triggered by a change in temperature. This allows the system to be locked into a snapped open state until a specific stimulus combination unlocks the system and triggers the release of stored elastic energy. The blocking and locking of the movement and the specific release mechanism are achieved by the material properties of the components and the combination of shape memory polymers with hydrogels. We suspect that the observed differences between the individual test runs are attributable to the reduction and build-up of internal stresses in the system. The test conditions were not changed between the test runs, and the demonstrators were all dried in the same way. This creates an unwanted variance within the system, an issue that will be investigated in further studies. A comparable hydrogel-based system is

the hydroscopic bi-stable sheet AVF of Lunni et al. [21], which responds to a 30% increase in relative humidity. Our hydrogel requires an increase of 35% in combination with the SMP backbone to create movement.

4.5. Overall System Discussion and Outlook

The novel motion sequence achieved here by combining the movement principles of two snap-trapping plants uses motion amplification for closure and snap buckling for opening. The closure movement temporarily stores energy via the deformation of the foil and backbone: through the bending of the attached backbone, the foil crease buckles, and the system snaps open. This novel motion pattern can be used for various applications in energy harvesting, safety switches, escape movements of UAVs and bioinspired architecture. Triggering and actuating the motion can be achieved through various actuation principles.

Compared with the biological model and other AVF systems, only the pneumatically actuated VFf requires less energy for actuation and shows a similar kinematic behavior to the biological model with curvature reversal of the lobes and a fast snapping motion. Moreover, the system is easy and inexpensive to produce, by using office supplies (overhead foil, magnets, double-sided adhesive tape) and 3D-printed parts with a low heat deflection temperature in the range of 50 °C. Our systems provide an alternative to the current state-of-the-art AVF in terms of actuation and environmental sensitivity and allow various types of actuations to be tested in the same base module.

For example, the pneumatic actuation system represents a suitable actuator to achieve precise and controllable motions. In combination with the specific structure of the VFf, the novel movement and snapping mechanism builds a mechanical energy buffer. During the closure movement, potential energy is mechanically stored in the system and is explosively released during parallel opening. The attachment of triboelectric harvesters to the lobes might allow the partial recuperation of the kinetic energy of the snapping motion (release of potential energy during opening 2.4 mJ), similar to the leaf harvesters of Meder et al. [1,31].

By using different materials and material combinations, the principle shown can also be transferred to other application areas. The autonomous actuation depends on the properties of the materials employed and can be achieved by other environmentally triggered shape memory materials, e.g., liquid crystalline elastomers [20,32–34]. Important here is the geometry and the combination of flexible and rigid material, equivalent to those of the foil and backbone, which enable a snapping motion in the first place. The system can also be implemented using a multilayer film system, whose individual films have different coefficients of thermal expansion, strengths, and stiffness.

The combination of the present actuation strategies into one system is yet to be achieved. Two combination strategies are possible. First, the combination of pneumatic actuation and the hydrogel/SMP-based system initialization mechanism should enable quick opening and closing via pneumatics and the locking of the system in place by hydrogel drying without having to expend energy. The second possibility arises from combination of the thermally driven SMA spring with a hydrogel latch creating a latch-mediated spring actuation (LaMSA) system [11,35]. The latch holds the spring in place, until an increase occurs in humidity. To function, the hydrogel-coated backbone must be stiff enough to withstand the contraction force generated by the SMA spring. This only applies if the system is heated above 65 °C, e.g., by direct sunlight, which causes the spring to contract and the SMP backbone to heat up beyond its T_C . In future studies, flexible sensors will be integrated into the system, representing a first step in the development of a fully autonomous AVF system.

5. Conclusions

In this study, we present a novel motion sequence for plant-inspired robotics that combines, for the first time, the motion principles of two snap-trap mechanisms, as observed in plants, into an artificial Venus flytrap, namely the artificial Venus Flyflap (VFf) system. This system is based on a compliant foil with a rigid backbone resembling the snap-traps

of plants. A closing step via kinematic coupling and motion amplification of the lobes and a fast opening through snap buckling of the VFFs backbone characterize the motion. A uniform resonance-like motion is achieved via actuation through rotating magnetic fields. Two autonomous environmentally triggerable versions are presented based on shape memory materials in combination with a hydrogel coating that reacts to changes in temperature and humidity. In addition, a novel selective locking mechanism is introduced that only unlocks if two environmental stimuli (in this case, changes in humidity and temperature) are present at the same time. The VFF system is characterized in terms of motion kinematics, speed, times, and energy requirements and is compared with the biological model and state-of-the-art AVF systems, all of which highlight the biomimetic potential and low energy demand of our system.

In future studies, the presented environmentally triggered actuators will be merged into one system with self-healing foil materials systems. In addition, the integration of soft flexible sensors and flexible solar cells as energy harvesters will lead to an autonomous system with embodied intelligence and energy. Hereby, we should achieve an autonomous, adaptive, and self-healing artificial Venus flytrap system advancing soft plant-inspired robotics and bringing technology one step closer to the ingenuity found in naturally occurring systems.

Supplementary Materials: The following supporting information can be downloaded at: <https://www.mdpi.com/article/10.3390/biomimetics7030099/s1>, Supplementary Material document including further information as well as the cited figures: Figure S1. The pneumatic test bench provided pressurized air for the demonstrator [25]. Figure S2. Setup for magnetic demonstrator testing. Figure S3. Frequency measurements of magnetic demonstrators. Figure S4. Determination of critical temperature and contraction behavior of the five SMA-springs. Figure S5. Climate chamber setup for SMA-spring demonstrator measurements. Figure S6. Temperature distribution inside the climate chamber at the different levels of the demonstrators. Figure S7. 3D printed SMP backbone for coating with hydrogel. Figure S8. Preparation of full assembly of environmentally triggerable systems stimulus combination system [36,37]. Figure S9. Determination of the opening angles and the torsion of the backbones. Table S1. Kinematic analysis of the *Dionaea muscipula* was performed with the same setup as the magnetic and pneumatic demonstrator. Table S2. Maximum force generated by SMA springs at 65 °C. Table S3. The actuation pattern, actuation time and actuation pressure that were used to achieve repetitive actuation are displayed. Table S4. Flapping frequency corresponding to different actuation speeds of the magnetic demonstrators. Table S5. Length change of SMA springs at different temperatures when mounted to a foil demonstrator. Table S6. Closing times of the SMA spring demonstrator at different temperatures [37].

Author Contributions: Conceptualization, F.J.T., F.D.S. and T.S.; methodology, F.J.T. and F.D.S.; formal analysis, F.J.T., F.D.S. and T.S.; investigation, F.J.T., P.A. and J.T.; data curation, P.A. and F.J.T.; writing—original draft preparation, F.J.T. and P.A.; writing—review and editing, F.J.T., F.D.S. and T.S.; visualization, P.A. and F.J.T.; supervision, F.J.T. and T.S.; project administration, F.J.T. and T.S.; funding acquisition, T.S. All authors have read and agreed to the published version of the manuscript.

Funding: This work was funded by the Deutsche Forschungsgemeinschaft (DFG, German Research Foundation) under Germany's Excellence Strategy-EXC-2193/1-390951807.

Data Availability Statement: Data is available in the supplementary material document and on request.

Acknowledgments: F.J.T. and T.S. are grateful to the Deutsche Forschungsgemeinschaft for funding their research. The authors thank R. Jones for improving the manuscript language. The authors thank various colleagues within the framework of the cluster of excellence "Living Materials Systems (livMatS)" for inspiring discussions.

Conflicts of Interest: The authors declare no conflict of interest. The funders had no role in the design of the study, in the collection, analyses, or interpretation of data, in the writing of the manuscript, or in the decision to publish the results.

References

1. Meder, F.; Must, I.; Sadeghi, A.; Mondini, A.; Filippeschi, C.; Beccai, L.; Mattoli, V.; Pingue, P.; Mazzolai, B. Energy conversion at the cuticle of living plants. *Adv. Funct. Mater.* **2018**, *28*, 1806689. [CrossRef]
2. Mazzolai, B. Plant-inspired growing robots. In *Soft Robotics: Trends, Applications and Challenges*; Laschi, C., Rossiter, J., Iida, F., Cianchetti, M., Margheri, L., Mazzolai, B., Eds.; Springer: Cham, Switzerland, 2017.
3. Must, I.; Sinibaldi, E.; Mazzolai, B. A variable-stiffness tendril-like soft robot based on reversible osmotic actuation. *Nat. Commun.* **2019**, *10*, 344. [CrossRef] [PubMed]
4. Mazzolai, B.; Mondini, A.; Dottore, E.D.; Sadeghi, A. Self-growing adaptable soft robots. In *Mechanically Responsive Materials for Soft Robotics*; Koshima, H., Ed.; Wiley-VCH: Weinheim, Germany, 2020; pp. 363–394. ISBN 3527822208.
5. Mazzolai, B.; Tramacere, F.; Fiorello, I.; Margheri, L. The Bio-Engineering Approach for Plant Investigations and Growing Robots. A Mini-Review. *Front. Robot. AI* **2020**, *7*. [CrossRef] [PubMed]
6. Poppinga, S.; Bauer, U.; Speck, T.; Volkov, A.G. Motile traps. In *Carnivorous Plants: Physiology, Ecology, and Evolution*; Ellison, A., Adamec, L., Eds.; Oxford University Press: Oxford, UK, 2018; pp. 180–193. ISBN 9780198779841.
7. Sachse, R.; Westermeier, A.; Mylo, M.; Nadasdi, J.; Bischoff, M.; Speck, T.; Poppinga, S. Snapping mechanics of the Venus flytrap (*Dionaea muscipula*). *Proc. Natl. Acad. Sci. USA* **2020**, *117*, 16035–16042. [CrossRef]
8. Poppinga, S.; Joyeux, M. Different mechanics of snap-trapping in the two closely related carnivorous plants *Dionaea muscipula* and *Aldrovanda vesiculosa*. *Phys. Rev. E* **2011**, *84*, 041928–041935. [CrossRef]
9. Raney, J.R.; Nadkarni, N.; Daraio, C.; Kochmann, D.M.; Lewis, J.A.; Bertoldi, K. Stable propagation of mechanical signals in soft media using stored elastic energy. *Proc. Natl. Acad. Sci. USA* **2016**, *113*, 9722–9727. [CrossRef]
10. Arrieta, A.F.; Bilgen, O.; Friswell, M.I.; Hagedorn, P. Dynamic control for morphing of bi-stable composites. *J. Intell. Mater. Syst. Struct.* **2013**, *24*, 266–273. [CrossRef]
11. Kim, Y.; van den Berg, J.; Crosby, A.J. Autonomous snapping and jumping polymer gels. *Nat. Mater.* **2021**, *20*, 1695–1701. [CrossRef]
12. Zhong, Y.; Du, R.; Guo, P.; Yu, H. Investigation on a new approach for designing articulated soft robots with discrete variable stiffness. *IEEE/ASME Trans. Mechatron.* **2021**, *26*, 2998–3009. [CrossRef]
13. Esser, F.J.; Auth, P.; Speck, T. Artificial Venus flytraps: A research review and outlook on their importance for novel bioinspired materials systems. *Front. Robot. AI* **2020**, *7*, 75. [CrossRef]
14. Pal, A.; Goswami, D.; Martinez, R.V. Elastic Energy Storage Enables Rapid and Programmable Actuation in Soft Machines. *Adv. Funct. Mater.* **2019**, *30*. [CrossRef]
15. Zhang, Z.; Li, X.; Yu, X.; Chai, H.; Li, Y.; Wu, H.; Jiang, S. Magnetic actuation bionic robotic gripper with bistable morphing structure. *Compos. Struct.* **2019**, *229*, 111422. [CrossRef]
16. Zhang, Z.; Chen, D.; Wu, H.; Bao, Y.; Chai, G. Non-contact magnetic driving bioinspired Venus flytrap robot based on bistable anti-symmetric CFRP structure. *Compos. Struct.* **2016**, *135*, 17–22. [CrossRef]
17. Shahinpoor, M. Biomimetic robotic Venus flytrap (*Dionaea muscipula* Ellis) made with ionic polymer metal composites. *Bioinspir. Biomim.* **2011**, *6*, 46004. [CrossRef]
18. Shi, L.; Guo, S.; Kudo, H.; Asaka, K. Development of a Venus flytrap-inspired robotic flytrap. In Proceedings of the 2012 IEEE International Conference on Robotics and Biomimetics (ROBIO), Guangzhou, China, 11–14 December 2012; pp. 551–556.
19. Wani, O.M.; Zeng, H.; Priimagi, A. A light-driven artificial flytrap. *Nat. Commun.* **2017**, *8*, 15546. [CrossRef]
20. Wani, O.M.; Verpaalen, R.; Zeng, H.; Priimagi, A.; Schenning, A.P.H.J. An artificial nocturnal flower via humidity-gated photoactuation in liquid crystal networks. *Adv. Mater.* **2018**, *31*, 1805985. [CrossRef]
21. Lunni, D.; Cianchetti, M.; Filippeschi, C.; Sinibaldi, E.; Mazzolai, B. Plant-Inspired Soft Bistable Structures Based on Hygroscopic Electrospun Nanofibers. *Adv. Mater. Interfaces* **2020**, *7*, 1901310. [CrossRef]
22. Esser, F.; Scherag, F.D.; Poppinga, S.; Westermeier, A.; Mylo, M.D.; Kampowski, T.; Bold, G.; Rühle, J.; Speck, T. Adaptive Biomimetic Actuator Systems Reacting to Various Stimuli by and Combining Two Biological Snap-Trap Mechanics. In *Biomimetic and Biohybrid Systems, Proceedings of the 8th International Conference, Living Machines, Nara, Japan, 9–12 July 2019*; Martinez-Hernandez, U., Vouloutsis, V., Mura, A., Mangan, M., Asada, M., Prescott, T.J., Verschure, P.F., Eds.; Springer: Cham, Switzerland, 2019; pp. 114–121. ISBN 978-3-030-24741-6.
23. Westermeier, A.S.; Sachse, R.; Poppinga, S.; Vögele, P.; Adamec, L.; Speck, T.; Bischoff, M. How the carnivorous waterwheel plant (*Aldrovanda vesiculosa*) snaps. *Proc. Biol. Sci.* **2018**, *285*, 20180012. [CrossRef]
24. Westermeier, A.; Poppinga, S.; Körner, A.; Born, L.; Sachse, R.; Saffarian, S.; Knippers, J.; Bischoff, M.; Gresser, G.T.; Speck, T. No joint ailments: How plants move and inspire technology. In *Biomimetic Architecture*; Knippers, J., Schmid, U., Speck, T., Eds.; Learning from Nature; Birkhäuser: Basel, Switzerland, 2019; pp. 32–41. ISBN 9783035617863.
25. Esser, F.; Krüger, F.; Masselter, T.; Speck, T. Development and characterization of a novel biomimetic peristaltic pumping system with flexible silicone-based soft robotic ring actuators. In *Biomimetic and Biohybrid Systems*; Vouloutsis, V., Halloy, J., Mura, A., Mangan, M., Lepora, N., Prescott, T.J., Verschure, P.F.M.J., Eds.; Springer: Cham, Switzerland, 2018; pp. 157–167. ISBN 978-3-319-95971-9.
26. Schindelin, J.; Arganda-Carreras, I.; Frise, E.; Kaynig, V.; Longair, M.; Pietzsch, T.; Preibisch, S.; Rueden, C.; Saalfeld, S.; Schmid, B.; et al. Fiji: An open-source platform for biological-image analysis. *Nat. Methods* **2012**, *9*, 676–682. [CrossRef]
27. Forterre, Y.; Skotheim, J.M.; Dumais, J.; Mahadevan, L. How the Venus flytrap snaps. *Nature* **2005**, *433*, 421–425. [CrossRef]

28. Jaffe, M.J. The role of ATP in mechanically stimulated rapid closure of the Venus's flytrap. *Plant Physiol.* **1973**, *51*, 17–18. [CrossRef] [PubMed]
29. Poppinga, S.; Kampowski, T.; Metzger, A.; Speck, O.; Speck, T. Comparative kinematical analyses of Venus flytrap (*Dionaea muscipula*) snap traps. *Beilstein J. Nanotechnol.* **2016**, *7*, 664–674. [CrossRef] [PubMed]
30. Kim, S.-W.; Koh, J.-S.; Lee, J.-G.; Ryu, J.; Cho, M.; Cho, K.-J. Flytrap-inspired robot using structurally integrated actuation based on bistability and a developable surface. *Bioinspir. Biomim.* **2014**, *9*, 36004. [CrossRef] [PubMed]
31. Meder, F.; Thielen, M.; Mondini, A.; Speck, T.; Mazzolai, B. Living Plant-Hybrid Generators for Multidirectional Wind Energy Conversion. *Energy Technol.* **2020**, *8*, 2000236. [CrossRef]
32. He, Q.; Wang, Z.; Song, Z.; Cai, S. Bioinspired design of vascular artificial muscle. *Adv. Mater. Technol.* **2019**, *4*, 1800244. [CrossRef]
33. Xiao, Y.-Y.; Jiang, Z.-C.; Zhao, Y. Liquid crystal polymer-based soft robots. *Adv. Intell. Syst.* **2020**, *2*, 2000148. [CrossRef]
34. Kim, H.; Ahn, S.; Mackie, D.M.; Kwon, J.; Kim, S.H.; Choi, C.; Moon, Y.H.; Lee, H.B.; Ko, S.H. Shape morphing smart 3D actuator materials for micro soft robot. *Mater. Today* **2020**, *41*, 243–269. [CrossRef]
35. Longo, S.J.; Cox, S.M.; Azizi, E.; Ilton, M.; Olberding, J.P.; St Pierre, R.; Patek, S.N. Beyond power amplification: Latch-mediated spring actuation is an emerging framework for the study of diverse elastic systems. *J. Exp. Biol.* **2019**, *222*, jeb197889. [CrossRef]
36. Rendl, M.; Bönisch, A.; Mader, A.; Schuh, K.; Prucker, O.; Brandstetter, T.; Rühle, J. Simple one-step process for immobilization of biomolecules on polymer substrates based on surface-attached polymer networks. *Langmuir* **2011**, *27*, 6116–6123. [CrossRef]
37. Motzki, P. Efficient SMA Actuation—Design and Control Concepts. In The 1st International Electronic Conference on Actuator Technology: Materials, Devices and Applications. The 1st International Electronic Conference on Actuator Technology: Materials, Devices and Applications. *Proceedings* **2020**, *64*, 20. [CrossRef]



Article

Bio-inspired Machine Learning for Distributed Confidential Multi-Portfolio Selection Problem

Ameer Tamoor Khan ^{1,†}, Xinwei Cao ^{2,*}, Bolin Liao ^{3,†} and Adam Francis ^{4,†}¹ Department of Computing, The Hong Kong Polytechnic University, Hong Kong 999077, China² School of Business, Jiangnan University, Wuxi 213031, China³ College of Computer Science and Engineering, Jishou University, Jishou 409811, China⁴ Faculty of Science and Engineering, Swansea University, Swansea SA1 8EN, UK

* Correspondence: xcao.fudan@gmail.com

† These authors contributed equally to this work.

Abstract: The recently emerging multi-portfolio selection problem lacks a proper framework to ensure that client privacy and database secrecy remain intact. Since privacy is of major concern these days, in this paper, we propose a variant of Beetle Antennae Search (BAS) known as Distributed Beetle Antennae Search (DBAS) to optimize multi-portfolio selection problems without violating the privacy of individual portfolios. DBAS is a swarm-based optimization algorithm that solely shares the gradients of portfolios among the swarm without sharing private data or portfolio stock information. DBAS is a hybrid framework, and it inherits the swarm-like nature of the Particle Swarm Optimization (PSO) algorithm with the BAS updating criteria. It ensures a robust and fast optimization of the multi-portfolio selection problem whilst keeping the privacy and secrecy of each portfolio intact. Since multi-portfolio selection problems are a recent direction for the field, no work has been done concerning the privacy of the database nor the privacy of stock information of individual portfolios. To test the robustness of DBAS, simulations were conducted consisting of *four* categories of multi-portfolio problems, where in each category, *three* portfolios were selected. To achieve this, 200 days worth of real-world stock data were utilized from 25 NASDAQ stock companies. The simulation results prove that DBAS not only ensures portfolio privacy but is also efficient and robust in selecting optimal portfolios.

Keywords: multi-portfolio; optimization; swarm algorithm; beetle antennae search; stochastic algorithm; distributed beetle antennae search; investment; stocks



Citation: Khan, A.T.; Cao, X.; Liao, B.; Francis, A. Bio-inspired Machine Learning for Distributed Confidential Multi-Portfolio Selection Problem. *Biomimetics* **2022**, *7*, 124.

<https://doi.org/10.3390/biomimetics7030124>

biomimetics7030124

Academic Editors: Stanislav N. Gorb, Giuseppe Carbone, Thomas Speck and Andreas Taubert

Received: 31 July 2022

Accepted: 19 August 2022

Published: 29 August 2022

Publisher's Note: MDPI stays neutral with regard to jurisdictional claims in published maps and institutional affiliations.



Copyright: © 2022 by the authors. Licensee MDPI, Basel, Switzerland. This article is an open access article distributed under the terms and conditions of the Creative Commons Attribution (CC BY) license (<https://creativecommons.org/licenses/by/4.0/>).

1. Introduction

Portfolio optimization is a hot research topic in academia, since it enables investors to make an optimal decision between profit and risk. This refers to the method of making the best investment in numerous stocks [1]. Apart from this, there are several other real-world constraints that researchers have taken care of over time, for instance, cardinality constraint, tax-aware constraint, lower and upper bounds, multiple portfolios, round-lot constraint, stock size, computational and time complexities.

There are several state-of-the-art algorithms that have been proposed over time to tackle these constraints. For instance, an unconstrained portfolio optimization problem can be easily solved using linear or quadratic programming, but constraints make it a complex optimization problem to solve. Ref. [2] showed that the simple addition of a cardinality constraint makes it an NP-complete problem. Therefore, there is no straightforward algorithm to compute the exact optimality of the problem. Techniques that use machine learning algorithms, heuristic algorithms, and black-box optimization are good alternatives to solve such highly complex, computationally and time-consuming problems. Ref. [3] proposed using multiple machine learning modules, i.e., coordinate descent, the proximal gradient, Dykstra, and alternating direction of multipliers. Their algorithm also accounts for

several constrained portfolios, i.e., equal risk contribution, diversified, and risk budgeting portfolios. Likewise, Ref. [4] combined several portfolio models, i.e., equal-weighted modeling (EQ), mean-variance model, and Monte Carlo simulation modeling. Furthermore, to improve the portfolio problem based on its time-series nature, they applied a long short-term memory (LSTM) model. However, the major drawback of these methods is the training of hundreds of hyper-parameters, which makes them computationally expensive and slow to compute.

In this paper, we are focused on the multi-portfolio selection problem while considering the investors' privacy. Since the multi-portfolio problem has only recently gained attention from academia and financial practitioners, no work has been conducted regarding the confidentiality and the secrecy of private databases and individual portfolios. The multi-portfolio selection problem enables the optimization of tens of hundreds of portfolios simultaneously, making it computationally economical and time efficient. There are several proposed methods for multi-portfolio optimization in the literature [5–17]. The authors of [18,19] were the pioneers of the multi-portfolio optimization domain. The objective was to maximize social welfare, which was the sum of the utility of the individual accounts. For instance, ref. [20] proposed a hybrid model that includes a heuristic and combinatorial framework and solved the multi-portfolio problem under a risk–budget constraint. Ref. [21] proposed a Cournot–Nash equilibrium framework to solve the multi-portfolio problem. The major drawback being that each portfolio was treated individually, assuming that the others gave the best response. Ref. [22] overcame this issue by proposing a joint optimization problem, where the model was able to optimize the portfolio as well as cost splitting among the portfolios. Ref. [23] employed an information pooling game mechanism for the multi-portfolio optimization. Ref. [24] added a risk measurement constraint along with the selection of multi-portfolios. Ref. [25] proposed fairness-aware multi-participant satisfying (FMS) criterion to model a target-oriented strategy which optimized client portfolios by maximizing the returns. The major drawback of these techniques is the lack of privacy for the investors. They also solve the multi-portfolio problem, collectively making asset data exposed, meaning data are not secure or confidential. In order to provide privacy to each investor, i.e., portfolios regarding their investment and portfolio selection, it is necessary to design a distributed framework that optimizes each portfolio locally and optimizes all portfolios collectively. The three types of optimizing models are shown in Figure 1. It shows that in local learning, all portfolios are optimized individually, which is computationally and time-wise inefficient. Likewise, typical swarm learning models do not account for the confidentiality of the data and portfolio, and the particles share critical information about the portfolios to reach the optimal solution. However, in the distributed system, each particle deals with a single portfolio locally, and the particles share the objective function value, i.e., gradients alone to each other. Thus, they efficiently optimize the multi-portfolio selection problem without violating privacy.

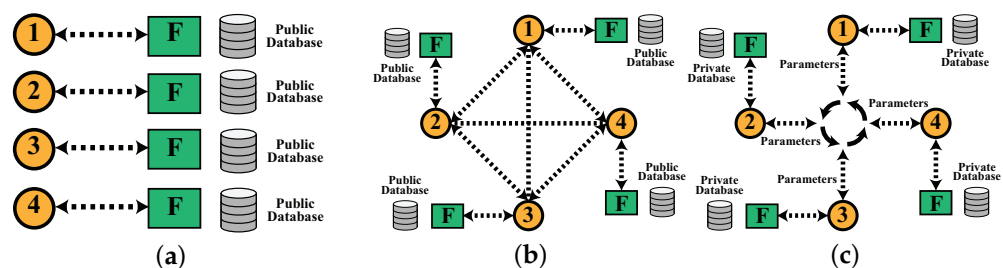


Figure 1. (a) shows the local learning where each BAS algorithm is assigned to one portfolio, and the objective is to optimize the respective portfolio. (b) shows the swarm architecture, where the swarm has access to a public database, where particles coordinate to obtain an optimal solution without considering the privacy of the database. (c) shows the distributed architecture, where particles only share the parameters, i.e., gradients, instead of the private information of the portfolios, i.e., private database, stock information, and client information.

In this paper, we propose a swarm variant of a known meta-heuristic algorithm known as Beetle Antennae Search (BAS). It mimics the food-collecting nature of the beetle in order to search for the optimal solution to a problem. BAS is a single particle searching algorithm, where the particle optimizes an objective function by searching the search space iteratively. The utility of BAS has expanded to several real-world problems [26–49], including the portfolio optimization. Ref. [50] employed BAS for the selection of the optimal portfolio under a non-convex cardinality constraint. Ref. [51] proposed a QBAS (Quantum Beetle Antennae Search) variant of BAS and solved the portfolio selection problem under cardinality constraint. Ref. [52] solved the time-varying portfolio selection problem under the transaction cost. Ref. [53] used the mean-variance model of portfolio optimization under two constraints: cardinality and transaction cost constraints. Ref. [54] proposed a hybrid framework of BAS-PSO and used it for portfolio optimization. From these research works, we can see the utility of BAS in portfolio optimization under real-world constraints. However, BAS has never been employed for the multi-portfolio optimization problem because of computational limitations. As mentioned earlier, BAS is a single particle searching algorithm, meaning it would be computationally challenging for BAS to optimize even a single portfolio with over 100 stock companies. Therefore, the efficiency of BAS will drop further if applied to the multi-portfolio selection problem.

We have proposed a swarm or distributed variant of BAS known as DBAS (Distributed Beetle Antennae Search). It is a hybrid variant with the swarm-like nature of Particle Swarm Optimization (PSO) and the BAS updating criteria. Each particle in DBAS will optimize a single portfolio, and collectively, the swarm will optimize all the portfolios without violating portfolio privacy. The DBAS will optimize the multi-portfolio in two stages by optimizing each portfolio locally and then optimizing all the portfolios globally without sharing any private data among portfolios. To the best of our knowledge, no researcher has considered the privacy issue while solving the multi-portfolio problem, since it is a newly emerging portfolio selection challenge. Through our proposed framework, we will optimize the multi-portfolio problem efficiently with low computation and time cost whilst ensuring the privacy of clients and their portfolios.

The rest of the paper is structured as follows: In Section 2, we will formulate the portfolio optimization problem. In Section 3, we will elaborate on the nature of BAS and will drive the DBAS variant. In Section 4, we will discuss the simulation results on a multi-portfolio selection problem with real-world stock data. In Section 5, we will conclude the paper with final remarks.

2. Problem Formulation

In this section, we will discuss the building blocks of the portfolio optimization problem. Later, we will elaborate on different portfolio models and select one for the DBAS algorithm. All the hyper-parameters are mentioned in Table 1.

Table 1. Hyper-Parameters.

Name	Notation	Values (Default)
Antennae Length	d	0.9
Step Size	τ	0.9
Personal Antennae Length	d_1	0.9
Global Antennae Length	d_2	0.9
Step Multiplier	η	0.99

2.1. Building Blocks of Portfolio Selection

Here, we will discuss the building blocks of portfolio selection, i.e., expected return (profit), risk, total investment, total transaction cost, and cardinality constraint.

2.1.1. Expected Return

The primary factor in portfolio optimization is the maximization of expected return: in other words, the profit that investors are expecting from their investment in stocks. Let us say there are K total stocks and the normalized investment in all K stocks is given as $E = [E_1, E_2, E_3, \dots, E_i, \dots, E_K] \in \mathbb{R}^K$, where i is the i -th stock and E_i is the normalized investment in the i -th stock. Now, let us say that the mean return of K stocks based on their past data is given as, $e = [\epsilon_1, \epsilon_2, \epsilon_3, \dots, \epsilon_i, \dots, \epsilon_K]^T \in \mathbb{R}^K$. The objective is to find the optimal E such that it maximizes the expected return, which is given as

$$\max_E \zeta(E) = Ee^T. \tag{1}$$

To further consolidate (1) and to ensure that the expected return is above a certain threshold k , the modification to (1) is given as,

$$\max_E \zeta(E) = Ee^T - k \geq 0. \tag{2}$$

here, k is a scalar quantity and $Ee^T - k = 0$ means the break-even point (no profit-loss).

2.1.2. Risk

The maximization of profit (expected return) does not avoid the risk factor. The second objective is to minimize the risk. The risk minimization is given as,

$$\min_E v(E) = EQE^T, \tag{3}$$

where Q is a covariance matrix, and it is given as,

$$Q = \begin{bmatrix} Q_{11} & Q_{12} & Q_{13} & \dots & Q_{1j} \\ Q_{21} & Q_{22} & Q_{23} & \dots & Q_{2j} \\ Q_{31} & Q_{32} & Q_{33} & \dots & Q_{3j} \\ \vdots & \vdots & \vdots & \ddots & \vdots \\ Q_{i1} & Q_{i2} & Q_{i3} & \dots & Q_{ij} \end{bmatrix}, \tag{4}$$

where Q_{ij} is the variance of the i -th stock with j -th stock in the portfolio.

2.1.3. Total Investment

Now, we will discuss one of the primary constraints: total investment. It ensures the allocation of the total asset in the stocks, and it is given as,

$$\mathbf{1}E^T = 1, \tag{5}$$

where $\mathbf{1}$ is a unit vector. As mentioned above, E^T is a normalized investment, so the sum of the amount invested in the portfolio should be 1 as shown in (5). To ensure this, we need an additional constraint which is given as,

$$\mathbf{0} \leq E \leq \mathbf{1}. \tag{6}$$

It will ensure that E remains positive and within $[0, 1]$.

2.1.4. Total Transaction Cost

The total transaction cost is another essential constraint in portfolio selection. The transaction cost is positive if the investor buys stock and is negative if the investor sells stock. Let us say that $\Phi(E)$ represents the transaction cost of the portfolio; it is given as,

$$\Phi(E) = [\Phi_1(E_1), \Phi_2(E_2), \Phi_3(E_3), \dots, \Phi_i(E_i)], \tag{7}$$

where $i \in \{1, 2, 3, \dots, K\}$ and $\Phi_i(E_i)$ represent the transaction cost of the i -th stock. The total transaction cost refers to the sum of all the individual stocks, which is given as

$$\Phi_t(\mathbf{E}) = \sum_{i=1}^K \Phi_i(E_i). \tag{8}$$

If $\Phi_t(\mathbf{E}) > 0$, it means more stock is bought than sold. Likewise, if $\Phi_t(\mathbf{E}) < 0$, it means that more stock is sold than bought. Generally, the transaction cost includes some additional charges, which we can formulate using a linear transaction model [55], which includes a linear function $\alpha = [\alpha_1, \alpha_2, \alpha_3, \dots, \alpha_i]$, where $i \in \{1, 2, 3, \dots, K\}$. The transaction cost of the i -th stock in the portfolio is given as,

$$\Phi_i(E_i) = \alpha_i E_i. \tag{9}$$

We can rewrite (7) using (9) as,

$$\Phi(\mathbf{E}) = \alpha \mathbf{E}^T. \tag{10}$$

We can combine (5) and (10) into a single constraint, which is given as,

$$\chi(\mathbf{E}) = (\mathbf{1} + \alpha) \mathbf{E}^T = 1. \tag{11}$$

2.1.5. Cardinality Constraint

Another real-world constraint in portfolio selection is known as the cardinality constraint. So far, we have assumed that investment is made in all of the K stocks. However, in a real case scenario, it is observed that the investor may want to exclude some stocks $n (< K)$ from the final portfolio selection, which is known as a cardinality constraint. We can make such a decision by introducing a binary decision vector, i.e., $\mathbf{b} = [b_1, b_2, b_3, \dots, b_i, \dots, b_n]$, where $b_i \in \{0, 1\}$. According to the cardinality constraint,

$$\sum_{i=1}^K b_i = n. \tag{12}$$

We also need to reformulate (6) according to (12), which is given as,

$$\mathbf{0} \leq \mathbf{E} \leq \mathbf{b}. \tag{13}$$

2.2. Portfolio Selection Models

Here, we will discuss the three known models for portfolio selection: mean variance model, efficient frontier model, and Sharpe ratio model.

2.2.1. Mean-Variance Model

The primary objective of the mean variance model is to minimize the risk involved in portfolio selection, and it treats the expected return (profit) as a constraint. We can formulate the mean variance model using (2), (3), and (11)–(13), which is given as,

Minimize:

$$\min_E v(\mathbf{E}) \tag{14}$$

Subject to:

$$\zeta(\mathbf{E}) = \mathbf{E}\mathbf{e}^T - k \geq 0 \tag{15}$$

$$\chi(\mathbf{E}) = (\mathbf{1} + \boldsymbol{\alpha})\mathbf{E}^T = 1 \tag{16}$$

$$\sum_{i=1}^K b_i = n \tag{17}$$

$$\mathbf{0} \leq \mathbf{E} \leq \mathbf{b}. \tag{18}$$

The mean variance model is not very flexible, since it restrains the growth in profits. To overcome it, we can make use of an efficient frontier model.

2.2.2. Efficient Frontier Model

In this model, we include expected return (profit) in the objective function. We can formulate the frontier model using (2), (3), and (11)–(13), which is given as,

Minimize:

$$\min_E \lambda v(\mathbf{E}) - (1 - \lambda)\zeta(\mathbf{E}) \tag{19}$$

Subject to:

$$\chi(\mathbf{E}) = (\mathbf{1} + \boldsymbol{\alpha})\mathbf{E}^T = 1 \tag{20}$$

$$\sum_{i=1}^K b_i = n \tag{21}$$

$$\mathbf{0} \leq \mathbf{E} \leq \mathbf{b}. \tag{22}$$

here, $\lambda \in [0, 1]$. If $\lambda = 0$, then the model will maximize the expected-return (profit). However, if $\lambda = 1$, then the model will minimize the risk. The value of λ between $[0, 1]$ will be a trade-off between profit and the risk. The only drawback of the model is that it involves the use of a hyper-parameter λ . To avoid this, we will look into a Sharpe model, which we will optimize using DBAS.

2.2.3. Sharpe Ratio Model

The Sharpe ratio model is another portfolio selection model which includes the ratio of profit $\zeta(\mathbf{E})$ and risk $v(\mathbf{E})$. The objective is to maximize the ratio, which is given as,

$$SR = \frac{\zeta(\mathbf{E})}{v(\mathbf{E})}. \tag{23}$$

We will inverse the formulation (23) to form a minimization problem. The Sharpe ratio model will help to avoid the additional hyper-parameter λ . Now, the objective is to

minimize $\frac{v(E)}{\xi(E)}$, which will in turn maximize the profit and minimize the risk. Again, we can formulate the model using (2), (3), and (11)–(13), which is given as,

Minimization:

$$\min_E \frac{v(E)}{\xi(E)} \tag{24}$$

Subject to:

$$\chi(E) = (\mathbf{1} + \boldsymbol{\alpha})E^T = 1 \tag{25}$$

$$\sum_{i=1}^K b_i = n \tag{26}$$

$$\mathbf{0} \leq E \leq \mathbf{b}. \tag{27}$$

This model will be used for the portfolio optimization. In the next section, we will formulate the Distributed Beetle Antennae Search (DBAS), which we will be used to solve the portfolio problem given in (24)–(27).

3. Distributed Beetle Antennae Search (DBAS)

In this section, we will elaborate on the nature of BAS, its formulation, and the algorithm. Later, we will develop DBAS and will discuss its underlying algorithm.

3.1. BAS Formulation and Algorithm

BAS has a biologically inspired meta-heuristic algorithm, which is inspired by the food-searching behavior of the beetle. It has two antennas, i.e., left X_l and right X_r . It registers the smell of the food on both antennae, and based on the intensity of the smell, it either moves in the left direction or right. The beetle repeats this procedure iteratively until it finally reaches the food source. Details on the behavior of beetles and BAS are presented in [56]. Here, we will look into updating the equations of the BAS algorithm, which are responsible for converging the searching particle toward the optimal solution.

Imagine a non-linear objective function $F(X)$, where X is a vector of optimizing variables. We can represent an objective function as,

$$\min_X F(X). \tag{28}$$

Here, we are solely considering an objective function, while the real-world problem would include additional constraints, as shown in (24)–(27). The objective of the BAS is to find the optimal solution of (28) by tweaking the values of X such that the maximum value of (28) is achieved. Here, it is worth mentioning that we can assume the maximization problem as well. The formulation will be a little different, which will be shown later during the derivation.

From this point forward, we will refer to the beetle as a particle. Let us say that the current position of the particle is $X \in \mathbb{R}^{1 \times K}$. To compute the new position of the particle, we will move it slightly to the right X_r and slightly to the left X_l , which is given as

$$X_r = X + db \tag{29}$$

$$X_l = X - db, \tag{30}$$

where $b \in \mathbb{R}^{1 \times K}$ is similar to X . Here, d is an antenna length, which determines how big or small a step should be taken in each iteration. In the beginning, d will have a larger value allowing the particle to explore more of the search space, and over time when the particle approaches the optimal solution, the value of d becomes small.

The next step is to compute the objective function value at X_r and X_l , so that BAS can decide its course, i.e., either in the X_r direction or X_l direction. The computation of $F(X)$ is given as,

$$F_r = F(X_r) \tag{31}$$

$$F_l = F(X_l), \tag{32}$$

where F_r and F_l are scalar values of the objective function at X_r and X_l respectively. Now, BAS will compute the next step based on the difference of the values of F_r and F_l , which is given as,

$$\Delta F = F_r - F_l \tag{33}$$

$$X = X - \tau \text{sgn}(\Delta F) \mathbf{b}, \tag{34}$$

where sgn is an activation function to translate the value of ΔF between $[-1, 1]$. Likewise, τ is another hyper-parameter, which is used to decide the step length of the BAS particle. This concludes the general framework of BAS. The algorithm is shown in Algorithm 1.

Algorithm 1 BAS Algorithm.

Objective Function:

$$F(X, O)$$

DBAS Initialization:

$$\eta = 0.99$$

$$d = 0.9$$

$$\tau = 0.9$$

Portfolio Initialization:

$$T = \text{iter}$$

$$D = \text{dim}$$

$$X = \text{randn}(1, D)$$

$$O = [M_n, C_n] \quad M_n : \text{Mean} \quad C_n : \text{Covariance}$$

$$F_{best} = F(X, P)$$

$$X_{best} = X$$

For $i = 1 : T$

$$\mathbf{b} = \text{randn}(1, D)$$

 Compute X_r and X_l using (29) and (30)

 Compute F_r and F_l using (31) and (32)

 Compute X using (34)

$$F = F(X, O)$$

If $F_{min} < F_{best}$:

$$\quad F_{best} = F_{min}$$

$$\quad X_{best} = X$$

Else:

$$\quad X = X_{best}$$

End If

$$d = \eta d + 0.01$$

$$\tau = \eta \tau$$

End For

This algorithm is designed for the portfolio selection problem. The objective function includes $F(X, O)$, where O includes all the parameters necessary for the portfolio problem, i.e., M means of the stocks, C covariance matrix of the stocks, and other constraints. The single-particle BAS algorithm is limited to single portfolio optimization because of its computational limitations. In order to optimize multiple portfolios at once, we need to

introduce a more robust nature in the already existing framework, which we will introduce in DBAS formulation.

Remark 1. The above formulation of BAS is for the minimization problem. For the maximization problem, we need to modify the (34), as shown below,

$$X = X + \tau \text{sgn}(\Delta F)b, \tag{35}$$

where the $-$ sign is replaced with the $+$ sign. It will help BAS to move up the valley in the search space.

In the next section, we will formulate the DBAS algorithm. Unlike BAS, the DBAS formulation will be better focused on the portfolio problem. However, it is worth mentioning that the algorithm is not problem-specific, as an objective function must be defined for any real-world problem. The schematic of the proposed algorithm is shown in Figure 2.

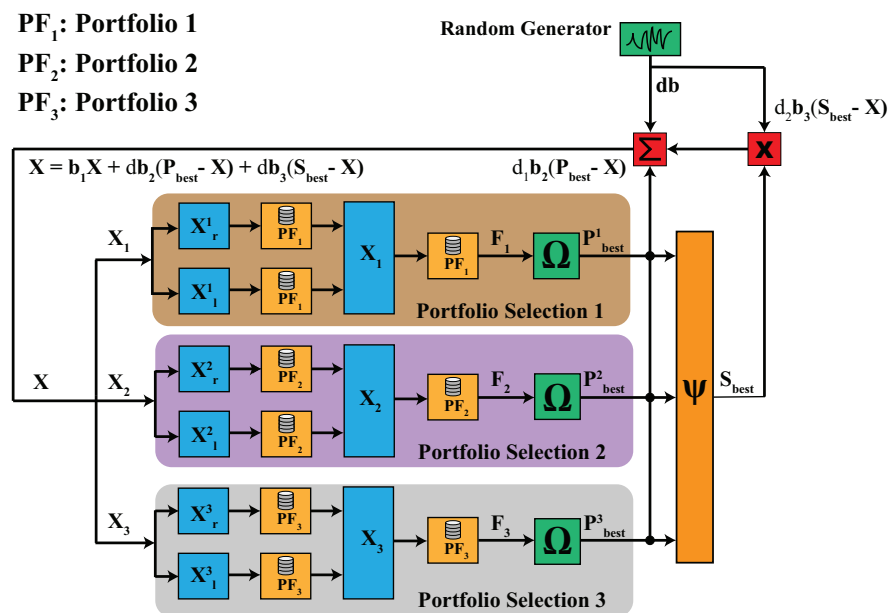


Figure 2. The schematic of the DBAS algorithm for the multi-portfolio selection problem. It consists of 3 portfolios and clearly shows that each particle $[X_1, X_2, X_3]$ optimizes portfolio $PF_1, PF_2,$ and $PF_3,$ respectively. It can be seen that particles do not share any portfolio database or stock information among the swarm, which ensures privacy.

3.2. DBAS Formulation and Algorithm

DBAS is a hybrid variant of BAS and PSO (Particle Swarm Optimization) algorithms. It mimics the swarm-like nature of PSO, where each step of the particles is based on the particle's best position P_{best} and the swarm's best position S_{best} . However, it uses the BAS updating strategy given in (34).

3.2.1. DBAS Updating Criteria

We will modify the updating criteria for X_r and X_l given in (29) and (30). The updating criteria depend on three factors: the particle's best position P_{best} , the swarm's best solution S_{best} , and the random direction db . The modified updating criteria is given as,

$$V = b_1 V + d_1 b_2 (P_{best} - X) + d_2 b_3 (S_{best} - X) \tag{36}$$

$$X_r = X + db + V \tag{37}$$

$$X_l = X - db - V, \tag{38}$$

where $\mathbf{b} \in \mathbb{R}^{D \times K}$ and $[b_1, b_2, b_3] \in \mathbb{R}$. Here, $\mathbf{X} \in \mathbb{R}^{D \times K}$ represents the particles positions, $\mathbf{P}_{best} \in \mathbb{R}^{D \times K}$ shows the particles best positions, and $\mathbf{S}_{best} \in \mathbb{R}^{D \times K}$ is the swarm's best position, which are stacked in a row to meet the dimensionality requirement. Likewise, $[d, d_1, d_2]$ are scalars. Typical swarm algorithms are used to compute a single objective function, but our objective is to optimize multiple objective functions since each portfolio comprises different stocks. Therefore, it is worth mentioning that $\mathbf{X} \in \mathbb{R}^{D \times K}$, where D and K represent the number of portfolios and portfolio size, respectively. Likewise, $\{\mathbf{b}_1, \mathbf{b}_2\} \in \mathbb{R}^{D \times K}$ are two random vectors and d represents the antenna size. Each particle in DBAS corresponds to a single portfolio. The objective is that each particle will optimize its corresponding portfolio locally, i.e., $\mathbf{P}_{best}^j \in \mathbb{R}^{1 \times K}$, where $j \in \{1, 2, 3, \dots, D\}$, and the swarm will optimize all portfolios, i.e., \mathbf{S}_{best} , collectively.

After computing \mathbf{X}_r and \mathbf{X}_l , the next step is to compute the objective function value for each portfolio, i.e., each particle. It is given as,

$$F_r = F(\mathbf{X}_r, \mathbf{O}) \tag{39}$$

$$F_l = F(\mathbf{X}_l, \mathbf{O}), \tag{40}$$

where \mathbf{O} includes all the parameters necessary for portfolio optimization as mentioned in the problem formulation section. Here, $\{F_r, F_l\} \in \mathbb{R}^{D \times 1}$ and $F(\cdot)$ is a vector of dimension D ; it includes the objective functions of all portfolios. Next, each position of particle \mathbf{X} is updated using,

$$\Delta F = F_r - F_l \tag{41}$$

$$\mathbf{X} = \mathbf{X} - \tau \text{sgn}(\Delta F) \mathbf{b}. \tag{42}$$

Then, the objective function value of each portfolio is computed, i.e., the particle at \mathbf{X} , which is given as,

$$F = F(\mathbf{X}, \mathbf{O}), \tag{43}$$

where F has similar dimensions as F_r and F_l . If the objective function value $F_j(\cdot)$ of a j -th particle at $\mathbf{X}_j \in \mathbb{R}^{1 \times K}$ is less than its personal best \mathbf{P}_{best}^j , then update \mathbf{P}_{best}^j with \mathbf{X}_j . Otherwise, retain the old best values. This updating rule for all the particles \mathbf{X} is given as,

$$\mathbf{P}_{best} = \Omega(\mathbf{X}) = \begin{cases} \mathbf{X}, & \text{if } F(\mathbf{X}) < \mathbf{P}_{best} \\ \mathbf{P}_{best}, & \text{otherwise.} \end{cases} \tag{44}$$

Now, the next step is to obtain the swarm's best position. This can be done by simply looking for the minimum value of the objective function in $F(\cdot)$, which is given as,

$$[F, j] = \min(F(\mathbf{X}, \mathbf{O})). \tag{45}$$

If the value of F is less than the swarm's best solution G_{best} , then update \mathbf{S}_{best} ; otherwise, retain the old best, which is given as,

$$\mathbf{S}_{best} = \psi(F) = \begin{cases} \mathbf{X}_j, & \text{if } F < G_{best} \\ \mathbf{S}_{best}, & \text{otherwise.} \end{cases} \tag{46}$$

To further randomize the process, we have included another condition to the update d and τ . We have included a random variable $r = \text{rand} \in [0, 1]$; if $r < 0.5$, then we will update the values of d and τ . The pseudocode is shown in Algorithm 2.

Algorithm 2 DBAS Algorithm.

Objective Function:
 $F(\mathbf{X}, \mathbf{O})$

DBAS Initialization:
 $\eta = 0.99$
 $d = 0.9$
 $d_1 = 0.9$
 $d_2 = 0.9$
 $\tau = 0.9$

Portfolio Initialization:
 $T = iter$ %Iterations
 $D = pop$ %Total Portfolios
 $K = dim$ %No. of Stocks In Each Portfolio
 $\mathbf{X} = \text{randn}(D, K)$
 $\mathbf{X}_{best} = \mathbf{X}$
 $\mathbf{O} = [\mathbf{O}_1, \mathbf{O}_2, \mathbf{O}_3, \dots, \mathbf{O}_K]$
 % \mathbf{O}_K Includes Parameters For k -th Portfolio
 % $\mathbf{O}_K = [M_K, C_K]$ M_K : Mean C_K : Covariance
 $\mathbf{P}_{min} = F(\mathbf{X}, \mathbf{P})$
 $[G_{best}, ind] = \min(F(\mathbf{X}, \mathbf{P}))$
 $\mathbf{S}_{best} = \mathbf{X}_{ind}$
For $i = 1 : T$
 $\mathbf{b} = \text{randn}(D, K)$
 $b_1 = \text{randn}(1, 1)$
 $b_2 = \text{randn}(1, 1)$
 $b_3 = \text{randn}(1, 1)$
 Compute \mathbf{V} using (36)
 Compute \mathbf{X}_r and \mathbf{X}_l using (37) and (38)
 Compute F_r and F_l using (39) and (40)
 Compute \mathbf{X} using (42)
 For $j = 1 : D$
 $F = F_j(\mathbf{X}_j, \mathbf{O}_j)$
 If $F < P_{min}^j$:
 $P_{min}^j = F$
 $\mathbf{P}_{best}^j = \mathbf{X}_j$
 End If
 End For

 $[F, ind] = \min(F(\mathbf{X}, \mathbf{O}))$

 If $F < G_{best}$:
 $G_{best} = F$
 $\mathbf{s}_{best} = \mathbf{X}_{ind}$
 $\mathbf{S}_{best} = \text{repmat}(\mathbf{s}_{best}, D, 1)$
 End If
 $r = \text{rand}$
 If $r < 0.5$:
 $d = \eta d + 0.01$
 $d_1 = \eta d_1 + 0.01$
 $d_2 = \eta d_2 + 0.01$
 $\tau = \eta \tau$
 End If

End For

3.2.2. DBAS Privacy Policy

Each particle in DBAS deals with a single portfolio. A particle alone has access to the private data of the assigned portfolio, including: stock names, investment amount, mean of the portfolio, and variance of the portfolio. The portfolio is like a black box. The particle X_j will enter the black box $F_j(X_j, O)$, will compute the objective function of the portfolio and will give out the objective function value F_j while keeping the privacy of the private database and portfolio information. The objective function value, i.e., gradient, will be available to all the other particles and based on all the gradients, i.e., objective function values of all particles, the DBAS algorithm will compute the swarm's best solution to decide the next step. It helps the DBAS to efficiently find the optimal selection of all portfolios without violating the confidentiality and privacy of portfolios. The concept of DBAS privacy is shown in Figure 3.

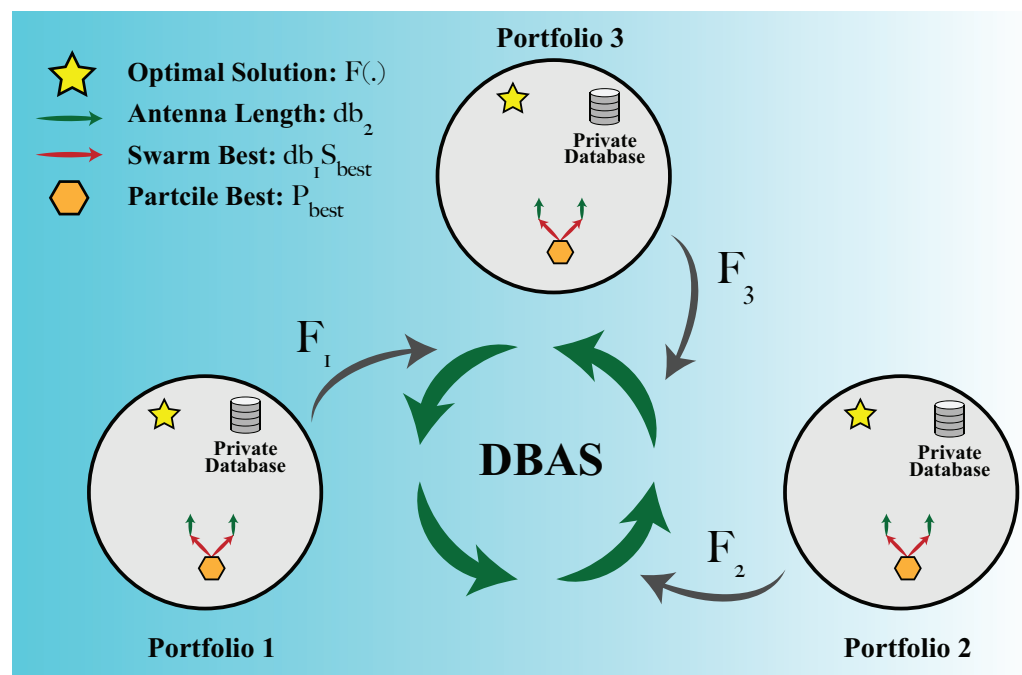


Figure 3. Each particle in DBAS is assigned to a single portfolio, and the particle alone has access to the private database of the portfolio. In DBAS, the particle in swarm only shares the objective function values F , i.e., gradients.

4. Simulation Results

In this section, we will discuss the stock data used for the multiple portfolio selection problem. Furthermore, the DBAS algorithm will be employed to solve the optimization problem formulated in the problem formulation selection.

4.1. Stock Data

For the simulation, we collected real-world stock data from the NASDAQ stock market in 2017. The data comprise several hundred stock companies. A total of 25 known companies were selected for the simulation. Then, 200 days worth of stock closing prices were collected for each company to understand the data trend in more detail and to provide more robust portfolios. All the 25 companies are shown in Table 2. The volatility of the stock market is shown in Figure 4. It can be seen how abruptly the stock prices (return rate) change over time.

Table 2. NASDAQ Symbols of The Stock Companies In Portfolio Selection.

Companies 1–5	GOOGL	MSFT	AMZN	FB	IBM
Companies 6–10	A	AA	AAU	AABA	AAC
Companies 11–15	AADR	AAL	AAMC	AAME	AAN
Companies 16–20	NCA	NCI	QAT	QD	CODI
Companies 20–25	EMR	EMXC	FET	FC	ABBV

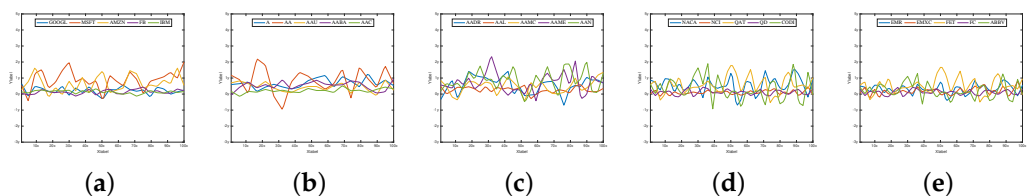


Figure 4. The return rate for all the 25 companies for 200 days of NASDAQ stock data in 2017. (a–e) represents the data of companies 1–5, companies 6–10, companies 11–16, companies 16–20, and companies 20–25, respectively.

In our simulation, there are four multi-portfolio optimization problems, i.e., 5 stock companies, 10 stock companies, 15 stock companies, and 20 stock companies. In each multi-portfolio selection problem, we will be optimizing *three* portfolios. For instance, in the *five* stock companies multi-portfolio selection problem, DBAS will optimize three portfolios, each looking for an optimal selection of stock companies. Considering the stochastic nature of the DBAS algorithm and how results can vary with each experiment, we performed simulation on each portfolio for 10 times, and the average or mean result is obtained. The computational resources used in the simulations are given below:

- Software: MATLAB;
- System: MacBook Pro;
- Processor: 2.2 GHz;
- Cores: 6–Core Intel Core i7;
- Memory: 6 GB 2400 MHz DDR4;
- Graphics: Radeon Pro 555X 4 GB.

4.2. Three Portfolios of Five Stock Companies

For the first simulation category, *three* portfolios were selected, each consisting of *five* companies. The objective is to optimize the three objective functions (24)–(27), i.e., portfolios, such that the raw data of each portfolio remain private and without sharing the private databases that DBAS optimizes. There are a few hyper-parameters in DBAS, i.e., antenna length d and particle step-size τ . We selected the values of these hyper-parameters through trial and error, e.g., $\tau = 0.900$, $d = 0.999$, and $\eta = 0.900$, which are shown in Table 3. In addition, a few other parameters were selected for the simulation, i.e., total iterations $T = 500$, swarm population $D = 3$, dimension of each portfolio $K = 5$.

Table 3. DBAS Convergence Profile for Different Portfolios.

	Companies: 5			Companies: 10		
	Portfolio 1	Portfolio 2	Portfolio 3	Portfolio 1	Portfolio 2	Portfolio 3
n	5	5	5	7	8	9
G_{best}	10^{-7}	10^{-7}	10^{-7}	10^{-6}	10^{-6}	10^{-6}
P_{best}	10^{-6}	10^{-7}	10^{-6}	10^{-6}	10^{-6}	10^{-4}
SR	72.348	24.804	39.582	9.108	5.319	3.151
$(1 + \alpha)E = 1$	1.116	1.179	1.065	1.153	1.140	0.964
DBAS:						
η		0.900			0.900	
$d = d_1 = d_2$		0.999			0.900	
τ		0.900			0.900	
sgn		$[-1, 1]$			$[-1, 1]$	
Some Additional Parameters:						
T		500			500	
D		3			3	
K		5			5	
$H(E, \sigma)$ Eval.		4500			4500	
	Companies: 15			Companies: 20		
	Portfolio 1	Portfolio 2	Portfolio 3	Portfolio 1	Portfolio 2	Portfolio 3
n	15	12	10	15	20	18
G_{best}	10^{-4}	10^{-4}	10^{-4}	10^{-7}	10^{-7}	10^{-7}
P_{best}	10^{-4}	0.020	0.001	10^{-7}	10^{-7}	10^{-6}
SR	7.088	3.667	4.667	58.71	21.56	191.6
$(1 + \alpha)E = 1$	0.930	1.088	1.103	0.9893	1.136	1.021
DBAS:						
η		0.850			0.950	
$d = d_1 = d_2$		0.900			0.900	
τ		0.850			0.850	
sgn		$[-1, 1]$			$[-1, 1]$	
Some Additional Parameters:						
T		500			500	
D		3			3	
K		5			5	
$H(E, \sigma)$ Eval.		4500			4500	

After setting all of the parameters. DBAS is ready to optimize the portfolio problem mentioned in (24)–(27). The simulation results are evaluated based on three parameters: swarm convergence G_{best} , particles convergence P_{best} , Sharpe ratio SR , and the total investment constraint $(1 + \alpha)E = 1$. The results are shown in Table 3 and the convergence profiles of G_{best} , P_{best} , SR and $(1 + \alpha)E = 1$ are shown in Figures 5–8a. For *three* portfolios of *five* stock companies, the swarm best solution turns out to be 10^{-7} , and the convergence profile in Figure 5a shows how efficiently and quick DBAS converges to the optimal solution. Likewise, the convergence of each particle, i.e., each portfolio, is also robust, as shown in Figure 6a. However, the convergence rates do not give us the relationship between the profit and risk. For that, the Sharpe ratio curve was computed. It can be seen in Figure 7a that each portfolio has achieved substantial profit with minimal risk involved. Finally, it is essential that the investment in stocks remains around ≈ 1 . We have shown the convergence profile of $(1 + \alpha)E = 1$ in Figure 8a, and it can be seen that all three investments converge to around 1, which is required. The detailed results are also shown in Table 3.

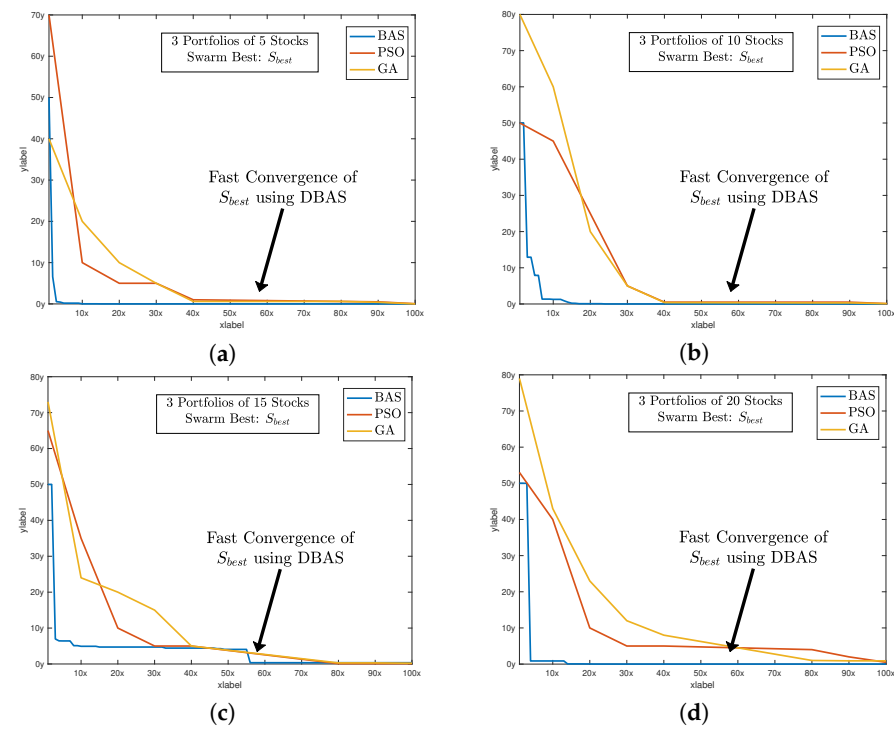


Figure 5. The sharp and fast convergence of DBAS swarm’s G_{best} toward the minima while selecting optimal configuration of all 3 portfolios. It also shows the comparison with PSO and GA algorithms, and it can be seen that the convergence profile of DBAS is fast compared to others. (a) shows the global convergence profile of all algorithms. Likewise, (b) shows the convergence of BAS, PSO, and GA. And finally, (c,d) shows the convergence of 15 and 20 stocks of all three algorithms respectively.

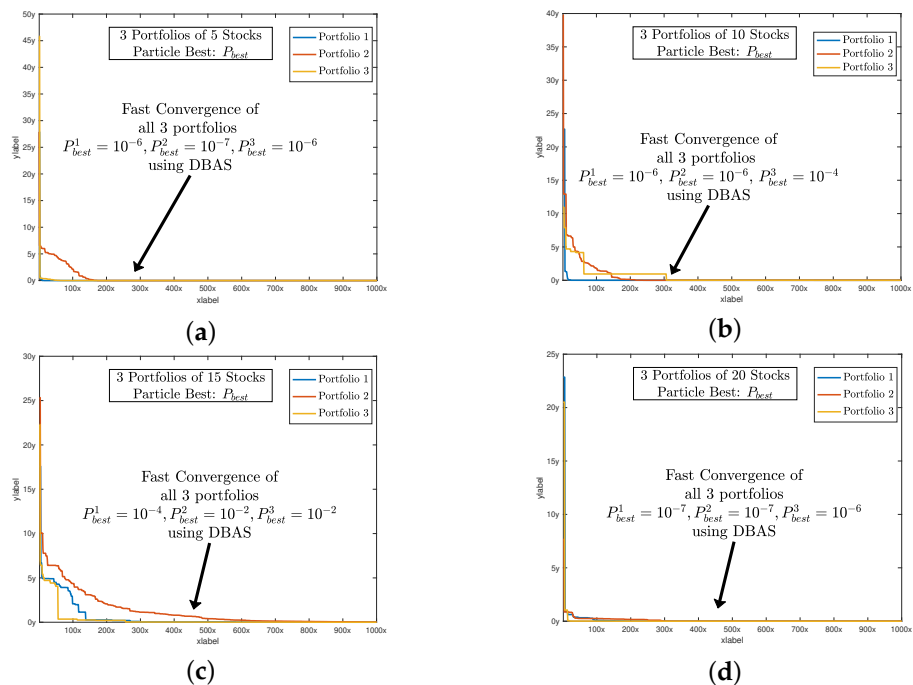


Figure 6. The sharp and fast convergence of DBAS particles P_{best} toward their respective minimas while selecting an optimal configuration of their portfolios. Since we are dealing with three portfolios, we can see the three convergence profiles. (a) shows the global convergence profile of all algorithms. Likewise, (b) shows the convergence of BAS, PSO, and GA. And finally, (c,d) shows the convergence of 15 and 20 stocks of all three algorithms respectively.

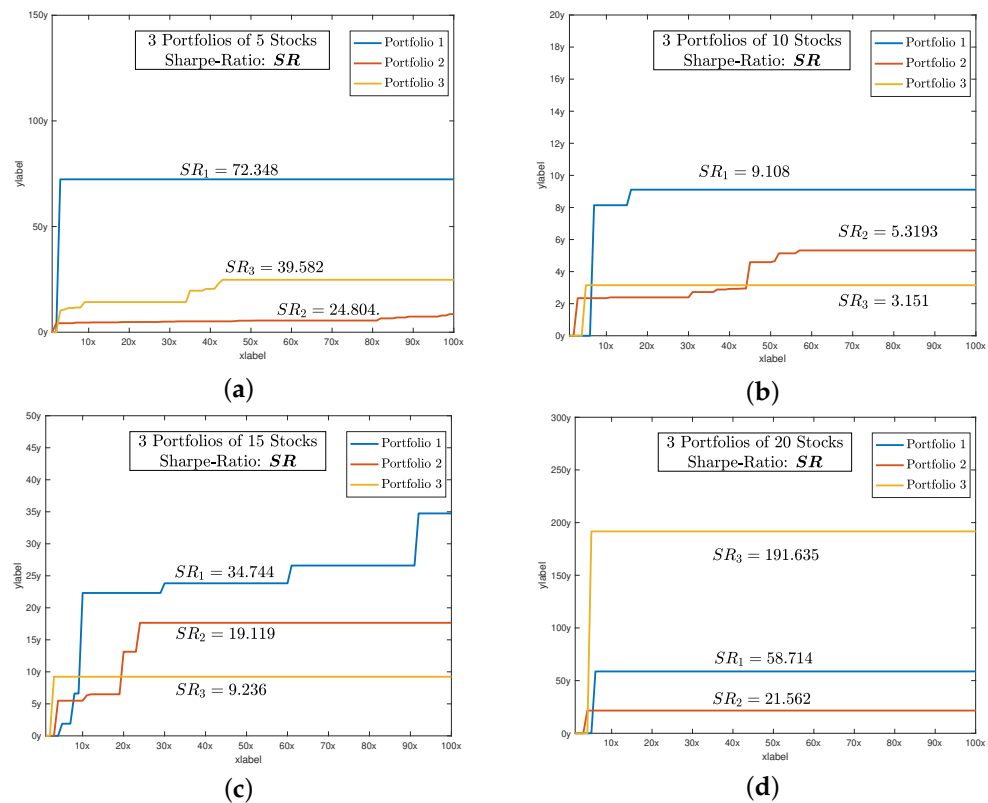


Figure 7. The rising trend of Sharpe ratio SR as the DBAS moves toward the optimal solution of portfolio selection problem. The higher value of SR indicates that each portfolio has a higher profit $\zeta(E)$ and lower risk $v(E)$, as shown in (23). (a) shows the convergence profile of sharpe-ratio of 5 stocks. Likewise, (b) shows the convergence of sharpe-ratio of 10 stocks. And finally, (c,d) shows the convergence of sharpe-ratio of 15 and 20 stocks respectively.

The main takeaway from the results is that DBAS can converge multi-portfolios and ensures the clients' secrecy and privacy. In the simulated results, it can be seen that each particle in DBAS only shares the objective function value P_{best}^j , i.e., gradient with other particles, whereas the private information of the portfolio remains inaccessible to other portfolios.

4.3. Three Portfolios of 10 Stock Companies

For the second simulation scenario, we again selected *three* portfolios, each consisting of 10 companies. The values of hyper-parameters were once again chosen through trial and error, which are also shown in Table 3. In addition, the other parameters for the simulation include total Iterations $T = 500$, swarm population $D = 3$, dimension of each portfolio $K = 10$.

The simulation results are shown in Table 3, and the convergence profiles of G_{best} , P_{best} , SR and $(1 + \alpha)E = 1$ are shown in Figures 5–8b. For the *three* portfolios of 10 stock companies, the swarm best solution turns out to be 10^{-6} . Its convergence profile is shown in Figure 5b. Likewise, the convergence of each particle, i.e., each portfolio, is also robust and shown in Figure 6b. Their convergence values turn out to be optimal, i.e., $P_{best} = [10^{-6}, 10^{-6}, 10^{-4}]$. The Sharpe ratio curve is shown in Figure 7b, and it can be seen that each portfolio has achieved substantial profit with minimal risk. We have also shown the convergence profile of $(1 + \alpha)E = 1$ in Figure 8b, where it can be seen that all three investments converge to around 1, which is again required. The detailed results are also shown in Table 3.

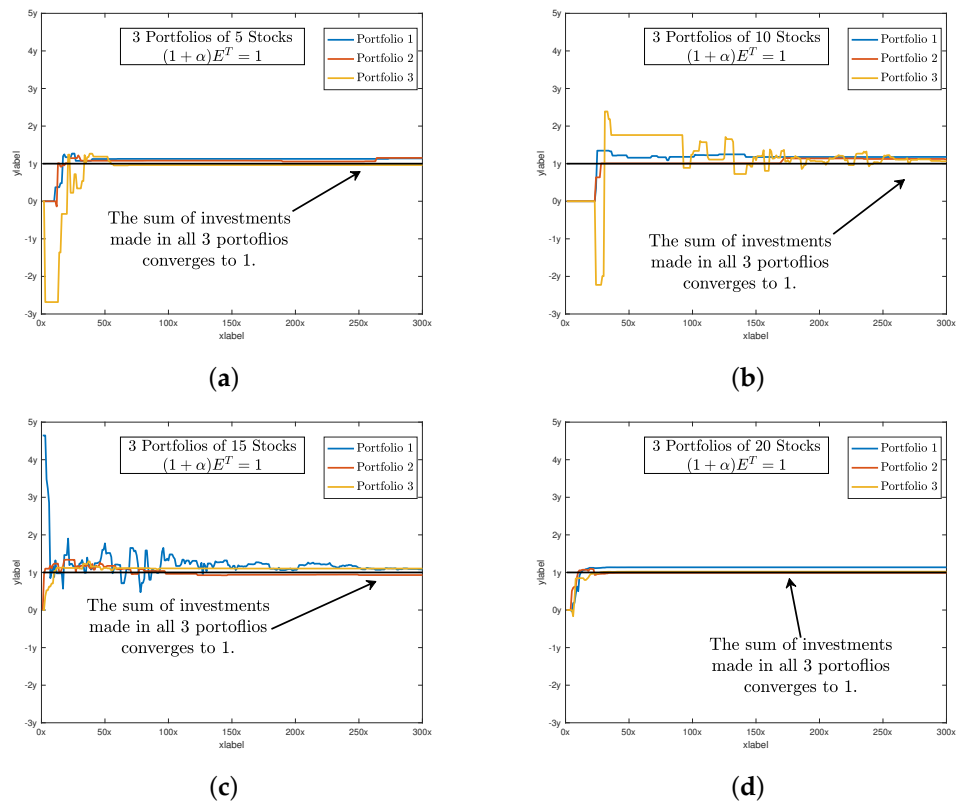


Figure 8. It shows that as the portfolio selection problem converges toward the optimal solution, the sum of normalized investment $(1 + \alpha)E \approx 1$. There are some spikes in the beginning; however, all the particles of the respective portfolio converge to 1. (a) shows the convergence of normalized investment $(1 + \alpha)E \approx 1$ of 5 stocks. Likewise, (b) shows the convergence of normalized investment of 10 stocks. And finally, (c,d) shows the convergence of normalized investment of 15 and 20 stocks respectively.

4.4. Three Portfolios of 15 Stock Companies

For the third simulation scenario, we again selected *three* portfolios, each consisting of 15 companies. Once again, the values of the hyper-parameters were chosen through trial and error, which are also shown in Table 3.

The simulation results are shown in Table 3 and the convergence profiles of G_{best} , P_{best} , SR and $(1 + \alpha)E = 1$ are shown in Figures 5–8c. For the *three* portfolios of 15 stock companies, the swarm’s best solution turns out to be 10^{-4} . Its convergence profile is shown in Figure 5c. Likewise, the convergence of each particle, i.e., each portfolio, is also robust and shown in Figure 6c. Their convergence values turn out to be again optimal, i.e., $P_{best} = [10^{-4}, 0.020, 0.001]$. The Sharpe ratio curve is shown in Figure 7b, and it can be seen that each portfolio has again achieved substantial profit with minimal risk. We have also shown the convergence profile of $(1 + \alpha)E = 1$ in Figure 8c, and it can be seen that all three investments converge to around 1, which is required. The detailed results are also shown in Table 3.

4.5. Three Portfolios of 20 Stock Companies

For the fourth and the last simulation scenario, we selected *three* portfolios, each consisting of 20 stock companies. Hyper-parameters are also shown in Table 3.

The simulation results are shown in Table 3 and the convergence profiles of G_{best} , P_{best} , SR and $(1 + \alpha)E = 1$ are shown in Figures 5–8d. For *three* portfolios of 15 stock companies, the swarm’s best solution turns out to be 10^{-7} . Its convergence profile is shown in Figure 5d. Likewise, the convergence of each particle, i.e., each portfolio, is also robust and shown in Figure 6d. Their convergence values turns out to be optimal, i.e.,

$P_{best} = [10^{-7}, 10^{-7}, 10^{-6}]$. The Sharpe ratio curve is shown in Figure 7b, and it can be seen that the ratio is again substantially high. We have also shown the convergence profile of $(1 + \alpha)E = 1$ in Figure 8d, and it can be seen that all three investments converge to around 1, which is required. The detailed results are also shown in Table 3.

The primary limitation of DBAS is the “Virtual particle,” which means that for each iteration, we have to compute the objective function value for three times for F_r , F_l , and F . It could make it computationally expensive and consume time. In the future, we will work on eliminating the “virtual particle” limitation, and we will also include some other meta-heuristic algorithms such as GSK [57] to compare with. Likewise, we will work on some additional statistical analysis including non-parametric statistical tests such as Wilcoxon Signed Rank Test and Friedman.

5. Conclusions

In this paper, a framework to ensure the privacy of stock portfolios in the multi-portfolio selection problem was proposed. This involved the design of a distributed variant of the BAS algorithm known as Distributed Beetle Antennae Search (DBAS). DBAS combines the swarm-like behavior of PSO with BAS’s updating rule. Each particle in the swarm is assigned to optimize a single portfolio, and the particles only share the gradient of their respective portfolio with the swarm, avoiding the exposure of the private database and stock information of portfolios. The algorithm was then simulated on real-world stock data extracted from the NASDAQ stock market for 25 stock companies. The simulation is divided into *four* categories, and in each category, *three* portfolio models were optimized. The simulation results show that DBAS not only ensures the privacy of portfolios but is also robust, computationally economical, and time efficient.

Author Contributions: A.T.K.: methodology, software, validation; X.C.: Conceptualization, resources; B.L.: funding acquisition, formal analysis; A.F.: data curation, visualization, writing—review and editing. All authors have read and agreed to the published version of the manuscript.

Funding: This work is supported by the National Natural Science Foundation of China under grant 61966014.

Institutional Review Board Statement: Not applicable.

Informed Consent Statement: Not applicable.

Data Availability Statement: Not applicable.

Conflicts of Interest: The authors declare no conflict of interest.

References

1. Bienstock, D. Computational study of a family of mixed-integer quadratic programming problems. *Math. Program.* **1996**, *74*, 121–140. [CrossRef]
2. Ertenlice, O.; Kalayci, C.B. A survey of swarm intelligence for portfolio optimization: Algorithms and applications. *Swarm Evol. Comput.* **2018**, *39*, 36–52. [CrossRef]
3. Perrin, S.; Roncalli, T. Machine learning optimization algorithms & portfolio allocation. In *Machine Learning for Asset Management: New Developments and Financial Applications*; Wiley: Hoboken, NJ, USA, 2020; pp. 261–328.
4. Ta, V.D.; Liu, C.M.; Tadesse, D.A. Portfolio optimization-based stock prediction using long-short term memory network in quantitative trading. *Appl. Sci.* **2020**, *10*, 437. [CrossRef]
5. Leung, M.F.; Wang, J. Minimax and Biobjective Portfolio Selection Based on Collaborative Neurodynamic Optimization. *IEEE Trans. Neural Netw. Learn. Syst.* **2021**, *32*, 2825–2836. [CrossRef] [PubMed]
6. Kadry, S.; Smaili, K. A design and implementation of a wireless iris recognition attendance management system. *Inf. Technol. Control.* **2007**, *36*, 323–329.
7. Kadry, S. On the generalization of probabilistic transformation method. *Appl. Math. Comput.* **2007**, *190*, 1284–1289. [CrossRef]
8. Katsikis, V.N. Computational methods in portfolio insurance. *Appl. Math. Comput.* **2007**, *189*, 9–22. [CrossRef]
9. Zhang, Y.; Gong, H.; Yang, M.; Li, J.; Yang, X. Stepsize Range and Optimal Value for Taylor–Zhang Discretization Formula Applied to Zeroing Neurodynamics Illustrated via Future Equality-Constrained Quadratic Programming. *IEEE Trans. Neural Netw. Learn. Syst.* **2019**, *30*, 959–966. [CrossRef]

10. Liao, B.; Zhang, Y. Different Complex ZFs Leading to Different Complex ZNN Models for Time-Varying Complex Generalized Inverse Matrices. *IEEE Trans. Neural Netw. Learn. Syst.* **2014**, *25*, 1621–1631. [CrossRef]
11. Katsikis, V.N. *An Alternative Computational Method for Finding the Minimum-Premium Insurance Portfolio, Proceedings of the AIP Conference Proceedings, Penang, Malaysia, 10–12 April 2016*; AIP Publishing LLC: Melville, NY, USA, 2016; Volume 1738, p. 480020.
12. Stanimirović, P.S.; Katsikis, V.N.; Li, S. Integration enhanced and noise tolerant ZNN for computing various expressions involving outer inverses. *Neurocomputing* **2019**, *329*, 129–143. [CrossRef]
13. Lai, Z.R.; Dai, D.Q.; Ren, C.X.; Huang, K.K. A Peak Price Tracking-Based Learning System for Portfolio Selection. *IEEE Trans. Neural Netw. Learn. Syst.* **2018**, *29*, 2823–2832. [CrossRef] [PubMed]
14. Stanimirović, P.S.; Ćirić, M.; Katsikis, V.N.; Li, C.; Ma, H. Outer and (b, c) inverses of tensors. *Linear Multilinear Algebra* **2020**, *68*, 940–971. [CrossRef]
15. Brajević, I.; Ignjatović, J. An upgraded firefly algorithm with feasibility-based rules for constrained engineering optimization problems. *J. Intell. Manuf.* **2019**, *30*, 2545–2574. [CrossRef]
16. Brajević, I.; Stanimirović, P. An improved chaotic firefly algorithm for global numerical optimization. *Int. J. Comput. Intell. Syst.* **2018**, *12*, 131–148. [CrossRef]
17. Lai, Z.R.; Dai, D.Q.; Ren, C.X.; Huang, K.K. Radial Basis Functions With Adaptive Input and Composite Trend Representation for Portfolio Selection. *IEEE Trans. Neural Netw. Learn. Syst.* **2018**, *29*, 6214–6226. [CrossRef] [PubMed]
18. O’Cinneide, C.; Scherer, B.; Xu, X. Pooling Trades in a Quantitative Investment Process. *J. Portf. Manag.* **2006**, *32*, 33–43. [CrossRef]
19. Liao, B.; Hua, C.; Can, X.; Katsikis, V.N.; Li, S. Complex Noise-Resistant Zeroing Neural Network for Computing Complex Time-Dependent Lyapunov Equation. *Mathematics* **2022**, *10*, 2817. [CrossRef]
20. Ji, R.; Lejeune, M.A. Risk-budgeting multi-portfolio optimization with portfolio and marginal risk constraints. *Ann. Oper. Res.* **2018**, *262*, 547–578. [CrossRef]
21. Savelsbergh, M.W.P.; Stubbs, R.A.; Vandenbussche, D. Multiportfolio Optimization: A Natural Next Step. In *Handbook of Portfolio Construction*; Guerard, J.B., Ed.; Springer US: Boston, MA, USA, 2010; pp. 565–581. [CrossRef]
22. Iancu, D.; Trichakis, N. Fairness and Efficiency in Multiportfolio Optimization. *Oper. Res.* **2014**, *62*, 1285–1301. [CrossRef]
23. Jing, F. Information pooling game in multi-portfolio optimization. *Contrib. Game Theory Manag.* **2017**, *10*, 27–41.
24. Zhang, G.; Zhang, Q. Multiportfolio optimization with CVaR risk measure. *J. Data Inf. Manag.* **2019**, *1*, 91–106. [CrossRef]
25. Yu, G.; Cai, X.; Long, D.Z. Multi-Portfolio Optimization: A Fairness-Aware Target-Oriented Model 2020. Available online: https://papers.ssrn.com/sol3/papers.cfm?abstract_id=3740629 (accessed on 30 July 2022).
26. Khan, A.H.; Li, S.; Luo, X. Obstacle avoidance and tracking control of redundant robotic manipulator: An RNN-based metaheuristic approach. *IEEE Trans. Ind. Informatics* **2019**, *16*, 4670–4680. [CrossRef]
27. Khan, A.H.; Cao, X.; Li, S.; Katsikis, V.N.; Liao, L. BAS-ADAM: An ADAM based approach to improve the performance of beetle antennae search optimizer. *IEEE/CAA J. Autom. Sin.* **2020**, *7*, 461–471. [CrossRef]
28. Khan, A.T.; Li, S.; Cao, X. Control framework for cooperative robots in smart home using bio-inspired neural network. *Measurement* **2021**, *167*, 108253. [CrossRef]
29. Khan, A.T.; Li, S. Human guided cooperative robotic agents in smart home using beetle antennae search. *Sci. China Inf. Sci.* **2021**, *65*, 122204. [CrossRef]
30. Khan, A.T.; Li, S.; Li, Z. Obstacle avoidance and model-free tracking control for home automation using bio-inspired approach. In *Advanced Control for Applications: Engineering and Industrial Systems*; Wiley: Hoboken, NJ, USA, 2021; p. e63.
31. Khan, A.T.; Li, S.; Zhou, X. Trajectory optimization of 5-link biped robot using beetle antennae search. *IEEE Trans. Circuits Syst. II Express Briefs* **2021**, *68*, 3276–3280. [CrossRef]
32. Khan, A.T.; Cao, X.; Li, Z.; Li, S. Enhanced Beetle Antennae Search with Zeroing Neural Network for online solution of constrained optimization. *Neurocomputing* **2021**, *447*, 294–306. [CrossRef]
33. Zivkovic, M.; Bacanin, N.; Venkatachalam, K.; Nayyar, A.; Djordjevic, A.; Strumberger, I.; Al-Turjman, F. COVID-19 cases prediction by using hybrid machine learning and beetle antennae search approach. *Sustain. Cities Soc.* **2021**, *66*, 102669. [CrossRef]
34. Wu, Q.; Shen, X.; Jin, Y.; Chen, Z.; Li, S.; Khan, A.H.; Chen, D. Intelligent beetle antennae search for UAV sensing and avoidance of obstacles. *Sensors* **2019**, *19*, 1758. [CrossRef]
35. Li, X.; Jiang, H.; Niu, M.; Wang, R. An enhanced selective ensemble deep learning method for rolling bearing fault diagnosis with beetle antennae search algorithm. *Mech. Syst. Signal Process.* **2020**, *142*, 106752. [CrossRef]
36. Huang, J.; Duan, T.; Zhang, Y.; Liu, J.; Zhang, J.; Lei, Y. Predicting the permeability of pervious concrete based on the beetle antennae search algorithm and random forest model. *Adv. Civ. Eng.* **2020**, *2020*, 8863181. [CrossRef]
37. Sun, Y.; Zhang, J.; Li, G.; Wang, Y.; Sun, J.; Jiang, C. Optimized neural network using beetle antennae search for predicting the unconfined compressive strength of jet grouting coalcretes. *Int. J. Numer. Anal. Methods Geomech.* **2019**, *43*, 801–813. [CrossRef]
38. Khan, A.T.; Cao, X.; Li, S.; Katsikis, V.N.; Brajevic, I.; Stanimirovic, P.S. Fraud detection in publicly traded US firms using Beetle Antennae Search: A machine learning approach. *Expert Syst. Appl.* **2021**, *191*, 116148. [CrossRef]
39. Khan, A.T.; Cao, X.; Brajevic, I.; Stanimirovic, P.S.; Katsikis, V.N.; Li, S. Non-linear Activated Beetle Antennae Search: A Novel Technique for Non-Convex Tax-Aware Portfolio Optimization Problem. *Expert Syst. Appl.* **2022**, *197*, 116631. [CrossRef]
40. Khan, A.H.; Cao, X.; Xu, B.; Li, S. Beetle Antennae Search: Using Biomimetic Foraging Behaviour of Beetles to Fool a Well-Trained Neuro-Intelligent System. *Biomimetics* **2022**, *7*, 84. [CrossRef]

41. Liao, B.; Han, L.; He, Y.; Cao, X.; Li, J. Prescribed-Time Convergent Adaptive ZNN for Time-Varying Matrix Inversion under Harmonic Noise. *Electronics* **2022**, *11*, 1636. [CrossRef]
42. Liao, B.; Huang, Z.; Cao, X.; Li, J. Adopting Nonlinear Activated Beetle Antennae Search Algorithm for Fraud Detection of Public Trading Companies: A Computational Finance Approach. *Mathematics* **2022**, *10*, 2160. [CrossRef]
43. Khan, A.T.; Cao, X.; Li, Z.; Li, S. Evolutionary Computation Based Real-time Robot Arm Path-planning Using Beetle Antennae Search. *EAI Endorsed Trans. Robot.* **2022**, *1*, 1–10. [CrossRef]
44. Chen, Z.; Walters, J.; Xiao, G.; Li, S. An Enhanced GRU Model With Application to Manipulator Trajectory Tracking. *EAI Endorsed Trans. Robot.* **2022**, *1*, 1–11. [CrossRef]
45. Ijaz, M.U.; Khan, A.T.; Li, S. Bio-inspired BAS: Run-time Path-planning And The Control of Differential Mobile Robot. *EAI Endorsed Trans. Robot.* **2022**, *1*, 1–10. [CrossRef]
46. Hameed, S.W. Peaks Detector Algorithm after CFAR for Multiple Targets Detection. *EAI Endorsed Trans. Robot.* **2022**, *1*, 1–7. [CrossRef]
47. Khan, A.T.; Cao, X.; Li, S. Dual Beetle Antennae Search system for optimal planning and robust control of 5-link biped robots. *J. Comput. Sci.* **2022**, *60*, 101556. [CrossRef]
48. Khan, A.H.; Cao, X.; Li, S. Obstacle avoidance based decision making and management of articulated agents. In *Management and Intelligent Decision-Making in Complex Systems: An Optimization-Driven Approach*; Springer: Berlin/Heidelberg, Germany, 2021; pp. 1–29.
49. Khan, A.H. Neural Network and Metaheuristic Based Learning and Control of Articulated Robotic Agents. Ph.D. Thesis, Hong Kong Polytechnic University, Hong Kong, China, 2021.
50. Khan, A.T.; Cao, X.; Li, S.; Hu, B.; Katsikis, V.N. Quantum beetle antennae search: A novel technique for the constrained portfolio optimization problem. *Sci. China Inf. Sci.* **2020**, *64*, 152204. [CrossRef]
51. Khan, A.H.; Cao, X.; Katsikis, V.N.; Stanimirović, P.; Brajević, I.; Li, S.; Kadry, S.; Nam, Y. Optimal portfolio management for engineering problems using nonconvex cardinality constraint: A computing perspective. *IEEE Access* **2020**, *8*, 57437–57450. [CrossRef]
52. Chen, T.; Zhu, Y.; Teng, J. Beetle swarm optimisation for solving investment portfolio problems. *J. Eng.* **2018**, *2018*, 1600–1605. [CrossRef]
53. Katsikis, V.N.; Mourtas, S.D.; Stanimirović, P.S.; Li, S.; Cao, X. *Time-Varying Mean-Variance Portfolio Selection under Transaction Costs and Cardinality Constraint Problem via Beetle Antennae Search Algorithm (BAS)*, *Proceedings of the Operations Research Forum, Online, 31 August–3 September*; Springer: Berlin/Heidelberg, Germany, 2021; Volume 2, pp. 1–26.
54. Khan, A.R.; Khan, A.T.; Salik, M.; Bakhsh, S. An optimally configured HP-GRU model using hyperband for the control of wall following robot. *Int. J. Robot. Control Syst.* **2021**, *1*, 66–74. [CrossRef]
55. Zhu, H.; Wang, Y.; Wang, K.; Chen, Y. Particle Swarm Optimization (PSO) for the constrained portfolio optimization problem. *Exp. Syst. Appl.* **2011**, *38*, 10161–10169. [CrossRef]
56. Jiang, X.; Li, S. BAS: Beetle Antennae Search Algorithm for Optimization Problems. *arXiv* **2017**, arXiv:1710.10724.
57. Mohamed, A.W.; Hadi, A.A.; Mohamed, A.K. Gaining-sharing knowledge based algorithm for solving optimization problems: A novel nature-inspired algorithm. *Int. J. Mach. Learn. Cybern.* **2020**, *11*, 1501–1529. [CrossRef]

MDPI
St. Alban-Anlage 66
4052 Basel
Switzerland
Tel. +41 61 683 77 34
Fax +41 61 302 89 18
www.mdpi.com

Biomimetics Editorial Office
E-mail: biomimetics@mdpi.com
www.mdpi.com/journal/biomimetics





Academic Open
Access Publishing

www.mdpi.com

ISBN 978-3-0365-8468-3